CROSS SECTIONS AND ANALYZING POWERS FOR NUCLEON SCATTERING FROM ^{6}Li AND PROTON SCATTERING FROM ^{27}Al

by

Harold Gerdes Pfützner

Department of Physics
Duke University

Date: Aug 10, 1987

Approved:

Richard L Walter
Richard L. Walter, Supervisor

Harold W. Lewis

Thos R. Fortune

Dana W Mance

Edward G. Bilpuch

Dissertation submitted in partial fulfillment of the requirements for the degree of Doctor of Philosophy in the Department of Physics in the Graduate School of Duke University

1987

ABSTRACT

(Physics-Nuclear)

CROSS SECTIONS AND ANALYZING POWERS FOR NUCLEON SCATTERING FROM ^{6}Li AND PROTON SCATTERING FROM ^{27}Al

by

Harold Gerdes Pfützner

Department of Physics
Duke University

Date: August 10, 1987

Approved:

Richard L. Walter

Richard L. Walter, Supervisor

Harold W. Lewis

Floyd J. Fats

Lana W. Nance

Edward G. Bilpuch

An abstract of a dissertation submitted in partial fulfillment of the requirements for the degree of Doctor of Philosophy in the Department of Physics in the Graduate School of Duke University

1987

ABSTRACT

CROSS SECTIONS AND ANALYZING POWERS
FOR NUCLEON SCATTERING FROM ^{6}Li
AND PROTON SCATTERING FROM ^{27}Al

by

Harold Gerdes Pfützner

Analyzing powers have been measured for neutron elastic scattering from ^{6}Li and inelastic scattering to the first excited state of ^{6}Li. These data were obtained in the neutron energy range of 5 to 17 MeV using the time-of-flight technique for determination of the neutron energy. A pulsed polarized deuteron beam was employed to produce a pulsed polarized neutron beam via the ^{2}H($\vec{d}$,$\vec{n}$)^{3}He reaction. Complementary proton analyzing power data as well as cross-section data were measured in the same energy range with four pairs of silicon surface-barrier detectors. An aluminum-foil backing used with the ^{6}Li foil target for the proton scattering measurement made it possible to simultaneously obtain analyzing power and cross-section data for ^{27}Al.

The neutron and proton scattering data obtained in this work along with previously existing neutron cross-section data were analyzed with the spherical optical model. The present optical model analyses extend a previous model describing ^{6}Li along with several other 1-p shell nuclei but based only on cross-section data in a smaller energy range. A global optical model parameter set is presented which adequately describes neutron and proton elastic scattering data between 10 and 17 MeV. Poor quality fits were obtained below 10 MeV where resonance or compound nucleus effects occur; such effects are not accounted for by the optical model.

Resonating group method calculations prepared by H. Hofmann of Erlangen University are presented for the ^{7}Be and ^{7}Li systems. The calculations for elastic scattering cross sections and analyzing powers agree well with the data considering that no variable parameters exist in the model.

The present ^{27}Al proton scattering data were combined with proton scattering data between 15 and 23 MeV and neutron scattering data between 11 and 17 MeV from the literature to form a nucleon-nucleus data set for ^{27}Al. These data were fit with a spherical optical model. Reasonable fits were obtained above 10 MeV with deficiencies in the fits below that energy. The model fits equally well the proton and neutron data with asymmetry and Coulomb correction terms only in the real central potential.

ACKNOWLEDGMENTS

It is a genuine pleasure to have the opportunity to thank all of the people who have contributed in some way to the completion of this dissertation. My heart-felt thanks go to my advisor Prof. Richard L. Walter for giving me the opportunity to work in his program and for his guidance, encouragement, and instruction throughout my stay at Duke. I would like to express a special thank you to certain generous and patient physicists who took time out from their own work to explain carefully various aspects of the experiments and of the theory. These include Garry Tungate, Kim Murphy, Calvin Howell, Robert Varner, Werner Tornow, and Richard Walter. These men all have special talents in the area of teaching and explaining, and whatever understanding I have of certain topics is largely due to them.

There are many people who contributed to the day-to-day functioning of the laboratory who deserve much more than simple recognition in this acknowledgment. Faculty members, staff members, and fellow graduate students all had a hand in this dissertation. Sidney Edwards, Paul Carter, Robert Rummel, Alton Lovette, Chris Westerfeldt, and Patrick Mulkey all worked diligently to improve, maintain, repair, and in some cases build the equipment in the lab. I am also grateful to them for their friendliness and their willingness to answer the many questions from me over the years. My thanks go to Dorothy "Mike" Bailey for her work on many of the drawings in this dissertation and to Patricia Gibson for keeping all the paperwork straight. Other members of the faculty who contributed substantially include Thomas Clegg, Chris Gould, Russell Roberson, and Worth Seagondollar. Members of the Neutron Time-of-Flight group, past and present, who helped in taking the data include Kim Murphy, Ron Pedroni, Calvin Howell, Gerard Honoré, Anli Li, Mark Roberts, and Paul Felsher. These are all amiable men and I have greatly enjoyed working with them on the experiments.

I am grateful to Hartmut Hofmann and his colleagues for providing the Resonating Group calculations for ^{6}Li which are the result of much effort on their part.

Lastly I would like to thank those who have influenced me personally. I am grateful to my wife Lenore for her encouragement and for her help in the preparation of the manuscript. My parents have always encouraged me strongly in my education and gave me many of the tools with which to succeed. Many thanks to my professors at Randolph-Macon College who made my enthusiasm for learning about many things including physics grow and grow. It is indeed humbling to acknowledge everyone that has helped me along the way. Many, many thanks to you all.

This work was supported in part by the United States Department of Energy.

TABLE OF CONTENTS

CHAPTER 3

PROTON SCATTERING MEASUREMENTS

CHAPTER 4

MODEL CALCULATIONS FOR ^{6}Li AND ^{27}Al

LIST OF FIGURES

LIST OF TABLES

CHAPTER 1

INTRODUCTION

The nucleon plus ^{6}Li system stands between two classes of nuclear systems; the first, a few-nucleon system which can be treated as an interaction of the nucleon with the individual nucleons in ^{6}Li, and the second, a system in which a potential can be written that describes the net effect of all the nucleons in the ^{6}Li nucleus. A seven nucleon system is more than can presently be handled in a calculation that considers all the nucleon-nucleon interactions separately. At the other extreme is the optical model viewpoint which is only concerned with the net potential for the nucleon-nucleus interaction. This model is most useful with nuclei consisting of many nucleons where any effects resulting from individual states in the nucleus average together due to their large number. Unfortunately, ^{6}Li is too light of a system for this averaging effect to be well accomplished. On the other hand with the resonating group method it is presently possible to consider the interaction of pairs of clusters within the system, where the nucleon-cluster and cluster-cluster interactions are the foundation. Such a model is currently evolving for the nucleon plus ^{6}Li system, but the development is very lengthy and complex.

Ideally, one desires a model in which the nucleon-nucleon interaction is known and explicitly taken into account, but no accurate one exists at present. The resonating group method does consider smaller portions of the nucleus and as such is a useful step in the direction of the ideal model. The optical model is very useful from a practical standpoint. It predicts amazingly well a huge volume of scattering data including medium to heavy weight nuclei in the energy range of 10 to 300 MeV. This is very important to anyone needing nucleon scattering cross sections whether he is an astrophysicist wishing to develop theories for the formation of stars or is in the nuclear energy industry . For example, information on the ^{6}Li plus nucleon system is particularly useful to studies of

fusion reactors where, for instance, the $^{6}Li(n,t)^{4}He$ reaction is primarily responsible for the production of tritium in the reactor.

Recent work has been expended on deriving a theoretical basis for the phenomenological optical model. These calculations start with a realistic nucleon-nucleon interaction. These so-called microscopic optical models have had surprising success in predicting scattering observables for larger nuclei. The success of a phenomenological optical model parametrization for the nucleon plus ^{6}Li system can serve as a basis for developing future microscopic optical models for light nuclei.

The data presented in this dissertation consist of cross sections and analyzing powers for neutron and proton scattering from ^{6}Li in the energy range of 5 to 17 MeV. The TUNL polarized ion source facility provides us with the capability of producing polarized proton beams and nanosecond bursts of polarized neutrons. This made it possible to accumulate a complete set of scattering data for the ^{6}Li plus nucleon system including both analyzing power and cross section observables.

From an experimental standpoint ^{6}Li is a fairly convenient nucleus for scattering studies. The first excited state of ^{6}Li is at 2.18 MeV [see Fig. (1-1)]. This large energy separation between the ground and first excited states is important for neutron time-of-flight experiments where energy resolution can be a limiting factor. Also, the first excited state is well separated from higher lying states making it convenient to measure inelastic scattering observables for this state. Neutron scattering analyzing powers for the first excited state were obtained at all energies at which elastic data were obtained. Proton scattering cross sections and analyzing powers for the first excited state were also measured along with the proton elastic scattering data. The resolution of the TUNL neutron spectrometer is sufficient to resolve the two peaks in the time-of-flight spectrum. In addition there is an adequate supply of separated ^{6}Li with which to make the relatively large neutron scattering sample.

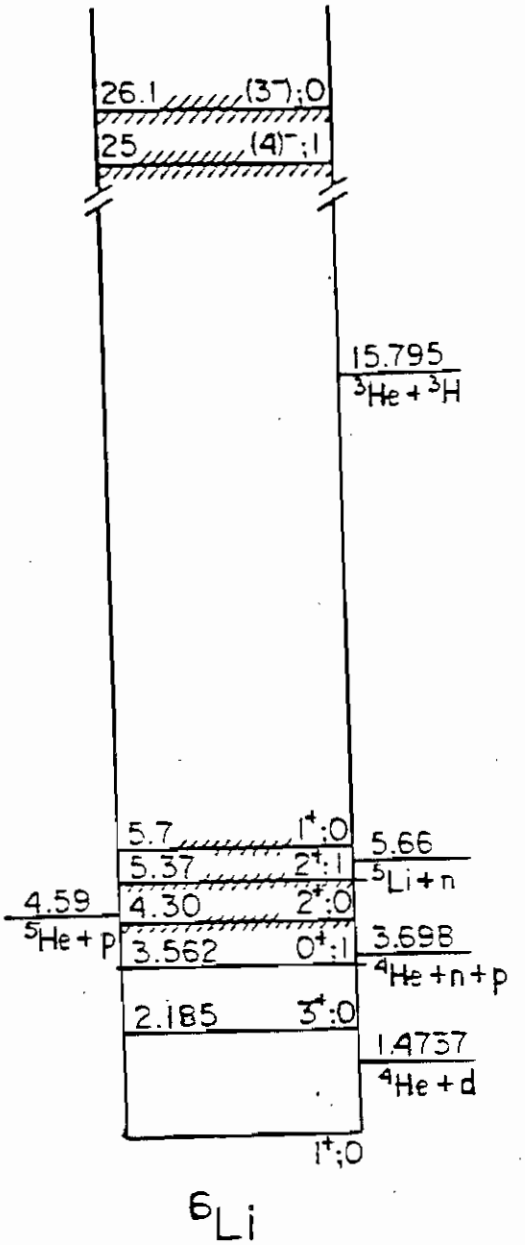

Fig. (1-1) Energy level diagram for ^{6}Li showing the large spacing between the ground, first, and second excited states. [Obtained from (Ajzenberg 74) p.51].

An inconvenience associated with lithium is its strong reactivity which typically results in contaminants of nitrogen and oxygen from the air. This makes the production of a thin foil necessary for the proton scattering measurements a difficult procedure. Additionally the softness of the metal necessitates the use of a suitable foil backing. As is common, for the present proton scattering experiment, aluminum was selected for the backing material. The inherently greater resolution of proton scattering spectrometers makes it possible to obtain well resolved peaks for elastic and inelastic proton scattering from ^{6}Li and from ^{27}Al, so that reliable results were obtained. Nitrogen and oxygen contaminants did adversely affect the results for neutron scattering, but methods developed for applying corrections to the data were straightforward.

A beneficial side-effect of the proton scattering measurements was a prominent peak for elastic scattering of protons from ^{27}Al in the spectra coming from the aluminum backing of the lithium foil. Conveniently the abundance of natural aluminum is 100% ^{27}Al so that isotopically pure results could be obtained from analyzing yields from this peak. Cross sections and analyzing powers were obtained for protons elastically scattered from ^{27}Al for the incident energy range of 5 to 17 MeV. No inelastic data were obtained for ^{27}Al. The elastic scattering proton data along with higher energy data from another laboratory, and neutron data from this laboratory have been fit with a spherical optical model. This analysis on the nucleon plus ^{27}Al system is a continuation of the work of Martin and Walter who undertook a similar optical model parametrization for ^{27}Al, but with a much more limited data base.

The body of the dissertation consists in part of two chapters covering the details of the neutron and proton measurements. Since the experimental techniques differ greatly for the two types of measurements these are discussed in two separate chapters. The experimental chapters contain descriptions of the techniques, details of the equipment used, explanations of the experimental analysis of the data, discussion of ancillary measurements

made for correction purposes, and discussions of the corrections to the data.

A chapter is devoted to describing the steps taken in the theoretical analyses of the data. Included in this chapter is a discussion of the spherical optical model analysis for nucleon scattering from ^{6}Li. Also shown are the results of calculations for the ^{6}Li plus nucleon system based on the resonating group method obtained from H. Hofmann of Erlangen University. These calculations are compared to the present neutron and proton data. Finally the spherical optical model analysis for ^{27}Al is discussed in detail and comparisons to the data as well as to the parametrization of Martin and Walter are presented.

The data presented in this dissertation and the models developed should assist applied physicists in the fields of fusion reactor research as well as astrophysics in need of evaluating or estimating nuclear data for ^{6}Li. The results of the experiments and analyses should be useful to nuclear theorists wishing to understand the extension of the nucleon-nucleon interaction to few nucleon systems. In addition, extensions of the microscopic model to very light nuclei is certainly a possibility worth investigating. Lastly, future efforts to develop further the resonating group model for the nucleon plus ^{6}Li system will certainly benefit from this data and from the results of the comparisons presented here.

CHAPTER 2

NEUTRON SCATTERING MEASUREMENTS

Introduction

Generally speaking, in attempting to measure neutron scattering analyzing powers or cross sections one is faced with several obstacles owing to the fact that the neutron has no charge. The net effect of these problems is a counting rate which is much lower than that for a comparable proton scattering measurement. The first difficulty is the inability to accelerate a neutron by itself. This is overcome by making use of one of several reactions available for neutron production, which in the case of this experiment was the $^2H(\vec{d},\vec{n})^3He$ reaction. As a result of the production of the neutrons through this nuclear reaction, a deuteron beam of 6×10^{11} particles/s translates into a neutron flux of 2×10^6 particles/s at the sample. This example was calculated for 14 MeV neutrons where the 0^o neutron production cross section is maximum.

In addition, the lack of charge of the neutron necessitates the use of relatively thick detectors. Even though the organic liquid scintillators employed for the measurements reported here were 5 cm thick, they are at best only about 23% efficient at low energies ($E_n \approx 4$ MeV) and are less than 15% efficient at energies around 15 MeV. Because the detectors normally do not absorb all the energy of the interacting neutron, time-of-flight techniques employing a pulsed beam are necessary for energy determination. The concomitant beam pulsing equipment typically reduces the deuteron flux by about 20%. The rather low neutron flux requires that certain compromises be made in choosing the sample size and sample location. A large scattering sample is used in these experiments in order to increase the number of nuclei in the sample. So as to increase the number of neutrons incident on the sample, the sample is positioned close to the source of neutrons. Unfortunately, a large sample results in a higher percentage of the incident neutrons which

scatter more than once in the sample. Having a large sample close to the source of neutrons also results in a large spread in the effective scattering angle. It is possible to correct for these effects by performing time consuming Monte Carlo calculations.

Of course, the absence of charge on the neutron, which is the root of these difficulties, is one of the very aspects that makes the neutron a particularly useful probe of the nucleus. No charge implies there is no Coulomb interaction between the probe and target nucleus that might otherwise be confused with the effects of the nuclear force. In describing the details of the measurements of neutron scattering from ^{6}Li, the specifics of how these problems are handled will be discussed.

Beam Production

There are several essential aspects to producing a pulsed, polarized beam of neutrons at the TUNL facility. Among these are the Lamb-shift polarized ion source, the high efficiency bunching system, the Van de Graaff accelerator, an analyzing magnet plus NMR system for energy definition, beamline optics and steerers, and a deuterium gas cell for the neutron production target. These items can be seen schematically in Fig. (2-1) and the significant features of all of these items will in turn be elucidated.

Lamb-Shift Polarized Ion Source

The vector polarized deuteron beam is produced in TUNL's Lamb-shift polarized ion source (PIS). A detailed description may be found in a Ph.D. dissertation (Trainor 73) and in a review article (Clegg 74). Briefly, deuterium gas is injected into a duoplasmatron source head where it is dissociated, ionized positively, and accelerated to 1100 eV. This deuteron beam passes through a cesium vapor canal where a single electron is added such that the resulting deuterium atom is preferentially placed in the $2S_{1/2}$ metastable state. The resulting neutral beam passes through a 575 G solenoidal magnetic field which splits the $2S_{1/2}$ state into its six hyperfine levels. The $2P_{1/2}$ state is also split and the three $2S_{1/2}$,

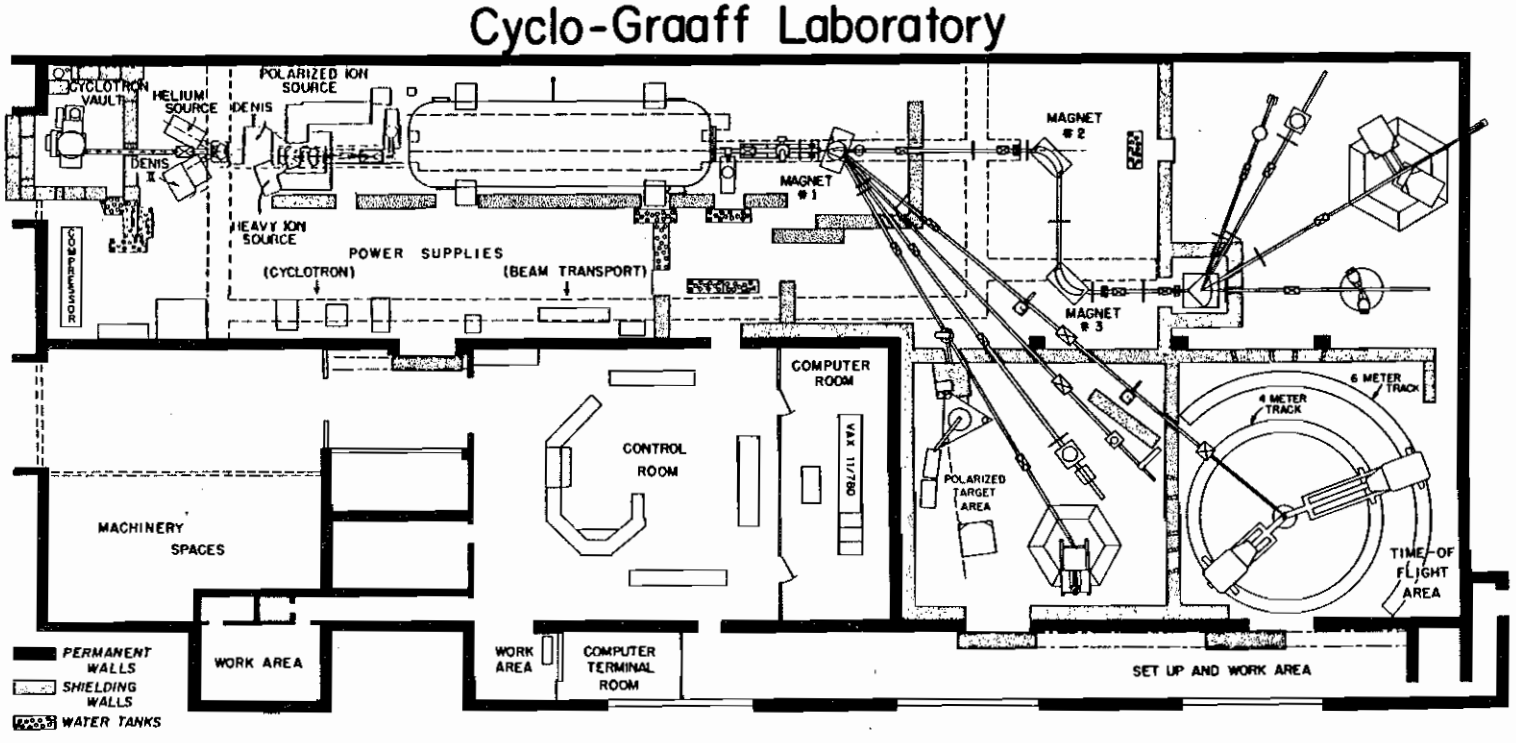

Fig. (2-1) Diagram showing the location of major pieces of equipment at TUNL.

$m_j = -1/2$ levels cross the three $2P_{1/2}$, $m_j = +1/2$ levels, making it possible for the $2S_{1/2}$, $m_j = -1/2$ levels to quickly decay to the ground state. Within the solenoid is a "spin filter" consisting of a split-sector rf resonance cavity tuned to 1600 MHz. A transverse dc voltage applied across two of the four sectors, in combination with the longitudinal rf field, has the effect of coupling two of the three remaining states to the $2P_{1/2}$ states, which quickly decay to the ground state. For these experiments the nuclear spin state having $m_I = +1$ was selected from among the three available states. The neutral beam next passes through an argon canal where a second electron is added preferentially to the remaining metastable atoms. The resulting negative ions are then accelerated up to ground potential from the source potential of 50 kV.

The process of mixing the $2S_{1/2}$ and $2P_{1/2}$ levels such that the $2S_{1/2}$ level is depopulated is referred to as quenching. In the TUNL PIS this can be accomplished by applying a dc voltage of about 200 V to plates located just after the cesium canal. Those metastable atoms that would be ionized in the argon canal and ultimately become the polarized component of the beam are quenched into the ground state and will not be ionized in the argon canal. Thus a comparison of the beam read on a beam stop, with the quench voltage successively on and off, will give a measure of the deuteron beam polarization, P_b, as follows:

$$P_b = 1 - \frac{Q}{UQ} - \frac{QB}{UQ} \qquad (2\text{-}1)$$

where Q = the measured beam current with the quench voltage on,

UQ = the measured beam current with the quench voltage off,

QB = the quenchable background, *i.e.*, the difference between the unquenched and the quenched beam currents, both measured with the 575 G field detuned.

A small correction to P_b of typically less than 2% must be made for so-called quenchable background. Quenchable background refers to a small portion of the unpolarized

component of the beam which is eliminated from the beam when the quench voltage is applied, thus causing an overestimate of the beam polarization. The magnitude of the quenchable background was measured every few hours during the course of the experiment, most often just after someone had tuned parameters on the source, since this is when the level of the quenchable background is most likely to change. When measuring the quenchable background the 575 G solenoidal field is decreased by a small amount. This "detuning" causes the polarized component of the beam to decay to the ground state and thus be eliminated from the beam, while the unpolarized component of the beam is unaffected. By applying the quench voltage in this condition one can measure directly QB, that is, the portion of the unpolarized beam which goes away upon quenching.

The beam polarization was measured about every fifteen minutes, which was sufficiently frequent that at least two measurements each of the spin-up and spin-down polarizations were made for each detector angle setting. These values were averaged for each angle setting and the quenchable background correction applied. The deuteron beam polarization available during these experiments ranged from 60% to 70%. An error of 1 to 2% was assigned to the beam polarization values to cover the uncertainty in the quench-ratio technique and instabilities of the beam during the measurement.

Beam Pulsing

The time-of-flight technique as applied to the TUNL polarized neutron facility requires a pulsed beam. The pulsing (described in detail in Howell 84) is accomplished in three stages: ramping of the very low beam-energy voltage supply in the PIS duoplasmatron, bunching of the 50 keV beam in a pair of double-drift bunchers, and finally chopping away the background beam occurring between the pulses.

Ramping is accomplished by applying a 4 MHz ramp wave form with a peak-to-peak voltage of 70 V to the anode of the duoplasmatron. This has the effect of modulating the +1100 eV energy of the deuteron beam. Compression of the beam into

about 65% of a cycle (the period of the cycle is 250 ns) occurs as the deuteron beam drifts the 1.5 m from the duoplasmatron to the argon charge-exchange region.

The beam next enters a pair of double-drift bunchers. The linear region of a sine wave extends for less than 15% of the period of the wave. Bunching occurs in this linear region and so 15% is the highest efficiency one can expect from a single buncher. A second buncher operating at twice (8 MHz) the frequency of the first and 180^0 out of phase effectively applies a correction to the first buncher's sine wave so that the corrected wave form has a linear region for 65% of the wave period. The 65% compression provided by the ramp matches the phase acceptance of 65% of the pair of bunchers. These bunching signals are applied to the 50 kV deuteron beam approximately 4 m prior to entering the Van de Graaff accelerator.

A final element in the pulsing system is a chopper located immediately at the entrance to the Van de Graaff accelerator. It consists of two parallel plates with a 4 MHz sine wave applied to one of them. The sine wave is phased so that ions present between the pulses produced by the ramp and bunchers are deflected out of the beam. This removes the time uncorrelated background from the beam. The pulsing system as a whole is at least 80% efficient and produces pulses on target of less than 2 ns duration.

Acceleration and Beam Energy Determination

The final acceleration of the beam occurs in the FN Tandem Van de Graaff. The terminal voltage ranged from 1.9 MV to 7.3 MV to produce the 3.8 MeV to 14.6 MeV deuteron beams used in this experiment. A thin carbon foil (around 10 $\mu g/cm^2$), located inside the terminal dome, served to strip off the two electrons to produce the positively charged deuteron beam. The thin carbon foil is preferred over the gas stripper (also available at this Van de Graaff) since it produces negligible depolarization of the beam.

For accurate determination of the beam energy a momentum-analyzing magnet with an NMR feedback system was employed. This magnet also serves to bend the beam

toward the TOF experimental area located on a beam leg which is 38° off the axis of the accelerator. An NMR system monitors the field in the magnet and adjusts the magnet current supply to maintain the desired field. Located just after the magnet is an adjustable vertical slit. The fractions of the beam deposited on the left and right halves of the slit are measured and a difference taken. If the voltage on the accelerator terminal is correct, the beam will be deflected by the magnet so that equal amounts of beam will be deposited on both halves of the slit. Unequal beams on the two halves (*i.e.*, a non-zero difference) implies the accelerator voltage has deviated from its correct value. An amplified output of the slit difference circuit is applied as a correction to the corona voltage which controls the amount of discharge or corona leaking off the dome. The feedback system reduces the energy spread of the deuteron beam to about 10 keV. The slit configuration for the 38° beam leg has been calibrated to produce an absolute uncertainty in the beam energy of about ± 50 keV.

Beam Transport

Transport of the beam from the PIS to target was accomplished with the aid of many focussing and steering elements. Three electrostatic einzel lenses and one triplet quadrupole magnetic lens provided focussing from the PIS to the accelerator. In addition, three magnetic steerers were located on this same section of beam pipe. The accelerator by its nature provides focussing, and an electrostatic steerer is located inside the terminal dome. Post-acceleration focussing was provided by two triplet quadrupole magnetic lenses and two doublet quadrupole magnetic lenses. Two electrostatic steerers and four magnetic steerers were available between the accelerator and the target. Vacuums of about 5×10^{-6} Torr were provided by several oil or mercury diffusion pumps at various locations. The polarized deuteron beam current on target ranged from 100 to 175 nA for most energies. For neutron source energies of 5 to 7 MeV the accelerator was operated between 1.4 and 2.0 MV terminal voltage. This is a region of poor beam transmission

through the accelerator and the beam current on target ranged only from 70 to 90 nA.

Source Reaction

As stated earlier, the $^{2}H(\bar{d},\bar{n})^{3}He$ reaction is used to produce the polarized neutron beam. Polarized deuterons enter a deuterium gas cell located at the end of the beam pipe. Emerging at a 0^{o} reaction angle is a so-called monoenergetic beam of neutrons bearing about 90% of the vector polarization of the incident deuteron beam. The reaction has a Q-value of +3.269 MeV and has a high cross section at 0^{o} which drops off rapidly with angle. An undesirable feature of this source reaction comes from neutrons which are the result of the $^{2}H(d,np)^{2}H$ and the $^{2}H(d,np)np$ reactions with Q-values of -2.22 MeV and -4.44 MeV respectively. These neutrons, loosely called break-up neutrons, result in the large background "hump" appearing in the low energy end of the neutron source spectra. Scattering of these break-up neutrons from ^{6}Li produces a similar hump in the spectra of the measurements here. Fortunately, the first inelastic state of ^{6}Li (2.18 MeV) occurs well above this large background in all but the higher energy back-angle spectra. As the energy is increased the cross section for production of break-up neutrons increases relative to the cross section for the production of monoenergetic neutrons. Consequently, the break-up hump grows relative to the elastic and inelastic peaks. In the 14 and 17 MeV back-angle spectra, the inelastic peak is sitting on top of the large tail on the high energy side of the break-up hump.

The low-mass gas cell used in these measurements is the gas cell "C" referred to in the dissertation of R. Pedroni (Pedroni 86). The cylindrical gas volume is 3.16 cm in length and was pressurized to as much as 7.8 bar. A 0.25 mil (6.4 μm) thick Havar foil separated the deuterium filled region of the gas cell from the evacuated region of the deuteron beam tube.

Other relevant features of the gas cell include the fact that the gas cell is electrically isolated. In addition, the deuterons not interacting to produce neutrons are

stopped by a tantalum disk (beam stop) at the end of the gas cell and by a tantalum sleeve lining the side walls of the gas cell. Tantalum is the preferred material for this task because of its low neutron production cross section for deuteron induced reactions. The charge collected on the gas cell is carried to a beam current integrator, whose digitized output is stored in the computer during an experiment. This makes it possible to take account of differences in the deuteron flux by normalizing sample-in counts to sample-out counts by the ratio of charge accumulated during a sample-in run to the charge accumulated during a sample-out run.

As indicated above, for terminal voltages less than 2 MV the transmission through the accelerator deteriorates. For producing neutron energies of 5 and 6 MeV it was decided to insert slowing-down foils in front of the gas cell foil in order to permit keeping the deuteron energy above 3.5 MeV. Two 0.25 mil (having a combined thickness of 12.9 μm) Havar foils were added to the existing foil to provide about a 1 MeV loss in energy for a 4 MeV deuteron beam.

Another problem associated with low energies is that the energy loss in the deuterium gas increases as one decreases the deuteron energy. The spread in energy of the neutron beam arises from the fact that neutrons are produced in the $^{2}H(\vec{d},\vec{n})^{3}He$ reaction at different locations along the length of the gas cell. Deuterons arriving at these various locations have lost different amounts of energy. The full energy spread in the neutron beam is approximately equal to the energy lost by a deuteron travelling the full length of the gas cell. To keep this neutron energy spread below 600 keV the gas pressure was decreased in stages from 7.8 bar at neutron energies of 9 MeV and above to 2.4 bar at 5 MeV. The actual neutron energy spreads, which ranged from 280 to 600 keV, are recorded for each energy in the Appendix along with the analyzing power data.

Scattering Sample

The ^{6}Li scattering sample consisted of lithium metal contained in a thin-walled

aluminum can. The inner dimensions of the can are a radius of 0.950 cm and a height of 2.756 cm. According to the manufacturer, the lithium has been enriched to 95% ^{6}Li by mass, leaving 5% ^{7}Li. From the neutron spectra obtained during the experiments it became evident that ^{16}O and ^{14}N contaminants were present in the sample. At backward scattering angles, where kinematic separation of the peaks is greatest, a contaminant peak is clearly evident, although individual ^{16}O and ^{14}N peaks cannot be resolved inside this peak; however, the width of the contaminant peak suggests the presence of two peaks of approximately equal magnitudes.

In order to verify the composition of the contaminant peak, scattering samples of ^{16}O and ^{14}N were obtained in the form of liquid hydrazine (N_2H_4) and liquid water (H_20) contained in thin-walled stainless steel cans. Spectra were obtained under identical conditions for the hydrazine, water and lithium samples at a backward angle of 155^{o}. It is clear from Fig. (2-2) that the contaminant peak is composed of combined ^{14}N and ^{16}0 peaks. By extracting the ^{6}Li and contaminant yields from several back angle spectra, taking into account the known ^{6}Li, ^{16}O, and ^{14}N elastic scattering cross sections, and assuming equal amounts of ^{14}N and ^{16}O, one concludes that the sample is composed of 86% Li, 7% ^{16}O and 7% ^{14}N, where the percentages are given as number of nuclei. As explained later, the forward angle analyzing power measurements must be corrected for these contaminants. For the purposes of the multiple scattering corrections to be described later one must know the number of lithium nuclei in the sample, which is 3.66×10^{23}. Since all the data reported here include the 5% ^{7}Li contaminant, the number of ^{7}Li nuclei is included in this number.

Neutron Time-of-Flight Spectrometer

The various features of the spectrometer evident from Fig. (2-3) are adequately described in several sources (Glasgow 76, Beyerle 81 and Pedroni 86). The most prominent items in the TOF experimental hall are the two neutron detectors. The large

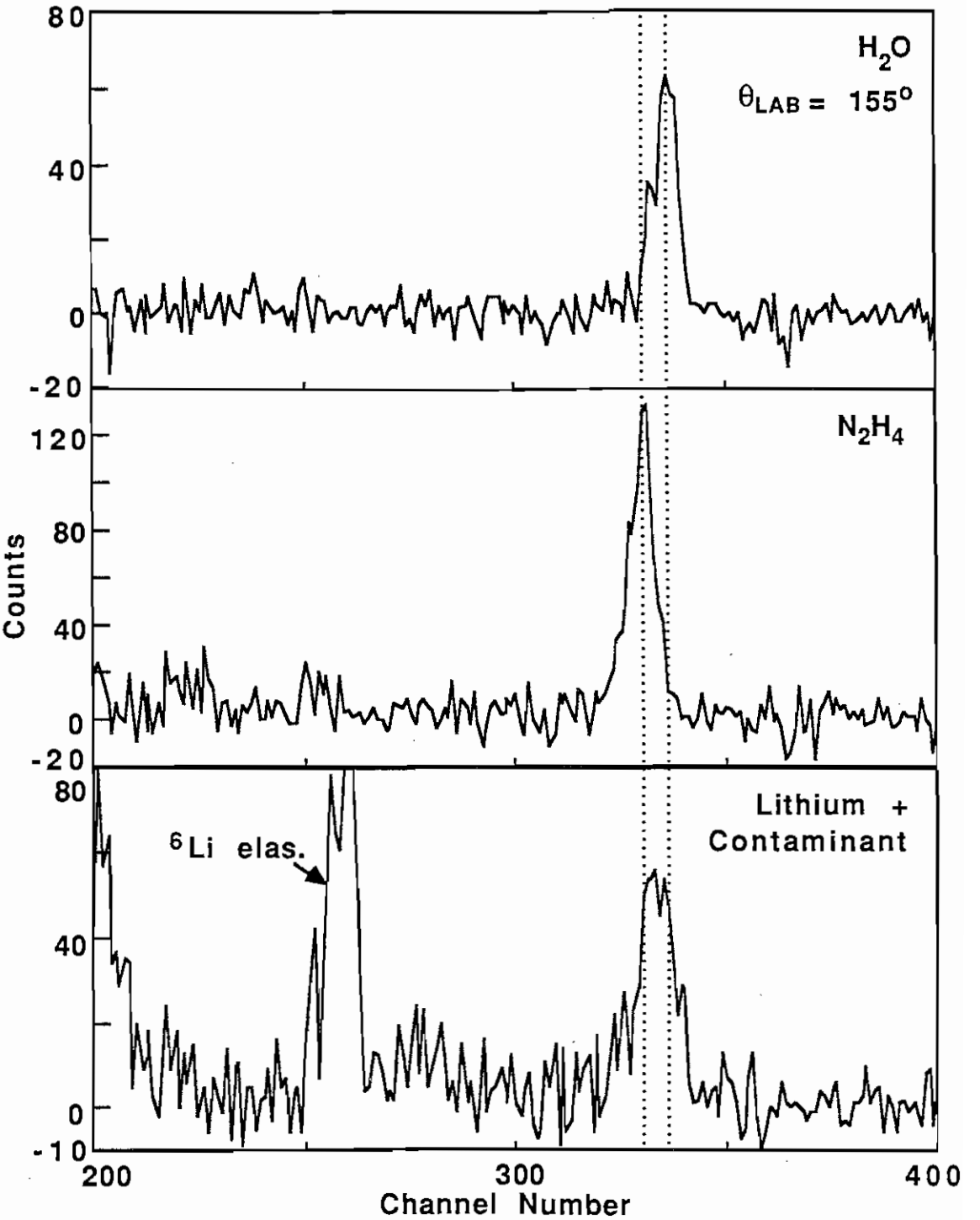

Fig. (2-2) Left detector time-of-flight spectra obtained at a back angle of 155° with detector at full flight path, using water, hydrazine and lithium samples. This demonstrates the presence of oxygen and nitrogen contaminants in the lithium sample.

housings contain substantial amounts of lithium-loaded paraffin, lead, and copper used as shielding material. The left and right detectors [left and right with respect to the incident beam direction, as indicated in Fig. (2-3)] contain NE-213 and NE-218 organic liquid scintillators, respectively. These two liquids are preferred because of their superior pulse-shape discrimination (PSD) properties which allow distinguishing between γ-rays and neutrons. The detectors can be rotated about a common pivot point which is the scattering sample. These measurements took advantage of the two-detector spin-flip method and so the two detectors were positioned at equal left and right angles ranging from 20^{o} to 160^{o}. The detectors can also be moved closer to or farther away from the sample. The right detector was positioned at its longest possible separation from the sample throughout most of the measurements. This so-called flight path, measured from the center of the scattering sample to the center of the scintillator was 3.76 m. The left detector was moved in from its maximum flight path of 5.70 m to 3.89 m for the majority of the measurements. This was done to increase the left detector solid angle and as a result increase its counting rate. Decreasing the flight path is allowable for ^{6}Li since the first excited state has an excitation of 2.18 MeV; the inelastic scattering and elastic scattering peaks are still very well resolved at the shorter left-detector flight path.

In effect, a rectangular collimator was constructed around the path from the sample to the scintillator face. Three sides were fashioned from rectangular copper blocks with the tungsten shadow bar serving as the fourth side. In addition to the conventional tungsten shadow bars, which shield the detectors from the direct neutron flux emanating from the gas cell, a second set of shadow bars was installed when these measurements were initiated. This second set eliminated a contribution to the background which is due to neutrons scattering from air in the vicinity of the lithium sample. These air-scattered neutrons appeared in the TOF spectra in the region of the elastic scattering peak. Neutron trajectories from the air, above, below, or at the sides of the sample to the scintillator were

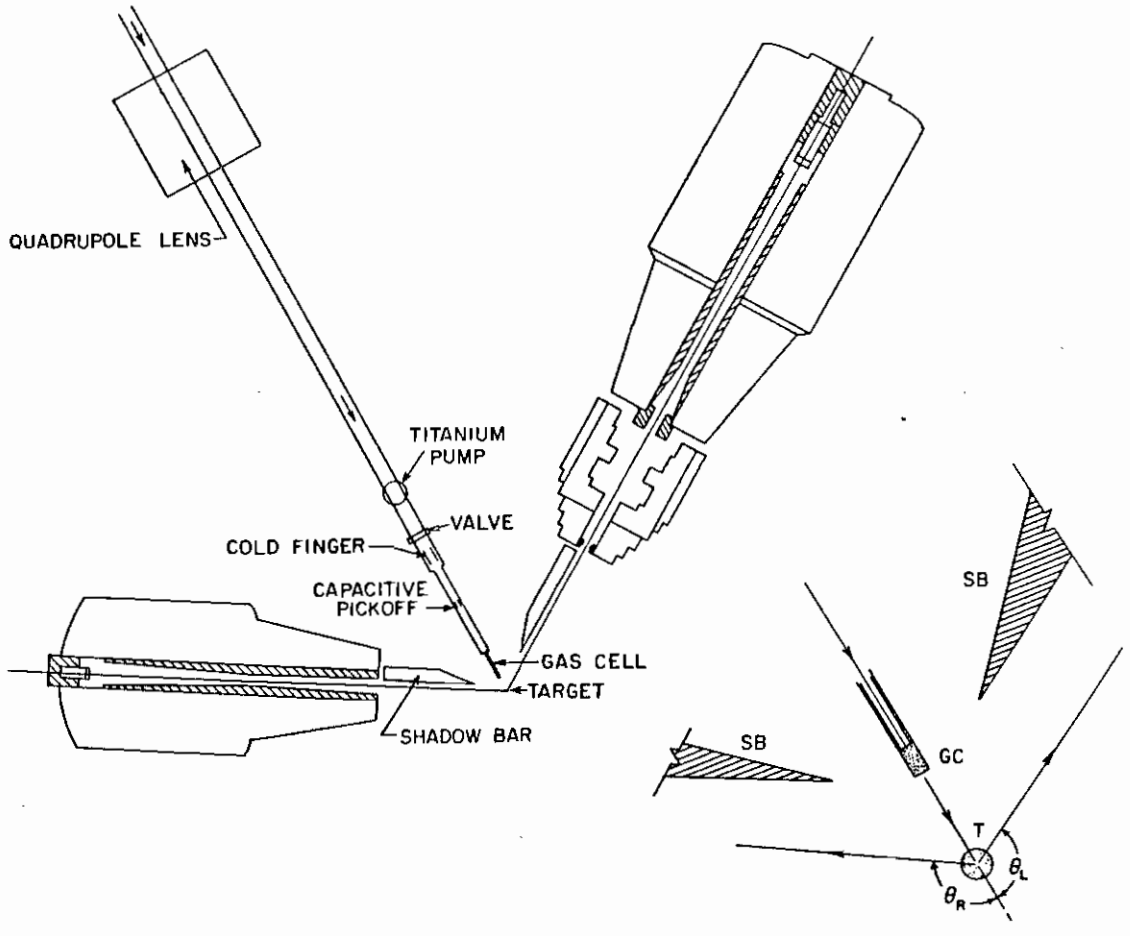

Fig. (2-3) Details of the neutron time-of-flight beam leg and detectors are shown along with a schematic indicating the relative positions of neutron source, sample, and primary shadow bars for a back-angle measurement.

effectively blocked by the combination of copper and tungsten. The second set also helped to minimize the contribution from neutrons scattered from the opposite shadow bar. This second set permitted the use of a "tighter" shadow bar geometry than otherwise possible.

With the detectors at back angles, the copper is shielded by the tungsten from direct flux from the gas cell. Exposing the copper to the direct flux would result in a significant number of neutrons scattering off the copper and into the detector, thus adding to the background rather than reducing it. As the detectors are moved forward in angle, the copper blocks must be moved closer to the detector so that they are still shielded by the adjacent tungsten shadow bar, and so that they help to shield the detector from seeing the opposite tungsten shadow bar. Two special tables were constructed for the secondary shadow bars which were placed alongside the primary shadow bars and 2 in. below the scattering plane. The tables were installed with linear bearings that ride on cylindrical rails to facilitate moving the copper. At angles less than 35^{o} for the present detector flight paths, it is not possible to shield the copper from the direct flux and so the secondary shadow bars must be removed altogether.

Several items in the experimental area relating to the beam pulsing must be mentioned. First is the capacitive pick-off located in front of the gas cell. Charged pulses of beam passing through the short tube comprising the pick-off induces a series of pulses on the pick-off tube itself. The time between the occurrence of a pulse in the pick-off and the detection of an event in the detector is considered the time of flight for the detected particle. The second item is a time profile monitor consisting of an unshielded NE-213 scintillator located at 0^{o} in the scattering plane at a distance of about 4 m from the deuterium gas cell. This detector is exposed to the direct neutron flux produced in the gas cell. The count rate in this detector is large and good statistics can be obtained in about 60 s. The time-of-flight spectrum obtained with this detector records the time distribution of neutrons emerging from the gas cell. The width and tails of the sharp peak resulting

from the $^{2}H(\bar{d},\bar{n})^{3}He$ reaction is very sensitive to the duration and tails of the deuteron pulse. It is this shape which one attempts to optimize when adjusting the pulsing and bunching equipment.

Detector Electronics

The shaping and culling of detector pulses is performed by identical sets of electronics for the left, right and timing-monitor detectors. The primary functions of the electronics are to create a pulse whose amplitude is proportional to the time between the pick-off pulse and the detector pulse, to discriminate against γ-rays, and to discriminate against detector pulses of insufficient amplitude via an energy bias.

The block diagram in Fig. (2-4) shows the ORTEC and Canberra NIM-compatible modules which perform these tasks. A fast pulse derived from the detector and the beam pick-off signal serve as "start" and "stop" pulses, respectively, to a time-to-amplitude converter (TAC). The TAC output whose voltage is proportional to the time of flight of the detected particle is input to a linear gate stretcher (LGS). Gate signals also input to the LGS determine if the TAC signal is passed by the LGS. These gate signals are present whenever the set of discrimination requirements have been met. A TAC range of 200 ns was sufficient to observe the entire spectrum of scattered neutrons.

The detector pulse is additionally sent to two other modules where the discrimination occurs. The energy bias is applied by a combination amplifier and single channel analyzer (AMP-SCA). A gate signal is output by the AMP-SCA whenever the amplitude of the input pulse is greater than a certain level. This amplitude bias level is determined and set in a reproducible manner (described in Pedroni 86) and corresponded to a neutron energy of 2 MeV in all but the measurements at the extreme energies. In this case the bias corresponds to the light output produced by the maximum energy Compton-recoil electrons for a ^{137}Cs source where $E_{\gamma} = 0.662$ MeV. An exception is the data taken at 17 MeV where the amplitude bias level was doubled to give a neutron energy

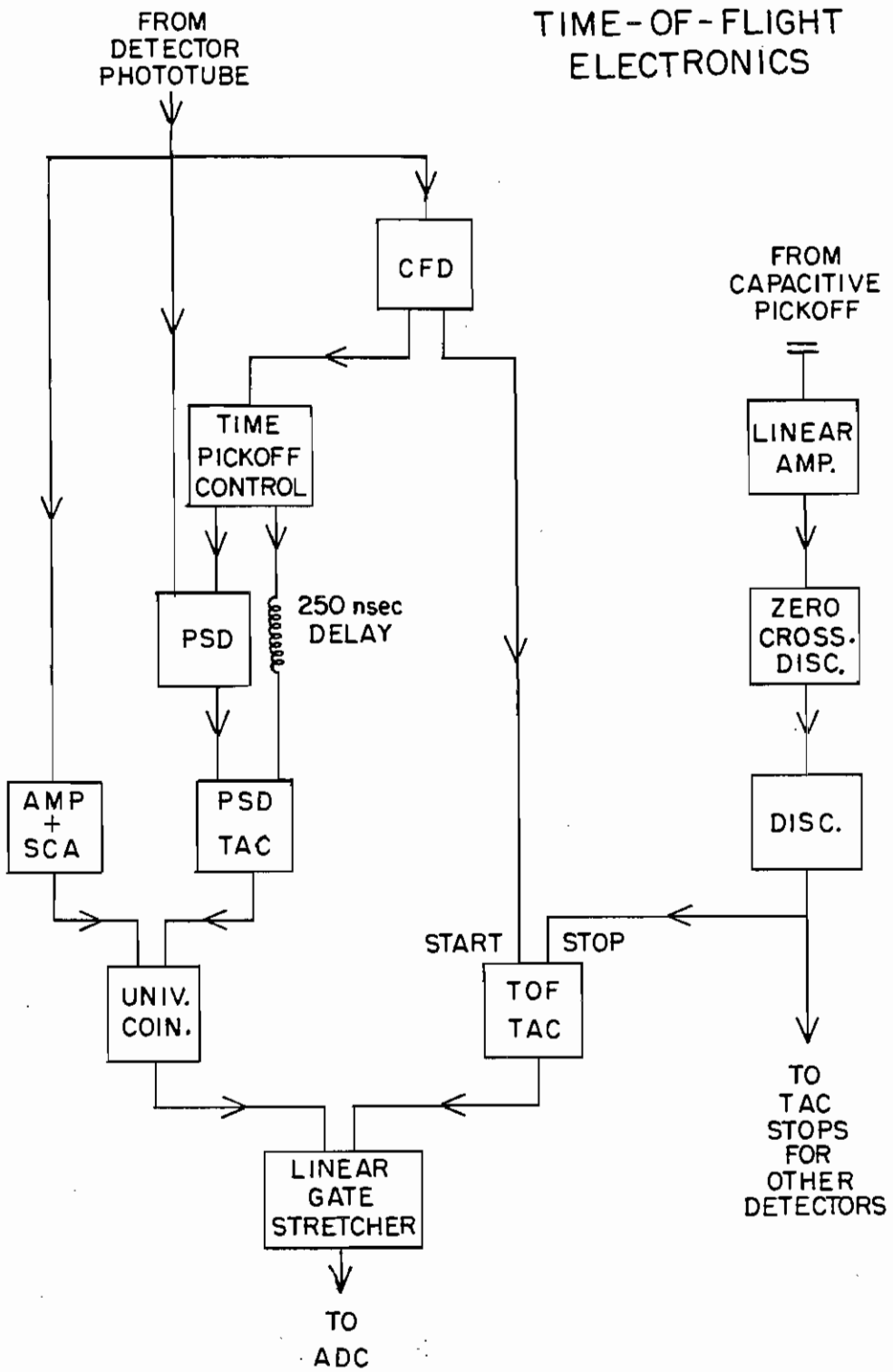

Fig. (2-4) Block diagram of the detector electronics and pick-off electronics used in the time-of-flight measurements.

bias of about 3.2 MeV, in order to improve the signal-to-noise ratio in the time-of-flight spectra. For the 5 and 6 MeV data the standard amplitude bias level was reduced by half to give a neutron energy bias of 1.3 MeV, in order to improve the counting rate.

Discrimination against γ-ray induced events is accomplished with the pulse-shape discrimination (PSD) method which takes advantage of the fact that detector pulses produced by the electron recoils from γ-rays have faster rising trailing edges than do pulses from recoil protons produced by the neutrons. Two fast pulses, one triggered by the leading edge and one by the trailing edge of the detector pulse, are produced by the constant fraction discrimination and the pulse shape discriminator, respectively. These serve as the start and stop pulses to the PSD-TAC. The resulting PSD-TAC spectrum reveals two distinct peaks, one for γ-rays and one for neutrons. A window can be set on the neutron peak using the SCA which is integrated into this TAC module. A gate is produced by the PSD-TAC whenever a detector pulse falls within this window, thereby meeting the requirement for a neutron event.

The two SCA gates for the energy bias and the PSD requirement are inputs to a universal coincidence module which gives a single output gate whenever the two input gates arrive in coincidence. It is this output signal which gates the previously mentioned LGS to determine whether TOF-TAC signals are passed. The TOF-TAC signal passed by the LGS as well as the gate input to the LGS are sent to an ADC.

Data Acquisition

The data are accumulated for the three detectors in four experimental configurations: sample-in spin-up, sample-in spin-down, sample-out spin-up, and sample-out spin-down. Data accumulated with a lithium, hydrazine, or water sample in place are called sample-in data. Data accumulated with an empty aluminum or stainless steel can in the sample position are called sample-out data. Spin-up and spin-down refer to the polarization direction of the incident neutron beam. The sorting and storing of data

in spectra for the various configurations was accomplished with a system built around the VAX 11/780 computer using a microprogrammable branch driver (MBD-11) as an interface between the scalers and ADC's and the VAX. Events from the left, right, and time profile monitor detectors were sent to three separate fast Northern ADC's which generated 512 channel spectra. Separate channels in the MBD-11 were assigned for each detector in which the digitized events were temporarily stored as they came in. These events stored in the MBD-11 were transmitted to the VAX, then sorted and stored in data areas in the VAX according to detector, spin direction, and sample in or out. Additional data areas were available for difference spectra which contain the sample-in spectra with the corresponding BCI-normalized sample-out spectra subtracted from them. Companion data areas for each difference data area were set aside for error arrays containing the statistical uncertainty of each channel.

Several scalers were counting during each run. The digitized output of the beam current integrator, a 10 Hz clock, and the gates from the three detectors were all counted by scalers. A count-down scaler was also available. The BCI output went to this scaler as well and decremented the scaler from a "preset" value determined by the experimenter down to zero. Upon reaching zero the data accumulation was halted. The accumulated counts for the scalers were stored in VAX data areas for future reference.

All controlling of the MBD and ADC's, data sorting, calculations, and graphic displays of spectra were accomplished with the aid of the TUNL XSYStem software package. The XSYStem contains a set of general purpose commands useful to all nuclear physics experiments performed at TUNL. DEC Command Language (DCL) programs incorporating these XSYS commands have been written specifically for the polarized time-of-flight (PTOF) experiments. The programs make it possible to set windows on peaks of interest within a spectrum, define backgrounds, calculate differences of two spectra (sample-in and sample-out) and obtain background-subtracted peak yields. These

yields go into the calculation of the asymmetry ε as follows:

$$\varepsilon = \frac{\gamma - 1}{\gamma + 1} \tag{2-2}$$

where $$\gamma = \sqrt{\frac{LU \times RD}{RU \times LD}} \ . \tag{2-3}$$

Here *LU* refers to the peak yield in the left-detector spin-up spectrum and the other terms are similarly defined. The analyzing power $A_y(\theta)$ is calculated from the asymmetry and neutron beam polarization P_n:

$$A_y(\theta) = \frac{1}{P_n} \times \varepsilon \ . \tag{2-4}$$

The neutron beam polarization is deduced from the deuteron beam polarization by a factor related to the polarization transfer coefficient for the $^2H(\vec{d},\vec{n})^3He$ reaction (Lisowski 75).

Data Reduction

The setting of windows, determination of backgrounds and other aspects of the data reduction must be considered in greater detail. For the elastic scattering peak at back angles, where the contaminant peak due to scattering from the ^{14}N and ^{16}O in the sample is completely resolved, a window was set at a level above the background equal to 10 to 20% of the peak height. It is convenient to choose a window which does not include the tails of the peak since the tails have a lower signal-to-noise ratio and may therefore introduce a greater uncertainty in the extracted asymmetry. For a given detector the ratio of spin-up counts to spin-down counts appears in the equation for ε. Therefore, ε is independent of the fraction of the counts in the peak which are included in the window, as long as the window (or fraction) is the same for spin-up and spin-down.

At 5, 6, and 7 MeV for scattering angles less than 75^o the contaminant peak was not resolved from the peak of interest. This was also true for scattering angles less than 60^o for energies between 8 and 17 MeV. Sample spectra at 8 MeV are given in Figs. (2-5)

and (2-6) and at 14 MeV in Fig. (2-7). In these instances the window was set at the 10 to 20% level on the composite peak. Corrections for the effects of the nitrogen and oxygen on the analyzing power for these cases are discussed in a later section of this chapter.

The lithium elastic scattering peak and contaminant peak are adequately but not completely resolved at angles between 75° and 95° at 5, 6, and 7 MeV and at angles between 60° and 80° at 8 MeV and above. In these cases an asymmetric window was set on the peak such that the left side of the window was at the usual 10 to 20% level and the right side was set at a higher level which excluded contributions from the contaminant peak. This of course also excluded valid lithium scattering events on the right side of the peak. To demonstrate that excluding events on the right side did not affect the calculated analyzing power, tests were conducted on peaks which were totally resolved from the contaminant peak. As expected, choosing a window on a well resolved peak which was symmetric about the peak or choosing a window which excluded the right side of the peak did not produce a significant difference in the calculated analyzing powers.

For the peak associated with the inelastic scattering from ^{6}Li to the 2.18 MeV excited state, there was no interference from contaminant peaks. Here, however, the number of counts in the peak was usually much lower than for inelastic scattering because of the lower cross section. The spectra showed much greater statistical fluctuation in the region of the inelastic peak, making the distinction between peak and background less obvious. It was convenient, therefore, to set the window at a level above the background equal to 20 to 40% of the peak height.

The appearance of the background in the spectra is dominated in most cases by the elastic scattering of break-up neutrons from the target. The Q-values for the break-up reactions are -2.22 and -4.44 MeV and the threshold is $E_{d(lab)} = 4.45$ MeV. For the 5 and 6 MeV neutron beams where E_d is less than 4 MeV no break-up neutrons can occur and such are not apparent in the spectra.

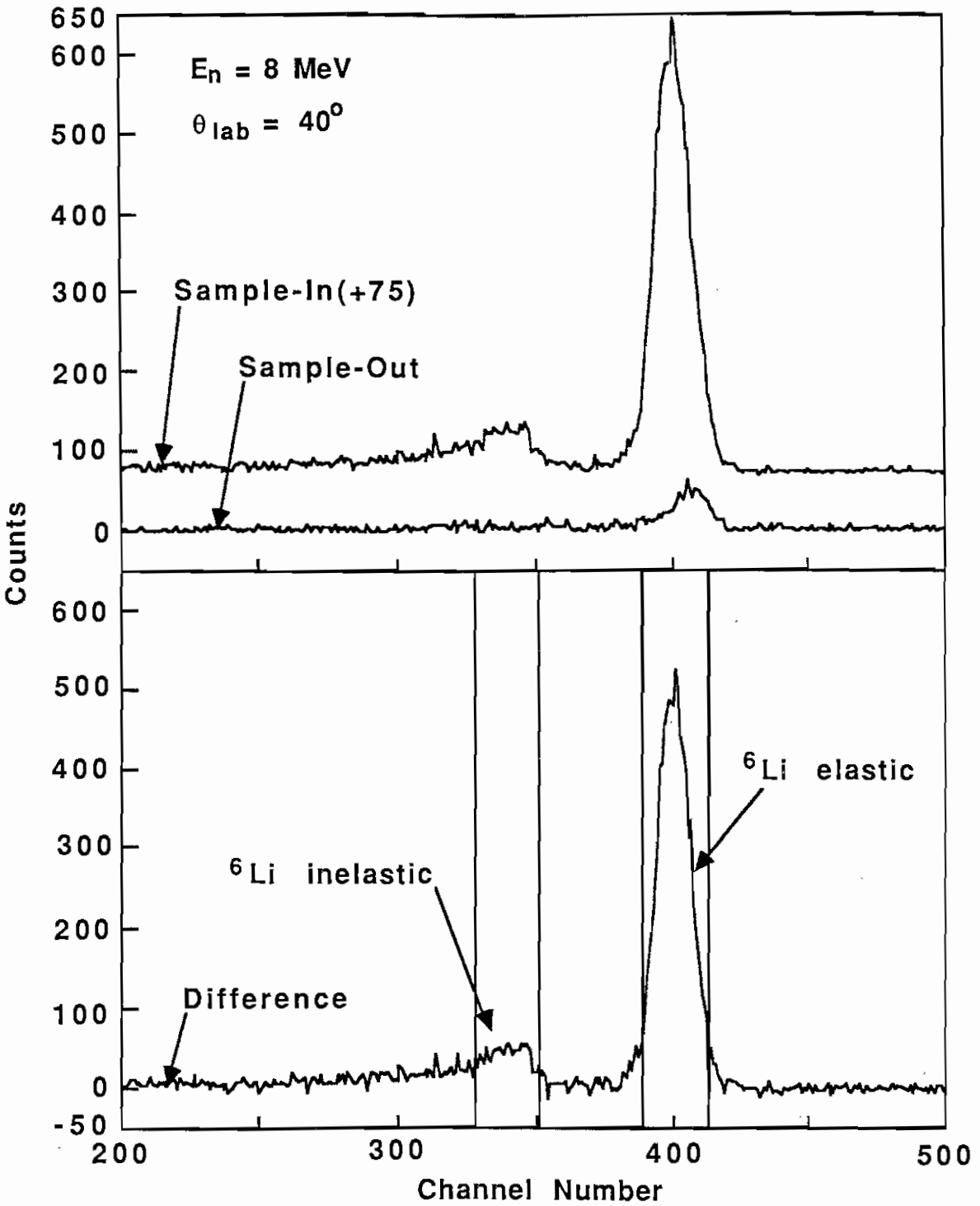

Fig. (2-5) Sample-in, sample-out and difference spectra obtained with the left detector at $\theta = 40°$ and $E_n = 8$ MeV.

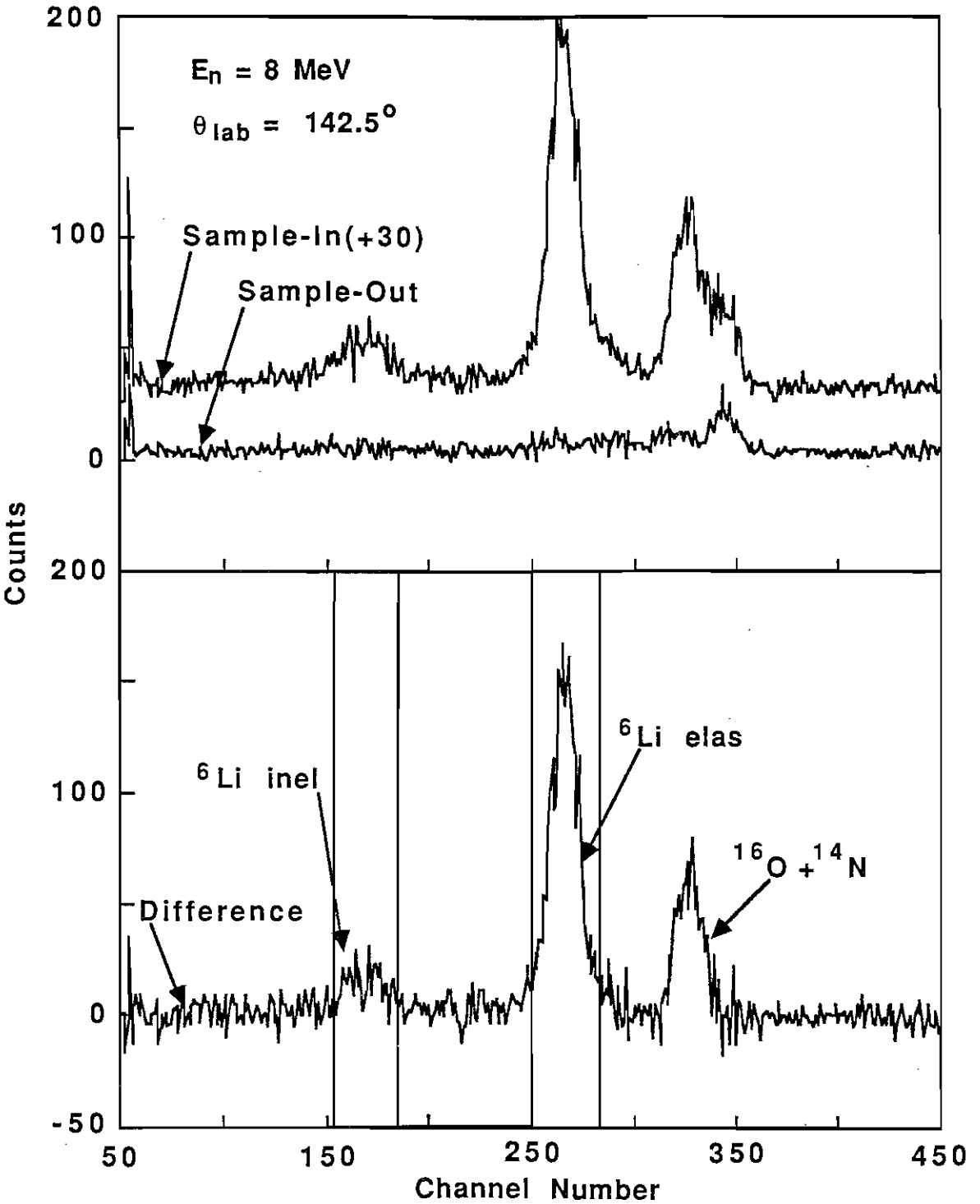

Fig. (2-6) Sample-in, sample-out and difference spectra obtained with the left detector at $\theta = 142.5°$ and $E_n = 8$ MeV.

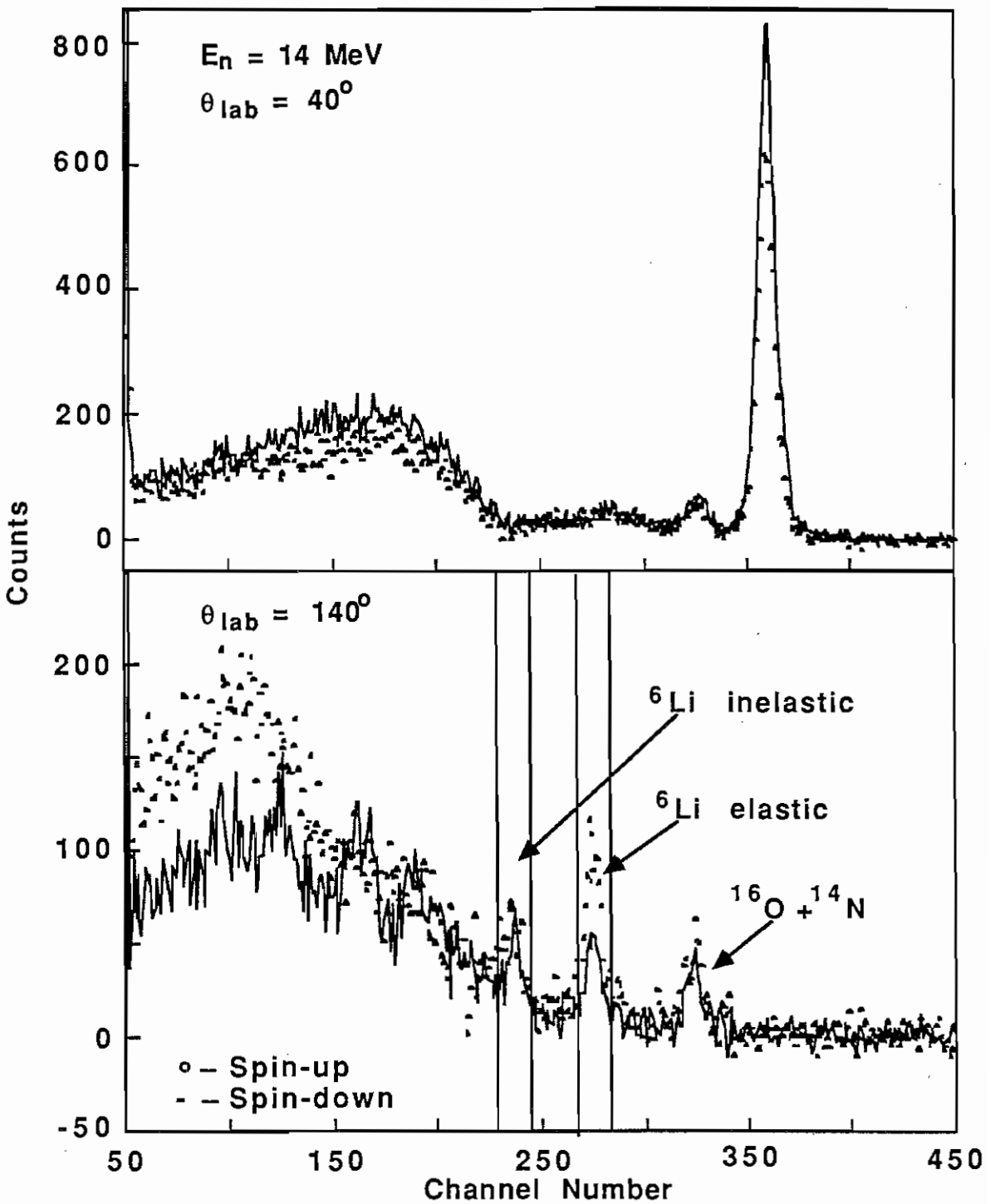

Fig. (2-7) Spin-up and spin-down difference spectra shown superimposed for the left detector at $\theta = 40°$ and at $\theta = 140°$ with E_n = 14 MeV.

Accordingly the background is very flat and nearly zero. The source of this time uncorrelated background is primarily neutrons which have scattered many times from the floor and walls of the experimental hall as well as neutrons which have interacted with and penetrated the massive detector shielding. Determining a simple constant background level was sufficient then at 5 and 6 MeV. This constant is set equal to the average number of counts in two specified sets of channels to the left and right of the region of the elastic, inelastic and contaminant peaks. To obtain this value four markers were placed in the spectra to bracket the two sets of channels designated for the calculation of the background. In all cases, the same calculated backgrounds were used for the spin-up and spin-down spectra which is an acceptable simplification since the backgrounds in these spectra were observed to have zero asymmetry within statistical uncertainties. Understandably, the spectra for the left and right detectors were different and so different backgrounds were calculated for each detector. All of the background levels here and in the discussion below are determined by calculating a constant or linear least-squares fit to the counts in channels which are outside of the region of the peak.

At 7 and 8 MeV additional contributions to the background are evident to the left of the inelastic peak. Here, we see the effects of break-up neutrons whose energy is above the energy bias for these incident energies. A linear background with a small negative slope is a good representation of the background in the region of the peaks. Above 8 MeV, contributions to the background from the break-up neutrons continue to increase with energy. The prominent break-up hump is very evident in Fig. (2-7) which shows 14 MeV spectra. The inelastic peak is always affected more and so separate linear backgrounds are calculated for the elastic and inelastic peaks; the level is higher and the slope more negative for the inelastic peak.

Because of large statistical fluctuations in and around the inelastic peak it was often impossible to determine the background level very accurately. Instead an attempt

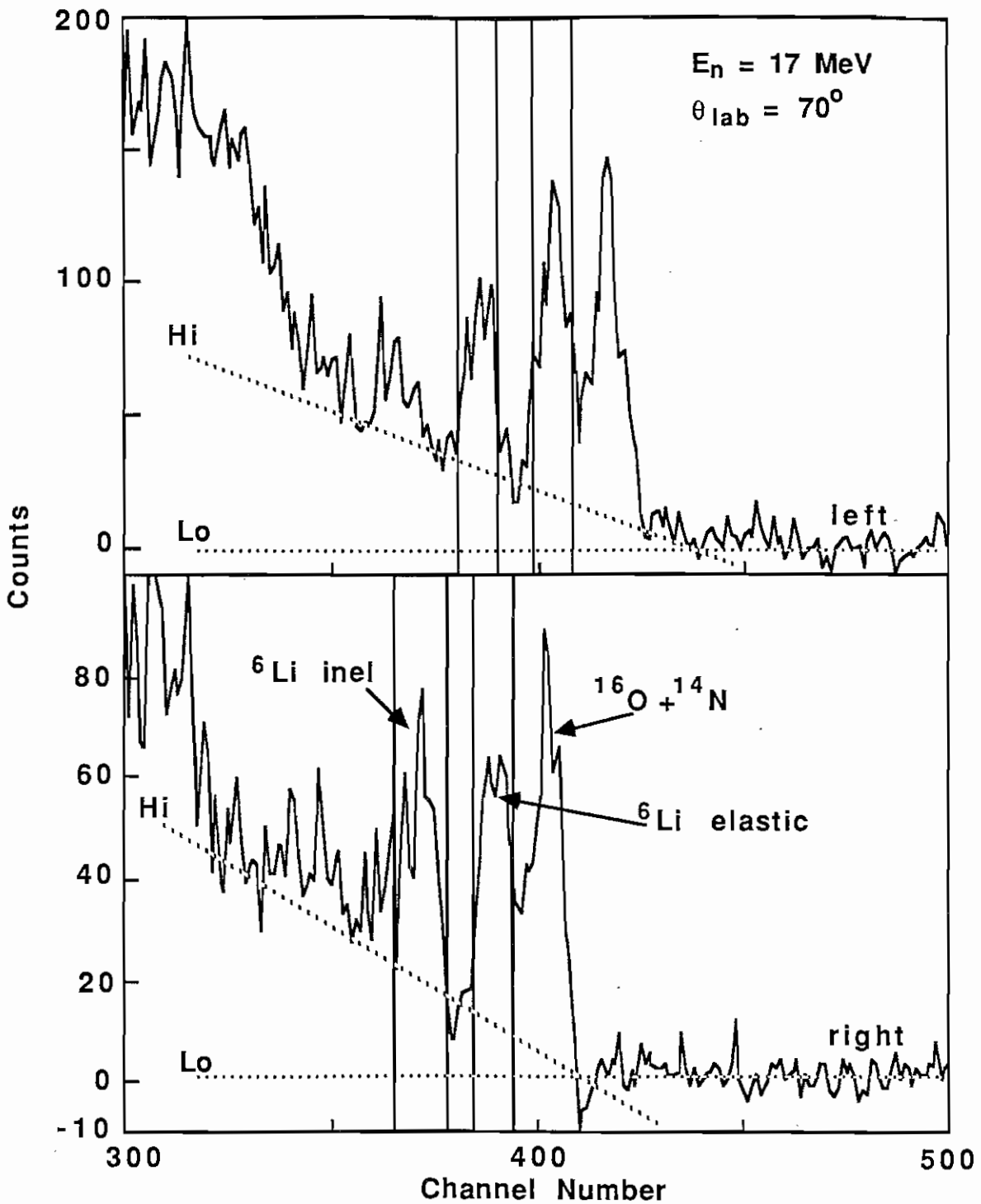

Fig. (2-8) Time-of-flight spectra for the left and right detectors showing the high and low backgrounds used in the calculation of $A_y(\theta)$ for inelastic scattering. (These spectra were obtained with spin-up).

was made to bracket a range of possible backgrounds for the 9 to 17 MeV spectra. Two analyzing powers were calculated for the inelastic peak, one with a high estimate of the background and one with a low estimate. The average of the two values was assumed to be correct, but an error bar was assigned such that it would include the range covered by the two original values (with an estimate of the associated statistical uncertainties added in). In equation form one has:

$$A_y(\theta) = \frac{A_y(\theta)_H + A_y(\theta)_L}{2} \tag{2-5}$$

and

$$\Delta A_y(\theta) = \mathrm{MAX}\left[\Delta A_y(\theta)_H,\ \Delta A_y(\theta)_L\right] + \frac{1}{2}\left|A_y(\theta)_H - A_y(\theta)_L\right|, \tag{2-6}$$

where $A_y(\theta)_H$ and $A_y(\theta)_L$ are the analyzing power values calculated with high and low backgrounds, respectively. Fig. (2-8) shows typical high and low backgrounds set for the left and right detectors at 17 MeV. The low background was in most cases suitable for the elastic peak.

Multiple Scattering, Finite Geometry, and Attenuation Corrections

Using a large sample is a convenient way of increasing the counting rate in an experiment, but this method has several disadvantages. First of all with a large sample it is more likely for an incident neutron to interact with more than one nucleus before exiting the sample. The analyzing power for such multiple scattering events is generally not the same as for a single scattering event. Secondly, the combination of a finite-sized sample, detector, and neutron source means that the analyzing power measured at a given angle is actually the analyzing power for a range of angles. For the case of the lithium sample the full range in scattering angle was approximately 10^{o}. Finally, attenuation of the beam in the sample implies that the portion of the sample closest to the neutron source is more highly illuminated by the neutron beam than the rest of the sample. This shifts the effective center of the sample closer to the neutron source, which causes the effective scattering

angle to be smaller than the nominal laboratory angle.

The calculations necessary to correct for these effects are incorporated in the Fortran codes JANE and COR. The details of JANE (adapted at TUNL from a version originally written by E. Woye of Tübingen University) have been documented in a TUNL internal report (Honoré 83). The quantity one would like to obtain is A_p^s, the analyzing power for point geometry, single scattering. What one has from the experiment is A_f^t, the analyzing power for finite geometry, total scattering. (Total scattering refers to the combination of single and multiple scattering). The two quantities are assumed to be related through the following equations:

$$A_f^t = P_s A_f^s + P_m A_f^m \tag{2-7}$$

$$\Delta_{fp} = A_p^s - A_f^s. \tag{2-8}$$

where, P_s = the probability of neutrons scattering in the sample once,

P_m = the probability of neutrons scattering in the sample more than once (note that $P_m + P_s = 1$),

A_f^s = the analyzing power for finite geometry, single scattering,

A_f^m = the analyzing power for finite geometry, multiple scattering,

Δ_{fp} = the correction for finite geometry.

Details of the experiment must be supplied to JANE as input. Geometry details, including dimensions of the neutron-production gas cell, sample, and detector are required. The incident deuteron beam energy, gas cell pressure, sample composition, and detector flight paths are other input quantities. The uncorrected data are used as a first guess for the finite geometry, single scattering analyzing powers at the incident neutron energy. Total neutron cross sections in 200 keV steps, angular distributions of elastic and inelastic scattering cross sections in 1^o steps, and angular distributions of elastic and inelastic scattering analyzing powers in 1^o steps were all compiled in a library for a range of energies covering the incident neutron energy and energies below. The total neutron cross-section data used in the library for the present calculations were obtained from the Brookhaven National

Laboratory tabulations (BNL 64). The low energy elastic differential cross-section data were obtained from Smith *et al.* (Smith 82) and Knox *et al.* (Knox 79) while the higher energy data were taken from Hogue (Hogue 79). The low energy inelastic differential cross-section data were obtained from Batchelor *et al.* (Batchelor 63) and the higher energy data were also taken from Hogue. One elastic scattering analyzing power angular distribution at 1.8 MeV taken from Lane *et al.* (Lane 64) was used in the library along with the present data. No low energy inelastic analyzing power data have been published so the low energy inelastic data for the library were assumed to be equal to the 5 MeV data of the present work. The calculations were performed for each energy separately starting with the lowest. A Legendre polynomial fit to the uncorrected experimental data was used as a first guess for the analyzing power angular distributions at the energy at which the corrections were being calculated. As the data sets at each energy were corrected they were added to the library for the next higher energy, since the library must contain data at the incident neutron energy for which the corrections are being made and at lower energies.

JANE uses the Monte Carlo technique to randomly generate so-called neutron histories. A neutron history is a set of locations with one location in the gas cell, one or two locations in the sample, and a location in each detector. The gas cell location becomes the production site of the neutron. The one or two sample locations are the interaction sites for single or double scattering. The position in the detector is the site where the neutron interacts with the scintillator material. The 4500 multiple scattering histories and 500 single scattering histories used were sufficient to provide randomly and evenly distributed sets of locations, considering the statistical accuracy of the experimental data. The neutron flux arriving at the detector after having scattered at the designated locations is calculated. JANE also keeps track of the time of flight for each neutron history. Simulated time-of-flight spectra are generated on the basis of this information. Separate spectra are created for left and right detectors, spin up and spin down, single and multiple scattering.

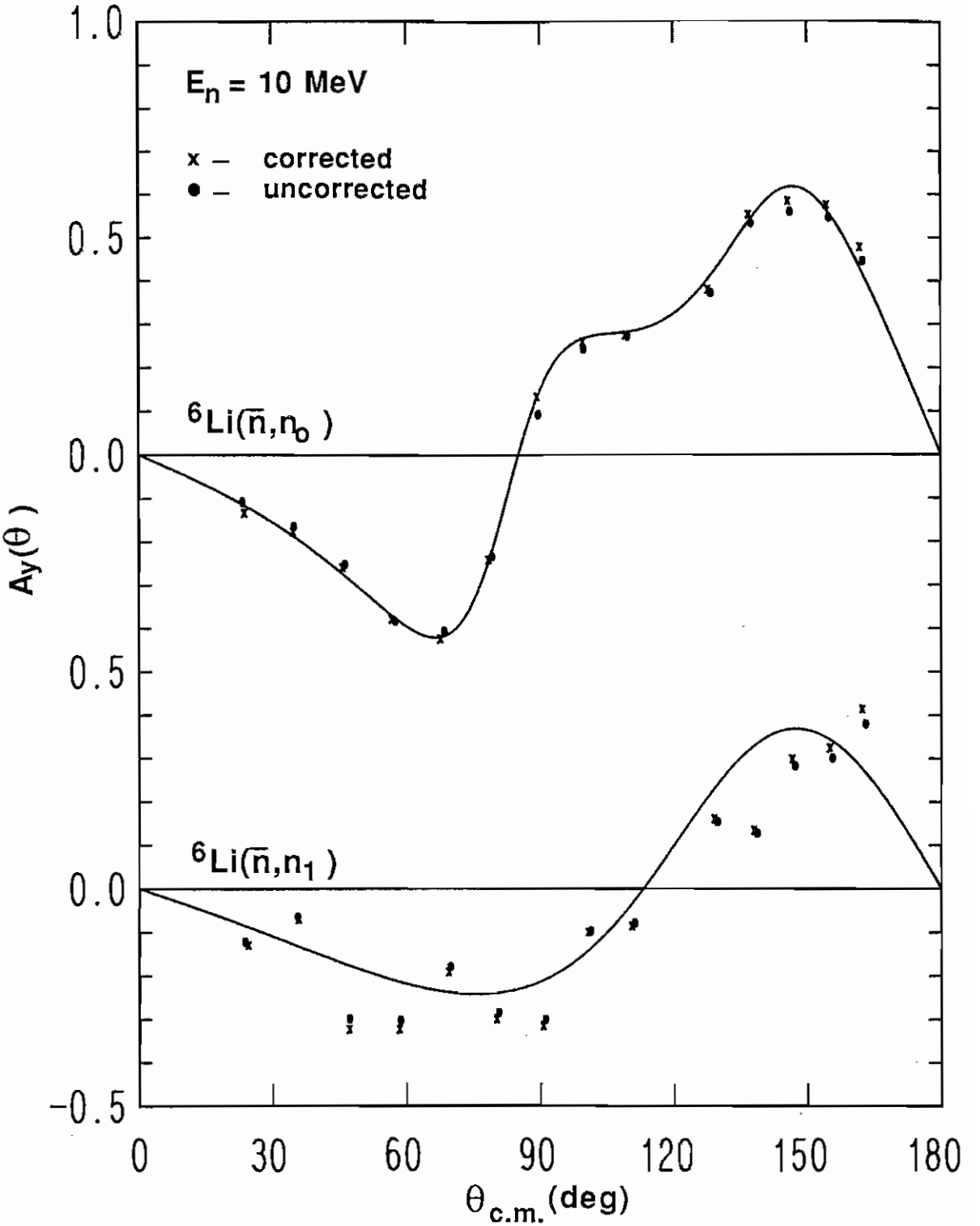

Fig. (2-9) The magnitude of the multiple scattering and finite geometry corrections are indicated. The error bars have been removed for clarity. The curves are the energy dependent associated Legendre polynomial fits obtained later.

For these spectra JANE calculates P_s, P_m, A_f^m, and Δ_{fp}.

The quantities calculated in JANE are then input to the correction code COR along with the uncorrected experimental data, A_f^e. COR then makes several different calculations using Eqs. (2-7) and (2-8) under different assumptions. The first calculation is a new estimate of A_f^s using the values of P_s, P_m, and A_f^m from JANE and assuming A_f^l is equal to A_f^e. This new estimate of A_f^s is used in an updated input data set for a second iteration of JANE. This value of A_f^s is also used in Eq. (2-8) along with the value of Δ_{fp} from JANE to obtain a new estimate of A_p^s. This new estimate of A_p^s is put into an updated version of the JANE library for the second iteration.

COR uses Eq. (2-7) to calculate a new estimate of A_f^l. The same values of P_s, P_m, and A_f^m are used along with the values of A_f^s used in the input set to JANE. This estimate of A_f^l will eventually converge to A_f^e upon successive iterations of JANE and COR. It is this convergence which determines when sufficient iterations have been performed. In fact only two iterations were necessary for all of the data presented here although three iterations were performed. The number of detected events that correspond to triple-scattering processes is small. COR allows for a correction for these processes as well. The values of A_p^s calculated in the last iteration of COR are considered to be the final corrected values. These corrected values are reported at angles which have been adjusted by JANE for the finite geometry effects.

The most notable effect of multiple scattering is to reduce the magnitude of the analyzing power for single scattering. Fig. (2-9) shows the measured, or uncorrected, and the corrected 10 MeV elastic and inelastic data as an example. In the Appendix the uncorrected and the corrected data are listed for comparison. The multiple scattering corrections were typically less than 5% and seldom more than 10% of the final A_p^s.

Corrections for Nitrogen and Oxygen Contaminants

As stated earlier ^{14}N and ^{16}O contaminants of approximately 7% each were

present in the lithium sample. At scattering angles greater than 75° the time-of-flight system had sufficient resolution to separate the peaks for Li scattering from those due to the contaminant nuclei. However, in forward angle spectra the contaminant peak and lithium elastic scattering peak were totally unresolvable. For those cases where the Li data could not be summed independently of the contaminants, corrections were applied to the data. The lithium, oxygen and nitrogen together give an observed $A_y(\theta)$ which can be expressed as:

$$A_{y\ Meas} = A_{y\ O}\frac{\sigma_O}{\sigma_{Li}}\frac{N_O}{N_{Li}} + A_{y\ N}\frac{\sigma_N}{\sigma_{Li}}\frac{N_N}{N_{Li}} + A_{y\ Corr}\left[1 - \frac{\sigma_O}{\sigma_{Li}}\frac{N_O}{N_{Li}} - \frac{\sigma_N}{\sigma_{Li}}\frac{N_N}{N_{Li}}\right]. \quad (2\text{-}9)$$

The quantities indicated are

$\sigma_O, \sigma_N, \sigma_{Li}$ = the differential cross sections at the specified angle for oxygen, nitrogen and lithium respectively,

N_O, N_N, N_{Li} = the number of oxygen, nitrogen and lithium nuclei in the sample (note $\frac{N_O}{N_{Li}} = \frac{N_N}{N_{Li}} = 0.08$),

$A_{y\,O}, A_{y\,N}$ = the analyzing powers for oxygen and nitrogen at the specified angle,

$A_{y\ Corr}$ = the actual lithium analyzing power,

$A_{y\ Meas}$ = the measured analyzing power.

An equation for the uncertainty in $A_{y\ Corr}$ was derived based on errors in all of the above quantities.

The differential cross section values were obtained from the literature. Values for $A_{y\,O}$ and $A_{y\,N}$ were measured in an ancillary experiment using the water and hydrazine samples. The nitrogen data also appear as part of a spherical optical model analysis for nitrogen (Li 86). The oxygen data were analyzed by Anli Li and presented by him at an A.P.S. meeting (Li 85). They were included in these calculations after private communications with him. The contaminant corrections were applied to the JANE-corrected values. Since in most cases the forward angle analyzing powers for

nitrogen and for oxygen were not greatly different from the values for lithium, the corrections to the data were very small; corrections were typically less than 2%.

Presentation of Data

It is customary and useful to fit the cross-section and analyzing power data to Legendre polynomials. At TUNL a computer program, ASSFITE, has been available which simultaneously fits data at several energies to Legendre polynomials (documented in Murphy 84). The program provides the polynomial coefficients expressed as a function of energy. In general, a cross-section angular distribution can be written as a Legendre polynomial expansion as follows:

$$\sigma(E_j,\theta) = \sum_l a_l(E_j)\, P_l(\cos\theta) \ . \tag{2-10}$$

If one expands the a_l's in terms of some energy dependent functions, $f_l^n(E)$ then one has:

$$\sigma(E_j,\theta) = \sum_l \Big[\sum_n k_l^n \ f_l^n(E_j) \Big] P_l(\cos\theta) \ . \tag{2-11}$$

Legendre polynomial coefficients obtained in this way have been demonstrated to reliably represent cross sections at energies between the energies at which actually measured data exist. This is because the coefficients calculated in this way are highly correlated, as they should be. The code can also provide coefficients for associated Legendre polynomial fits to the product of cross-section and analyzing power data where:

$$A_y(E_j,\theta) \times \sigma(E_j,\theta) = \sum_l b_l(E_j) P_l^1(\cos\theta) \ . \tag{2-12}$$

Figs. (2-10) through (2-14) are plots of the $a_l(E)$'s and $b_l(E)$'s for elastic and inelastic scattering. The a_l's and b_l's were taken to be geometric polynomials in E of third order or lower. The $A_y(\theta)$ data corrected for multiple scattering are presented along with the associated Legendre polynomial fits in Figs. (2-15) through (2-18). Cross-section data were not available at certain energies at which analyzing power data were taken. In order

to calculate the product of $A_y(\theta)$ and $\sigma(\theta)$ at these energies, values of $\sigma(\theta)$ were obtained from the energy dependent Legendre polynomial coefficients. These coefficients were also useful later in generating cross-section data sets at several energies to be used in the optical model analysis described below. In the Appendix, tables of the elastic and inelastic scattering analyzing power data are presented along with the calculated values from the associated Legendre polynomial fits.

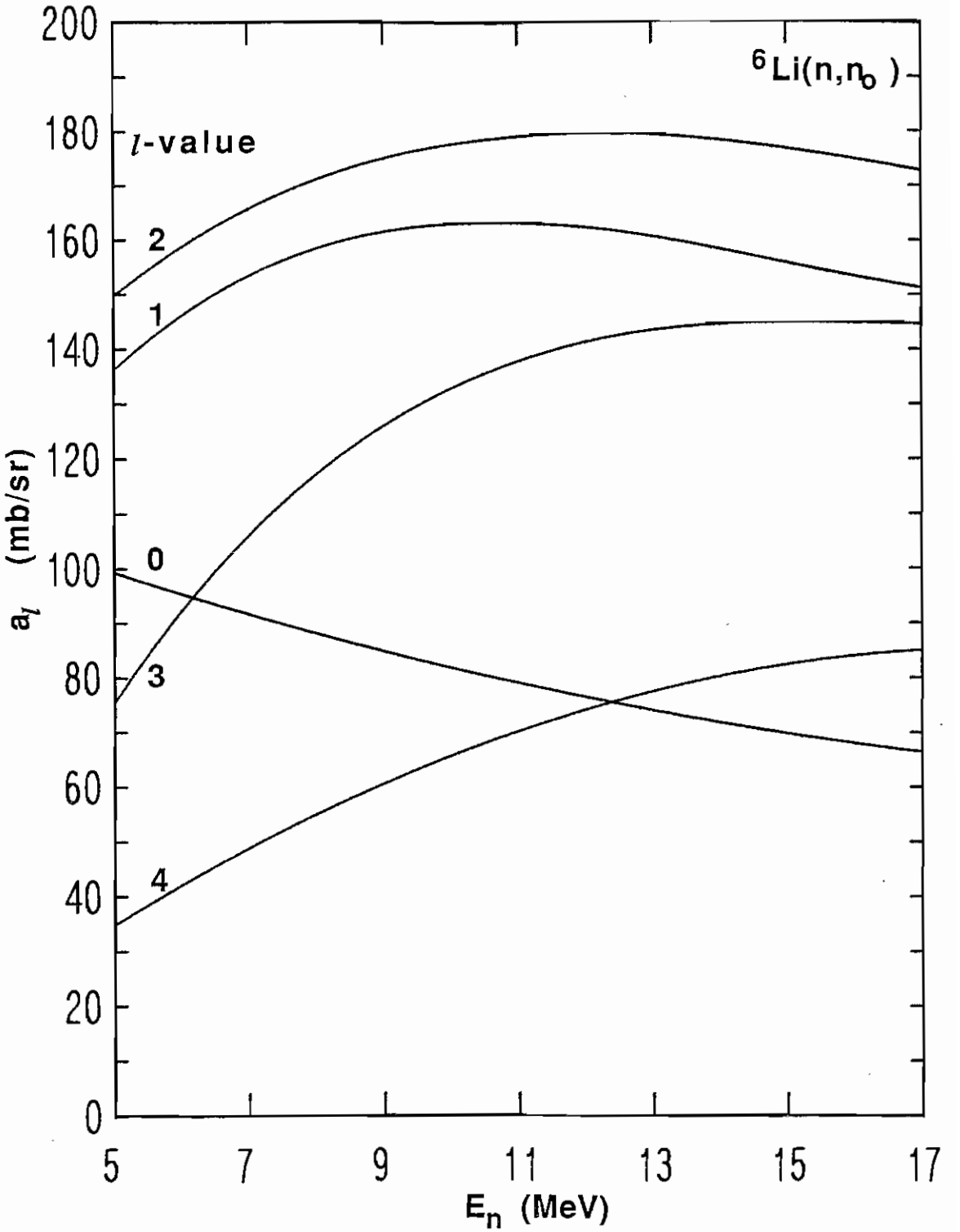

Fig. (2-10) Plots of first five $a_l(E)$'s obtained from ASSFITE which represent the ^{6}Li neutron elastic scattering cross-section data of Hogue and of Knox.

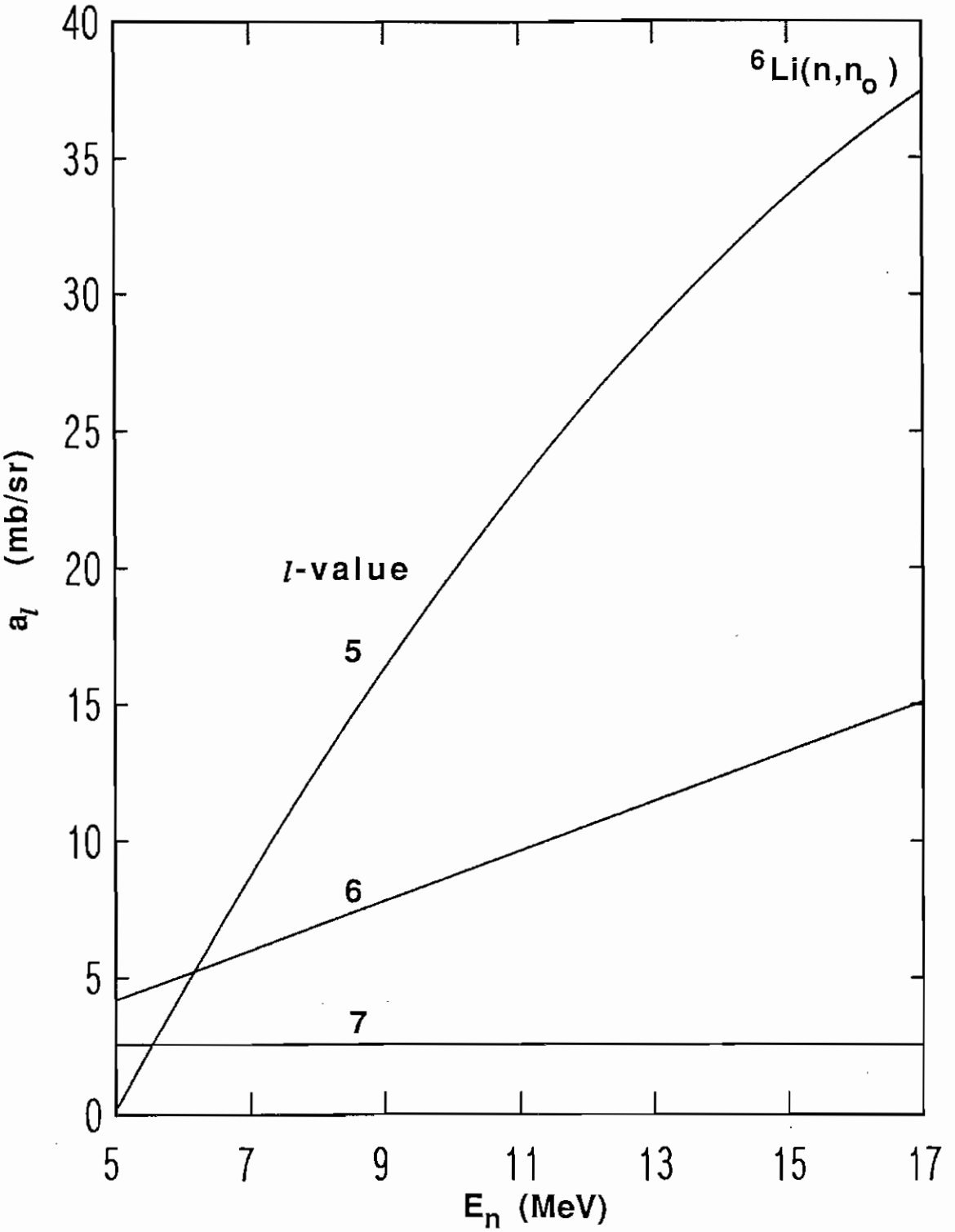

Fig. (2-11) A continuation of Fig. (2-10) showing the remaining $a_l(E)$'s for ^{6}Li neutron elastic scattering cross-sections.

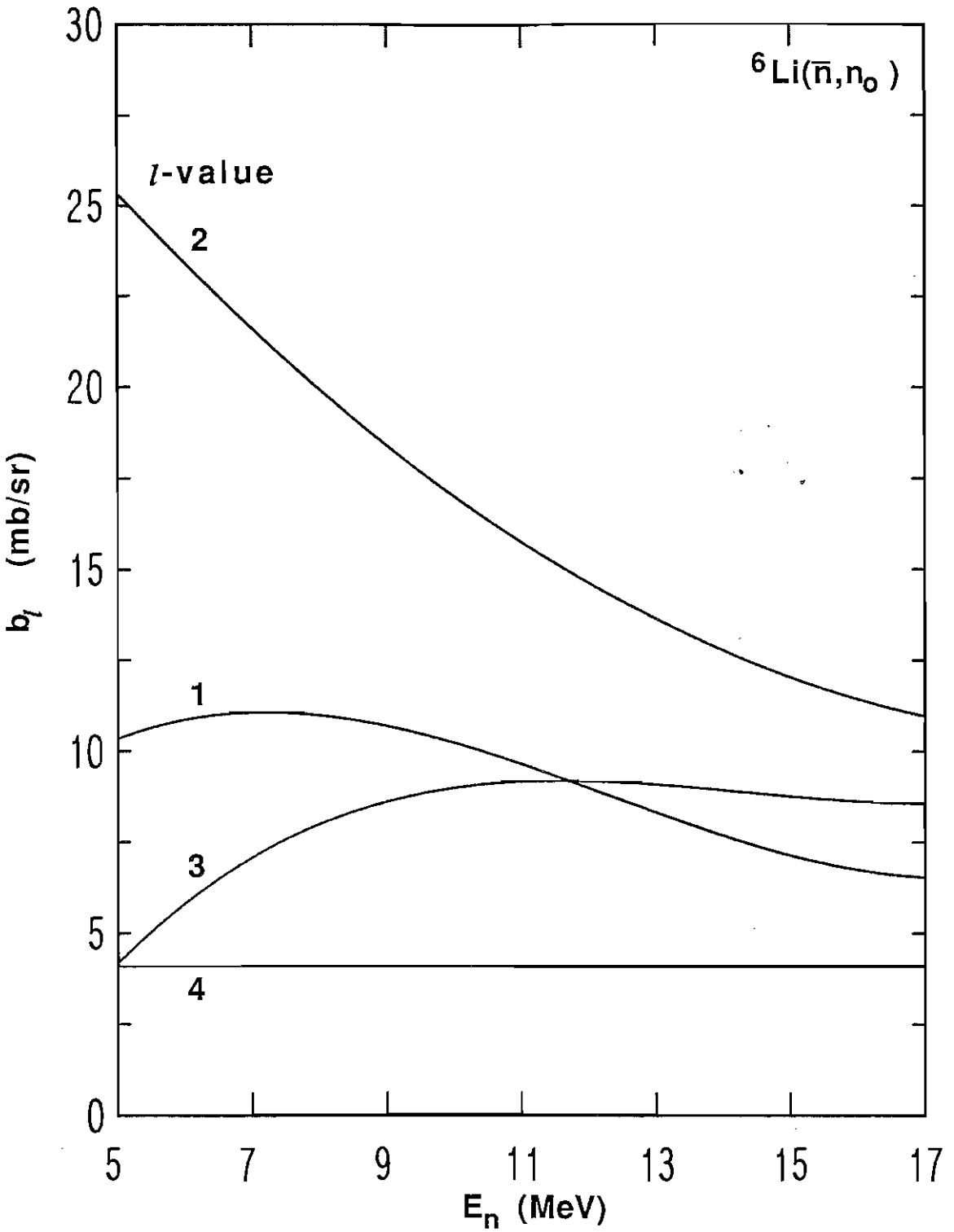

Fig. (2-12) Plots of first four $b_l(E)$'s obtained from ASSFITE which represent the ^{6}Li neutron elastic scattering analyzing power data.

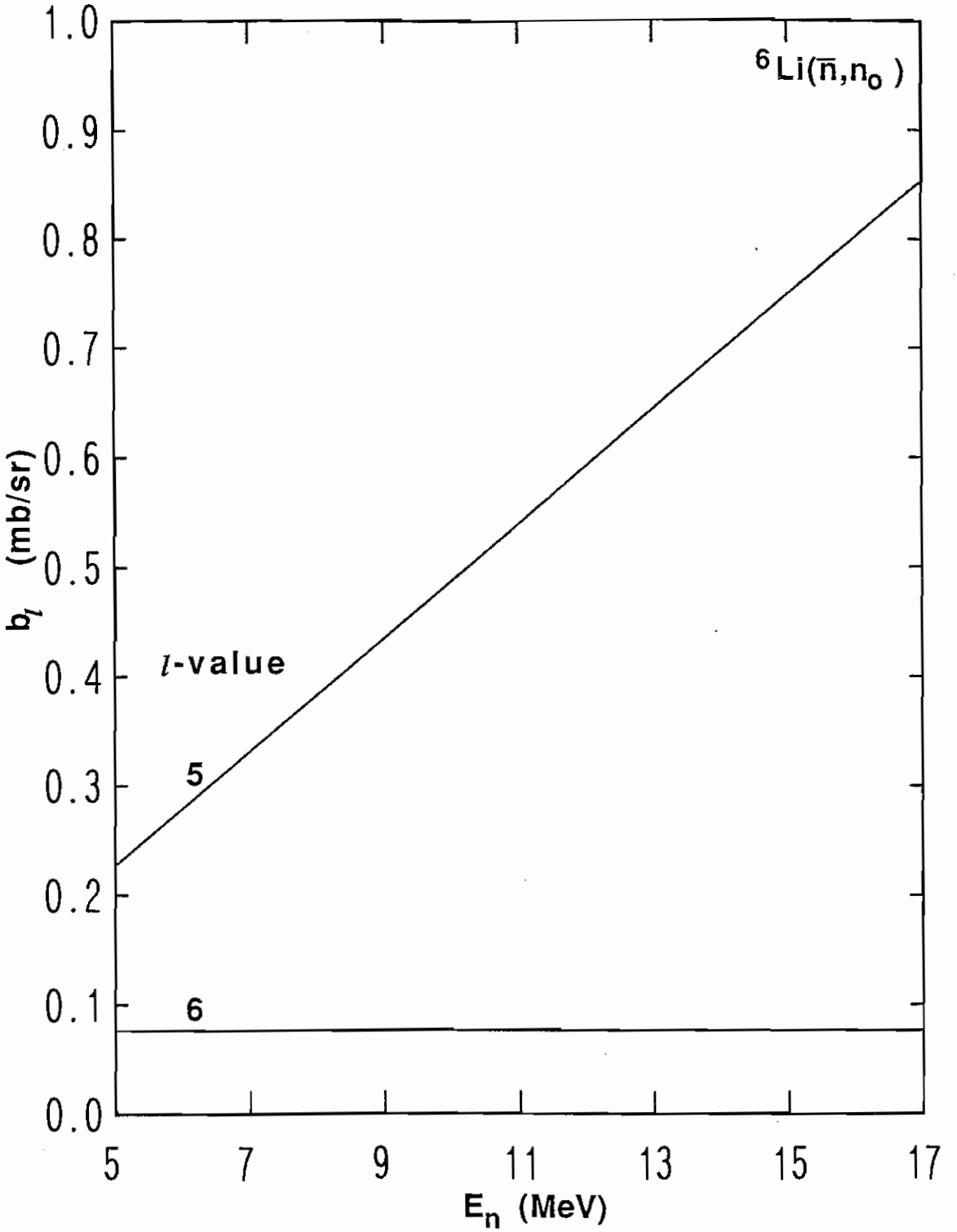

Fig. (2-13) A continuation of Fig. (2-12) showing the remaining $b_l(E)$'s for ^{6}Li neutron elastic scattering analyzing powers.

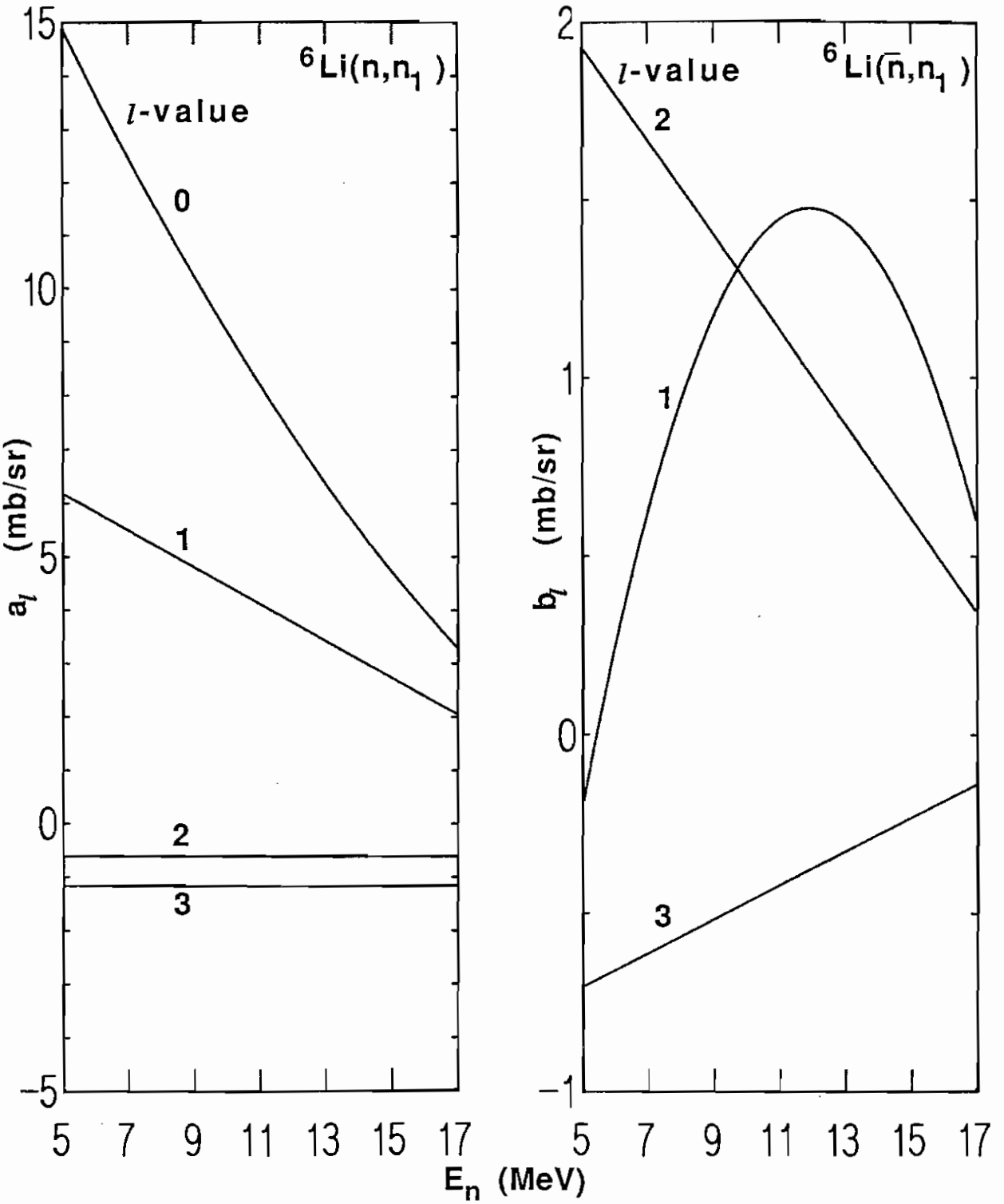

Fig. (2-14) The $a_l(E)$'s (left) and $b_l(E)$'s (right) obtained from ASSFITE which represent the ^{6}Li neutron inelastic scattering cross-sections and analyzing powers, respectively.

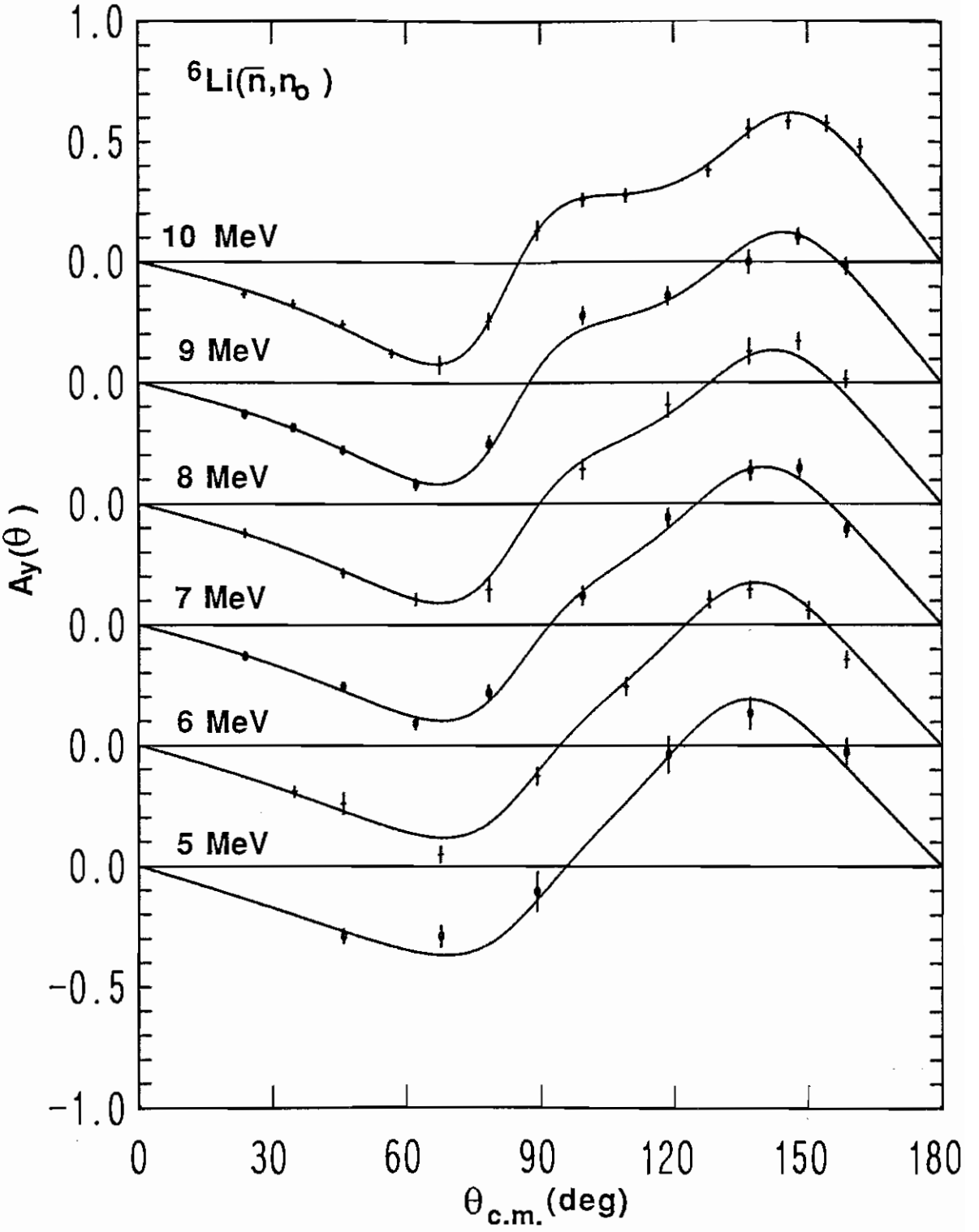

Fig. (2-15) Analyzing power data for neutron elastic scattering from ^{6}Li at 5 to 10 MeV along with energy dependent associated Legendre polynomial fits.

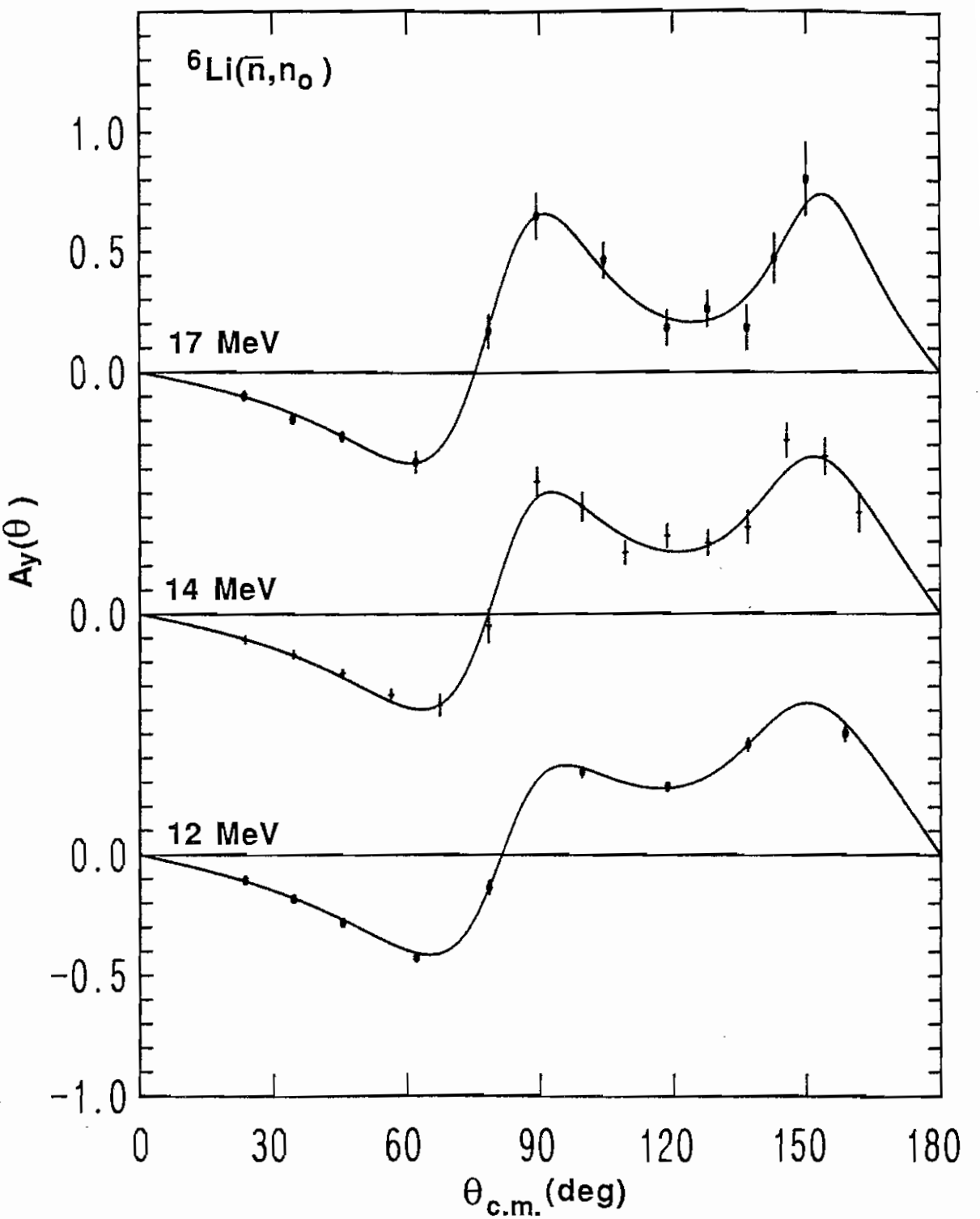

Fig. (2-16) Continuation of Fig. (2-15) showing elastic data and fits at 12, 14, and 17 MeV.

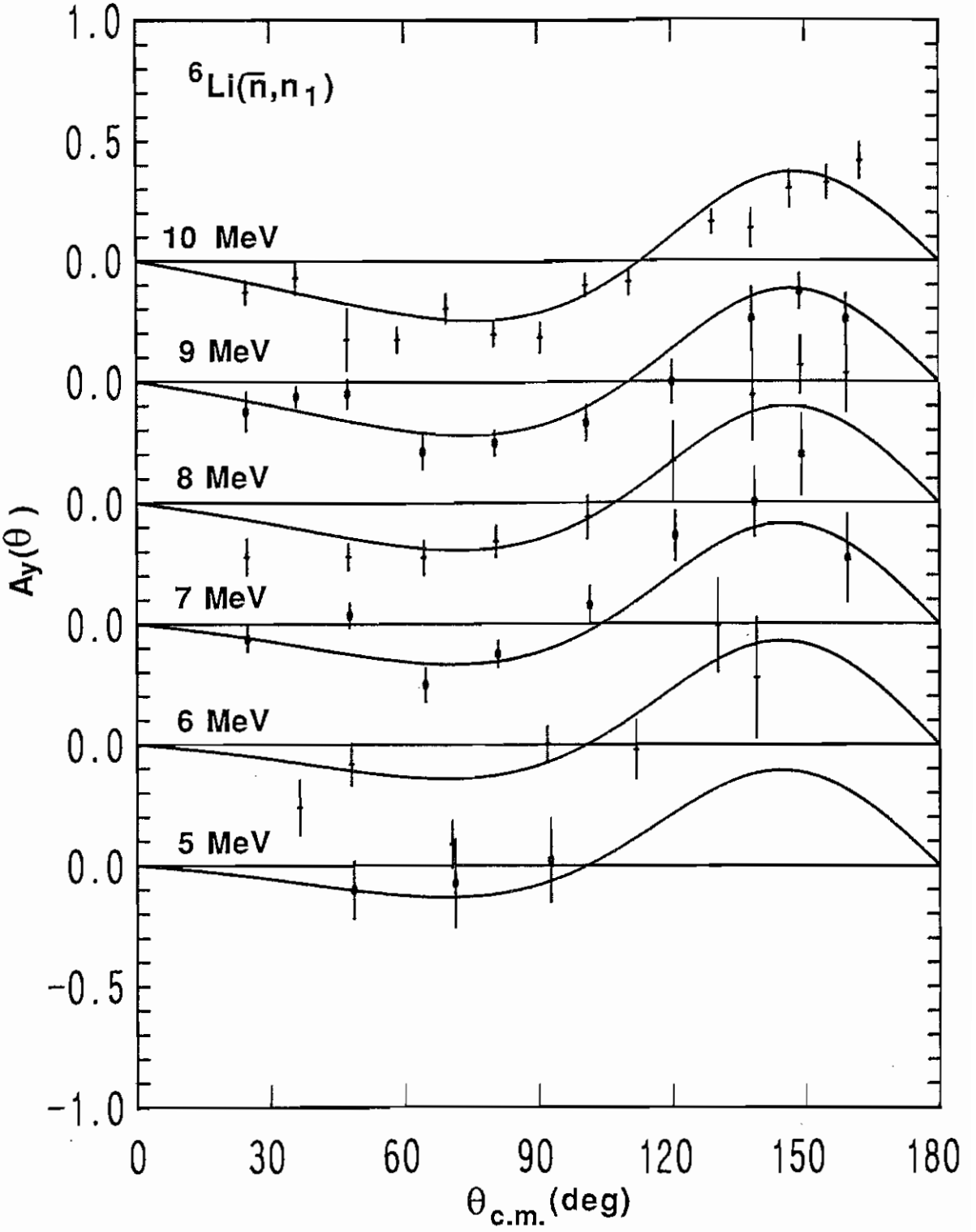

Fig. (2-17) Analyzing power data for neutron inelastic scattering from ^{6}Li at 5 to 10 MeV along with energy dependent associated Legendre polynomial fits.

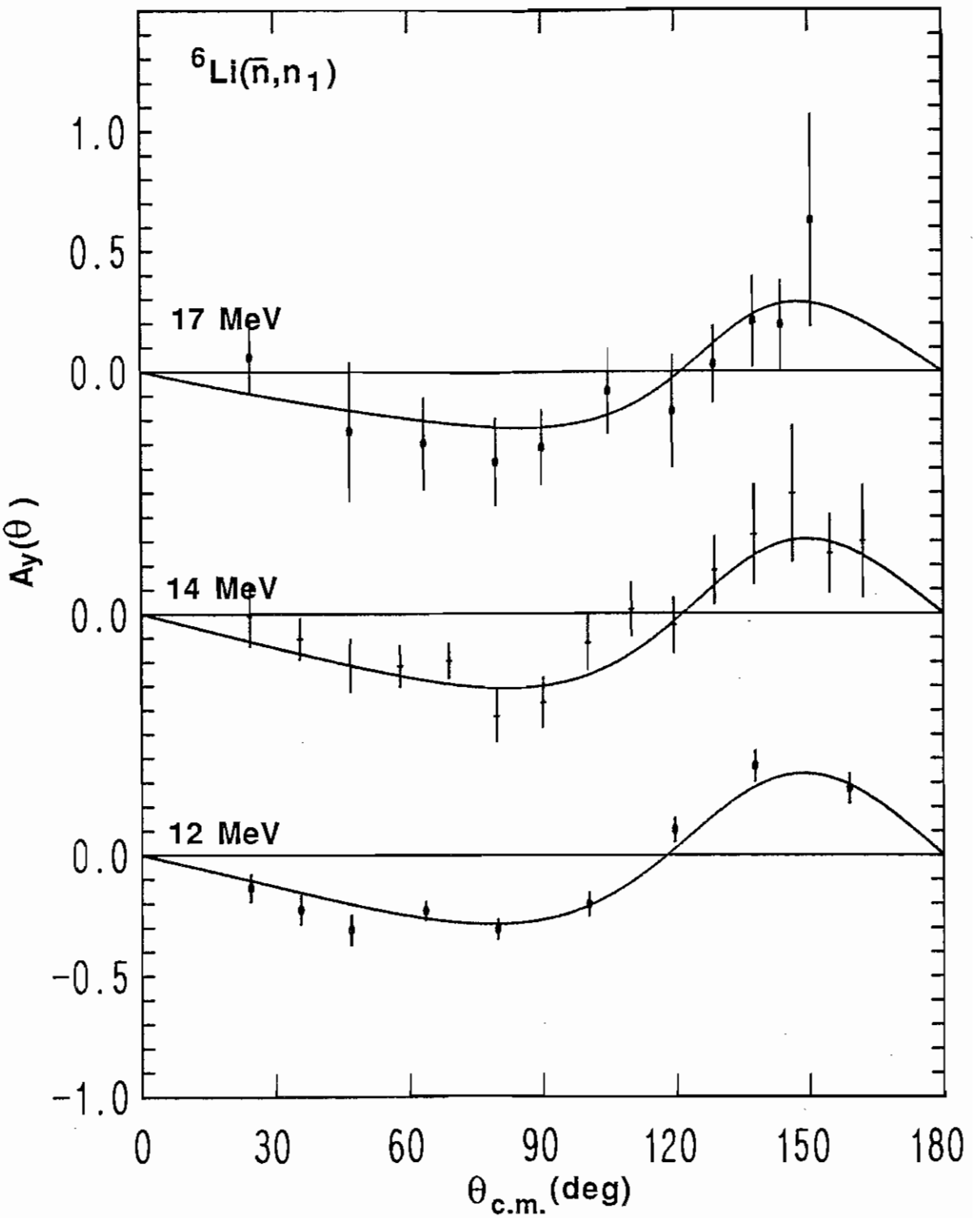

Fig. (2-18) Continuation of Fig. (2-17) showing inelastic data and fits at 12, 14, and 17 MeV.

CHAPTER 3

PROTON SCATTERING MEASUREMENTS

Introduction

The measurements of proton scattering from ^{6}Li required use of entirely different techniques from those of neutron scattering. The type of beam used, the foil target, the detection system, detector electronics, data acquisition procedures, and the method of data analysis will be described in detail. Those elements in common with the neutron experiments will be mentioned summarily.

In this experiment, cross section and analyzing power values were obtained simultaneously as a function of angle at proton energies from 5 to 17 MeV. The data were taken using the widely accepted two-detector spin-flip method. In this case, where one accumulates counts in separate spectra for left-detector spin-up, right-detector spin-up, left-detector spin-down, and right-detector spin-down, the expression for the analyzing power is given as:

$$A_y(\theta) = \frac{1}{P_b}\frac{\gamma - 1}{\gamma + 1} \tag{3-1}$$

where,
$$\gamma = \sqrt{\frac{LU \times RD}{RU \times LD}}\ . \tag{3-2}$$

In the expressions for γ and $A_y(\theta)$,

LU = the number of counts in the peak for left-detector spin-up,

LD = the number of counts in the peak for left-detector spin-down,

RU = the number of counts in the peak for right-detector spin-up,

RD = the number of counts in the peak for right-detector spin-down,

P_b = the proton beam polarization.

A definition for the differential cross section which is applicable to a non-ideal experiment is:

$$\sigma(\theta) = \frac{1}{R_o\, n x}\,\frac{dR}{d\Omega} \qquad (3\text{-}3)$$

where n = the number of nuclei per volume,

x = the thickness of the target,

R_o = the number of particles incident on the scatterer in a given time interval,

$d\Omega$ = the solid angle of the detector,

dR = the number of scattered particles detected within the solid angle during the time interval.

In terms of actually measured quantities one has:

$$n x = \frac{TTHICK \times CSOLID}{M \times \cos(\theta_T)}\ , \qquad (3\text{-}4)$$

$$d\Omega = \frac{A}{r^2}\ , \qquad (3\text{-}5)$$

$$R_o = \frac{BCI}{CBEAM \times DTC}\ , \qquad (3\text{-}6)$$

dR = the weighted mean of $SIGUP = R\,U + L\,U$ and $SIGDN = R\,D + L\,D$. (3-7)

The quantities indicated above are:

$TTHICK$ = the target thickness in $\mu g/cm^2$,

M = the atomic weight of the target element in a.m.u.,

θ_T = the angle between the incident beam direction and the normal to the target foil,

$CSOLID$ = a constant factor to convert $TTHICK$ to units of particles/mb,

A = the area of the detector entrance slit,

r = the distance from the target to the detector entrance slit,

BCI = the total integrated beam current incident on target, in nA,

DTC = the electronics and computer dead-time correction factor,

$CBEAM$ = a constant factor to convert BCI counts to number of incident

particles.

As described below, a foil target was used consisting of ^{6}Li evaporated onto an aluminum foil backing. Consequently, a well resolved ^{27}Al elastic peak was present in all of the spectra. Also, data were taken with a foil comprised of aluminum only, for the primary purpose of monitoring the position of the inelastic scattering peaks to determine if and when one of them overlaps the ^{6}Li elastic peak. In order to take advantage of this bonus data, $A_y(\theta)$ and $\sigma(\theta)$ were obtained for ^{27}Al at all energies and angles using both foils.

Beam Production

The beam production, acceleration and transport systems are in most cases identical to those used in the neutron scattering measurements, so only the differences will be described. The polarized ion source was supplied with hydrogen instead of deuterium gas, thus producing polarized negative hydrogen ions. The linear voltage ramp on the source was not turned on since a continuous beam was suitable. A dc beam also meant that the bunching and chopping systems were not used.

The terminal voltage on the accelerator was varied from 2.5 to 8.5 MV to produce the 5 to 17 MeV proton beams. The proton scattering chamber is located on the 52° beam leg on which are control slits similar to those on the 38° beam leg. Because of better beam optics for the momentum analyzing system for the 52° leg, the proton energy was known absolutely to within ± 5 keV. Following the analyzing magnet, there are two doublet quadrupole magnetic lenses available for focussing and three magnetic steerers for horizontal and vertical bending of the beam. The final steerer immediately before the scattering chamber was part of a beam steering feedback loop which derived its correction signal from a four-sector split faraday cup located just after the scattering chamber. The measured beam current on target varied from 15 to 35 nA, depending on the performance of the source and the requirements of the experiment. In many cases the beam was

deliberately reduced when too high counting rates adversely affected the dead-time.

Target Preparation

The preparation of the thin film target involved commonly known evaporation techniques. Owing to the softness and reactivity of lithium metal it was necessary to evaporate the lithium onto a previously prepared thin aluminum foil. Extra effort was put into making an ultra-thin aluminum foil so that the aluminum inelastic scattering peaks, which might overlap with the lithium peak, would be as small as possible. Inside an evacuated bell jar small amounts of cesium iodide and aluminum wire in a tungsten boat were heated resistively, evaporated, and condensed onto glass microscope slides. The cesium iodide coats the glass slide first since it evaporates at a lower temperature, and later acts as a release agent during a process of floating the foil off in a water bath. The target ring onto which the aluminum foil was floated has an inner diameter of 0.64 cm.

Special steps were taken to minimize contact between the target and air, since lithium is fairly reactive in air and since excessive contamination of the target would result otherwise. A special target rod, which holds a series of target rings in place in the scattering chamber, was also used to hold the aluminum foil target rings in place in the evaporation chamber during the lithium evaporation process. The rod is equipped with a sleeve with O-rings at top and bottom which can seal against the upper and lower portions of the rod, thus isolating the target rings. The sleeve was inserted into and sealed against one of the ports of the evaporation chamber. After evaporating the lithium metal in a tantalum boat, again by resistive heating, the evaporation chamber was filled with argon. The target ring section of the rod was pulled back into the sleeve, and the sleeve disconnected from the evaporation chamber, with little danger of air getting inside the sleeve and contaminating the lithium and aluminum foil. A second aluminum foil target ring was on the rod during the lithium evaporation, but it was shielded from exposure to the evaporated lithium.

Target Thickness

These two foils, the aluminum foil and the lithium thin film with aluminum backing, were used for all the measurements of 1985, however their thickness had not been determined. Later it was deemed desirable to extract the cross-section data in addition to the analyzing power data which had previously been the sole objective. This required determining the foil thickness.

In 1986 a second lithium foil with aluminum backing was prepared. Prior to evaporating the lithium, the thickness of the aluminum foil was measured by standard energy loss techniques. The 5.486 MeV α-particle from ^{241}Am was allowed to enter a charged particle detector unimpeded in the first instance, and in the second instance with the target in front of the detector. The detector output was amplified and input to a multi-channel analyzer (MCA). The energy loss was evidenced by the shift in the peak seen on the MCA. With lithium on the foil the α-particle energy loss measurement was repeated with target, detector, α-emitter, and two other detectors inside the main scattering chamber. Precautions were again taken to avoid contaminating the lithium with air. After taking into account contaminants described below, the lithium thickness and aluminum thickness for this second foil were found to be 76.78 $\mu g/cm^2$ and 14.17 $\mu g/cm^2$, respectively.

An unpolarized proton beam was introduced into the chamber and cross-section values at several angles at 8 and 14 MeV were remeasured. These were compared to the yields from the 1985 experiment and thicknesses were assigned to the aluminum foil and the lithium foil with aluminum backing. These thicknesses are recorded in Table (3-1).

Upon comparison of the ^{6}Li elastic cross-section data with earlier data of Harrison and Whitehead (Harrison 63), which covered the energy range of 2.4 to 12.0 MeV, it was evident that the foil thickness measurements for ^{6}Li were in error by a large amount. Similar comparisons of ^{27}Al elastic cross-section data with the earlier data

TABLE (3-1)

FOIL THICKNESSES AND RENORMALIZATION FACTORS

target	measured thickness ($\mu g/cm^2$)	renormalization factor	correct thickness ($\mu g/cm^2$)
^{6}Li	103.36	0.41	252.10
^{27}Al (foil backing)	14.09	0.72	19.56
^{27}Al (single constituent foil)	72.51	0.65	111.55

of Roy *et al.* (Roy 83) revealed that the ^{27}Al foil thickness measurements were also in error by a large amount. A reconsideration of the calculations involved showed no obvious sources of error. Since we are not able to recognize the cause of the error it must be assumed that the fault lies in the α-particle energy loss measurement. A final renormalization of the proton scattering cross-section data was made to the Harrison data and the Roy data for ^{6}Li and ^{27}Al, respectively. For the ^{6}Li data the normalization factor is 0.41 at all energies. For ^{27}Al the 5, 6, and 8 MeV data were obtained with the plain aluminum foil and the normalization factor for these data is 0.65. The ^{27}Al data at all other energies (7 MeV and 9 through 17 MeV) were obtained from the aluminum backing for the lithium film. In this case the ^{27}Al normalization factor is 0.72. In Table (3-1) the renormalized foil thicknesses are presented along with the values which are assumed to be in error.

^{6}Li Target Contaminants

The 1986 Li target was determined to be 92.78% ^{6}Li by atom number with contaminants of ^{16}O (5.28%) and ^{12}C (0.81%) determined by analysis of the proton scattering spectra. This analysis consisted of summing the ^{6}Li, ^{16}0 and ^{12}C peaks at several angles in the 14 Mev spectra. The number of ^{16}0 and ^{12}C nuclei relative to the number of ^{6}Li nuclei present in the foil can be calculated in the following manner:

$$\frac{N_{^{16}O}}{N_{^{6}Li}} = \frac{\sigma_{^{6}Li}}{\sigma_{^{16}O}} \frac{Y_{^{16}O}}{Y_{^{6}Li}} \tag{3-8}$$

and

$$\frac{N_{^{12}C}}{N_{^{6}Li}} = \frac{\sigma_{^{6}Li}}{\sigma_{^{12}C}} \frac{Y_{^{12}C}}{Y_{^{6}Li}} \tag{3-9}$$

where N = the number of nuclei,

σ = $\sigma(\theta)$, the differential cross section,

Y = the number of counts in the peak (the peak yield).

The cross-section values were obtained from optical model calculations using the parameters of Davé (Davé 83). A small ^{7}Li contaminant was apparent in most of the spectra as a small, well resolved peak near the ^{6}Li peak. A value of 1.12% for the ^{7}Li contaminant was provided by the manufacturer and this value was included in the calculation of the foil thickness described above.

Scattering Chamber

The multi-purpose scattering chamber available at TUNL was ideally suited for this experiment. It is shown schematically in Fig. (3-1). It consists of an aluminum cylinder, 60 cm in diameter, having beam entrance and exit ports, a removable lid, and pumping equipment providing a typical pressure of $7x10^{-6}$ Torr. Attached to the lid is a rotating plate with mounts for the four left detectors, which could be rotated to within 0.1^{o} of the desired angle with the aid of a vernier scale. A second rotating plate supporting the right four detectors is attached to the bottom of the chamber. The rotating plates have freon cooling to supply the low temperatures necessary for low-noise operation of the detectors.

The eight ORTEC silicon surface barrier detectors used were 2000 μm thick, which is sufficient to fully stop 17 MeV protons. Each detector fit into a holder to which was attached a snout containing collimators. To the front of the cylinder comprising the snout was attached a brass disk with a slit of approximate width 0.24 cm and length 0.95 cm. To the back (closest to the detector) was attached a tantalum disk with a 0.16 cm x 0.95 cm slit. This second disk, by virtue of its smaller slit size, defined the solid angle for the detector. The holders with their detectors and collimation snouts were mounted on tracks fixed to the rotating plate at 10^{o} intervals. The track allowed for varying the radial distance from target to detector. A typical distance from the target to the front of the tantalum disk was 6.159 ± 0.002 cm, giving a typical solid angle of $6.387 \times 10^{-4} \pm 0.067 \times 10^{-4}$ sr. Of course the radial distance and slit dimensions were measured and solid angles calculated separately for each detector.

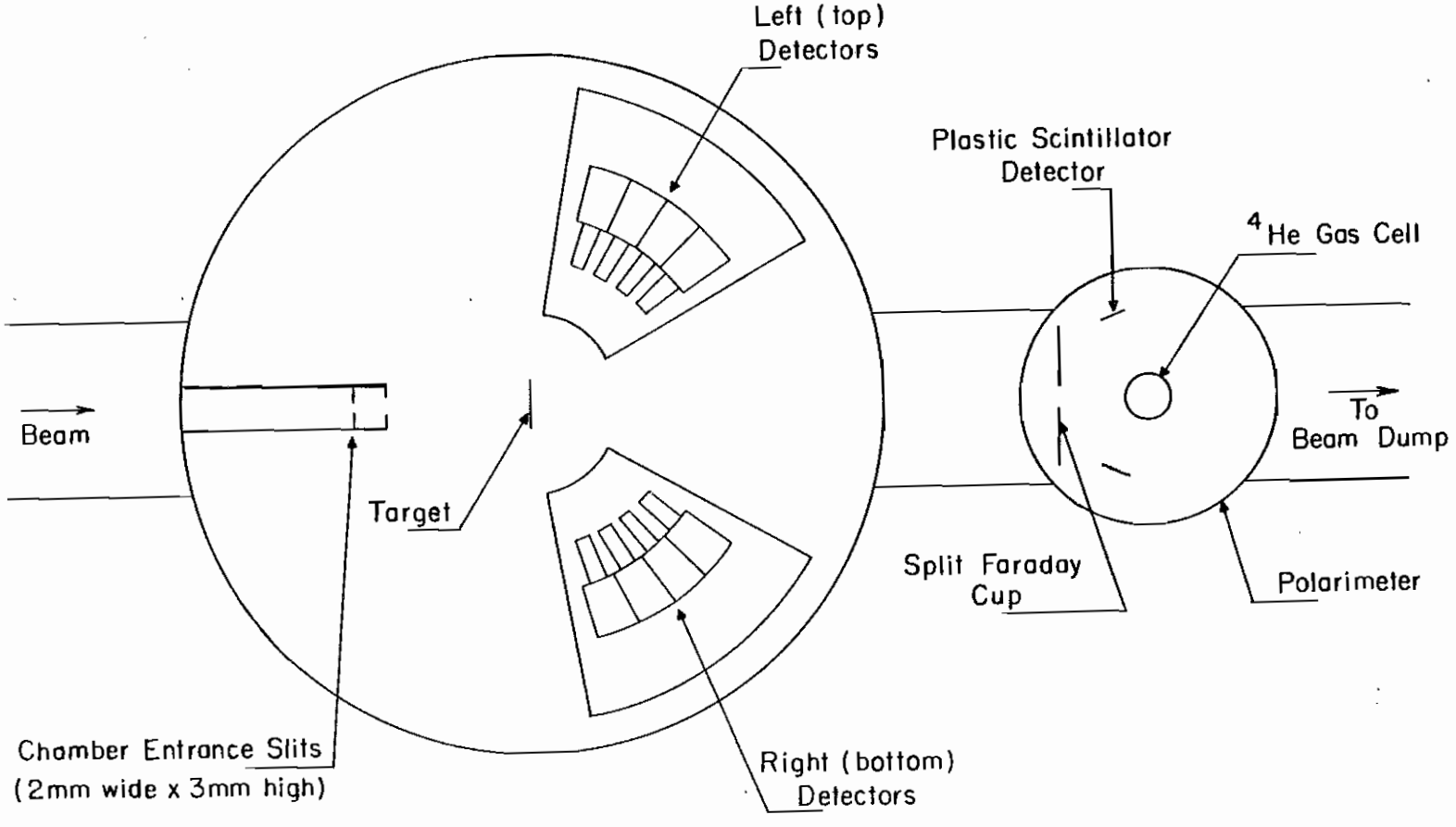

Fig. (3-1) Diagram showing the important features of the main charged particle scattering chamber at TUNL.

The target rod and its sleeve mounts vertically in the center of the chamber. During the 1985 experiment, of five available positions on the rod for mounting foils, one contained the thick Al foil, one contained the foil with ^{6}Li and Al backing, one contained a foil with ^{10}B and Al backing, and the two remaining were empty. Measurements on the ^{10}B foil were performed during this experiment and formed a portion of the work of K. Murphy (Murphy 87). The target rod can be rotated without disturbing the vacuum to allow for scattering angles at or near 90° which otherwise would not be possible because the target ring and target rod would be in the path of the scattered proton. For scattering angles of 60° to 110° the normal to the foil was rotated 50° away from the incident beam direction. For other scattering angles the foil was normal to the incident beam direction. The target rod angle could be set to within about 0.25°. Knowing this angle is important since the effective thickness of the target is related to the cosine of the target angle.

Beam Current Integration

Additional features of the chamber include a set of collimation slits at the entrance of height 3.0 mm and width 2.5 mm. Beam which passed through the target unscattered exited the chamber through the four-sector split faraday cup mentioned previously and entered a ^{4}He polarimeter attached to the exit port of the chamber. After the polarimeter was a section of beam pipe with an aluminum end-plate serving as a beam dump. The charge deposited on the four-sector cup and the charge collected on the beam pipe and end-plate were summed and fed into the beam current integrator (BCI). The digitized output of the BCI was counted and the total value stored for each run to permit proper normalization of the cross-section data.

Polarimeter

In addition to the quench ratio technique used in the neutron experiment, there was also a polarimeter used during the proton experiments for measuring the beam

polarization. The polarimeter makes use of the well known $^4He(\vec{p},p)$ analyzing power which has a magnitude near unity in a certain angular range. A small chamber attached to the exit port of the main scattering chamber contained a ^4He gas cell filled to 2 atm absolute and two plastic scintillation detectors located at $\pm 112^o$ with respect to the incident beam direction. This angle is at or near the maximum value in the analyzing power angular distribution for the proton energies used.

The calibration for the polarimeter is based on the phase shift analysis of Schwandt *et al.* (Schwandt 71). In a separate experiment performed by T.C. Spencer, the asymmetry

$$\varepsilon = \frac{\gamma - 1}{\gamma + 1} = P_b A_y \ , \tag{3-10}$$

was measured simultaneously in the polarimeter and in the main scattering chamber using a ^4He gas target and solid-state detectors at $\pm 112^o$. From these quantities an effective analyzing power,

$$A_{y\ eff} = \frac{\varepsilon_p}{\varepsilon_c} A_{y\,ps} \ , \tag{3-11}$$

can be calculated which is independent of the beam polarization. The quantities indicated are:

ε_p = the asymmetry measured by the polarimeter,

ε_c = the asymmetry measured by the main chamber,

$A_{y\,ps}$ = the analyzing power calculated from phase shift parameters,

$A_{y\ eff}$ = the effective analyzing power of the polarimeter assuming the analyzing power measured in the chamber would be identically equal to $A_{y\,ps}$.

The values of $A_{y\ eff}$ are plotted as a function of energy in Fig (3-2) along with the dashed curve representing the values of $A_{y\,ps}$. Clearly the polarimeter measures an analyzing power consistently lower than the true value. The smooth curve is the same

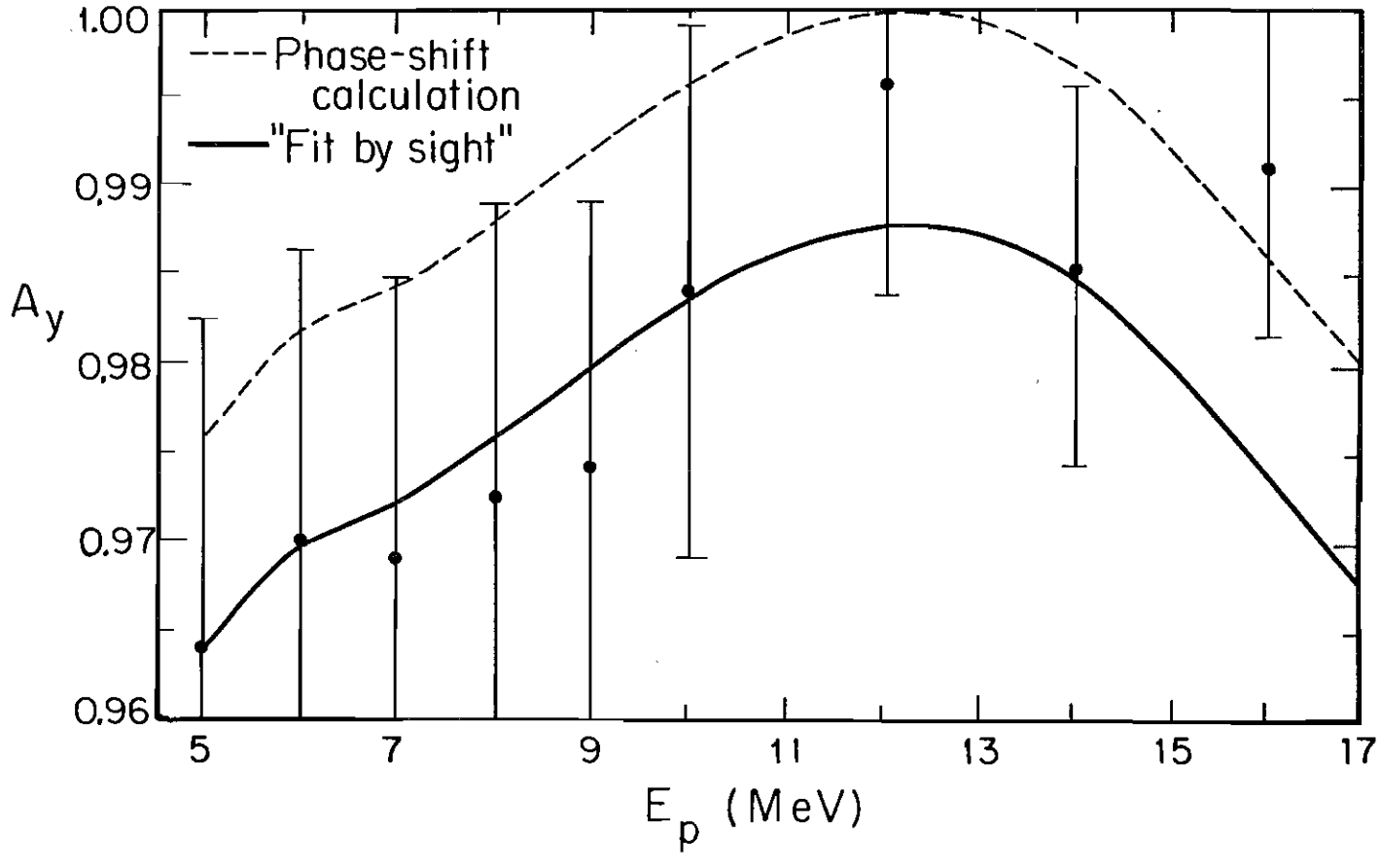

Fig. (3-2) A plot of the effective analyzing power of the polarimeter based on measurements of the ^{4}He($\vec{p}$,p) asymmetry made in the polarimeter and in the main scattering chamber. Dashed curve is a calculation for the ^{4}He($\vec{p}$,p)A_y based on a phase-shift analysis (Schwandt 71).

curve shifted down as a "fit by sight" to the $A_{y\,eff}$ values. This shifted curve was taken to be the effective analyzing power of the polarimeter, $A_{y\,p}$. Thus, during a normal experiment the measured beam polarization is:

$$P_b = \frac{\varepsilon_p}{A_{y\,p}} \,. \tag{3-12}$$

The data points deviate from $A_{y\,p}$ no more than 0.5% (*i.e.*, $\frac{\Delta A_{y\,p}}{A_{y\,p}} = 0.005$). This error and the statistical uncertainty in ε_p make up the uncertainty in P_b so that a typical value of P_b is 0.700 ± 0.004. Also a scale uncertainty of 0.5% exists due to uncertainty in the "fit by sight". This leads to an overall scale uncertainty of $\pm$ 0.75% in the analyzing power data reported for ^{6}Li and ^{27}Al.

Polarimeter Backgrounds

Backgrounds were significant in the spectra obtained with the polarimeter detectors. Figs. (3-3) through (3-5) show polarimeter spectra for spin-up and spin-down at 5, 10, and 17 MeV. At the low energy end of the spectrum is a large contribution presumably from neutrons produced in (p,n) reactions with the collimation slits and other parts of the polarimeter. This appears as an exponential tail which extends into the region of the ^{4}He($\vec{p}$,p) elastic scattering peak. In addition, to the right of the elastic peak a flat "white" background is evident. This is due to protons which have scattered several times within the chamber and thus have all energies up to the incident beam energy. One can safely assume this background extends along the entire spectrum in the region of the peaks of interest.

These backgrounds were dealt with in one of two ways depending on the beam energy. For energies 10 MeV and higher the elastic scattering peak is sufficiently shifted to the right of the exponential tail, so that a simple linear fit to the data points on both sides of the elastic peak adequately represents the background. Below 10 MeV both the linear

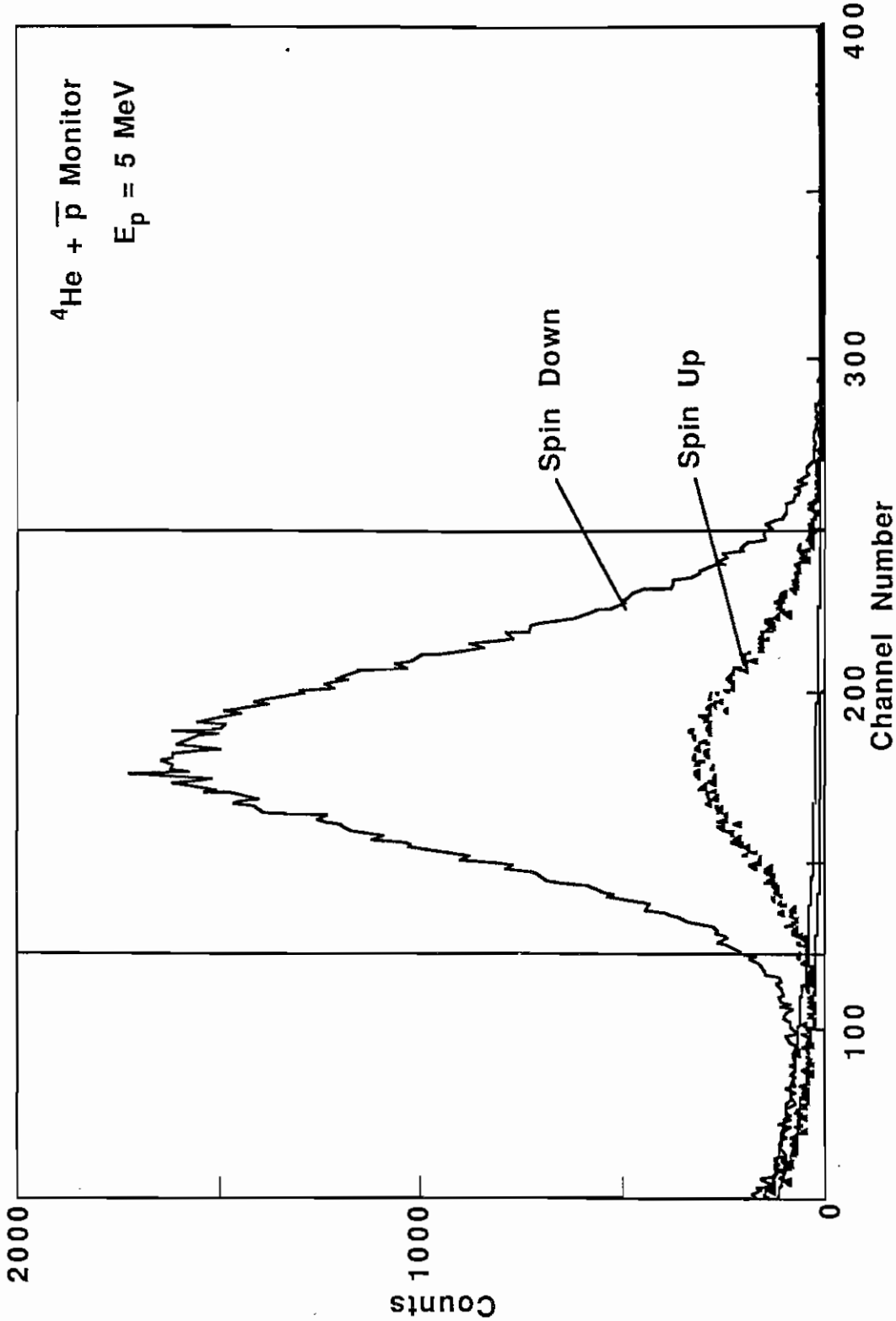

Fig. (3-3) ^{4}He($\bar{p}$,p) polarimeter spectra for the right detector showing spin-up and spin-down. Also shown are examples of the linear plus exponential backgrounds used at 5 MeV.

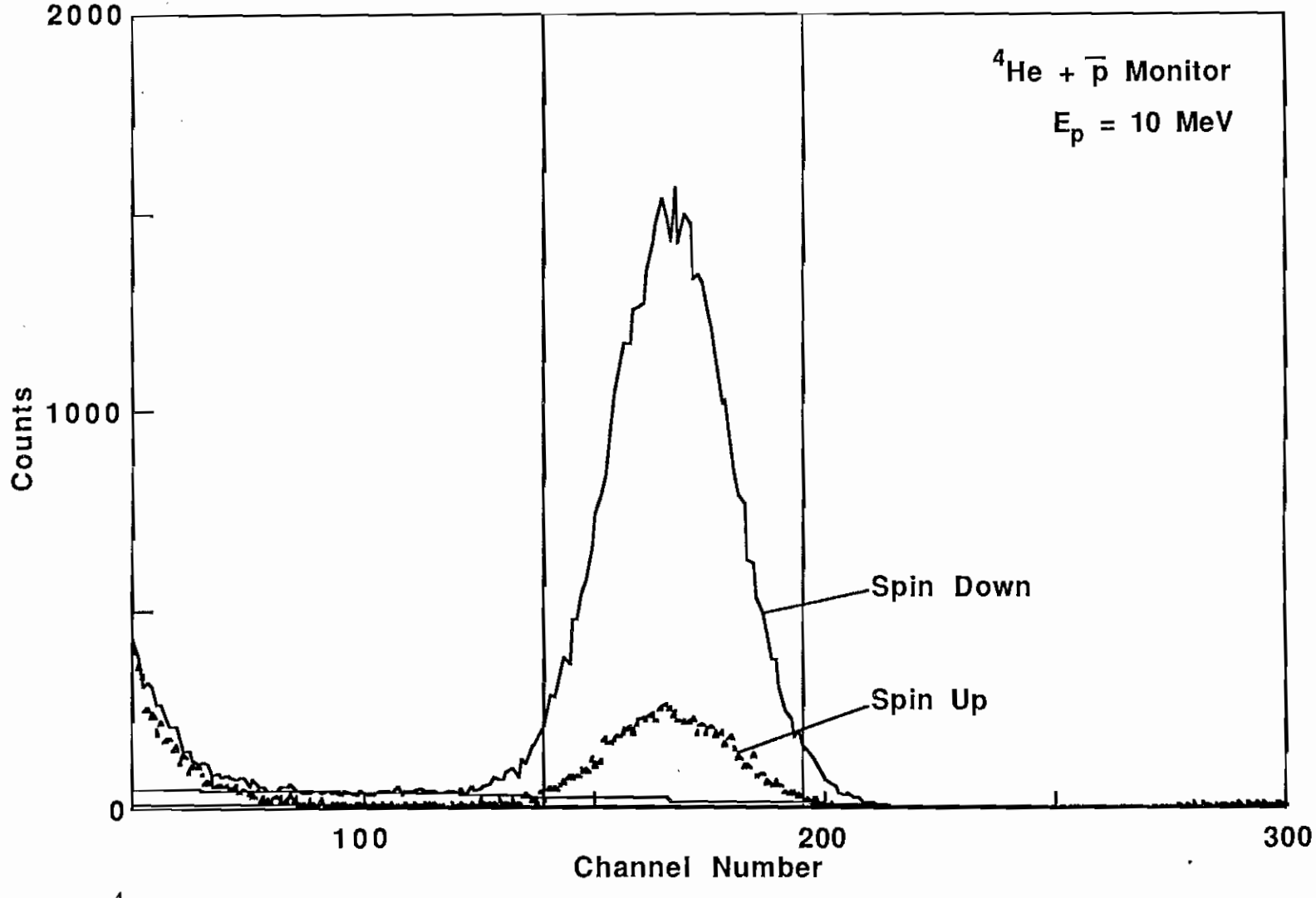

Fig. (3-4) ^{4}He($\bar{p}$,p) polarimeter spectra for the right detector showing spin-up and spin-down. Also shown are examples of the purely linear backgrounds used at 10 MeV.

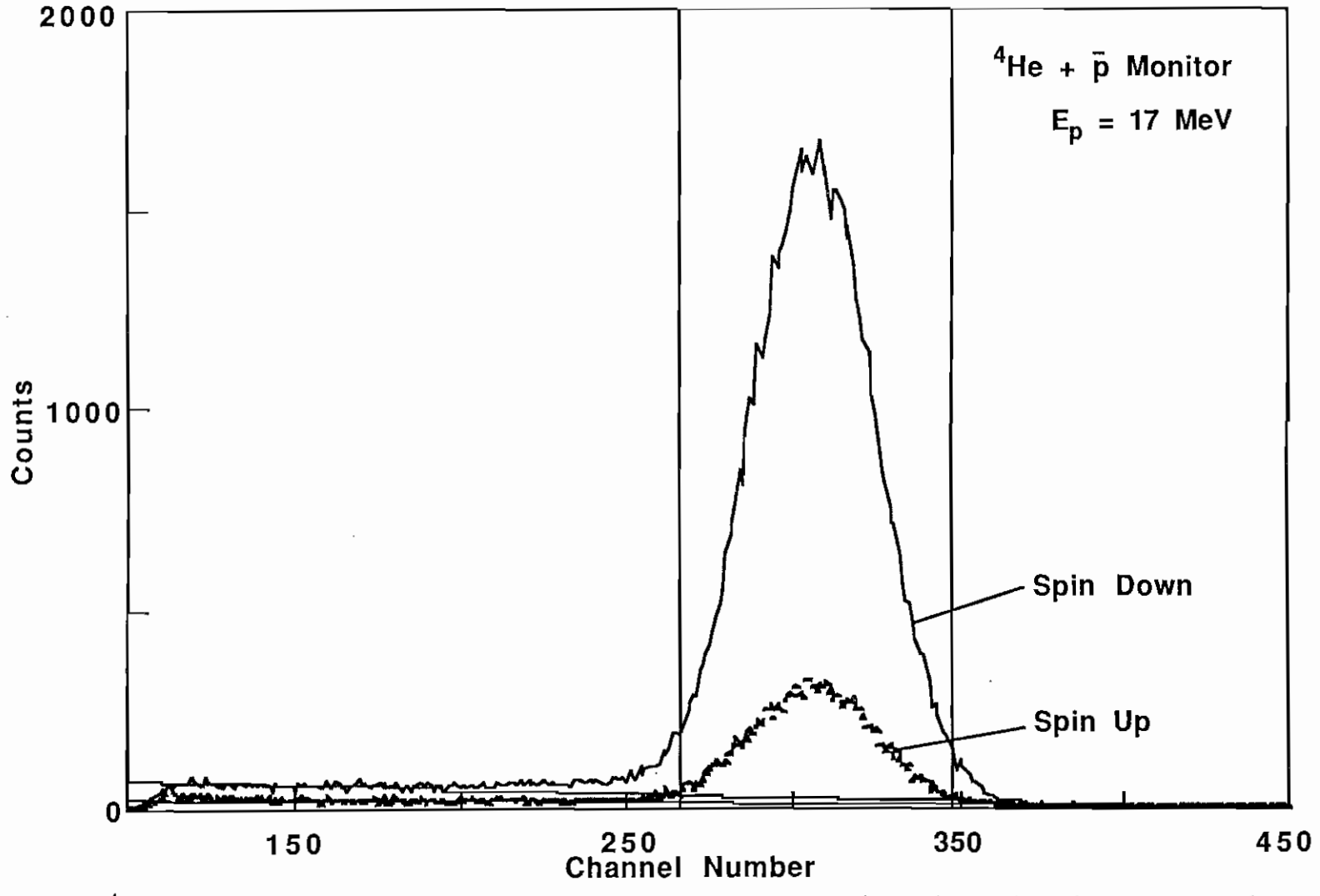

Fig. (3-5) ^{4}He($\bar{p}$,p) polarimeter spectra for the right detector showing spin-up and spin-down. Also shown are examples of the purely linear backgrounds used at 17 MeV.

component and the exponential component of the background must be dealt with. First, a linear fit to the data points to the right of the elastic peak was calculated, extrapolated, and subtracted from the entire spectrum. Then an exponential fit to the data points to the left of the elastic peak was calculated, extrapolated, and subtracted from the entire spectrum. A gate was set on the resulting background-subtracted elastic peak and the peak was summed. Because the analyzing power is so high in the ^{4}He($\vec{p}$,p) reaction, vastly different numbers of counts appeared in the up and down spectra and consequently the shapes and magnitudes of their respective backgrounds were different. As a result, it was necessary to calculate separate backgrounds for the four spectra (left-up, left-down, right-up, right-down). Examples of calculated backgrounds can be seen in Figs. (3-3) through (3-5) along with the spectra for proton energies of 5, 10, and 17 MeV.

Chamber Electronics

The signal processing for this experiment was accomplished with the same VAX 11/780 computer and XSYS data handling software as the neutron experiments. Detector signals were shaped and culled by the electronics, digitized by the ADC's, transmitted to the VAX via the MBD-11, sorted and stored in spectra.

The signal shaping for the four pairs of solid-state detectors in the scattering chamber followed well accepted practices, as can be seen from the block diagram in Fig. (3-6). The signal processing was accomplished with ORTEC NIM-compatible modules, located in the accelerator control room. The output signal from the detector went to a preamplifier just outside of the chamber and then to a spectroscopy amplifier located in the control room. The spectroscopy amplifier produced two linear outputs and a pulse pile-up rejection signal. The bipolar linear output went to a single channel analyzer (SCA) which made it possible to discriminate against low-energy events of no interest that would otherwise contribute to the computer dead time. The unipolar linear output went to a linear gate stretcher (LGS) which was gated by the SCA gate output, thus applying the

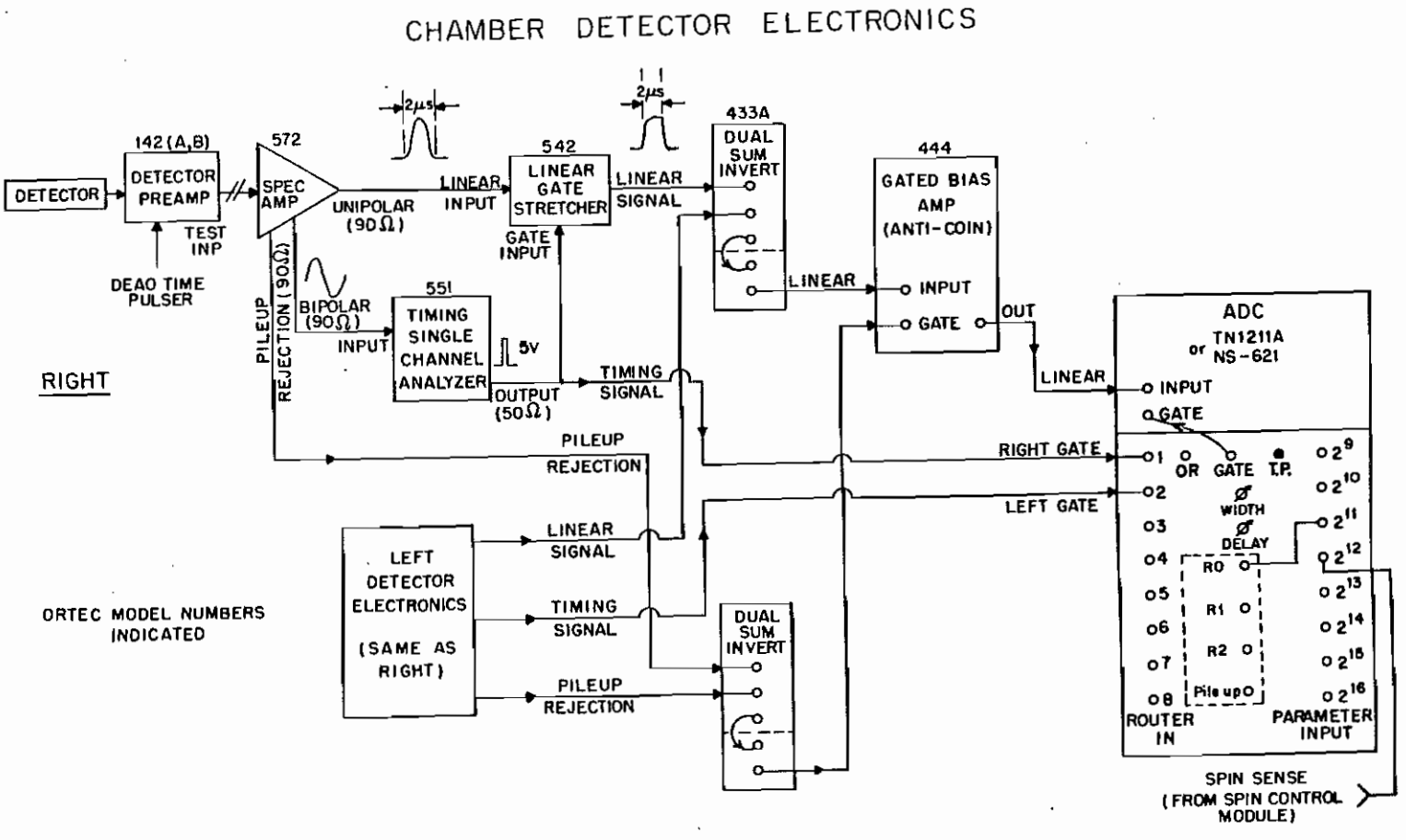

Fig. (3-6) Block diagram of the main chamber detector electronics used in the proton scattering measurements.

low-energy discrimination. Gated unipolar outputs for the right and left detectors of a pair are summed and then gated a second time by the pulse pile-up rejection gates which had also been summed. Finally, the signal entered one of four fast Northern ADC's, was digitized, stored in a channel of the MBD-11, transmitted to the VAX, and stored in the appropriate 1024 channel spectrum.

The SCA gate outputs, in addition to gating the LGS, were also sent to a TUNL-designed routing circuit which sent right and left detector events to the correct spectra. A spin-sense signal originating at the polarized source was also sent to this routing circuit to provide proper sorting of up and down events.

An additional feature of the circuit is the pulser dead-time correction capability. A 100 Hz pulser, whose output resembles a detector pulse in shape, was sent to the test input of all four right detector preamplifiers and also to a scaler. The gain of the pulser could be set separately for each detector, and was adjusted to put the "pulser peak" to the right of the elastic peak in the spectrum. This peak could be summed and compared to the scaler value to determine the dead-time correction.

Several other items were counted by scalers, in addition to the pulser. The summed right and left gates for each detector were counted and served as useful diagnostic aids. Similarly, the summed right and left polarization monitor gates were counted. The digitized output of the beam current integrator went to two scalers; a regular scaler used for normalization and a count-down scaler. The count-down scaler started with a "BCI preset" value determined by the experimenter. Upon reaching zero, a signal was sent which halted the data taking. Pulses from a "clock" consisting of a 10 Hz oscillator were also counted.

Polarimeter Electronics

The electronics for the polarimeter followed the scheme of the chamber detector electronics. Important differences evident from Fig. (3-7) were the absence of a

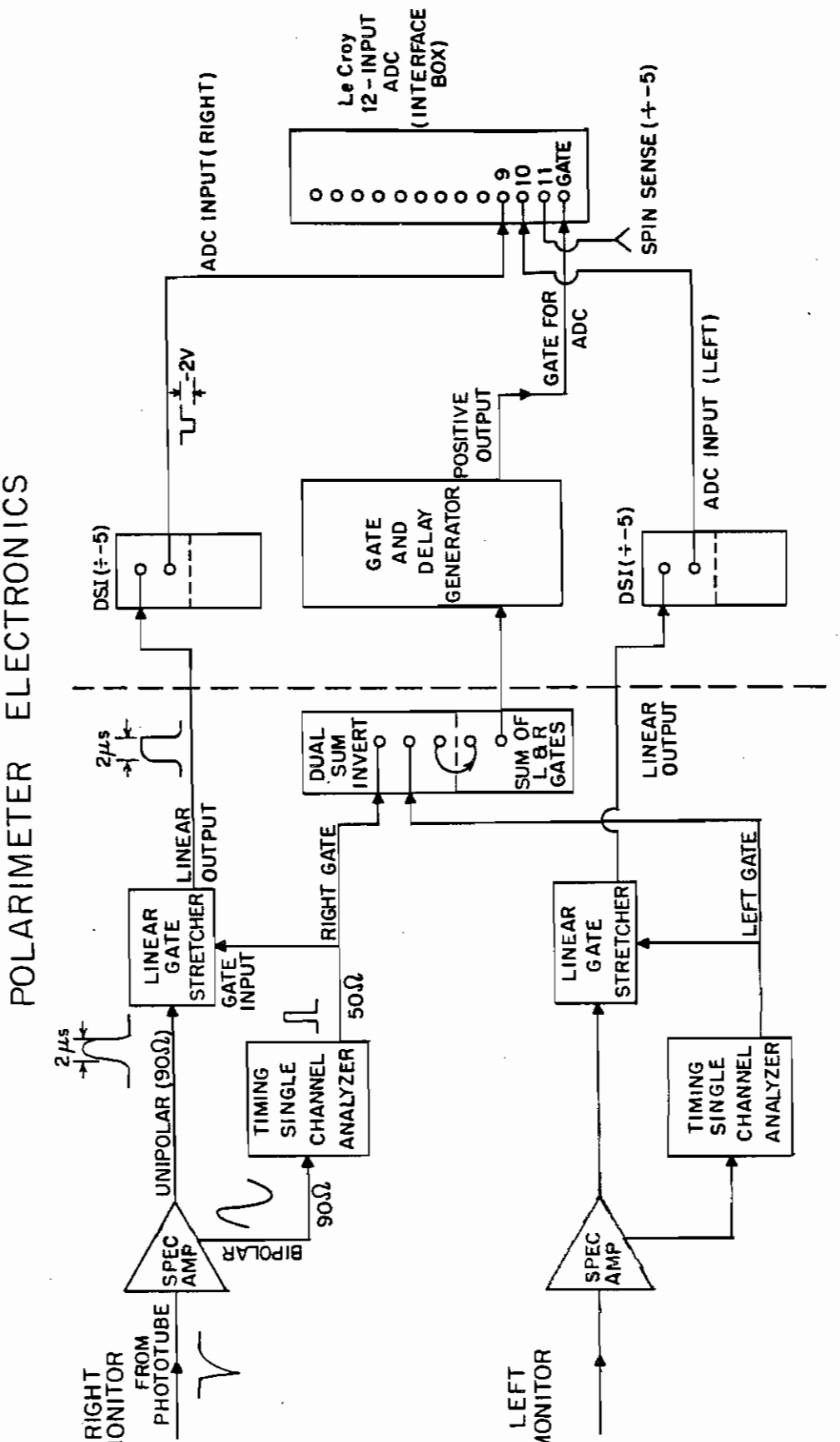

Fig. (3-7) Block diagram of the polarimeter detector electronics used in the proton scattering measurements.

preamplifier since scintillation detectors were used, the absence of a dead-time pulser, and the absence of pulse pile-up rejection. Discrimination against low energy events could be accomplished as above. Instead of the fast Northern ADC, a slower LeCroy 12-input ADC was used. Left and right linear detector signals were not summed, but rather were sent to separate inputs of the ADC. The left and right gates, however, were summed and served to gate the ADC on or off. The same spin-sense signal used for chamber detector routing was additionally sent to a third input of the ADC from where it could be read by the VAX. The data were stored in spectra consisting of 1024 channels.

Data Handling and Reduction

The handling of data, including the sorting and calculations, was accomplished within the framework of the TUNL XSYStem. Those programs specific to charged particle scattering experiments with polarized beam are the same programs written and documented by Varner in his dissertation (Varner 86) and in an in-house programming guide (Varner 85). Some modifications were made to the error calculations and to the background calculations for the present work. In describing the basic calculations, those modifications will be pointed out. The Fortran programming for the calculations can be divided into a number of categories: background calculation, peak summing and background subtraction, normalization calculation, calculation of the beam polarization, and calculation of final cross sections and analyzing powers.

As is evident from the spectra [Figs. (3-8) and (3-9)], the background in the region of the aluminum and lithium elastic peaks is quite different from the background in the region of the lithium inelastic peak. Two background windows were set; one encompassing the region of the two elastic peaks (^{27}Al and ^{6}Li) and one encompassing the region of the inelastic peak. A single, linear background, which was nearly zero in most cases, was obtained for the region of the two elastic peaks. A second linear background of much greater magnitude was determined for the inelastic peak. Separate backgrounds were

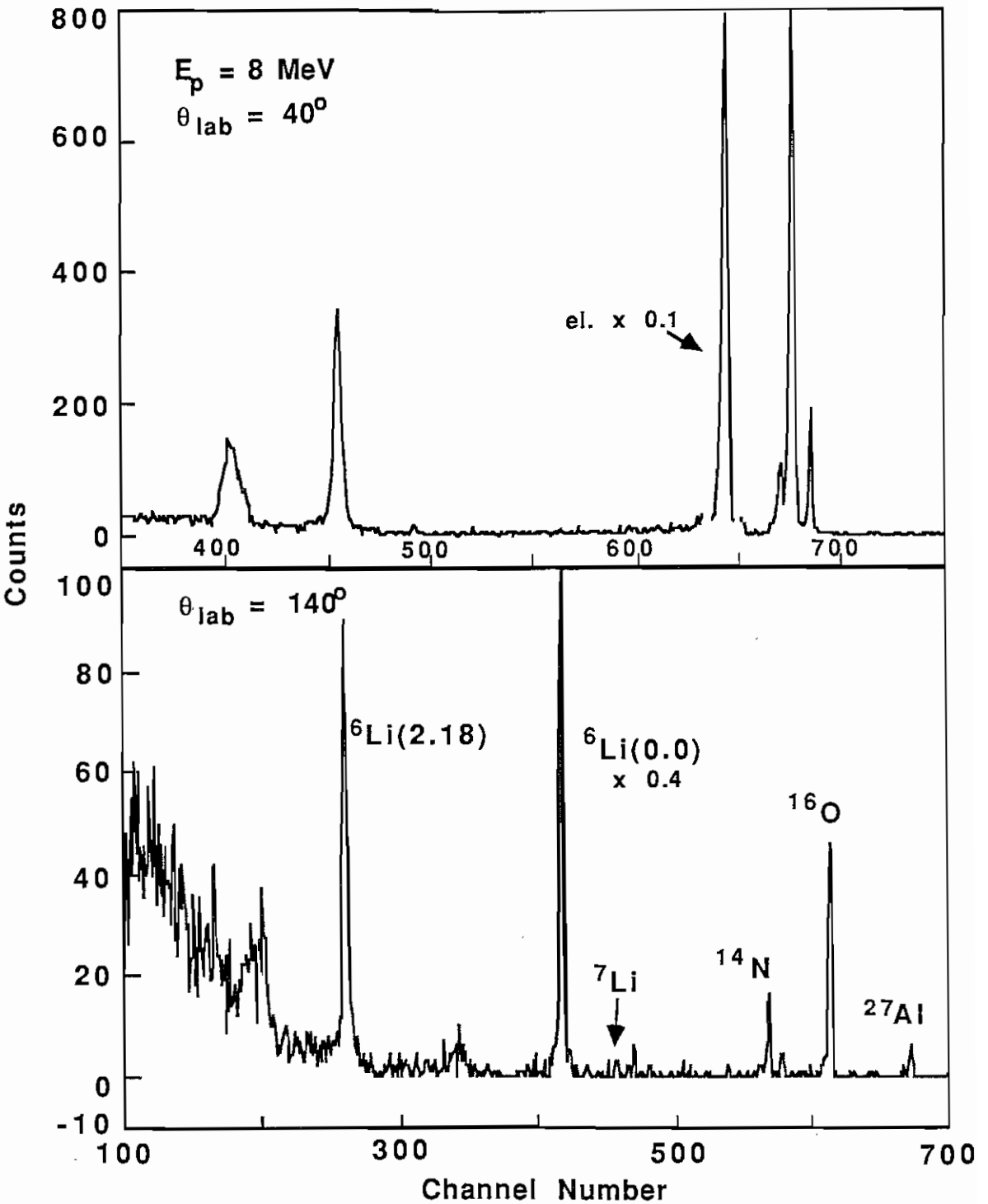

Fig. (3-8) Proton energy spectra obtained with right detectors and spin-up at 40° and 140° with E_p= 8 MeV.

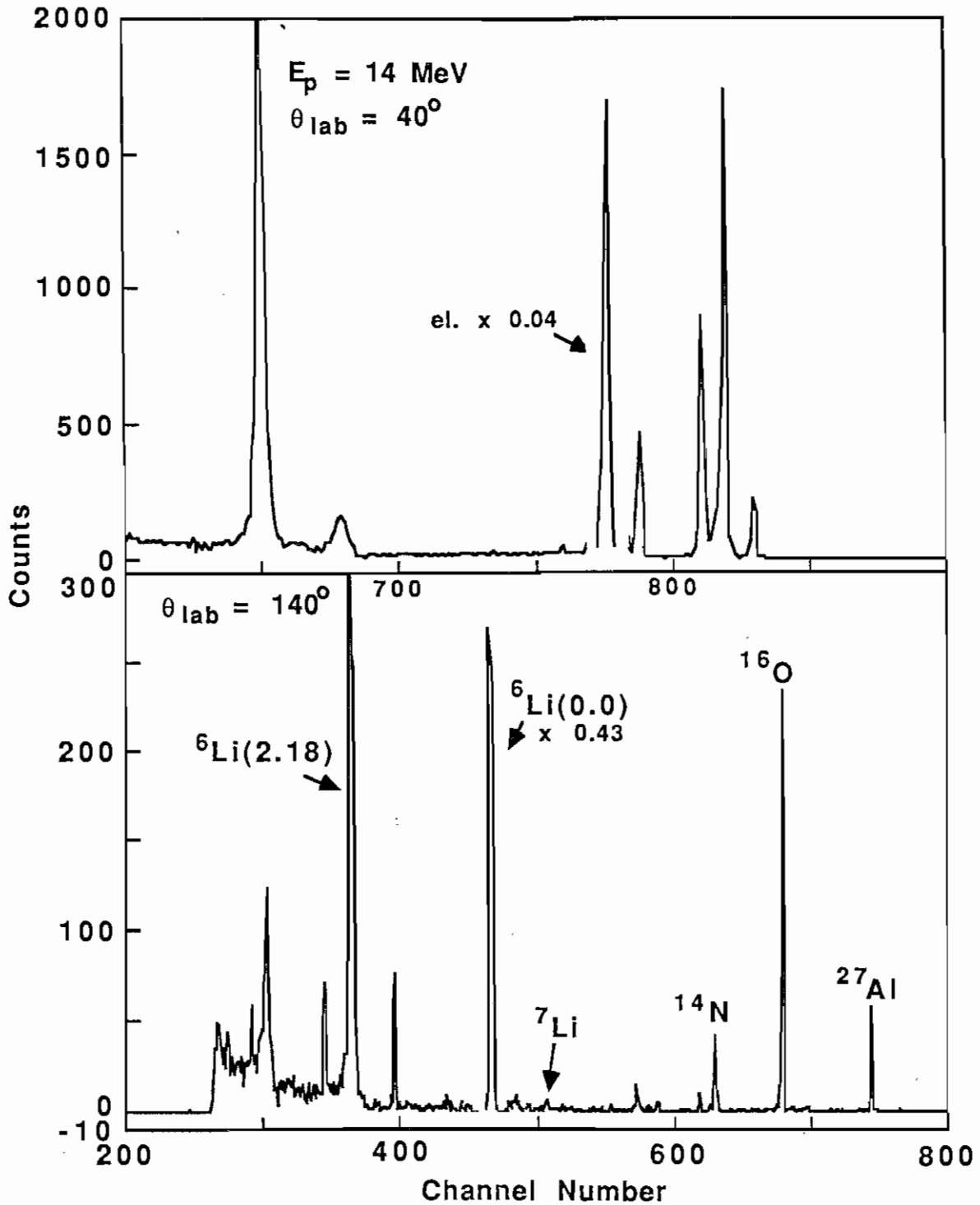

Fig. (3-9) Proton energy spectra obtained with right detectors and spin-up at 40° and 140° with E_p= 14 MeV.

calculated for the left, right, up and down spectra.

For the purpose of summing the peaks of interest, windows were set around these at the same time the background windows were set. They were set so as to include any tails on the peaks, since these tails contained valid events of interest. In cases where small contaminant peaks were in these tails, attempts were made to compromise between excluding contaminant events and including events of interest. The events within the windows were summed, the background subtracted and the statistical uncertainty calculated. This uncertainty included the statistical uncertainty in the calculated background, which in most cases was negligible.

Calculating the cross section involves combining the peak sums with the normalization factors. By putting the normalization terms of Eqs. (3-4) through (3-7) into Eq. (3-3) one gets,

$$\sigma(\theta) = \langle SIGUP, SIGDN \rangle \times \frac{CBEAM \times DTC \times M \times \cos(\theta_T)}{d\Omega \times BCI \times TTHICK \times CSOLID} \tag{3-13}$$

$$\text{where } \langle SIGUP, SIGDN \rangle = \frac{\dfrac{SIGUP}{\Delta SIGUP^2} + \dfrac{SIGDN}{\Delta SIGDN^2}}{\dfrac{1}{\Delta SIGUP^2} + \dfrac{1}{\Delta SIGDN^2}} . \tag{3-14}$$

The errors in these quantities were treated as random, and typical values are given here:

ΔDTC = 0.1% to 0.4%

$\Delta\cos(\theta_T)$ = 0.001% to 0.5%

$\Delta d\Omega$ = 0.5% to 1.3%

$\Delta SIGUP, \Delta SIGDN$ = 0.15% to 0.7% for the elastic scattering data
and 1% to 4% for the inelastic scattering data

$\Delta\sigma(\theta)$ = 0.5% to 1.5% for the elastic data
and 1% to 3% for the inelastic data.

An additional overall uncertainty or scale error of 5% due to the uncertainty in the target thickness is not included in these estimates or in the calculations.

The peak sums are combined with the beam polarization to give the analyzing power as in Eqs. (3-1) and (3-2). Errors arise from the statistical uncertainty in the peak sums and the uncertainty in the beam polarization. The uncertainty in the target thickness is not important in $A_y(\theta)$ determinations. Statistical uncertainty in the polarimeter peak sums, which is negligible, and the uncertainty in the polarimeter calibration of 0.5% give a typical beam polarization uncertainty of 0.55%. These factors yielded uncertainties in $A_y(\theta)$ ranging from 1% to 4%. An overall scale uncertainty of 0.75% in the $A_y(\theta)$ data is due to uncertainty in the polarimeter calibration as was discussed earlier.

Presentation of Data

The proton scattering data have also been fit with energy dependent Legendre polynomials using the same computer code ASSFITE described in Chapter 2. Figs. (3-10) through (3-18) are plots of the Legendre polynomial and associated Legendre polynomial coefficients as a function of energy. The elastic cross sections for ^{6}Li and ^{27}Al are dominated by Rutherford scattering at far forward angles. Since this data is lacking in our measurements the Legendre polynomials do not reflect this enormous forward angle cross section, but rather give a much lower value. Figs. (3-19), (3-20), (3-21), and (3-22) show the ^{6}Li proton elastic and inelastic scattering cross-section data along with the energy dependent Legendre polynomial fits. The forward angle portion of the curves are shown as dashed lines to indicate that those portions have no physical meaning and should not be used as predictions of the cross section. Of course the remaining portions are valid for extracting cross-section values.

Figs. (3-23) and (3-24) are plots of the ^{27}Al proton elastic scattering cross-section data along with the Legendre polynomial curves. Figs. (3-25) through (3-30) are plots of the ^{6}Li proton elastic and inelastic scattering analyzing power data and the ^{27}Al proton elastic scattering analyzing power data along with the associated Legendre polynomial curves. The error bars shown represent our estimate of all the uncertainties

associated with the data, except for a 0.75% scale error due to the uncertainty in measuring the proton beam polarization. Where no error bars can be discerned, the uncertainty is less than the symbol size. In the Appendix the data along with the calculated values from the Legendre polynomial fits are tabulated.

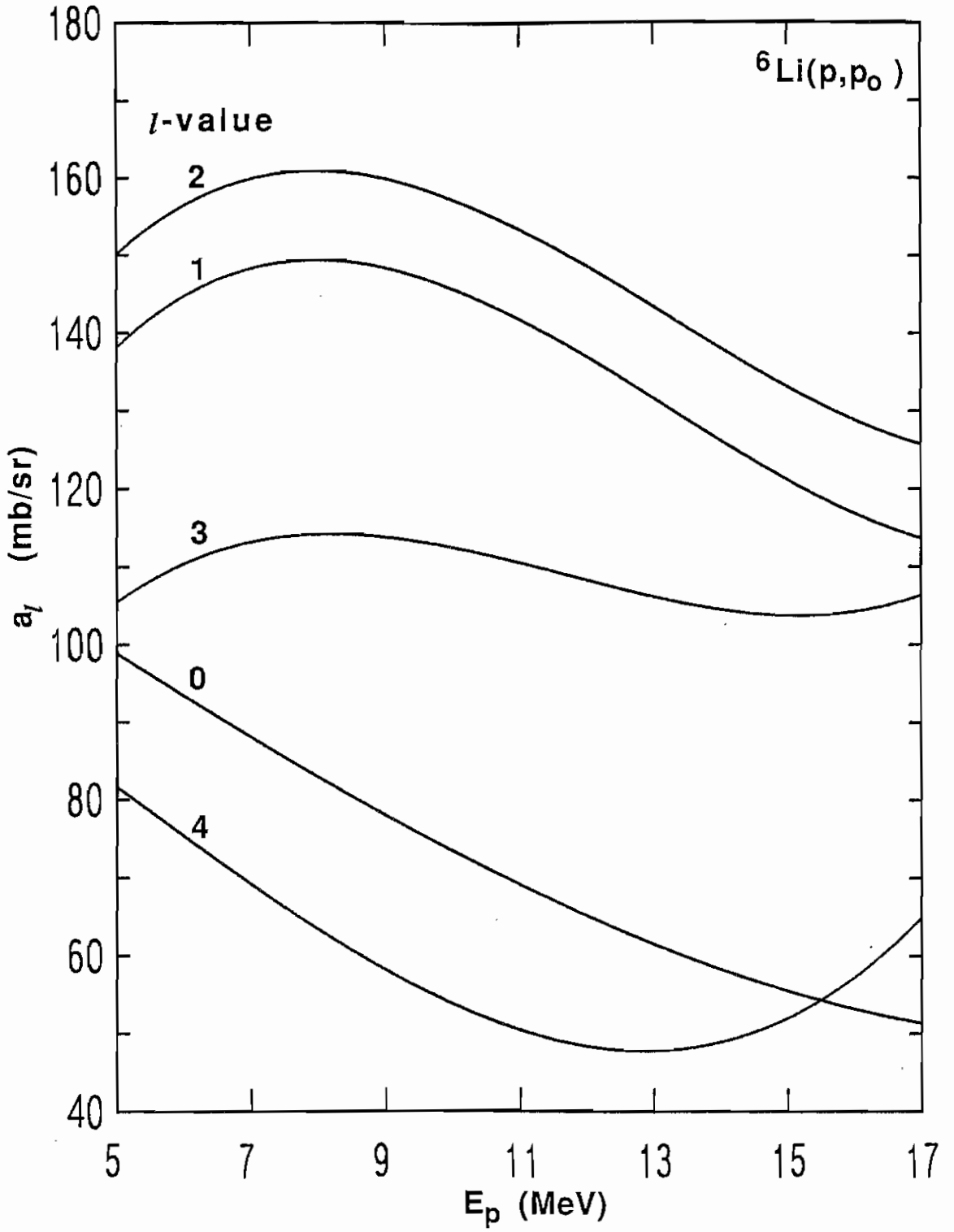

Fig. (3-10) Plots of the first five $a_l(E)$'s obtained from ASSFITE which represent the ^{6}Li proton elastic scattering cross-section data.

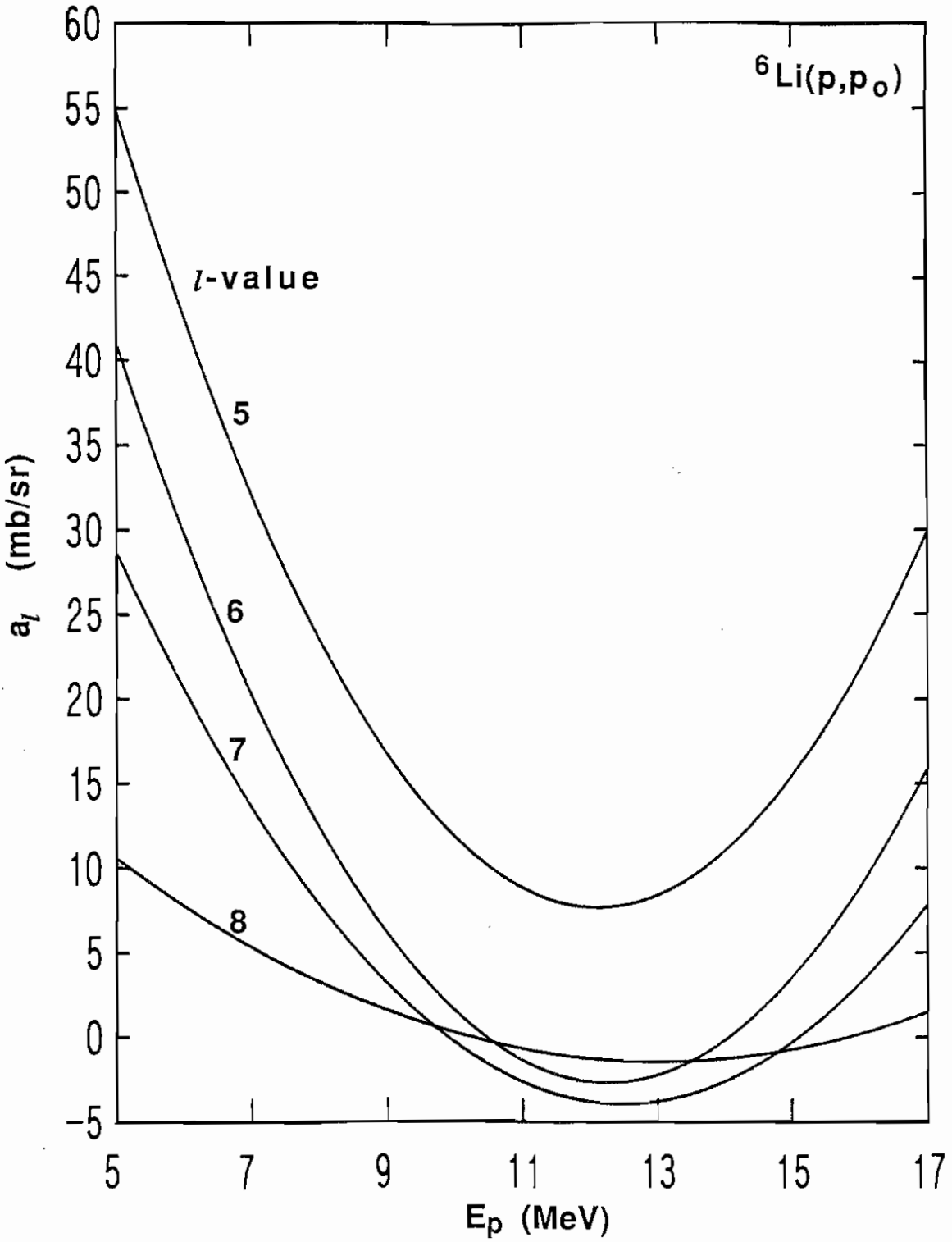

Fig. (3-11) A continuation of Fig. (3-10) showing the remaining $a_l(E)$'s for ^{6}Li proton elastic scattering cross sections.

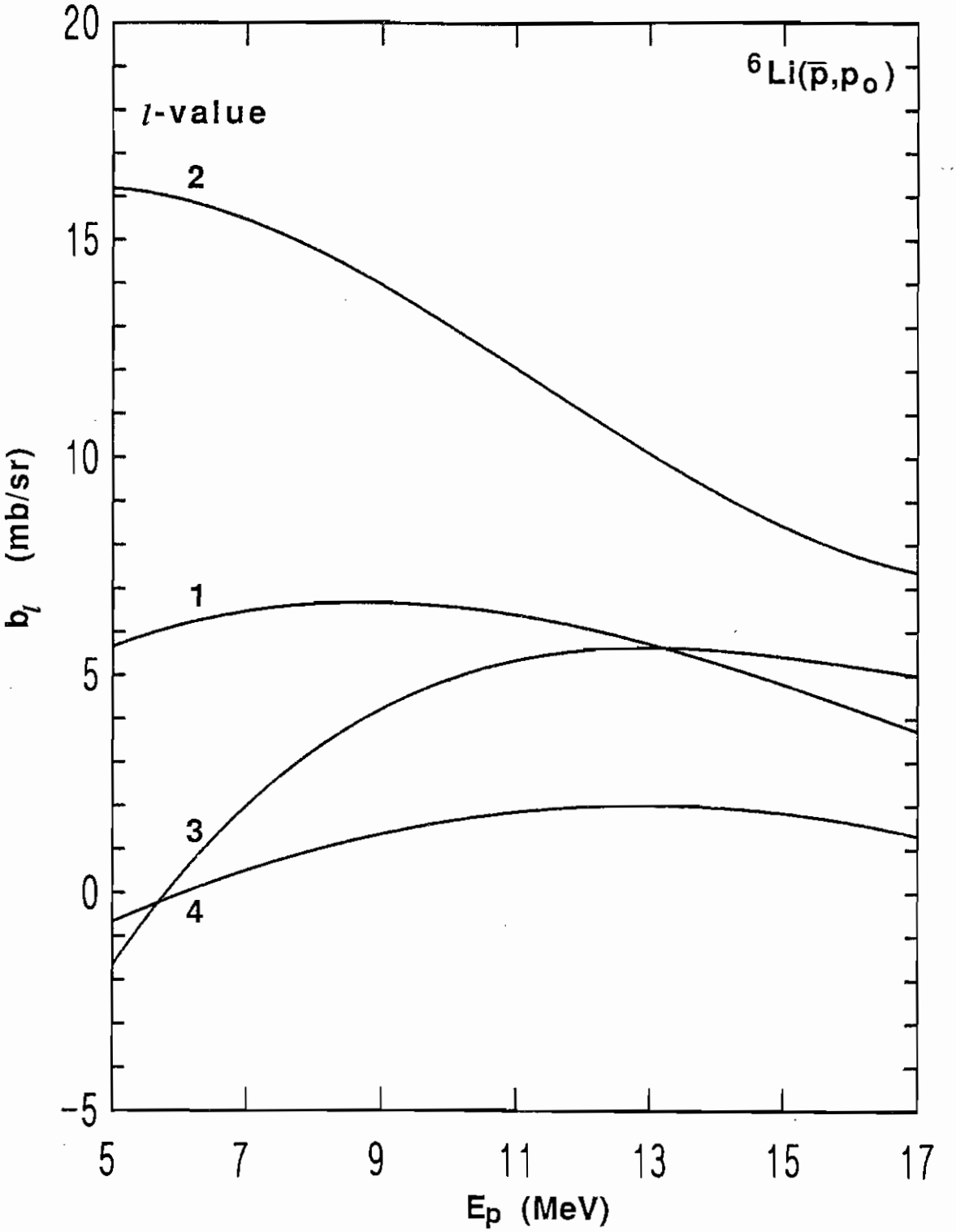

Fig. (3-12) Plots of the first four $b_l(E)$'s which represent the ^{6}Li proton elastic scattering analyzing power data.

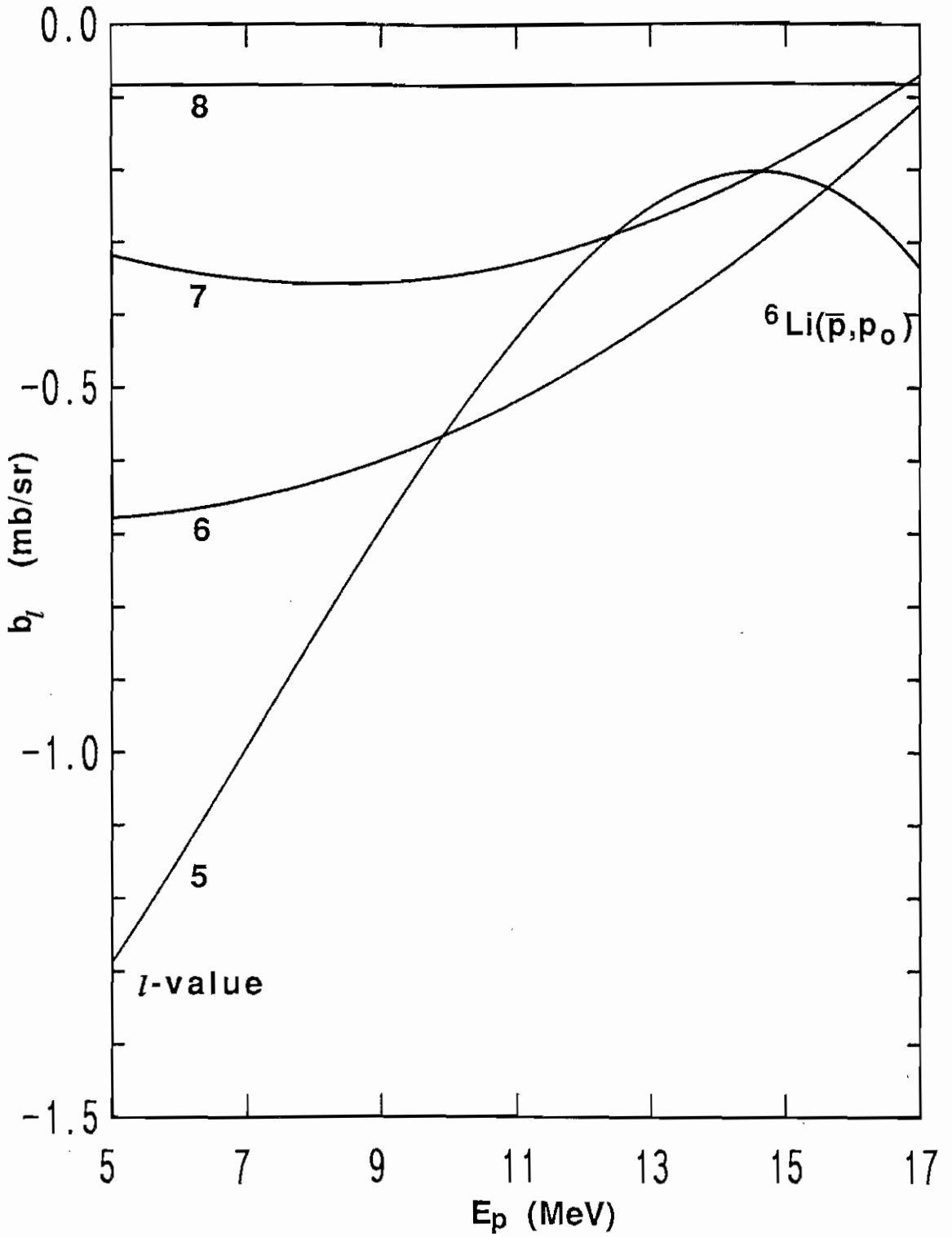

Fig. (3-13) A continuation of Fig. (3-12) showing the remaining $b_l(E)$'s for ^{6}Li proton elastic scattering analyzing powers.

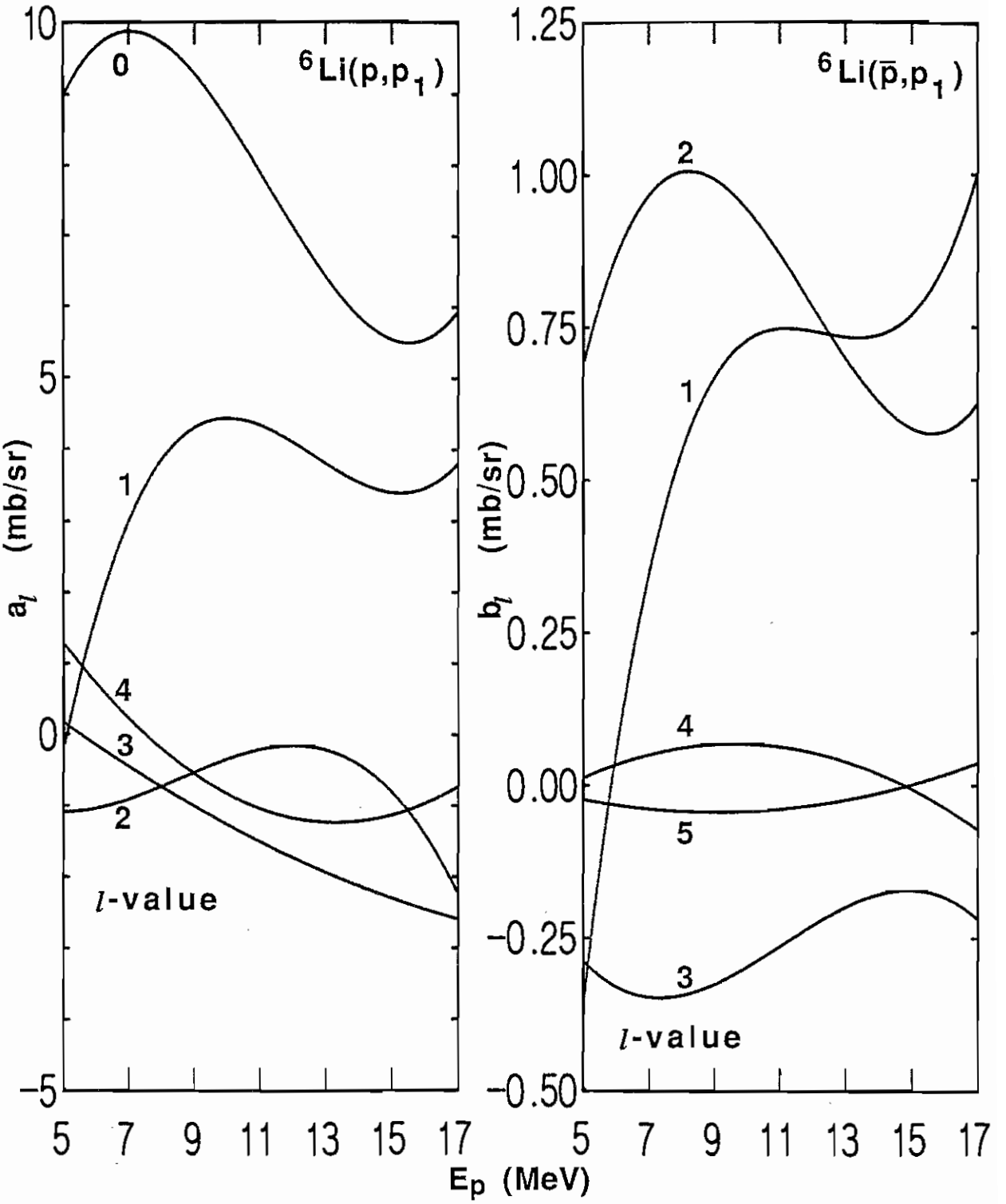

Fig. (3-14) The $a_l(E)$'s (left) and $b_l(E)$'s (right) which represent the ^{6}Li proton inelastic scattering cross sections and analyzing powers, respectively.

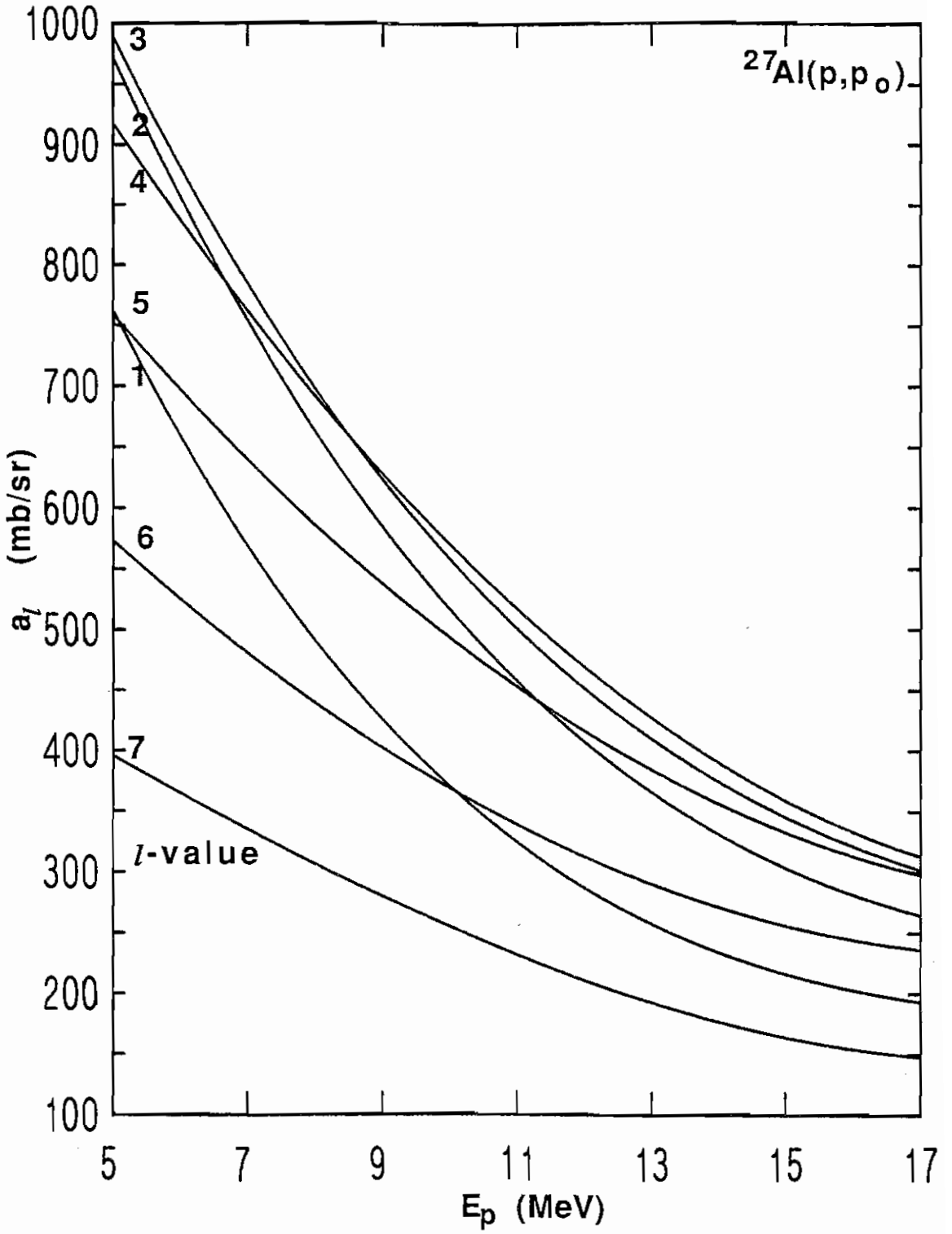

Fig. (3-15) Plots of $a_1(E)$ through $a_7(E)$ for ^{27}Al proton elastic scattering cross sections.

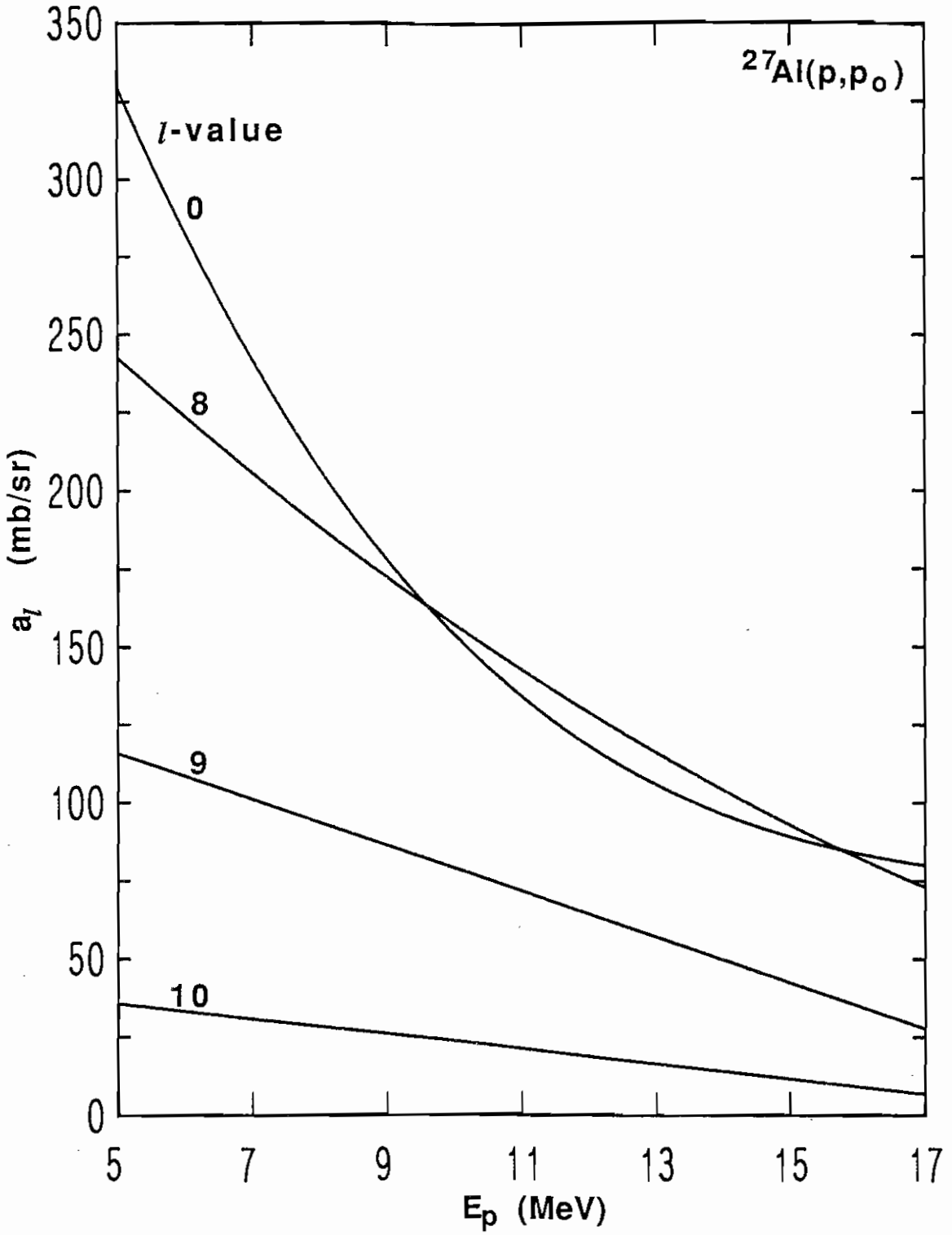

Fig. (3-16) A continuation of Fig.(3-15) showing the remaining $a_l(E)$'s for ^{27}Al proton elastic scattering cross sections.

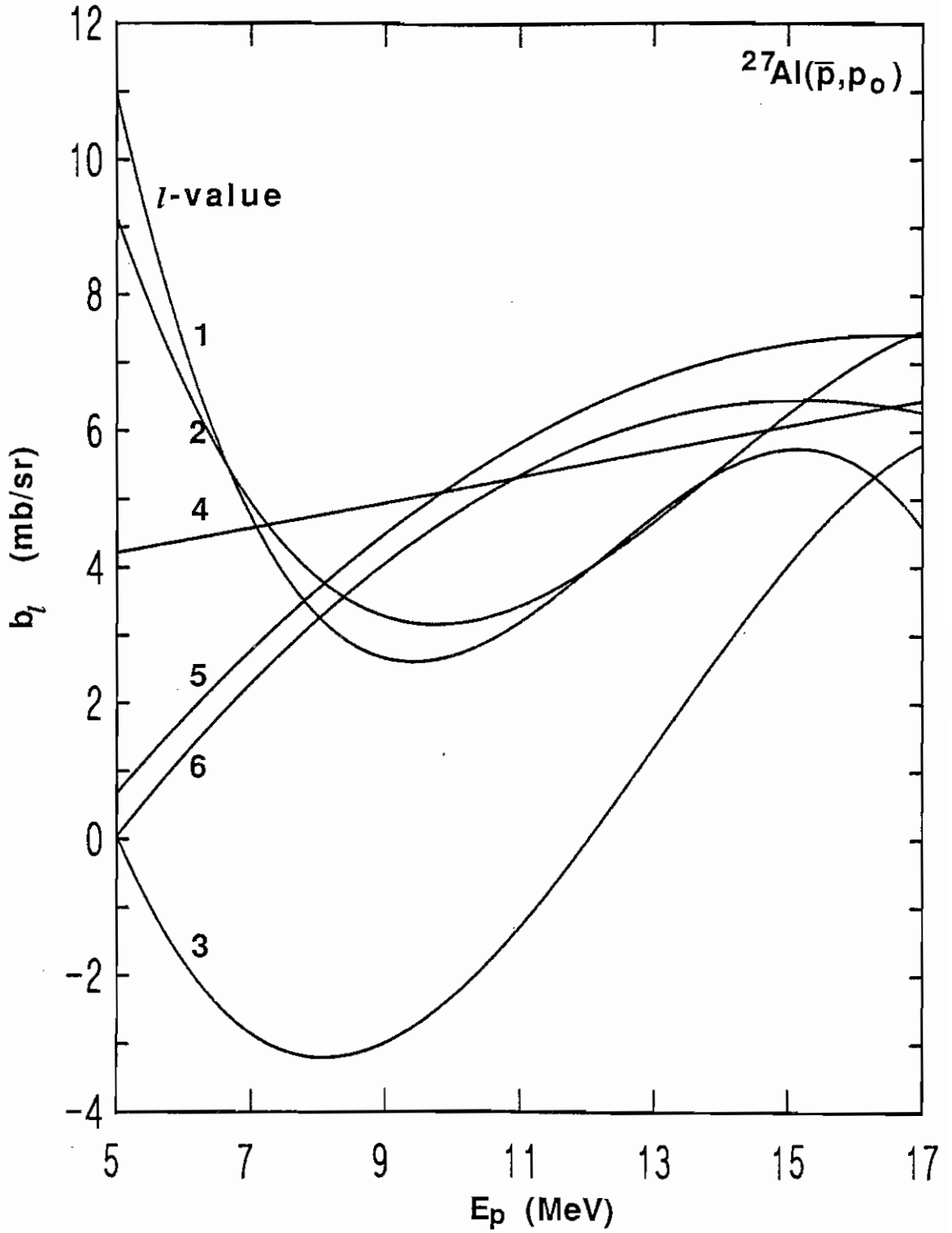

Fig. (3-17) Plots of first six $b_l(E)$'s for ^{27}Al proton elastic scattering analyzing powers.

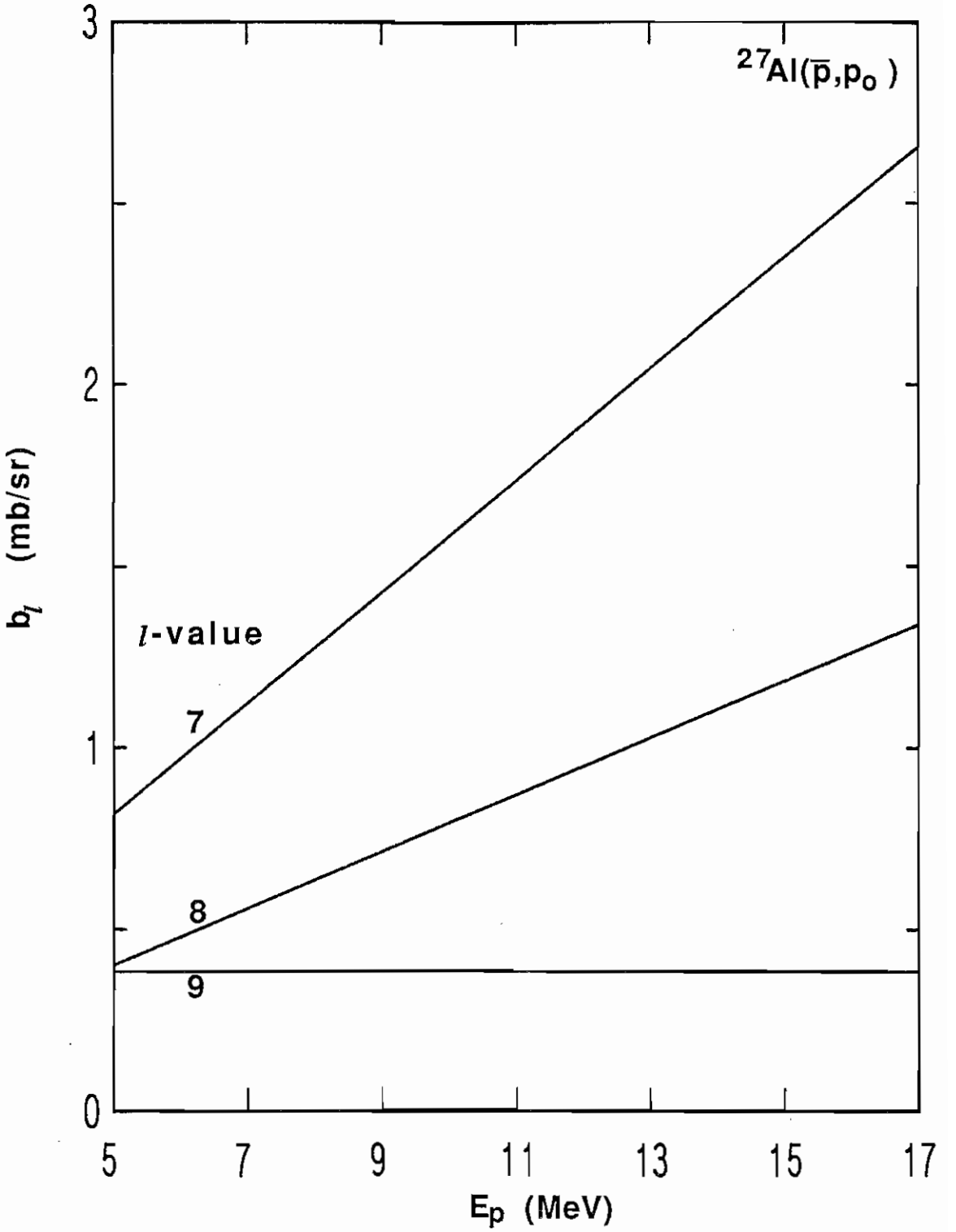

Fig. (3-18) A continuation of Fig. (3-17) showing the remaining $b_l(E)$'s for ^{27}Al proton elastic scattering analyzing powers.

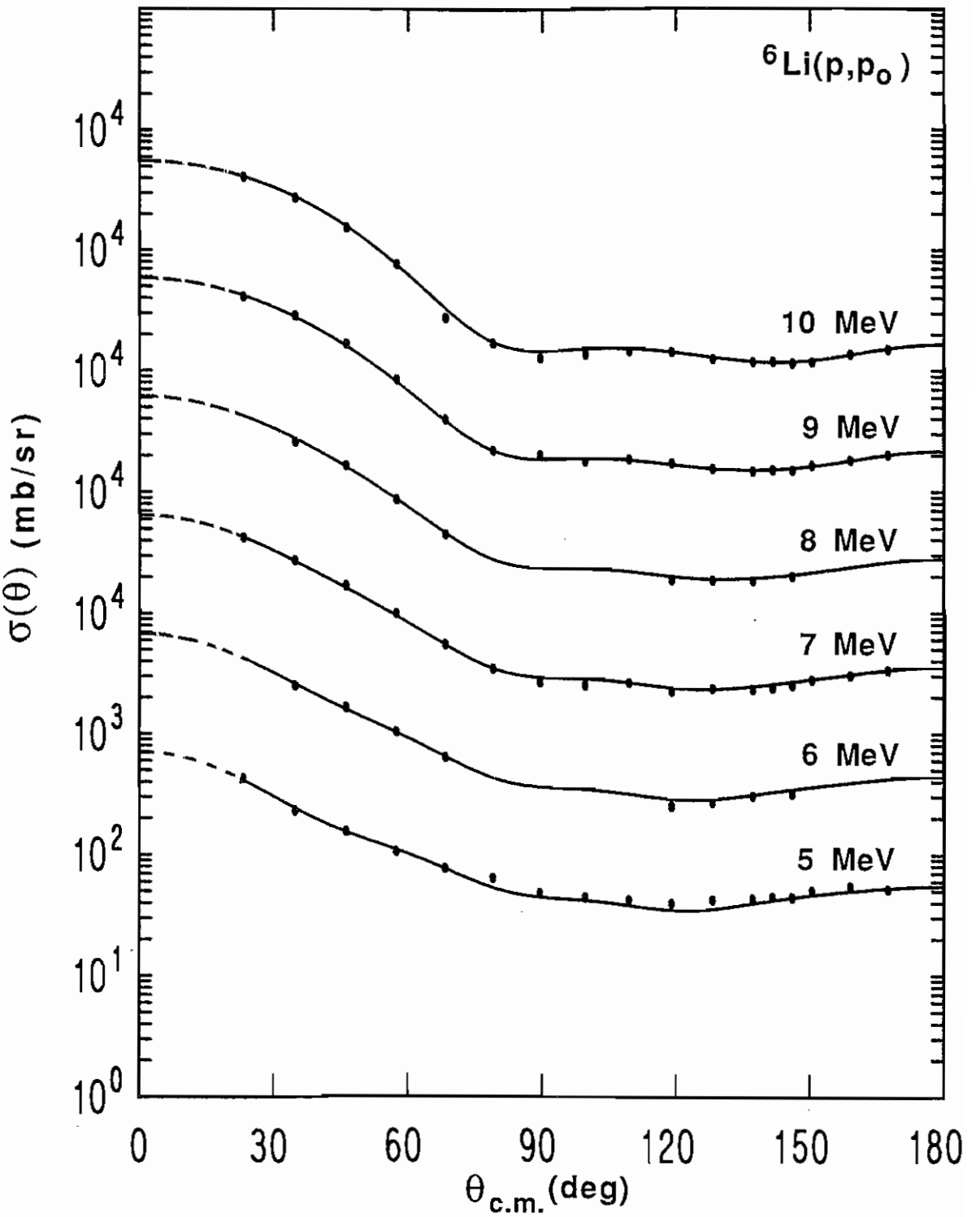

Fig. (3-19) Cross-section data for proton elastic scattering from ^{6}Li at 5 to 10 MeV along with energy dependent Legendre polynomial fits.

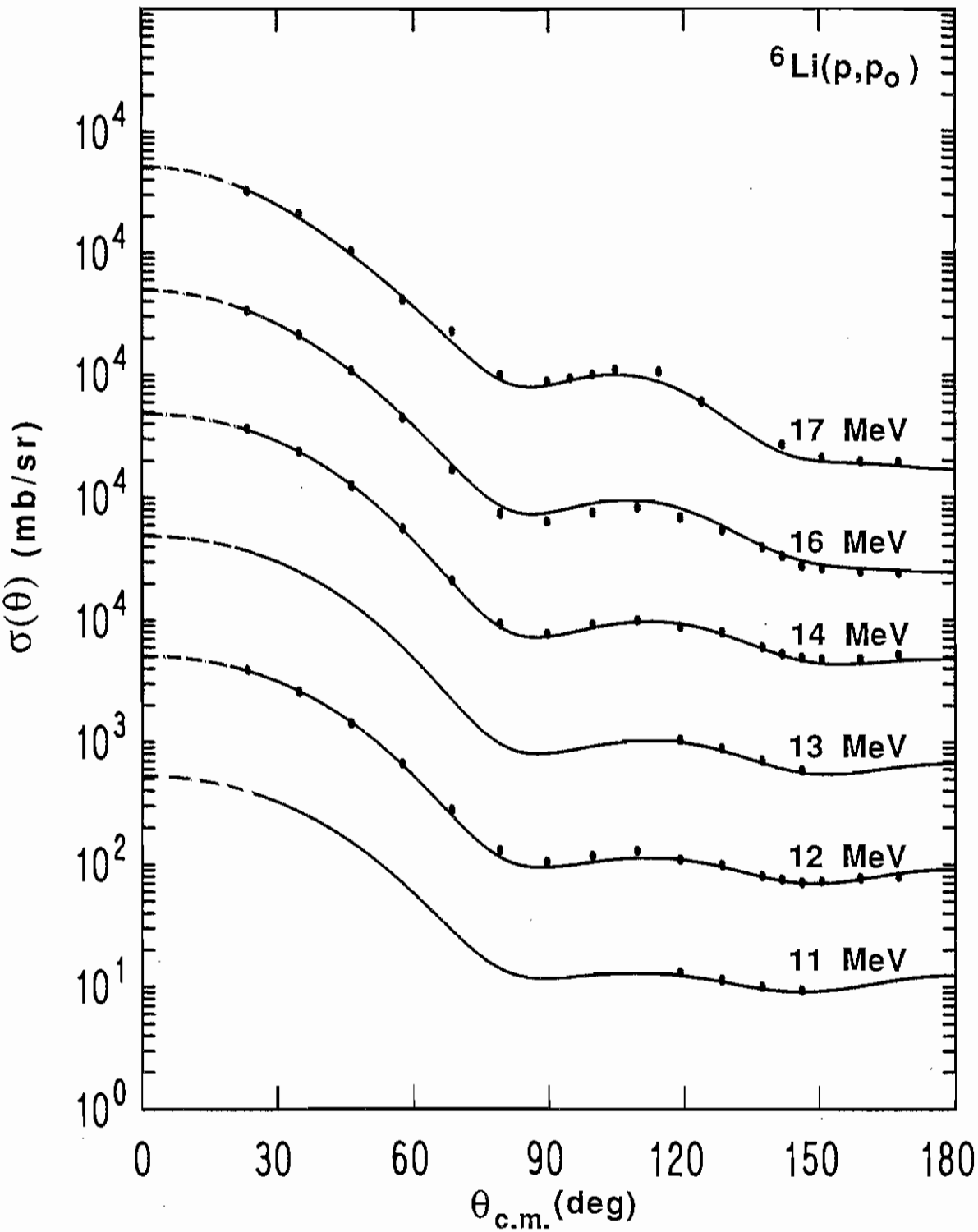

Fig. (3-20) A continuation of Fig. (3-19) showing the ^{6}Li elastic scattering cross-section data and fits at 11 through 17 MeV.

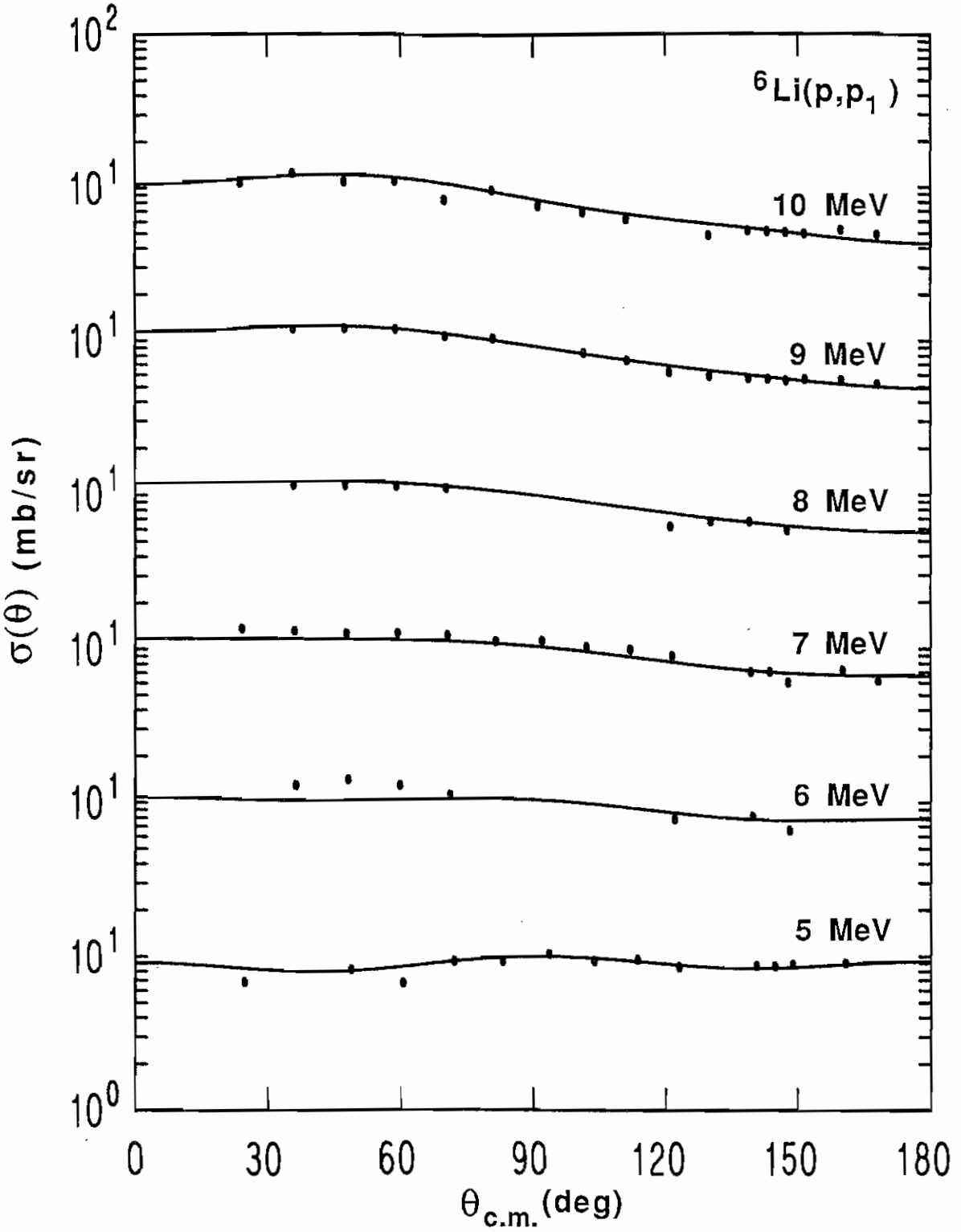

Fig. (3-21) Cross-section data for proton inelastic scattering from ^{6}Li at 5 to 10 MeV along with energy dependent Legendre polynomial fits.

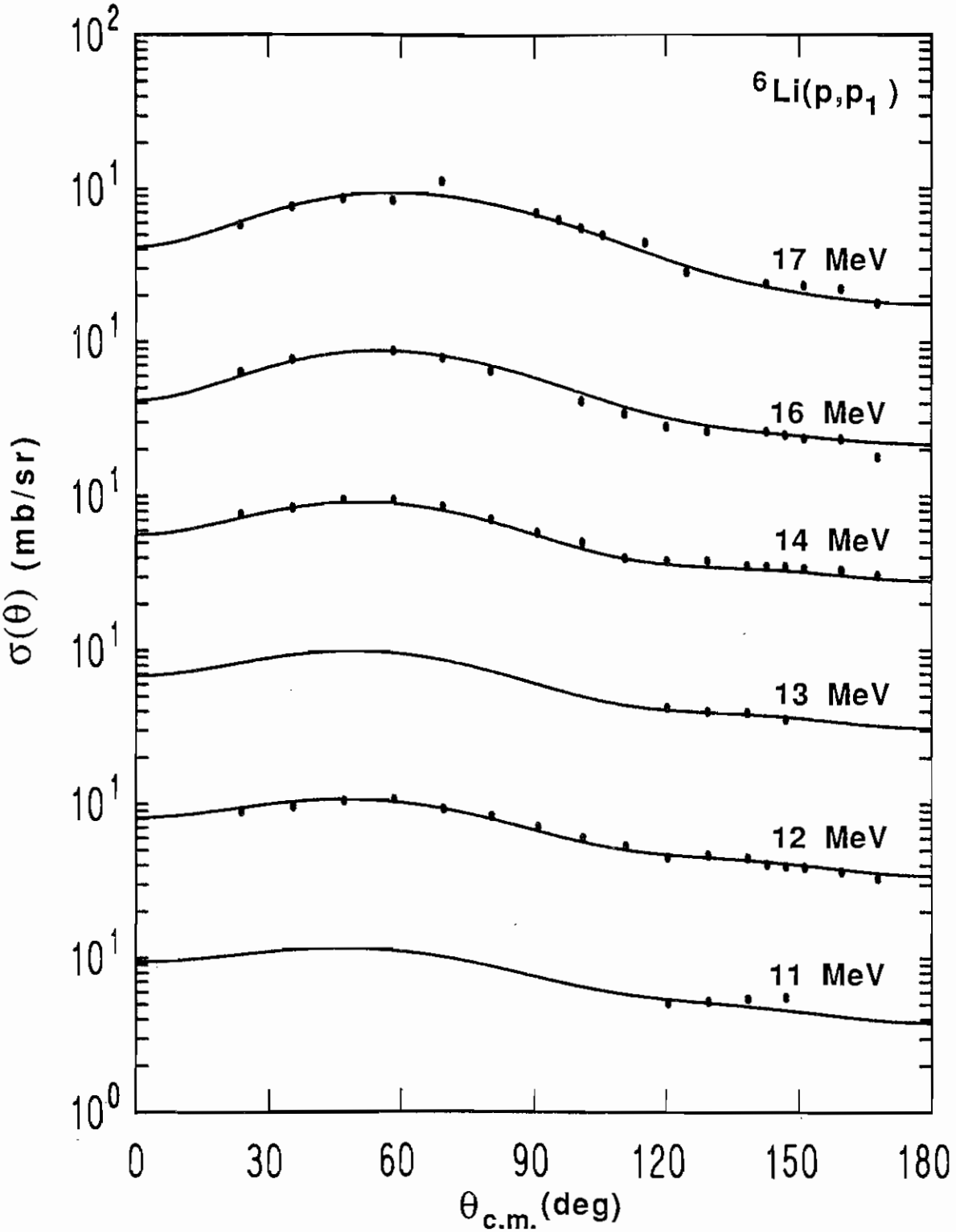

Fig. (3-22) A continuation of Fig. (3-21) showing the ^{6}Li proton inelastic scattering data and fits at 11 through 17 MeV.

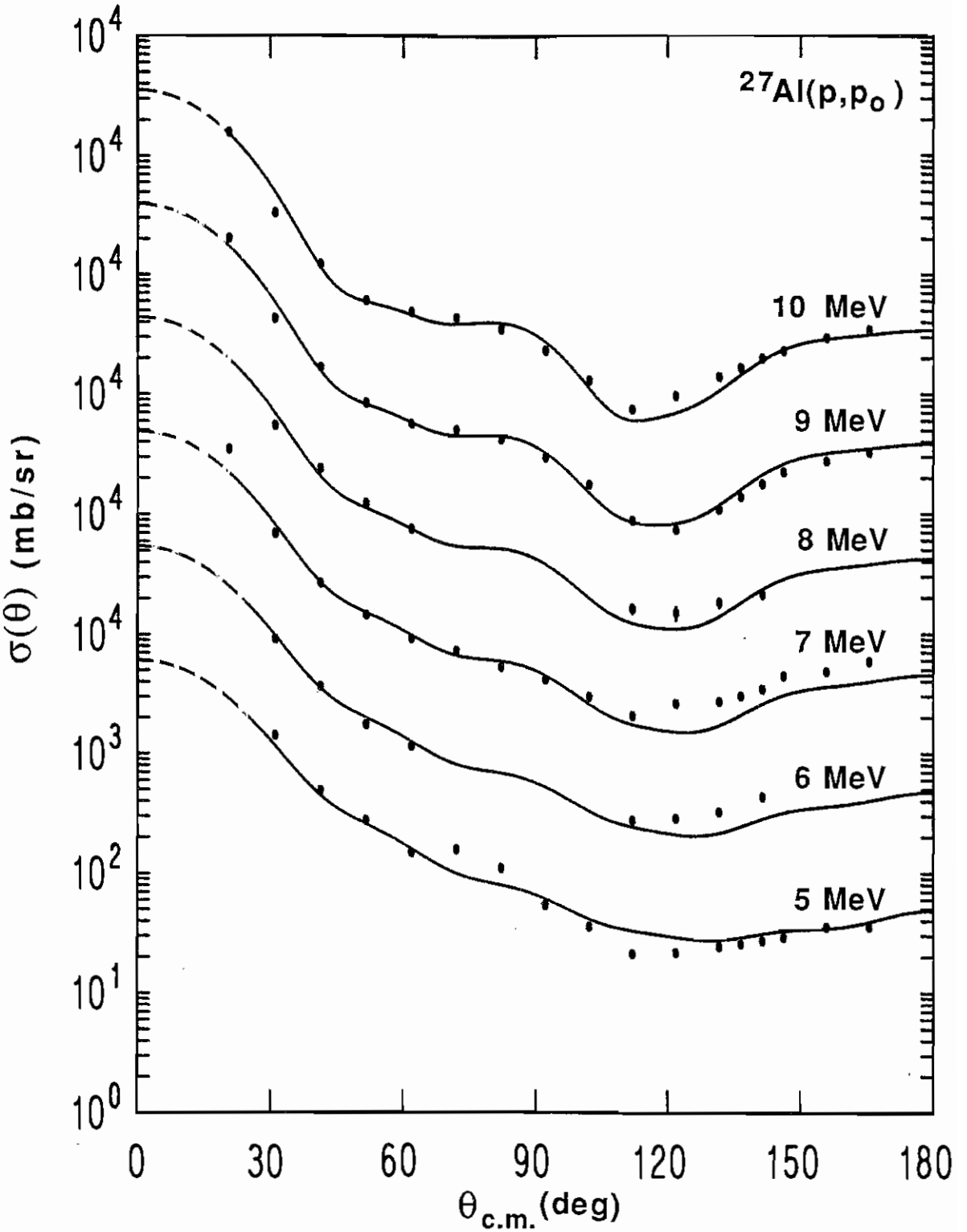

Fig. (3-23) Cross-section data for proton elastic scattering from ^{27}Al at 5 to 10 MeV along with energy dependent Legendre polynomial fits.

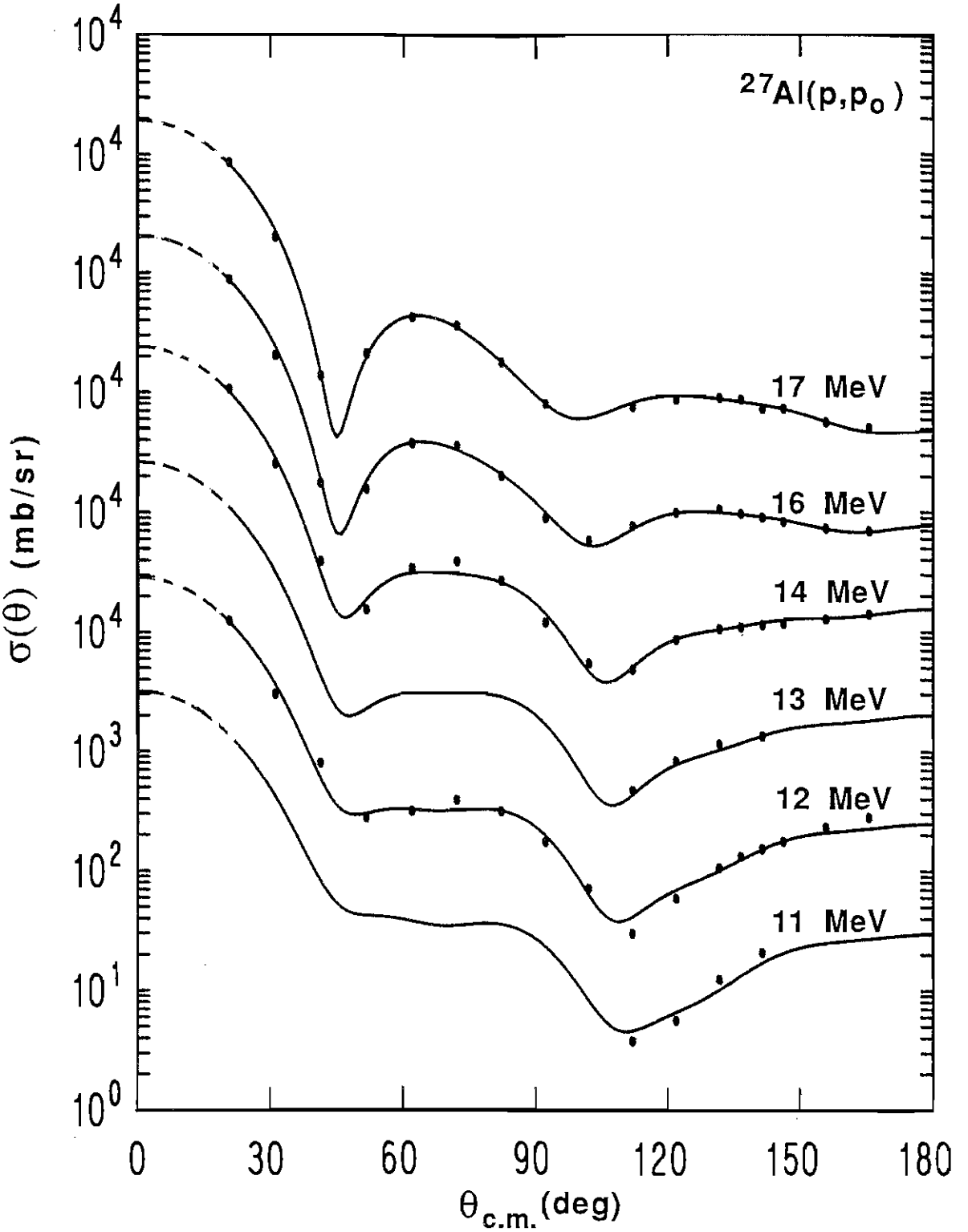

Fig. (3-24) A continuation of Fig. (3-23) showing ^{27}Al proton elastic scattering cross-section data and fits at 11 through 17 MeV.

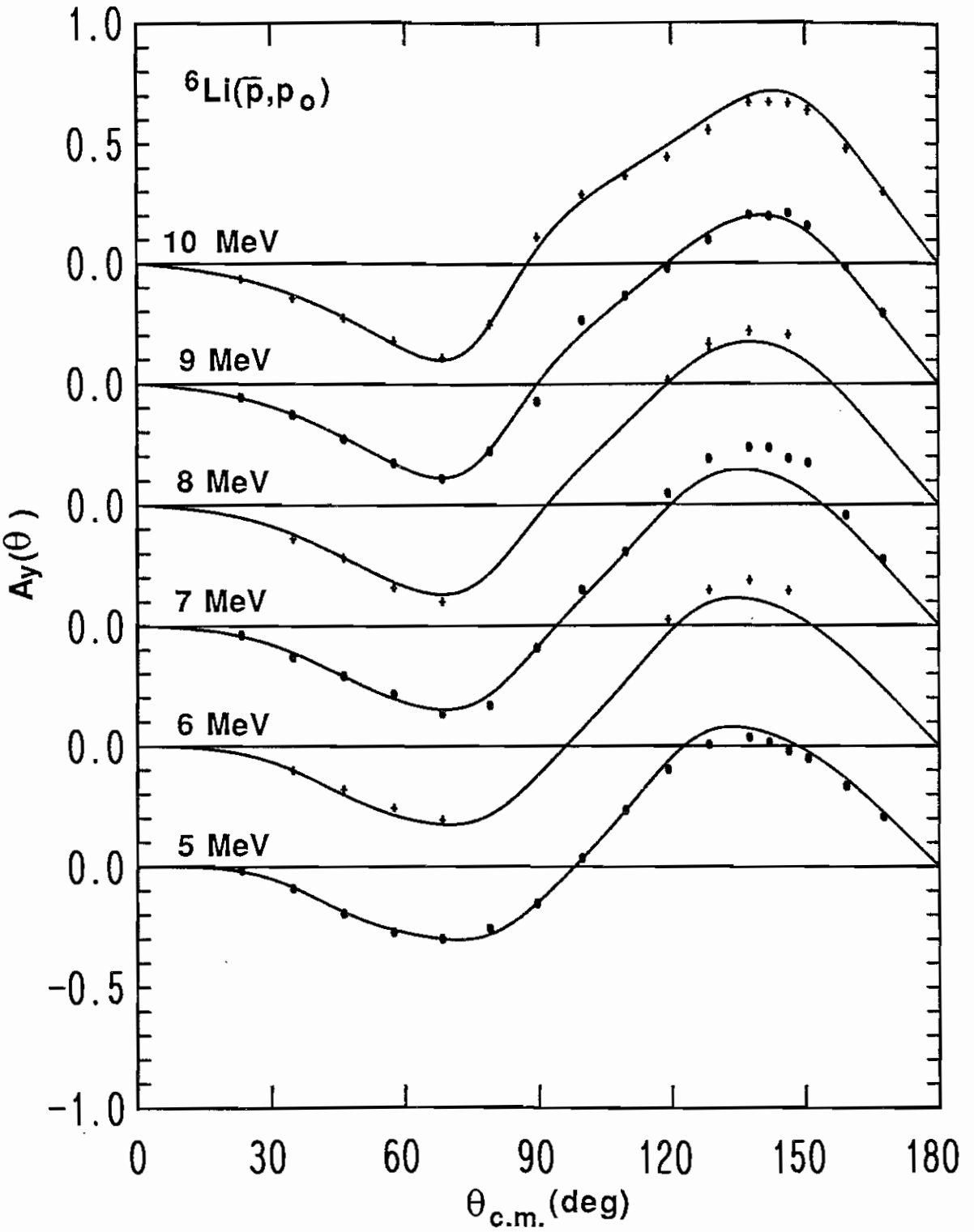

Fig. (3-25) Analyzing power data for proton elastic scattering from ^{6}Li at 5 to 10 MeV along with energy dependent associated Legendre polynomial fits.

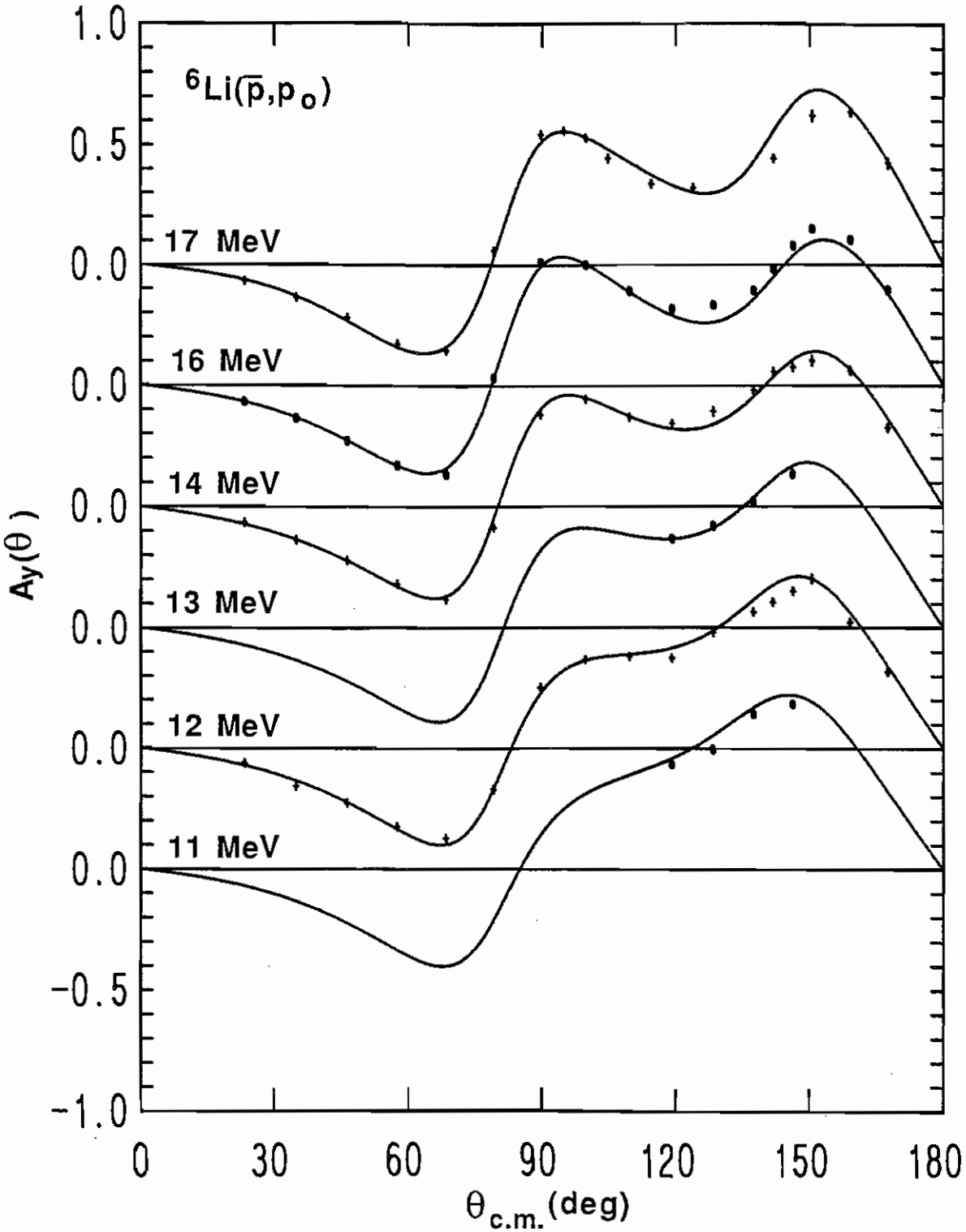

Fig. (3-26) A continuation of Fig. (3-25) showing ^{6}Li proton elastic scattering analyzing power data and fits at 11 through 17 MeV.

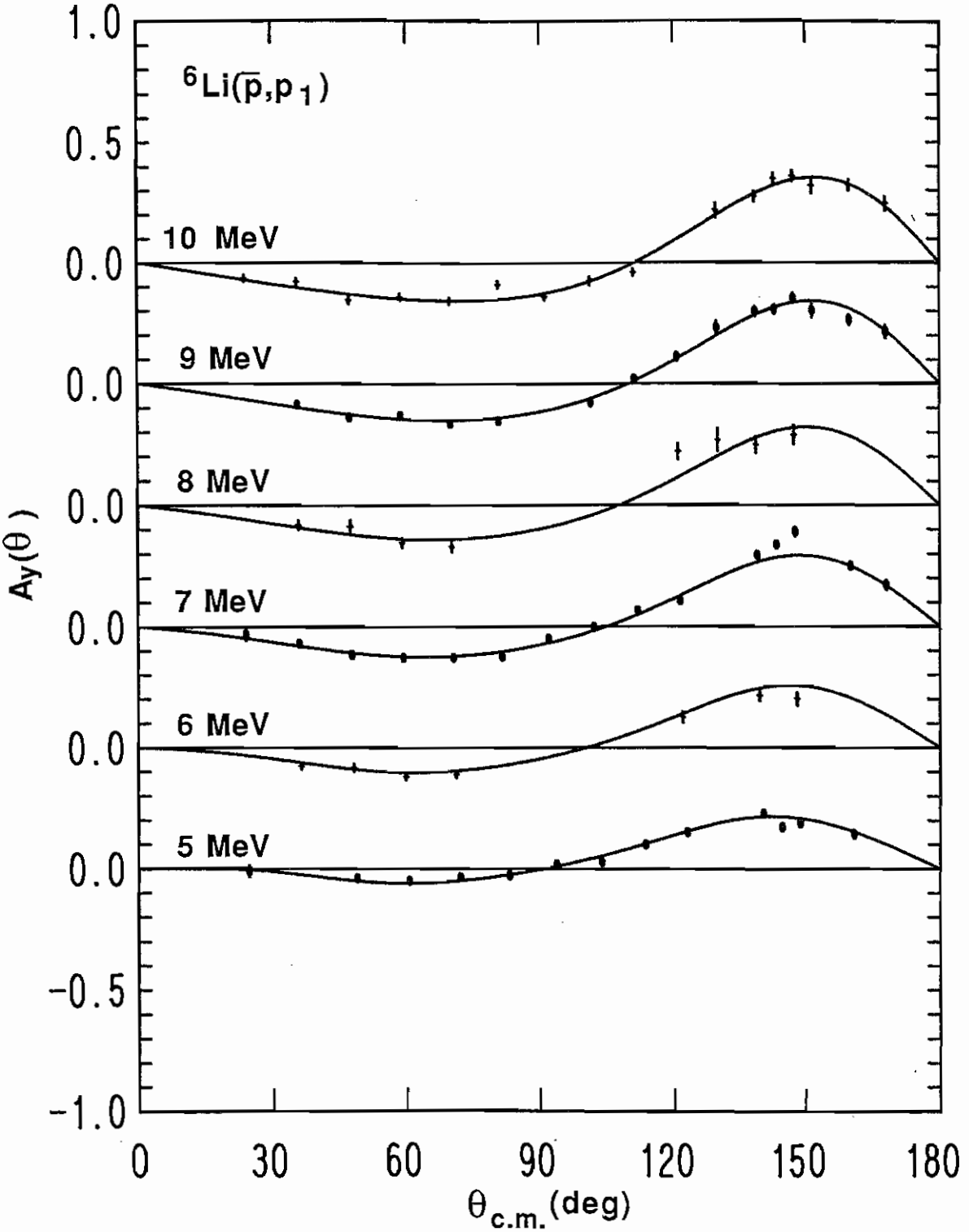

Fig. (3-27) Analyzing power data for proton inelastic scattering from ^{6}Li at 5 to 10 MeV along with energy dependent associated Legendre polynomial fits.

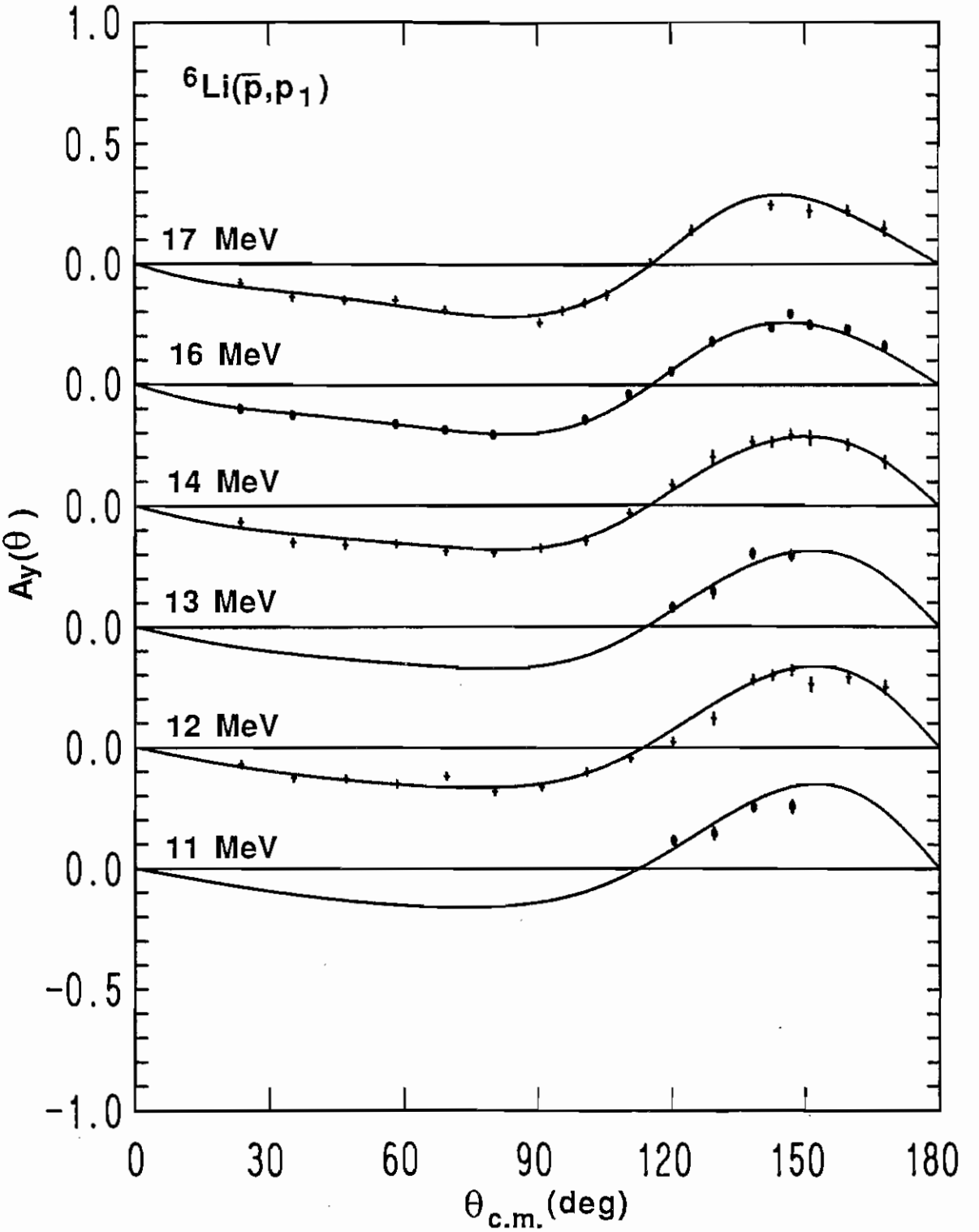

Fig. (3-28) A continuation of Fig. (3-27) showing ^{6}Li proton inelastic scattering analyzing power data and fits at 11 through 17 MeV.

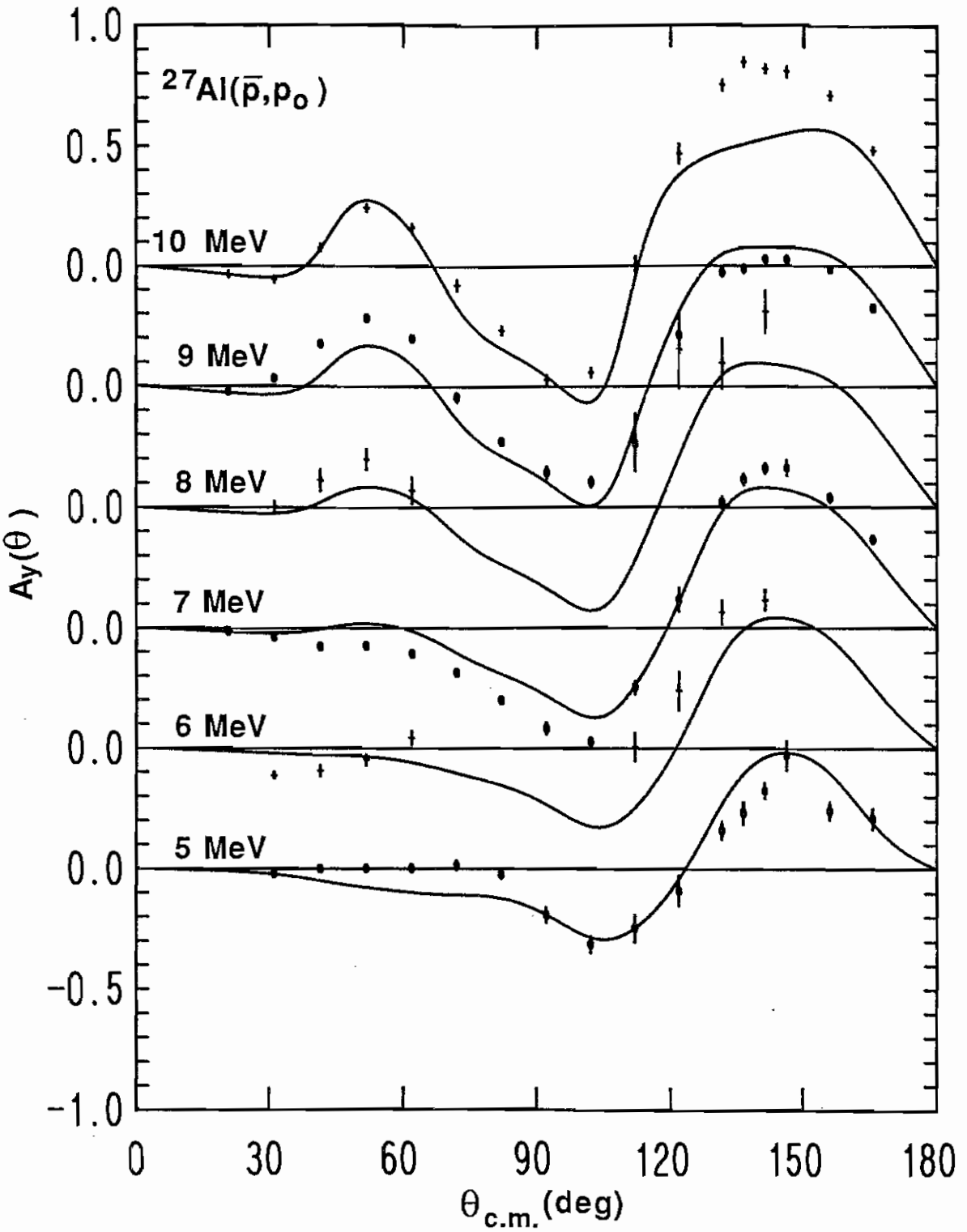

Fig. (3-29) Analyzing power data for proton elastic scattering from ^{27}Al at 5 to 10 MeV along with energy dependent associated Legendre polynomial fits.

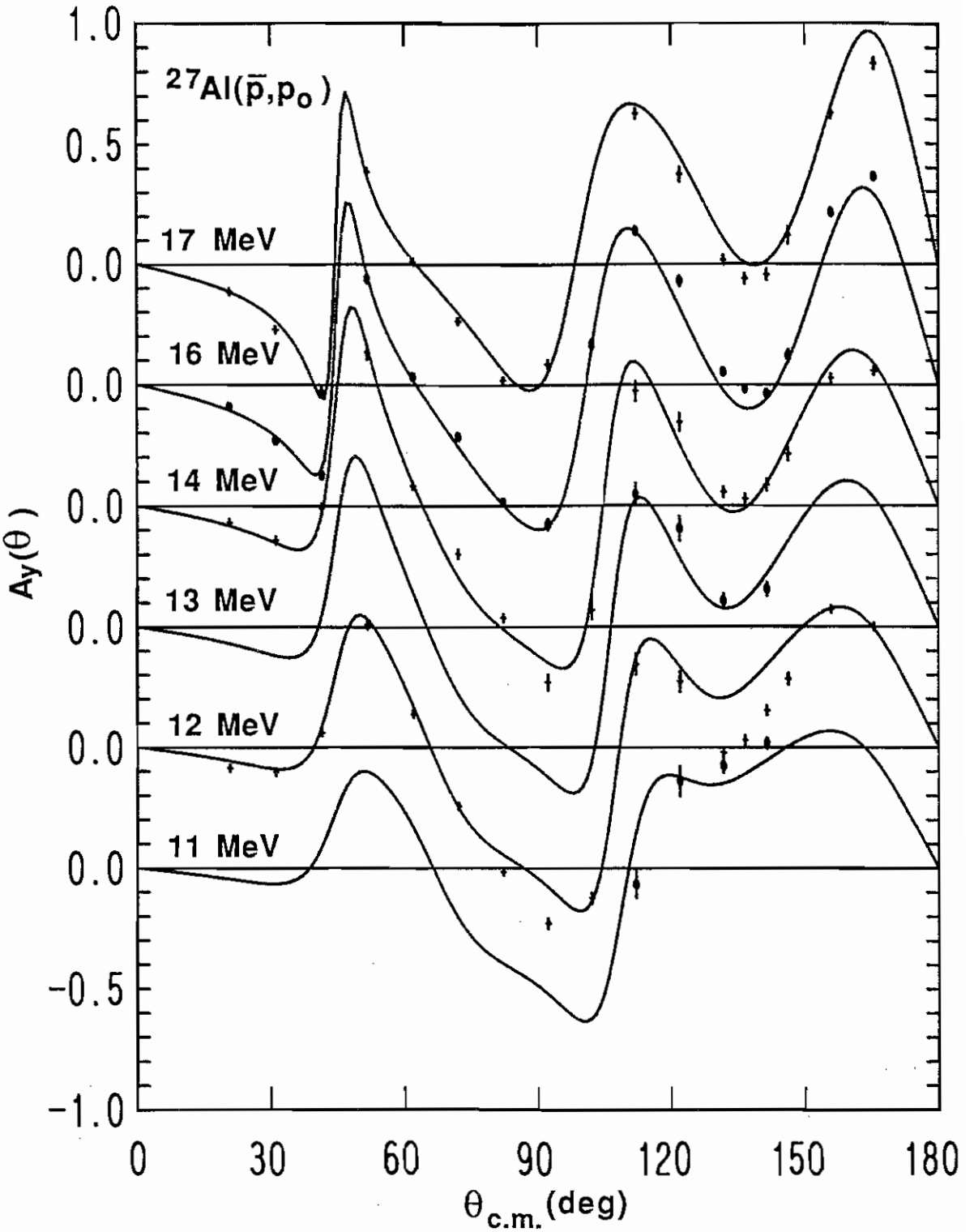

Fig. (3-30) A continuation of Fig. (3-29) showing ^{27}Al proton elastic scattering analyzing power data and fits at 11 through 17 MeV.

CHAPTER 4

MODEL CALCULATIONS FOR ^{6}Li AND ^{27}Al

Introduction

The optical model has shown itself to be a reliable and convenient model for representing neutron and proton elastic scattering from a large variety of nuclei over a wide range of bombarding energies. In its early forms the model consisted of a simple square well potential having real and imaginary parts, where the imaginary part was introduced to account for absorptive processes (Haeberli 74, Hodgson 63). The many-body interactions involved in scattering of a nucleon from a nucleus are ignored in the model in favor of a simpler two-body nucleon-nucleus interaction. This is similar to representing the scattering of light in a refracting and absorbing medium by a complex index of refraction rather than using a more complicated microscopic model which takes into account the individual interactions between the light and the atoms that make up the medium.

Fernbach, Serber and Taylor (Fernbach 49) introduced the optical model and performed calculations of the total and absorption cross section for 90 MeV neutrons interacting with nuclei ranging from ^{7}Li to ^{238}U. These calculations compared favorably to the measurements of Cook *et al.* (Cook 49). Later, Barschall (Barschall 52) measured neutron total cross sections from 0.1 to 3 MeV and neutron elastic scattering differential cross sections at 1 MeV for a large number of nuclei across the periodic table (Walt 54). Both sets of data showed surprisingly systematic behavior, which gave additional credence to an optical model description of neutron elastic scattering. Feshbach, Porter and Weisskopf (Feshbach 54) were able to represent the differential cross-section data fairly well with a complex square-well potential. They were also able to obtain reasonable agreement with Barschall's total neutron cross sections (Feshbach 53). Later the nucleon-nucleus spin-orbit potential was introduced, and it was dramatically shown by

Becchetti and Greenlees (Becchetti 69) that a surface type spin-orbit interaction could explain a large amount of polarization data.

A large number of options exist for describing observables for nucleon scattering from a nucleus. This dissertation is particularly concerned with ^{6}Li and ^{27}Al which are light nuclei. What follows is a brief summary of several models other than the spherical optical model, including the microscopic optical model, the coupled channels approach, the phase-shift approach, and the resonating group method, which have been applied in the past with some success to the problem of nucleon scattering from light nuclei.

Since the early successes with the optical model, various attempts have been made to provide a theoretical basis for the optical model potential. The different theoretical calculations of the potential are usually collectively referred to as microscopic optical models because they are all based on some explicit dependence on the underlying nucleon-nucleon interaction.

A major step toward making it possible to do such calculations has been the development of the Brueckner-Hartree-Fock method reviewed by Hodgson (Hodgson 71). As its name suggests, the method is an adaptation to nuclear physics of the well known Hartree-Fock method in atomic physics for calculating the net potential seen by an electron in a multi-electron atom. By analogy to the atomic physics case one would like to calculate a self-consistent potential felt by a nucleon in the presence of infinite nuclear matter. The nucleon-nucleon interaction is, however, strongly repulsive at very short range unlike the Coulomb interaction experienced by the electron. Brueckner has devised a method for calculating a self-consistent potential which uses a realistic repulsive core potential for the interaction of each nucleon with its nearest neighbors. This is combined with a net interaction to account for the long range interaction of each nucleon with the rest of the nuclear matter.

Several collaborations have used the Brueckner-Hartee-Fock method to calculate

the net potential in nuclear matter. Different assumptions have been made about the nature of the nucleon-nucleon interaction used in the calculations. To transform from the theoretically interesting case of nuclear matter to the realistic case of finite nuclei, an approximation (the local density approximation) is made for the radially dependent density expected in a nucleus as opposed to the constant density used in the nuclear matter calculation. Two noteworthy applications of this approach are from Jeukenne, Lejeune and Mahaux (Jeukenne 77A, Jeukenne 77B) and Brieva and Rook (Brieva 77A, Brieva 77B). Both groups have made calculations of the real and imaginary central potentials as well as calculations for the spin-orbit potential based on other methods. Using fixed geometries and allowing only scale factors for the real central, imaginary central and spin-orbit well depths fits to experimental differential cross-section data have been obtained (Hansen 85, Mellema 83, and Petler 85) for nuclei ranging from ^{9}Be to ^{209}Bi. The calculations for the light nuclei fit the data very well and give support to the hope that satisfying fits to the ^{6}Li data can also be obtained.

The coupled channels approach to calculating elastic and inelastic scattering cross sections and analyzing powers is also a variation on the spherical optical model. Earlier workers, departing from the then widely accepted shell model, suggested that the primary mechanism responsible for inelastic scattering was the excitation of collective states of the nucleus. The term collective refers to the collective motion of the nucleons within the target nucleus (Hodgson 71, Satchler 83). The collective states manifest themselves as deviations from sphericity of the nuclear shape. The nature of these deformations fall into two categories: vibrational and rotational states. Those nuclei labelled as vibrators have N or Z close to filled shells and experience oscillations about a spherical equilibrium shape when hit with a projectile. Rotators have N or Z far from filled shells and have a permanent deformation. The potential in the coupled channels framework is a combination of the spherical optical model potential plus a term to account for the non-spherical nature

of the nucleus. In practice this approach makes it possible to calculate observables for inelastic scattering to a small number of low-lying excited states. Contributions from giant resonances at high energies can also be treated in the coupled channels formalism.

Another well established method for calculating observables for elastic scattering is the phase-shift approach. In this technique the wave function which describes the elastic scattering of incident particles with a target nucleus is assumed to be composed of an incident plane wave and a scattered spherical wave as such,

$$\psi(r) \propto e^{ikz} + f(\theta)\frac{e^{ikr}}{r} \tag{4-1}$$

where $f(\theta)$, the coefficient of the spherical wave term, is referred to as the scattering amplitude (Marmier 69). By expanding an incident plane wave in terms of l, the orbital angular momentum, one gets terms representing an ingoing and an outgoing spherical wave. Introducing a coefficient in front of the outgoing spherical wave term allows one to take account of the disturbance of this wave by scattering. Reorganization of the terms back into the form of Eq. (4-1) gives the scattering amplitude as

$$f(\theta) = \sum_{l=0}^{\infty} (2l+1)\left(\frac{e^{i\delta_l}\sin\delta_l}{k}\right)P_l(\cos\theta) \tag{4-2}$$

where the δ_l are called the phase shifts, the P_l's are the Legendre polynomials, and k is the center of mass momentum of the projectile. Of course, from $f(\theta)$ one can calculate the elastic scattering cross section $\sigma_{el}(\theta)$.

The phase shifts δ_l can be searched on to give calculations of the elastic cross section which optimally fit the experimental data. Analyzing powers for elastic scattering can also be calculated within the phase-shift framework. Perhaps more significant however is the information that is revealed about the structure of the target nucleus. The different δ_l's are associated with different levels in the nucleus where the total angular momentum of the level J is related to the orbital angular momentum l of the incident partial

wave through the well known equation

$$J = l + s \qquad (4\text{-}3)$$

where s is the spin of the incident nucleon. When plotted as a function of incident energy the δ_l's show resonances. The energy at which the resonance occurs for a particular δ_l corresponds to the excitation energy of the nuclear level associated with that δ_l. The level widths may also be extracted from a phase-shift analysis.

The resonating group method provides yet another approach for modeling the nucleus. Because of the complicated nature of the calculations involved, this method is presently best suited for light nuclei. Calculations for the nucleon plus ^{6}Li system have been provided to us and are presented in a later section. A description of the working principles of this method are given in that section, but here it is sufficient to mention it as another alternative.

Thus it can be seen that a large number of models exist for predicting different aspects of nuclear scattering. Each model has its own strengths and weaknesses in predicting observables in addition to the fact that certain models are more applicable in some situations. All of the above approaches can be applied to the nucleon scattering from ^{6}Li problem and we expect the novel analyzing power data presented in the present work to be useful in developing these various approaches. The present data for elastic scattering show very systematic behavior and suggest that a simple model might suffice for explaining the energy dependence of both the analyzing power and differential cross section. Therefore the analysis in this dissertation concentrates on applying the spherical optical model to predicting neutron and proton elastic scattering cross sections and analyzing powers. Therefore, additional background information relating specifically to the spherical optical model will be presented here.

Mathematical Expression of the Optical Model Potential

The real refractive portion of the potential and the imaginary absorptive portion

combined give the basic potential for nucleon-nucleus scattering:

$$U(r) = V(r) + iW(r) \tag{4-4}$$

The later refinements of the model that replaced the simple square-well potential of Feshbach, Porter and Weisskopf use the more realistic Woods-Saxon form of the potential, which is:

$$V(r) = -V_R f(r, R_R, a_R) \tag{4-5}$$

$$\text{where, } f(r,R_R,a_r) = \left(1 + e^{\frac{(r - R_R)}{a_R}}\right)^{-1}. \tag{4-6}$$

This is essentially a flat-bottomed potential with rounded edges which is parametrized by a depth V_R (in MeV), a nuclear radius R_R (in fm), and a diffuseness a_R (also in fm). The real radius is usually parametrized in terms of the atomic weight, A, as follows:

$$R_R = r_R A^{1/3} \tag{4-7}$$

and the other radii to be mentioned are similarly parametrized.

The imaginary part, when parametrized in the same fashion, is referred to as the volume absorption term since with this form the absorption takes place throughout the volume of the nucleus. This is expressed as:

$$W_V(r) = -W_V f(r,R_V,a_V), \tag{4-8}$$

where $f(r,R_V,a_V)$ is the same Woods-Saxon form factor used for the real potential. It is observed however, that at lower bombarding energies absorption tends to take place more readily at the surface of the nucleus. For this reason, a surface absorption term is adopted which has a "derivative Woods-Saxon" form factor and is expressed as:

$$W_D(r) = 4 a_D W_D \frac{d}{dr} f(r, R_D, a_D). \tag{4-9}$$

This part of the potential is peaked at the surface and has zero magnitude at the center of the nucleus for a medium weight or heavy nucleus. The greater absorption at the surface comes about largely because of the exclusion principle. That is, the innermost

nucleons in the nucleus are the ones in the lowest energy states (in a shell-model view). The valence nucleons at the surface can be more readily elevated to excited states, through inelastic scattering. As the bombarding energy increases, there is sufficient energy to raise these nucleons to excited states. Hence, at low energies the absorptive potential is usually represented by a surface form and as the energy increases there is a combination of surface and volume. Above 50 to 80 MeV, usually the pure volume form is adequate for describing nucleon-nucleus scattering data.

An additional important term in the optical model potential is the spin-orbit term. Adair (Adair 54) first suggested including it in the optical potential because of its importance to the shell model. It is assumed to have the familiar Thomas form, from atomic physics,

$$U_{so}(r) = \left(V_{so} + i\, W_{so}\right)\left(\frac{\hbar}{m_\pi c}\right)^2 \frac{1}{r}\frac{\mathrm{d}}{\mathrm{d}r} f(r, R_{so}, a_{so})\,(\sigma \cdot \ell)\,. \qquad (4\text{-}10)$$

The surface-peaked derivative Woods-Saxon form factor appears in this term also. From a microscopic point of view, the interaction is due to the separate nucleon-nucleon spin-orbit interactions. It is clear that this interaction should be zero at the interior of a heavy-weight nucleus. Deep within the nucleus, the incident nucleon interacts with an equal number of nucleons on the left and right due to the short-range of the nucleon-nucleon interaction. The sign of $\sigma \cdot \ell$ is opposite on the two sides and consequently the interaction averages to zero.

Because of the energy dependence of the nucleon-nucleon interaction and of absorptive processes, the strengths of the real central potential, imaginary volume potential, imaginary surface potential, and real and imaginary spin-orbit potentials are also energy dependent. For nucleon energies in the 8 to 40 MeV region, these dependences are commonly expressed in the following manner:

$$V_R = V_{oR} - \alpha_R E$$

$$W_V = W_{oV} + \alpha_V E$$

$$W_D = W_{oD} - \alpha_D E$$

$$V_{so} = V_{SO} - \alpha_{SO} E$$

and $$W_{so} = W_{SO} - \alpha_{W_{so}} E \qquad (4\text{-}11)$$

where E is the bombarding energy. The α's are typically constant in value; more elaborate energy dependences are often employed for energies below 8 MeV (less absorption) and above 40 MeV.

There are several small terms in the optical model potential which allow for differences between neutron and proton scattering (and which allow for describing (p,n) reactions to the isobaric analog state, that is, quasielastic scattering). A correction to the real and imaginary central potential depths for the Coulomb repulsion present in proton scattering is allowed for by the Coulomb correction terms which are:

$$\Delta V_c = b_c \frac{Z}{A^{1/3}} \qquad (4\text{-}12)$$

$$\Delta W_c = d_c \frac{Z}{A^{1/3}} \qquad (4\text{-}13)$$

where b_c is usually taken to be about 0.4 MeV and d_c will be taken to be zero in the present analysis. There is also a term which takes into account the common Coulomb repulsion felt by a charged projectile in the presence of the charged target, which is expressed as:

$$V_C = \frac{Z z e^2}{2 R_C} \left[3 - \left(\frac{r}{R_C}\right)^2\right] \qquad \text{for } r < R_C$$

$$V_C = \frac{Z z e^2}{r} \qquad \text{for } r \geq R_C \qquad (4\text{-}14)$$

where the Coulomb radius is often taken to be $R_C = R_R$ as it is in the present work. This expression for the Coulomb potential V_C is based on the assumption that the target is a homogeneously charged sphere of radius R_C.

So-called asymmetry terms are allowed for in the real central potential and the

imaginary surface potential depths. These terms take into account the fact that the interaction is stronger between unlike nucleons than between like nucleons. They are expressed as multiples of the symmetry parameter ε where

$$\varepsilon = \frac{N-Z}{A} \quad . \tag{4-15}$$

The full potential with all terms included is:

$$\begin{aligned} U(r) = & \left[(V_{oR} - \alpha_R E) \pm V_{IR}\,\varepsilon + \Delta V_c \right] f(r, R_R, a_R) \\ & + i \left(W_{oV} + \alpha_V E \right) f(r, R_V, a_V) \\ & + i\,4\,a_D \left[(W_{oD} - \alpha_D E) \pm W_{ID}\,\varepsilon + \Delta W_c \right] \frac{d}{dr} f(r, R_D, a_D) \\ & + \left(V_{so} + i W_{so} \right) \left(\frac{\hbar}{m_\pi c} \right)^2 \frac{1}{r} \frac{d}{dr} f(r, R_{so}, a_{so}) \, (\sigma \cdot \ell) \\ & + V_C \quad . \end{aligned} \tag{4-16}$$

The importance of the various terms in the optical model analyses of ^{6}Li and ^{27}Al will be discussed later. However, it is noteworthy here that $\varepsilon = 0$ for ^{6}Li, and therefore the only difference between (p,p) and (n,n) is the Coulomb correction term (and the usual Coulomb repulsion). For completeness, it is useful to note that the Coulomb correction V_c is taken to be real. The nature of the correction to the absorptive potential is not well understood; it is believed to be small, however. Also, the symmetry term for the U_{so} potential is not well understood and is usually taken to be zero.

Limitations of the Spherical Optical Model

Because of the nature of the model, it is generally less successful below 10 MeV bombarding energy. This is primarily because the model makes no allowance for scattering from discrete resonances and compound nucleus effects, aside from the absorption terms in the potential which are smoothly varying with energy and atomic mass.

The model can predict the total cross section which is composed of the shape elastic scattering cross section and the absorption cross section:

$$\sigma_T = \sigma_{SE} + \sigma_A. \tag{4-17}$$

Absorbed nucleons can initiate nuclear reactions or they can be reemitted with their initial energy after a time delay following compound nucleus formation. Thus the absorption cross section σ_A is composed of a reaction cross section and a compound elastic scattering cross section:

$$\sigma_A = \sigma_{CE} + \sigma_R. \tag{4-18}$$

It is this compound elastic cross section which is indistinguishable from the shape elastic cross section in a typical scattering experiment.

At low energies few states in the compound nucleus are available, which leaves compound elastic scattering as a very probable exit channel. At higher energies more channels open up, compound elastic scattering is less probable and the model predictions are more satisfactory.

Additionally, at low energies those available states in the compound nucleus are fairly sharp and well separated. The absorption cross section calculated by the optical model can only account for the average effects of many broad, closely-spaced states which is the case at higher energies. The inherent energy spread in the incident beam is beneficial in averaging over the effects of the individual states. At low energies one expects variations in the scattering cross section which cannot be reproduced by the optical model. A similar problem with averaging over energy levels in the compound nucleus is encountered with light nuclei. The energy levels in heavier nuclei are more closely spaced and one can expect more satisfying results from the optical model calculations. This is of course a significant problem for scattering from ^{6}Li.

Spherical Optical Model Analysis for ^{6}Li Neutron Elastic Scattering

A goal of the ^{6}Li optical model analysis is to obtain a global set of parameters

which fit neutron and proton elastic scattering data from 5 to 17 MeV. No attempt was made at this time to fit the inelastic data with some other relevant model. As preliminary steps toward that goal global parameter sets were obtained for proton and neutron scattering separately. The calculations were done using GENOA85, a modified form of the combined automatic parameter search code GENOA of Perey (Perey 63).

The neutron data used in the searches consisted of the nine analyzing power angular distributions from 5 to 17 MeV of the present work. The differential cross-section data at 8.96, 9.96, 10.95, 12.04, 12.94, and 13.94 MeV of Hogue (Hogue 79) were used. Angular distributions in 10^{o} steps were generated at 5.08, 5.90, 6.92, and 7.92 MeV from the energy dependent Legendre polynomial coefficients which had been fit with ASSFITE to the Knox (Knox 79) and the Hogue data. These values derived from the Legendre fits were assumed to have errors of 5%, which is consistent with the reported uncertainties of Hogue and Knox. Cross-section data were not available at 17 MeV and none were used in the searches. Total cross-section and reaction cross-section values were obtained from the Brookhaven tabulations (BNL 64) and included at each energy.

The starting values for the optical model parameters were taken from the work of Davé and Gould (Davé 83). This work assumes the optical potential to consist of a real central well, a surface imaginary well, and a real spin-orbit term. The real central and surface imaginary strengths were given linear energy dependences. Values of Davé's parameters are given in Table (4-1). The data used in this analysis consisted of neutron differential, total, and reaction cross sections and proton differential cross sections for 1-p shell nuclei ranging from ^{6}Li to ^{16}O. There were no analyzing power data used in Davé's analysis. Consequently the spin-orbit parameters were fixed at the same commonly accepted values for all nuclei.

The first step in our analysis of the neutron data was to find "best fit" parameters at each energy. Single energy searches were performed on the following sets of

parameters in the order presented: V_R and W_D, V_{so}, r_{so} and a_{so}, r_R and a_R, r_D and a_D, V_R, and r_R. After each search, the original value was replaced by the optimum value obtained, unless it seemed too extreme. The values obtained from the searches reflected a relatively smooth variation with energy in the range of 7 to 14 MeV. Large deviations from a smooth energy dependence occurred at 5 and 6 MeV for V_R, r_R, and W_D. In addition, the searches on V_R and W_D at 17 MeV resulted in values which were inconsistent with values at the other energies.

It is not surprising that V_R and r_R both experienced large excursions because of the well known ambiguity associated with these two parameters. It is the volume integral J_V calculated from the real central potential as follows:

$$J_V = V_R \frac{4}{3}\pi R_R^3 \left(1 + \pi^2 \frac{a_R^2}{R_R^2}\right) \tag{4-19}$$

which primarily determines the cross section and analyzing power (Greenlees 68) and since V_R and $r_R{}^3$ appear in the volume intregral as multiplicative factors, the effect of a change in one can be offset by a change in the other. During the searches which followed the search on r_R, the values of r_R at 5, 6, and 17 MeV were set to values which were consistent with the values at the other energies.

The deviant values of V_R and W_D at 5 and 6 MeV reflect a problem with the model at low energies. The model predicts cross sections at 5 and 6 Mev which are low by as much as a factor of four across the whole angular distribution. It also incorrectly predicts the shapes of the cross sections and analyzing power angular distributions in the mid-angle region. The magnitude of the cross section is particularly sensitive to the values of V_R and W_D. Specifically, lowering W_D raises the back-angle cross section while lowering V_R lowers the back-angle and raises the forward-angle cross section. Lowering V_R raises the magnitude of the back-angle analyzing power. The large changes in V_R and W_D reflect attempts by the search code to minimize chi-squared by coming close to either

the forward-angle or back-angle data. The result of this is to predict a shape for the cross section which does not resemble the data. Values for V_R and W_D consistent with the other energies were selected before continuing with subsequent searches. Fits using these values resemble the shape of the cross section to the greatest extent possible, but with low magnitudes. The agreement with the 5 and 6 MeV analyzing power is poor, with the forward-angle magnitude too high and the zero-crossing occurring too far back in angle. The fits at 7 and 8 MeV show similar problems to a lesser extent although the search code settled on values for V_R and W_D which were consistent with those at higher energies.

The unusual behavior of the parameters at 17 MeV can be linked with the poor agreement of the fits to the data between 130° and 160°. In this region, modest changes in W_D cause large changes in the magnitude of $A_y(\theta)$. A small W_D is necessary to obtain the large values of $A_y(\theta)$ at the back angles. V_R also influences this back-angle region to a lesser degree thus accounting for the deviation in this parameter. The fits at 17 MeV however do not suffer by setting V_R to a value in line with the lower energy values. At 17 MeV a value of W_D that is significantly lower than the values at lower energies is inescapable.

The neutron parameter set obtained in this manner served as a base from which to explore in greater detail the sensitivities of the various parameters. From these single-energy "best fits", energy averaged values or linearly energy dependent values were obtained for all the parameters. Average values for the spin-orbit and surface imaginary parameters were calculated with lower weight being given to the values at 5, 6, and 7 MeV. This practice of attributing low weight to the low energy data was carried on throughout the analysis. It became obvious early on in the analysis that the optical model could not adequately describe these data, so rather than sacrifice the quality of fits at higher energies it seemed appropriate to accept small compromises in the quality of fits at low energies. Average values for r_R and a_R were also obtained in this manner, as well as an

energy dependent parametrization of the real central well depth. These values are given in Table (4-1) under the heading of "Optimized n set".

A cursory check on the effect of W_V was performed. A value of 5 MeV was assigned to W_V with the geometry parameters, r_V and a_V set equal to r_R and a_R, respectively. All other parameters were kept fixed at the values which resulted from the preliminary searches already discussed. As one might expect the result was a lowering of all cross sections, but particularly in the mid-angle region. This tended to distort the shape of the angular distribution in the mid-angle region. The effect on the calculations for the analyzing power data was less noticeable, but generally the fits were worse. It was concluded from this check that including a volume imaginary term would not be beneficial at all energies. However, further exploration should be pursued in order to find whether volume absorption should definitely be excluded in this 5 to 17 MeV energy range.

Spherical Optical Model Analysis for ^{6}Li Proton Elastic Scattering

A separate analysis of the proton data was performed. The $A_y(\theta)$ and $\sigma(\theta)$ proton scattering data at 5 through 17 MeV were the only data sets used in this portion of the analysis. Again, the parameters of Davé served as starting values. The Coulomb correction term to the real central well used by Davé and having the standard value for b_c of 0.4 MeV was applied to her value for V_{oR} to provide a starting value for V_{oR}, but b_c was never included as a separate parameter on which to search. As can be seen from Fig. (4-1) a Coulomb correction term of some sort is necessary. The proton analyzing power data at several energies have been superimposed on plots of the neutron data at energies which are 2 MeV less than the proton energies. This difference is close to the 1.6 MeV lost by the proton as it approaches the charged nucleus. The data at these shifted energies agree closely indicating that a simple Coulomb correction term in the real or imaginary well depth may be useful.

Rather than performing single energy searches for all energies at the beginning of

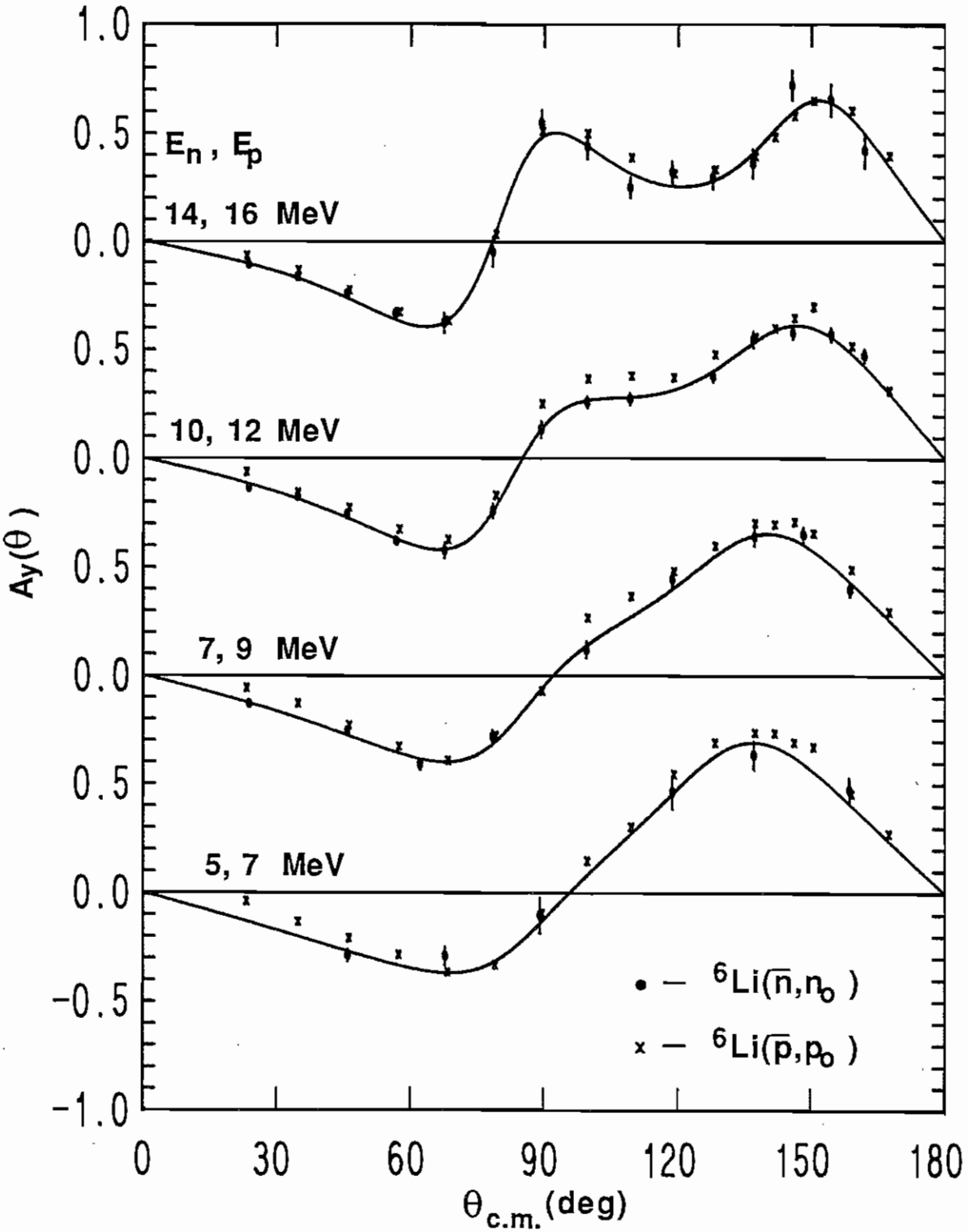

Fig. (4-1) Proton analyzing powers for ^{6}Li at 7, 9, 12, and 16 MeV are superimposed on the neutron data at 5, 7, 10, and 14 MeV, respectively. The curves are the associated Legendre polynomial fits to the neutron data.

the proton data analysis, it seemed expeditious to optimize the parameters at 10 MeV only, using the information about parameter sensitivities gained from the neutron analysis to guide our decisions. The sensitivities of all the parameters were tested with the 10 MeV data. The behavior of the parameters was consistent with what had been observed with the neutron data. It became clear that parameters similar to the neutron parameters would work well to describe the proton data. The parameter set finally obtained for the 10 MeV data differed significantly from the "Optimized n set" only in the values for V_R and W_D. This parameter set optimized at 10 MeV provided surprisingly good fits to all the data from 5 to 17 MeV. Problem spots existed in the fits to the $\sigma(\theta)$ and the $A_y(\theta)$ data in the mid-angle region at 5, 6, and 7 MeV. The predicted cross section was much lower than the data. The predictions for $A_y(\theta)$ in this same region were much higher in magnitude than the data.

Deficiencies also existed in the predictions of $\sigma(\theta)$ and $A_y(\theta)$ in the back-angle region at 16 and 17 MeV. The calculated cross section has a deep minimum centered about 155° which is not present in the data, while the calculated analyzing power drops in magnitude drastically in this same region whereas the data does not. These problems are reminiscent of those encountered with the neutron calculations. An investigation of the cause of the back-angle problem at 16 and 17 MeV quickly revealed that a much lower W_D was necessary to improve the fits. A value of 13.5 MeV instead of 16.25 MeV gave optimum fits at 17 MeV but the back-angle deficiencies still were evident to a lesser degree.

Optical Model Parameter Set for Neutron and Proton Scattering from ^{6}Li

With the information in hand gained from the separate analyses of neutron and proton scattering it is possible to find a compromise parameter set which fits both neutron and proton scattering data. The task is made simple by the fact that the geometry parameters for the real central, surface imaginary, and spin-orbit potentials resulting from the two analyses are essentially the same. The spin-orbit potential strength for the two sets

is also the same. Suitable energy dependences for the real central depth and surface imaginary depth which give adequate fits to both sets of data must be determined.

From the previous analyses it was evident that the quality of the fits were particularly sensitive to W_D. A careful examination of the sensitivity of W_D at each energy was undertaken. Upper and lower limits for W_D which gave acceptable fits to the data were determined at each energy. It was observed that the range of acceptable values of W_D was consistently lower for proton scattering than for neutron scattering. It was also observed that a constant W_D was required between 5 and 12 MeV and a W_D which decreased linearly with energy was unequivocably needed above 12 MeV. It was decided to introduce a constant ΔW_D which would be the difference between W_D for proton scattering and neutron scattering. W_D was further parametrized as a constant below some cut-off energy and as a linear function of energy above that energy. In equation form

$$\begin{aligned} W_D &= W_{oD} - \Delta W_D && \text{for } E < E_{cut\text{-}off\,W} \\ W_D &= W'_{oD} - \alpha_D E - \Delta W_D && \text{for } E > E_{cut\text{-}off\,W} \end{aligned} \tag{4-20}$$

where, $\Delta W_D = 0$ for neutron scattering. Starting values for these newly introduced parameters were chosen based on the single energy sensitivity tests, with the intention of searching on these values later as part of a global search on the neutron and proton data at all energies.

A compromise parametrization of V_R was also determined based on the values of V_R obtained during the separate neutron and proton analyses. V_R had a definite tendency toward lower values at higher energies, but seemed to give acceptable fits to the low energy data with a constant value. V_R was thus parametrized as

$$\begin{aligned} V_R &= V_{oR} && \text{for } E < E_{cut\text{-}off\,V} \\ V_R &= V'_{oR} - \alpha_R E && \text{for } E > E_{cut\text{-}off\,V} \end{aligned} \tag{4-21}$$

Choosing identical values of these parameters for neutron and proton scattering did not

impair the quality of the fits.

With these new parametrizations of V_R and W_D chi-squared searches were performed on a global data set consisting of the neutron and proton data at all energies. In these searches double the weight was given to the $A_y(\theta)$ data than was given to the $\sigma(\theta)$ data. In the cases of the neutron data, this was done to compensate for the fact that the analyzing power angular distributions have fewer data points than do the cross-section angular distributions. In addition, the error bars for the $A_y(\theta)$ data are larger and it was desired to force better systematic agreement. It was also desired to put extra weight on the $A_y(\theta)$ data in order to force a better determination of the spin-orbit parameters. For this reason the proton scattering analyzing power data were also given double the statistical weight.

Less weight was given to the data between 5 and 8 MeV. It was clear from the start of the analysis that the model was incapable of adequately fitting the low energy data. With equal weighting for low and high energy data the search routine would naturally adjust the parameters to fit the low energy data where the quality of fits was very poor, that is where chi-squared was very large. As was indicated in the discussion on the neutron data analysis, parameter sets for which chi-squared was minimized for the low energy data produced fits which were close to the data only in small portions of the angular distribution, but which did not resemble the shape of the distribution at all. For this reason the low energy data were given lower weight.

The final results of the global searches are given in Table (4-1) under the heading "Optimized n and p set". These values differ only by small amounts from the values obtained by compromising the separate neutron and proton sets. The value of ΔW_D was reduced to an inconsequential value after the final global searches. The values of the final parameters differ from the earlier neutron parameter set and proton parameter set primarily in the expression for the energy dependences for W_D and V_R.

Conclusions Drawn from ^{6}Li Optical Model Analysis

The optical model has done surprisingly well in predicting cross sections and analyzing powers for nucleon scattering from ^{6}Li. As mentioned earlier, the level spacing for the intermediate system (nucleon plus ^{6}Li) is quite wide and since the model can only make predictions for the average effect of many closely-spaced levels, many earlier workers simply took it for granted that the model could not be applied to ^{6}Li and consequently did not try.

Davé has succeeded in producing good quality fits to nucleon-nucleus cross-section data for some 1-p shell nuclei including ^{6}Li. Their analysis was lacking in that it included absolutely no analyzing power data. As a result, the values for the spin-orbit parameters in their model can only be given limited confidence. In addition, their energy range was restricted to 7 to 14 MeV. By extending the neutron energy range to 5 to 17 MeV, providing proton scattering data over this same energy range, and by adding analyzing power data at all energies, we expected to have a complete data base from which we could produce a more reliable optical model parametrization.

Calculations for neutron and proton cross sections and analyzing powers based on the present model are given in Figs. (4-6) through (4-13). The quality of the fits with the present model is poor for energies below 9 MeV, a region avoided by Davé. This can be seen in Figs. (4-6), (4-8), (4-10), and (4-12). At best the model can be said to reflect the general shape characteristics of the cross-section and analyzing power angular distributions, but the model misses magnitudes by factors of two or more in some cases. The deficiency of the present model is presumably a reflection of the nature of the compound nucleus effects at low energies which the optical model is in general ill-equipped to handle, for the reasons mentioned in the introduction to this chapter. The fits to the analyzing power data in Davé's energy range [see Figs. (4-11) and (4-13)] are in much better agreement with the data than the predictions of Davé. This is illustrated in

Figs. (4-4) and (4-5) where predictions from Davé and fits from this work are compared to neutron cross-section and analyzing power data at 10 and 14 MeV. The quality of fits to the cross-section data is comparable but the fits to the analyzing power data from this work are a significant improvement over the predictions of Davé.

The present model and Davé's model have certain common features. The geometry parameters for the two models are quite similar as can be seen from Table (4-1). Although all radii and diffusenesses were allowed to vary at several points in the analysis, no significant deviations from the Davé parameters occurred. The two models do not, however, have similar magnitudes or energy dependences for the three potential strength parameters.

Several significant differences are apparent in the two parameter sets for nucleon plus ^{6}Li. A large spin-orbit strength was found in the present analysis. Davé's real central well depth was only slightly energy dependent with a value of about 39.5 MeV, whereas our analysis showed a higher constant value to be helpful at lower energies and a more steeply sloped V_R to be needed at the higher energies. The fact that Davé's energy range was small allowed them to produce good fits with a nearly constant V_R.

The largest difference between the two models occurs with the surface imaginary well depth W_D. Davé has a W_D which increases with energy and having W_{oD} = 9.3 MeV. We concluded that W_D must definitely decrease with energy at the higher energies, although a constant value for W_D around 15 MeV is suitable at the lower energies. An interesting aspect of W_D is its sensitivity to the difference between proton and neutron scattering. The introduction of a small ΔW_D to account for this difference is in contrast to the use of a ΔV_c term in the Davé model. We found that identical values of V_R for neutron and proton scattering were suitable, *i.e.* $\Delta V_c = 0$. The values of the real central, surface imaginary and spin-orbit potentials as a function of the nuclear radius are given in Fig. (4-2) in order to demonstrate their shapes.

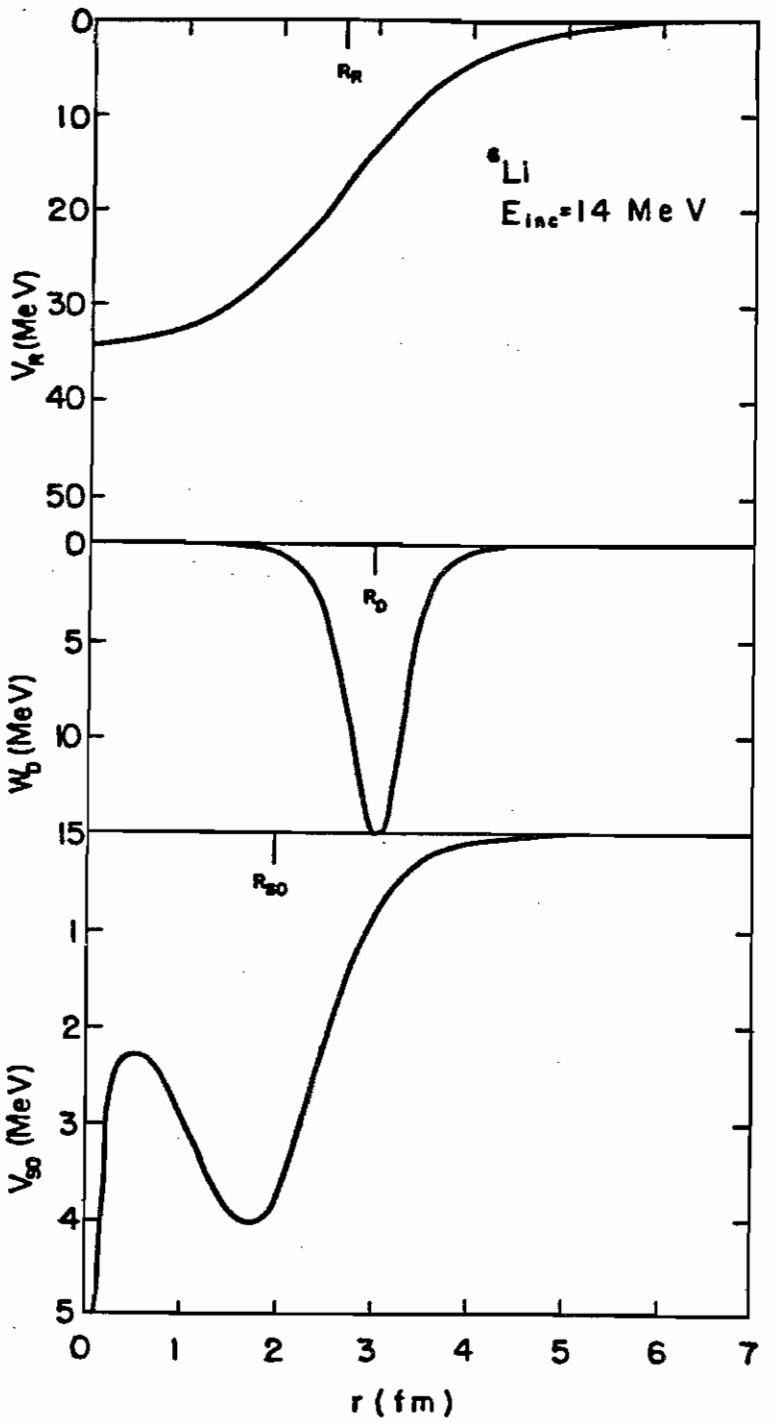

Fig. (4-2) The real central, surface imaginary, and spin-orbit potentials for ^{6}Li are shown as a function of nuclear radius at 14 MeV incident energy. V_{so} /($\sigma \cdot \ell$) is plotted for the spin-orbit potential.

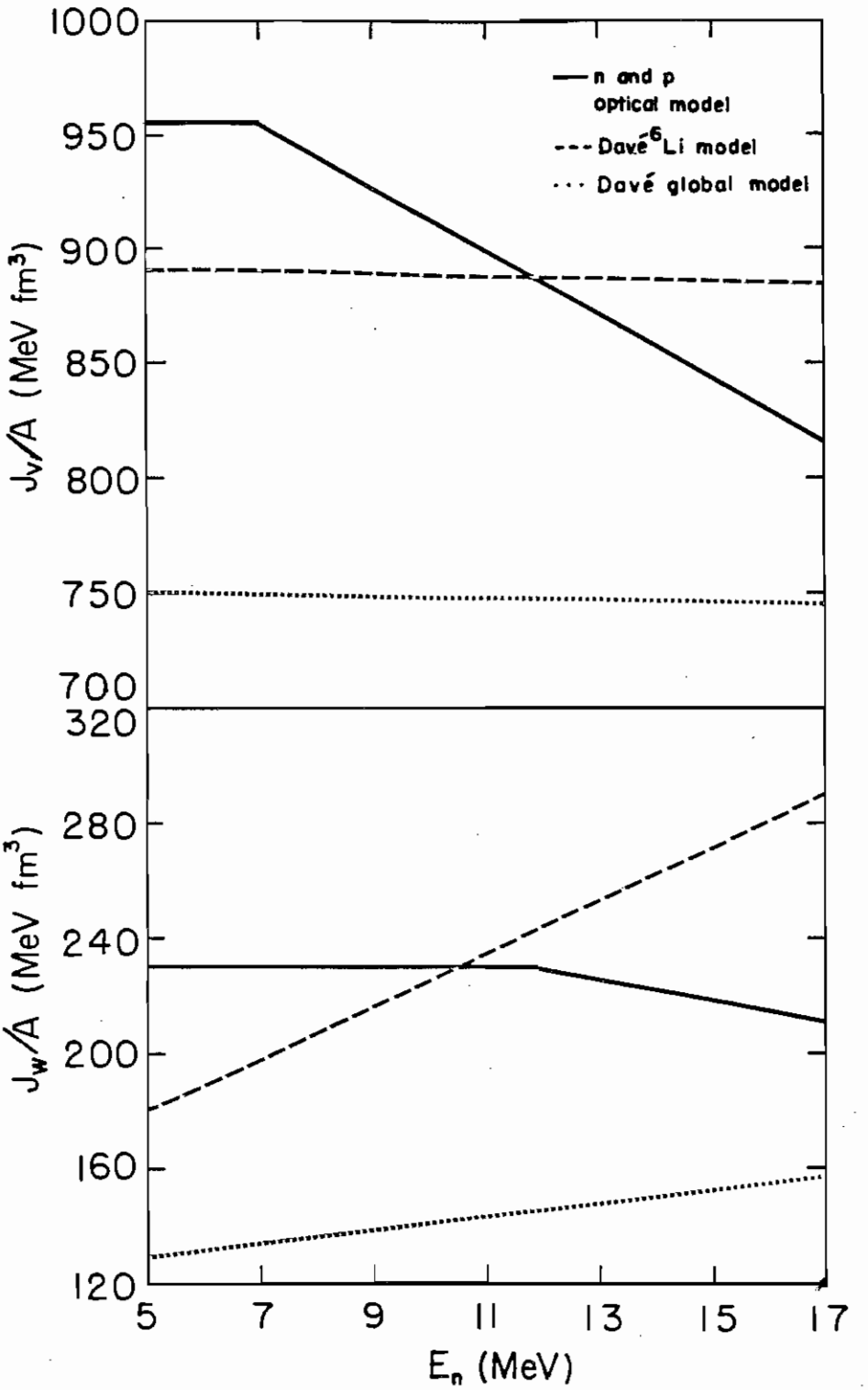

Fig. (4-3) Plots of the real central and surface imaginary potential volume integrals per nucleon for several models for ^{6}Li.

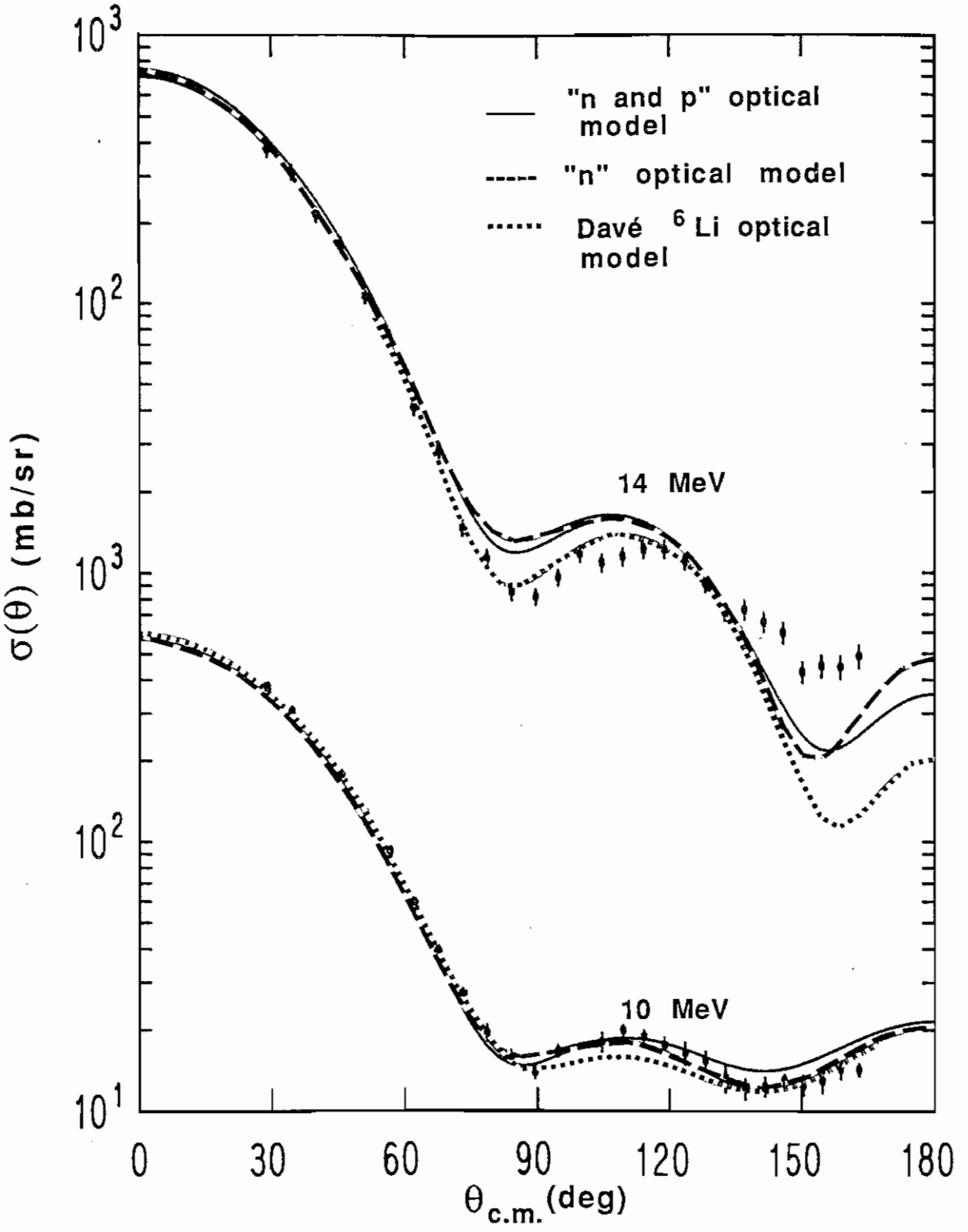

Fig. (4-4) Calculations of neutron cross sections based on the present "n and p" parameter set, the present "n" parameter set, and the ^{6}Li model of Davé are shown with data at 10 and 14 MeV.

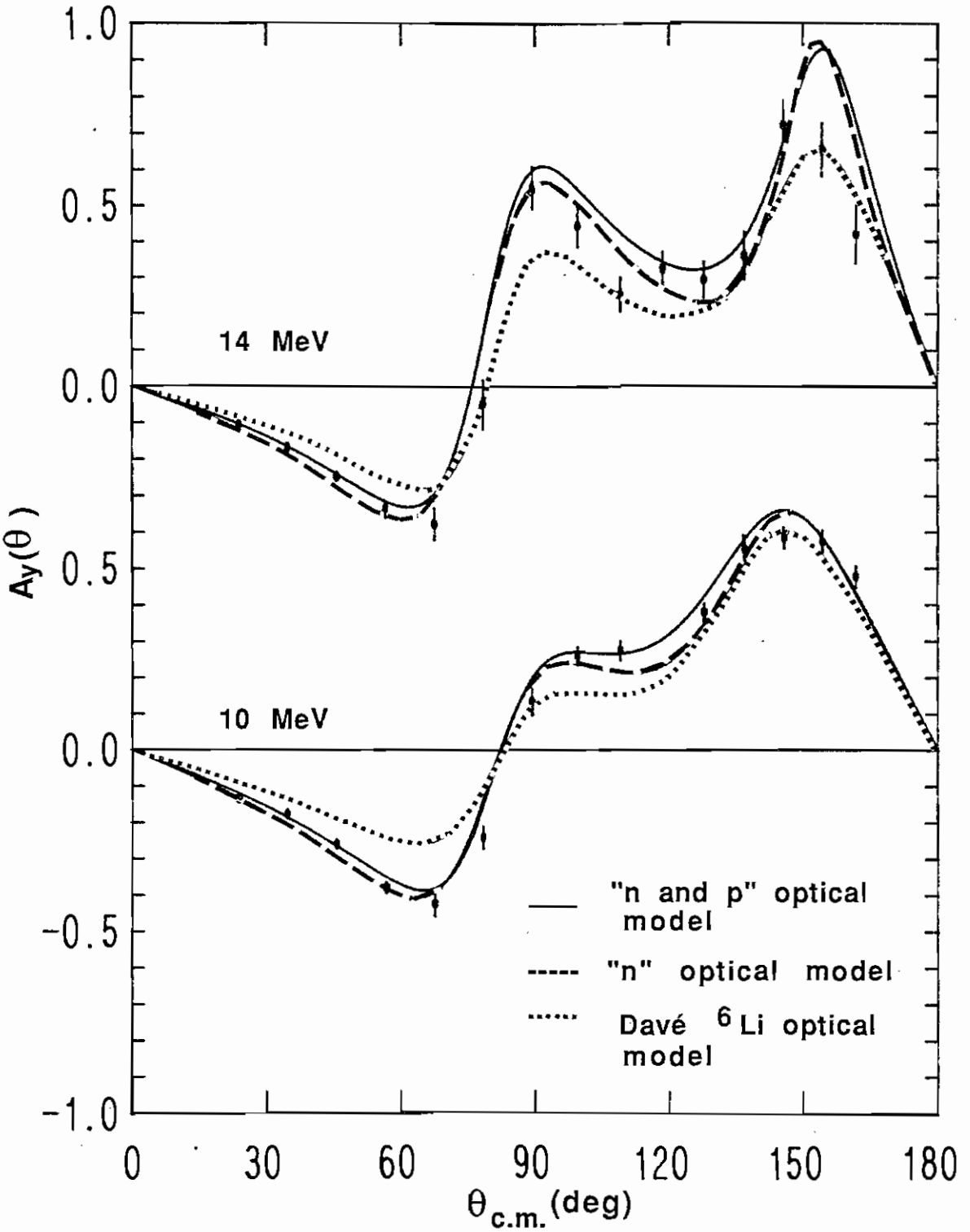

Fig. (4-5) Calculations of neutron analyzing powers based on the present "n and p" parameter set, the present "n" parameter set, and the ^{6}Li model of Davé are shown with data at 10 and 14 MeV.

TABLE (4-1)

^{6}Li OPTICAL MODEL PARAMETERS

	Davé ^{6}Li (N,N)	Murphy ^{11}B (n,n_0)	Optimized n-set	Optimized n and p set
V_{oR}	39.62	54.0	44.0	43.760
α_R	0.027	--	0.208	0.630
$V_o'_R$	--	--	--	48.065
r_R	1.507	1.130	1.480	1.476
a_R	0.663	0.655	0.693	0.674
b_c	0.40	--	--	--
W_{oD}	9.298	14.0	16.25	15.654
α_D	-0.646	--	--	0.247
$W_o'_D$	--	--	--	18.597
r_D	1.616	1.504	1.616	1.660
a_D	0.196	0.156	0.196	0.190
ΔW_D	--	--	--	0.114
V_{so}	5.50	5.860	6.70	6.863
r_{so}	1.15	1.019	1.10	1.081
a_{so}	0.50	0.166	0.40	0.458

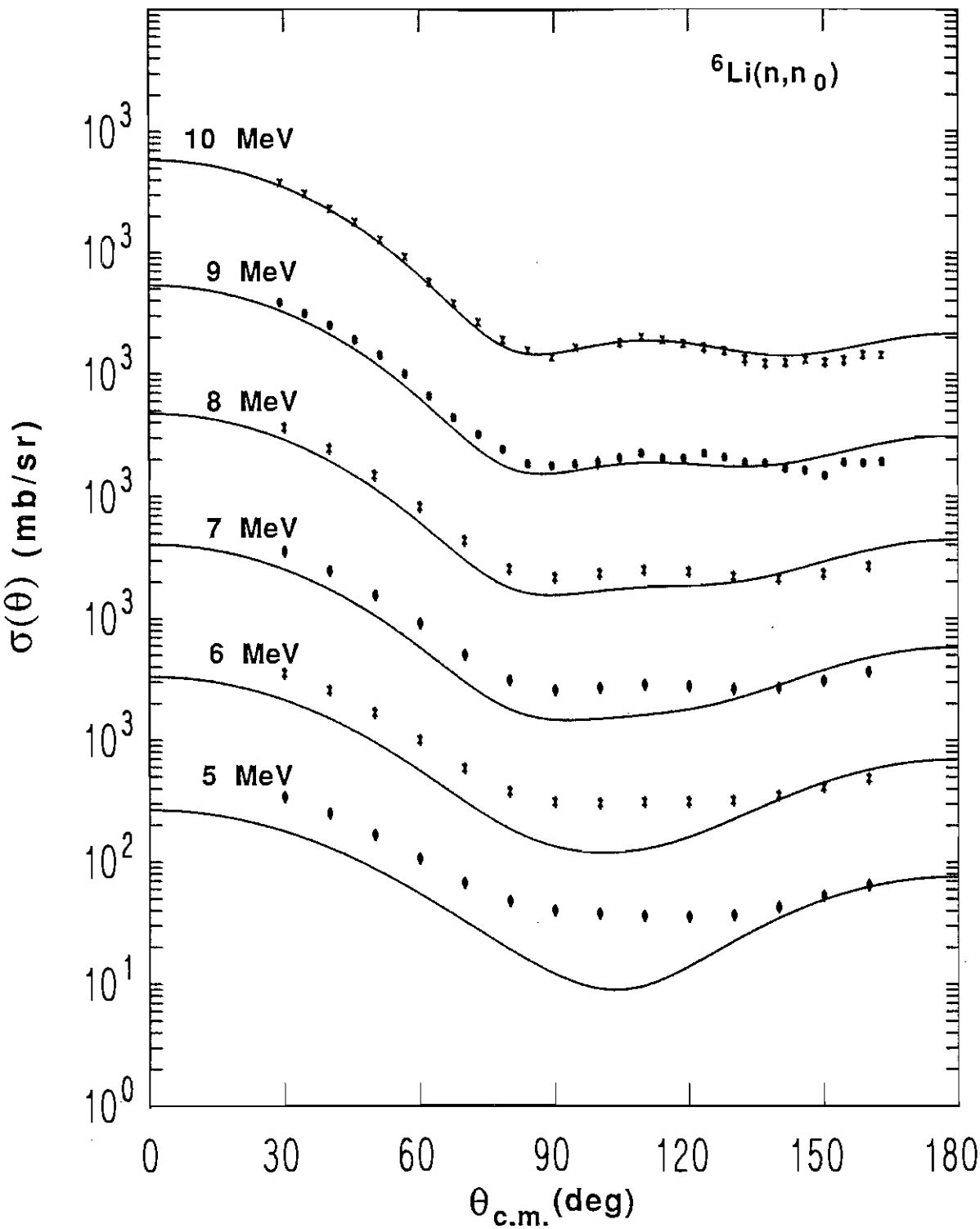

Fig. (4-6) Calculations of neutron cross sections at 5 to 10 MeV for ^{6}Li based on the "n and p" optical model are shown with data. Data at 5 to 8 MeV are derived from Legendre fits (see text). The 9 and 10 MeV data are from Hogue (Hogue 79).

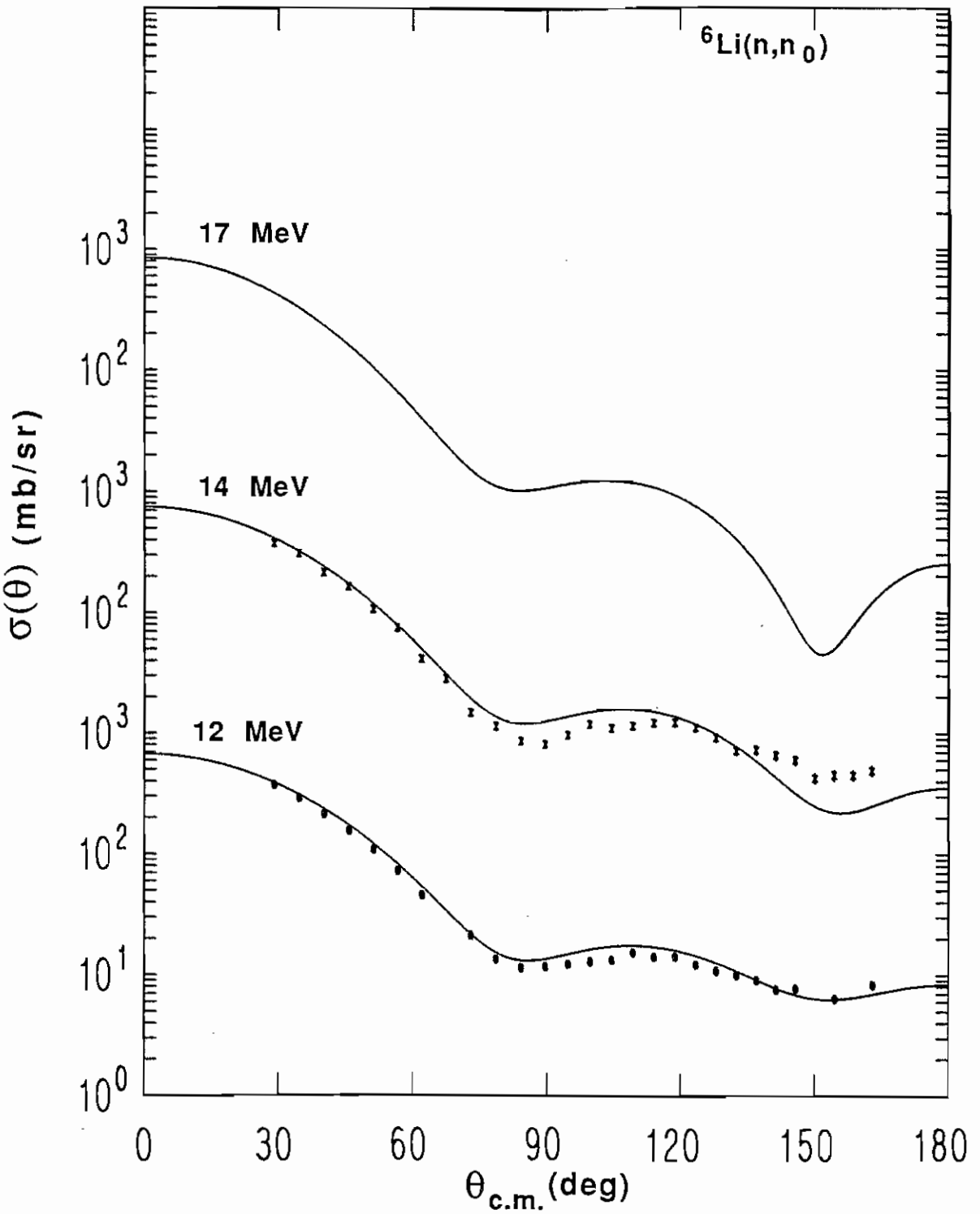

Fig. (4-7) Continuation of Fig. (4-6). Calculations of neutron cross sections at 12, 14, and 17 MeV for ^{6}Li based on the "n and p" optical model are shown with data at 12 and 14 MeV which are from Hogue.

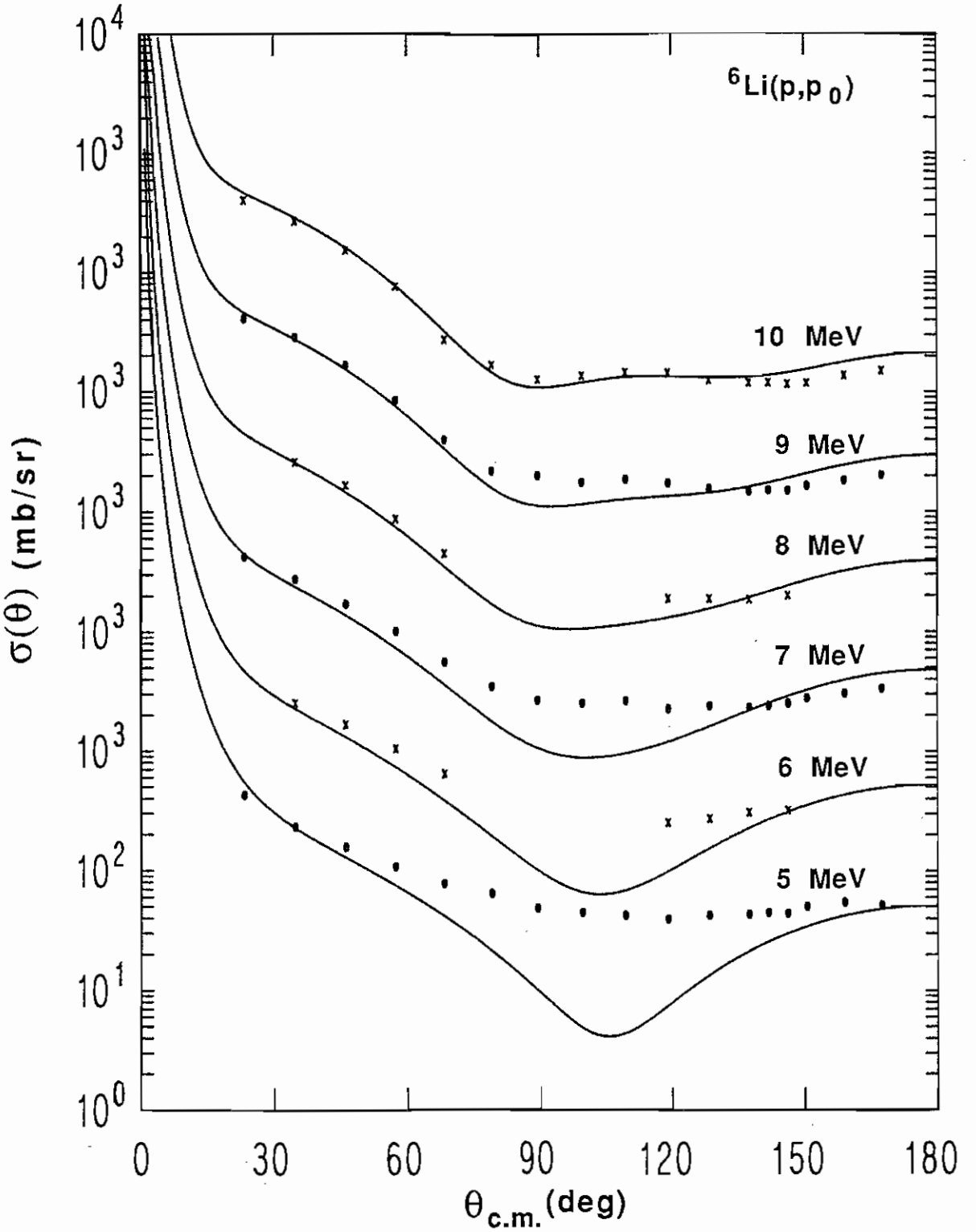

Fig. (4-8) Calculations of proton cross sections at 5 to 10 MeV for ^{6}Li based on the "n and p" optical model are shown with data.

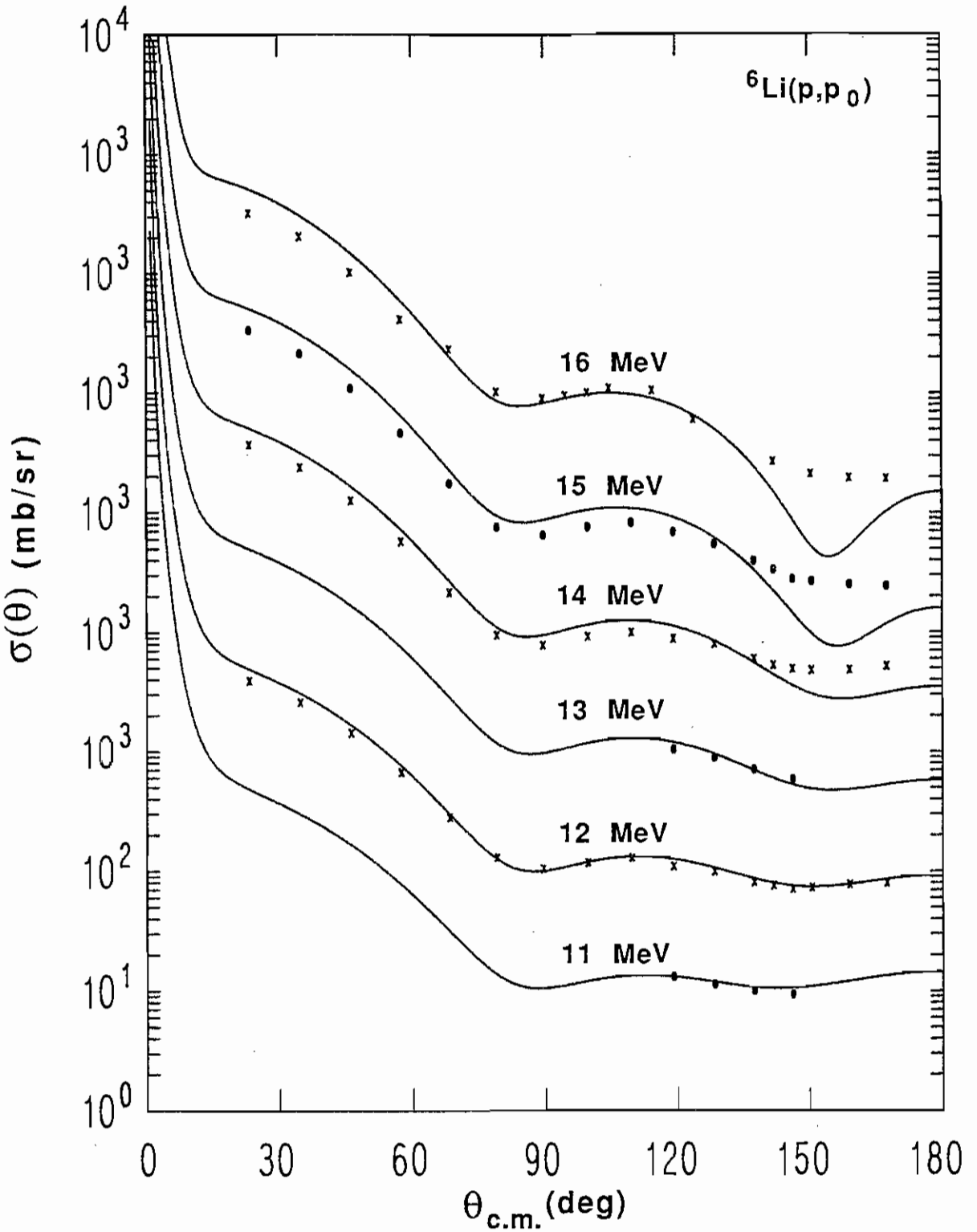

Fig. (4-9) Continuation of Fig. (4-8). Calculations of proton cross sections at 11 to 17 MeV for ^{6}Li based on the "n and p" optical model are shown with data.

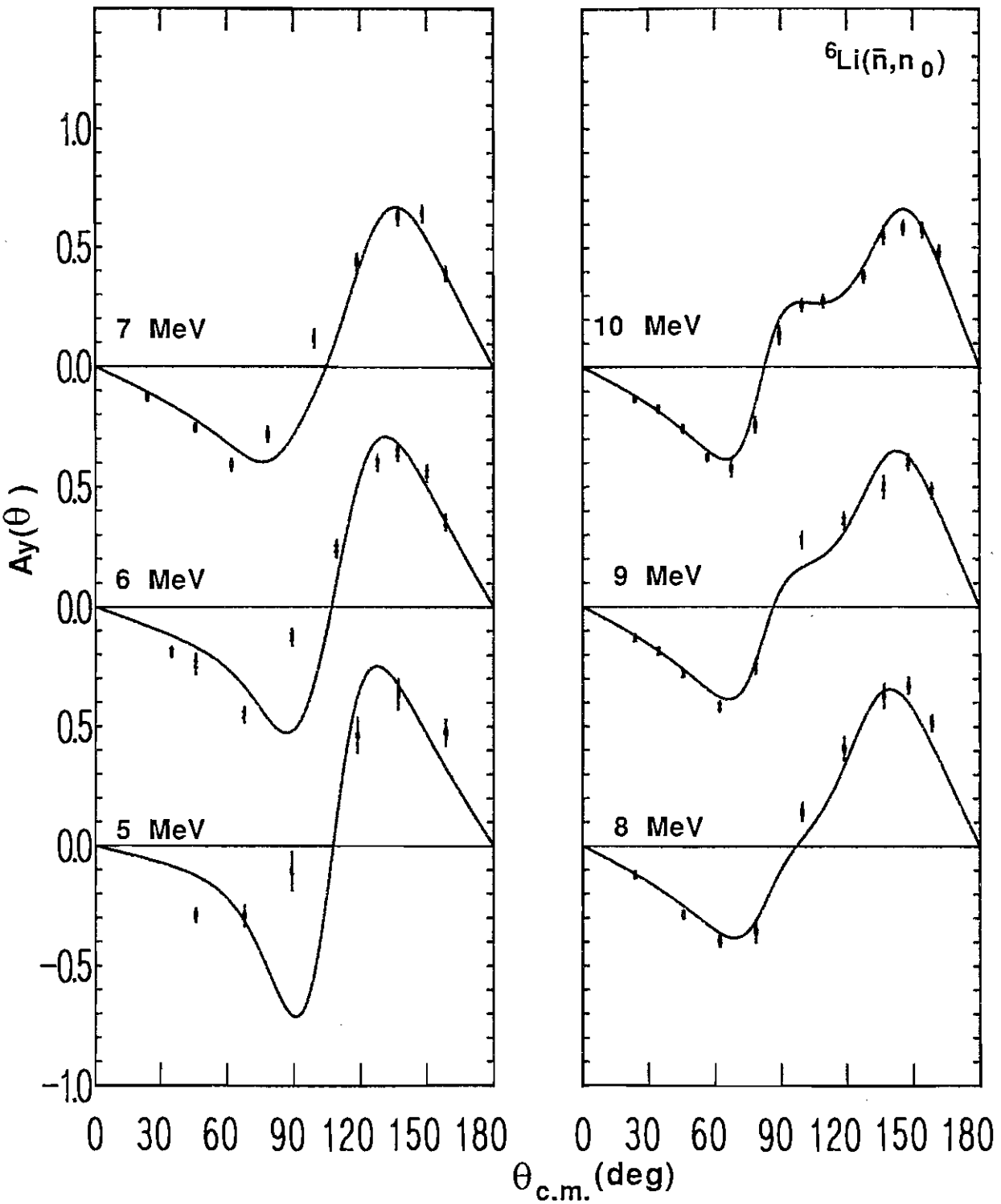

Fig. (4-10) Calculations of neutron analyzing powers at 5 to 10 MeV for ^{6}Li based on the "n and p" optical model are shown with data.

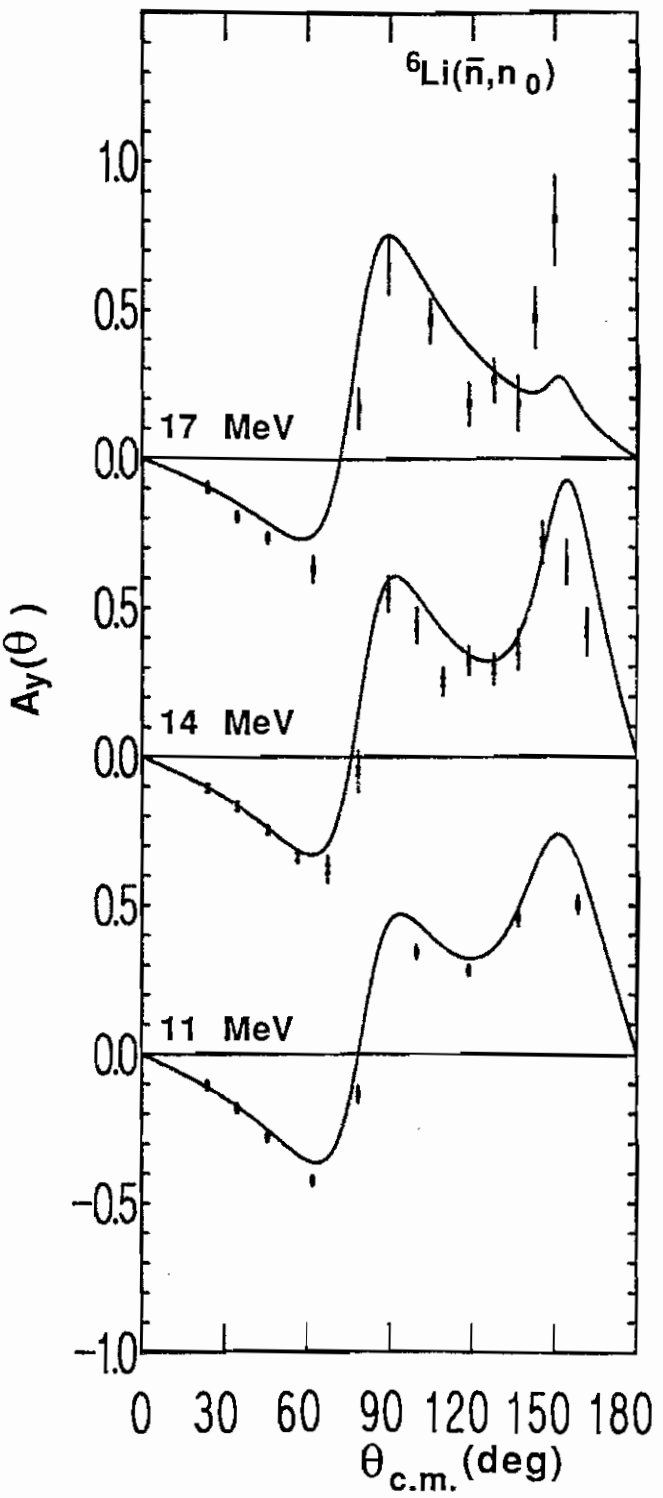

Fig. (4-11) Continuation of Fig. (4-10). Calculations of neutron analyzing powers at 12, 14, and 17 MeV for ^{6}Li based on the "n and p" optical model are shown with data.

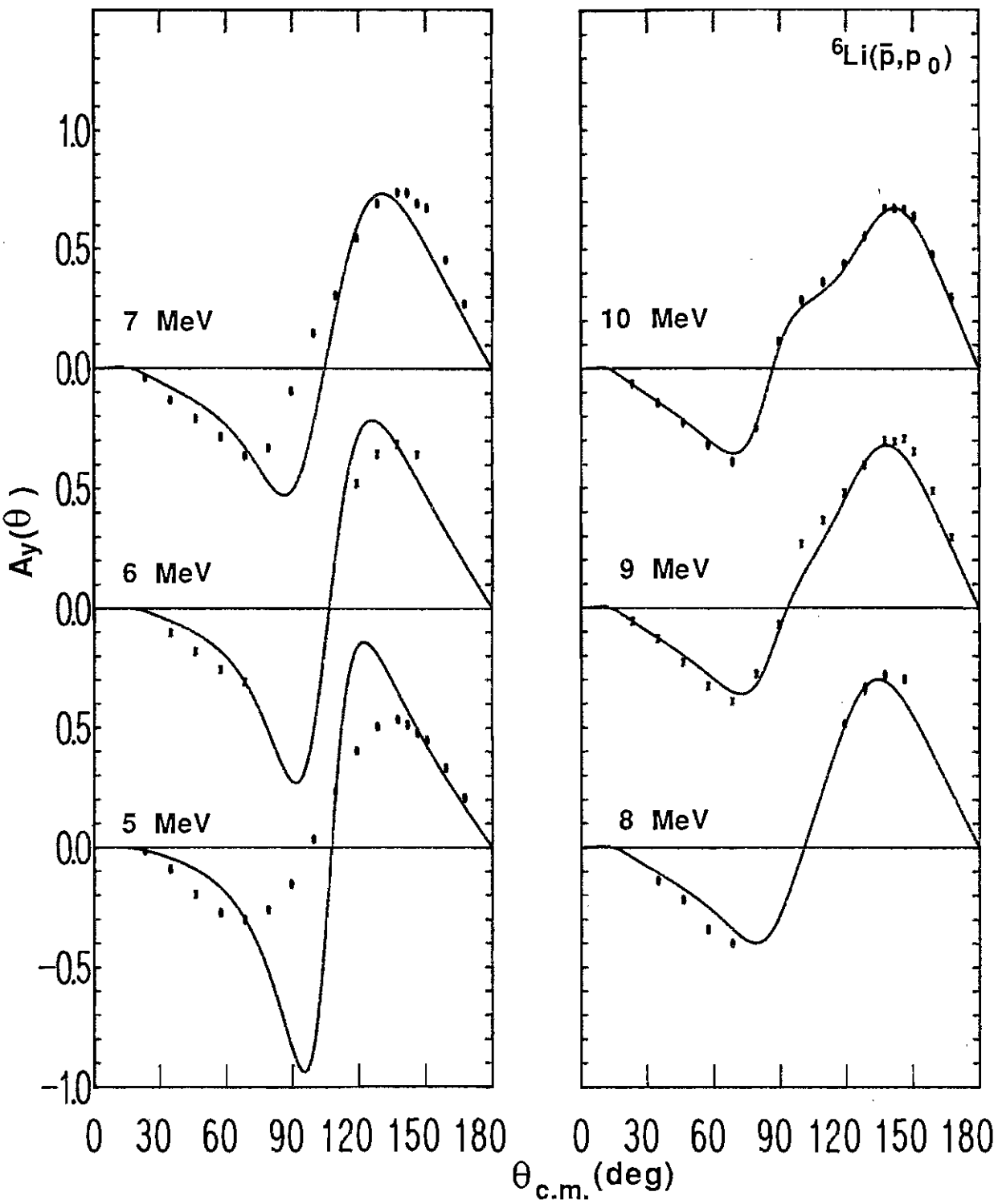

Fig. (4-12) Calculations of proton analyzing powers at 5 to 10 MeV for ^{6}Li based on the "n and p" optical model are shown with data.

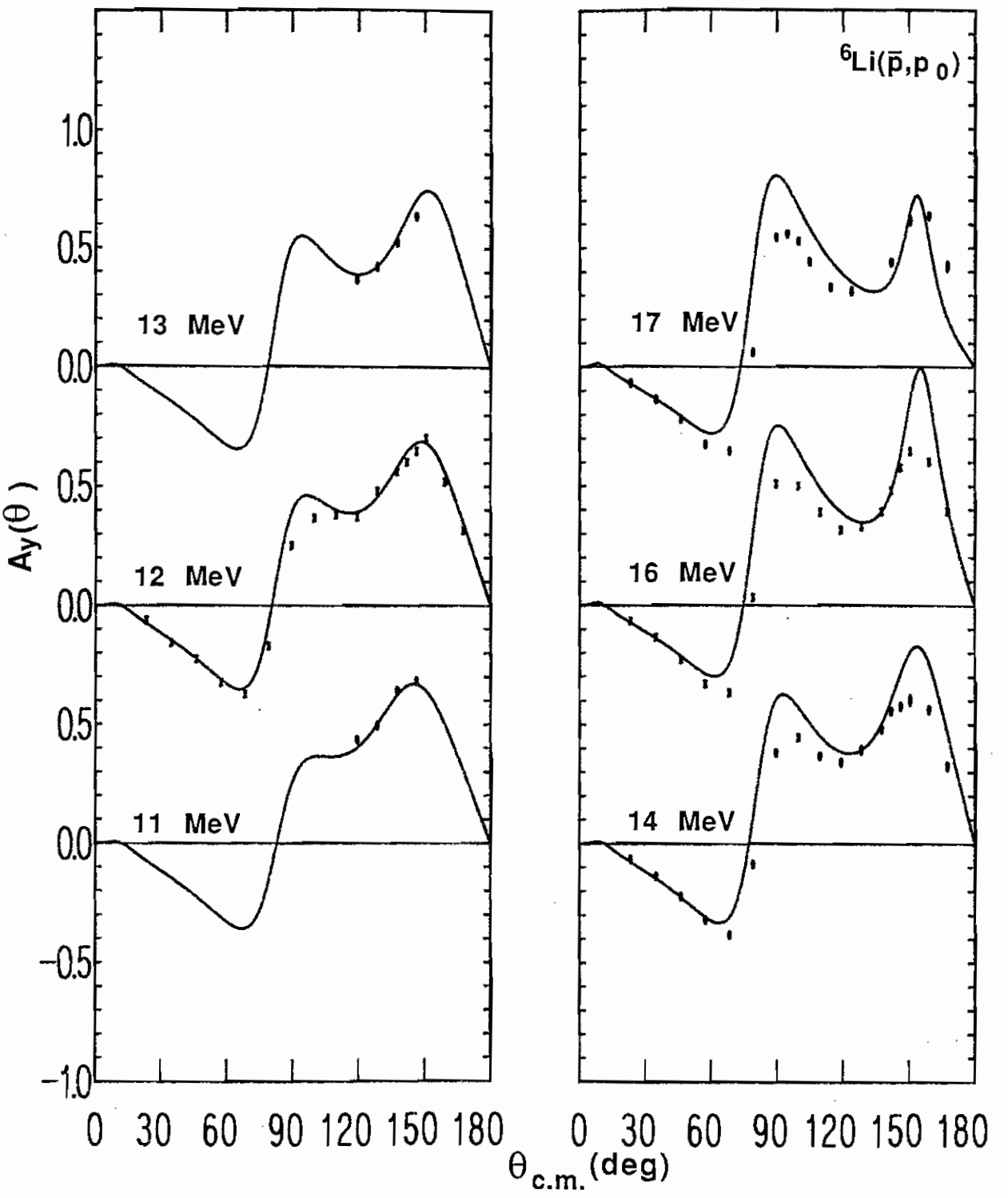

Fig. (4-13) Continuation of Fig. (4-12). Calculations of proton analyzing powers at 11 to 17 MeV for ^{6}Li based on the "n and p" optical model are shown with data.

A comparison of the present parameters to those from models in the literature for other light nuclei will indicate that many of the parameters exhibit a strong A dependence for low A. The Murphy model (Murphy 84) for $^{11}B(n,n_0)$ can serve as an example. The parameters for this model are listed in Table (4-1) along with the present parameter set. The spin-orbit diffuseness in Murphy's model is much smaller than ours, and the spin-orbit strength of Murphy is also somewhat smaller. The surface imaginary potential parameters are quite similar for the two models. The real central potential strength for ^{11}B is around 55 MeV at E_n = 10 MeV compared to a value of 42 MeV for the present ^6Li model. The value of r_R in Murphy's model is much lower than that for ^6Li giving rise to a much lower volume integral per nucleon for the real central potential J_V/A of ^{11}B. The volume integral per nucleon for the surface imaginary potential J_W/A for ^{11}B is also about half the value for ^6Li. The volume integrals for ^6Li are plotted in Fig. (4-3) for the present model, the global model of Davé, and the ^6Li model of Davé. These do agree reasonably well in terms of magnitudes but the differences in the energy dependences are readily evident.

Resonating Group Method Calculations for ^6Li

Introduction

At this point we depart from the spherical optical model and discuss one remaining model. This last model is singled out because early discussions with H. Hofmann stimulated us to measure data at the low energy end of our range at TUNL, a region which we usually avoid in our studies on heavier nuclei. This remaining model for describing the scattering is the cluster model or resonating group method. The method as first suggested by Wheeler in 1937 (Wheeler 37A and Wheeler 37B) was seen as the extension of a picture of a simple molecule in which the molecule was composed of several light and heavy groups. The heavy groups were the nuclei and the light groups were the

individual electrons. A nucleus can be viewed as composed of several fragments which in turn are clusters of nucleons. Naturally, a nucleus containing four or more nucleons has more than one set of clusters which can represent that nucleus. For example, an α-particle can be divided into two deuterons, a triton and proton, and a ^{3}He nucleus and neutron. In modern parlance, these different possible configurations are called channels. The wave function is then a linear combination of terms representing the different channels. The nucleus is said to "resonate" between these different configurations or channels. From this standpoint it is clear that the groups are not regarded as actually existing within the nucleus.

The resonating group approach has a number of characteristics which make it worth pursuing. In a general sense the method stands as a bridge between the shell model and the collective model. The shell model considers the individual nucleons in the nucleus and is able to predict the energy levels in the nucleus. The collective model stresses properties resulting from the coherent motion of nucleons in the nucleus. The resonating group method which looks at separate groups of nucleons acting coherently is able to predict energy levels of the nucleus, electromagnetic properties, scattering cross sections, and reaction cross sections.

A wave function may be written down as follows for the simple case of a nucleus which divides into two groups (Wong 75):

$$\psi = \mathcal{A}\left[\phi_1(x_1 - R_1)\ \phi_2(x_2 - R_2)\ f(R_1 - R_2)\right] \tag{4-22}$$

where x_1, x_2 = the sets of nucleon or single-particle coordinates within the clusters 1 and 2,

R_1, R_2 = the center of mass coordinates of the clusters 1 and 2,

$f(R_1 - R_2)$ = a wave function describing the relative motion between the clusters,

$\mathcal{A}$ = an antisymmetrization operator which ensures that the Pauli principle is not violated by the individual nucleons,

and ϕ_1, ϕ_2 = the internal wave function for the clusters.

A linear combination of these wave functions which allows for different two-cluster channels appears as

$$\Psi = \sum_c \mathcal{A}\left[\Phi_c\, f_c(r_c)\right] \tag{4-23}$$

where the index c stands for the different channels, $\Phi_c = \phi_{c1}\,\phi_{c2}$, and $r_c = R_{c1} - R_{c2}$.

The difficulty in the resonating group method comes in trying to determine the wave function Ψ (Wong 75, Wildermuth 77). Suitable wave functions such as the harmonic oscillator wave function may be chosen for the cluster internal wave functions ϕ. Calculation of the unknown functions $f_c(r_c)$ presents a major difficulty. Use of the variational principle $\delta E = 0$ in which the variation is applied to the functions $f_c(r_c)$ results in expressions for $f_c(r_c)$ which are in principle solvable.

Calculations of $A_y(\theta)$ and $\sigma(\theta)$

The present demonstration of the resonating group method is from the work of Hofmann *et al.* on the ^{7}Li and ^{7}Be systems (Hofmann 83, Hofmann 84). They have developed a code for the calculation of multi-channel resonating group wave functions from which they can calculate energy levels and phase shifts, and thereby scattering cross sections and analyzing powers. The channels included in the calculations for the ^{7}Li system were ^{6}Li + n, ^{4}He + ^{3}H, ^{5}He + d, and ^{6}He + p. Channels consisting of the ^{6}Li, ^{5}He, and ^{6}He clusters in excited states were also included. For the ^{7}Be system the ^{6}Li + p, ^{5}Li + d, and ^{4}He + ^{3}He channels were included as well as channels consisting of excited states of the ^{6}Li and ^{5}Li clusters.

Calculations of the analyzing powers and cross sections for proton and neutron elastic scattering from ^{6}Li were provided by Hofmann for the purpose of comparison to the data presented here. The proton scattering calculations obtained from consideration of the ^{7}Be system and the neutron scattering are obtained from the ^{7}Li system calculations. Figs. (4-14) through (4-17) show the calculations of $A_y(\theta)$ and $\sigma(\theta)$ at 7, 10, 14, and 17 MeV

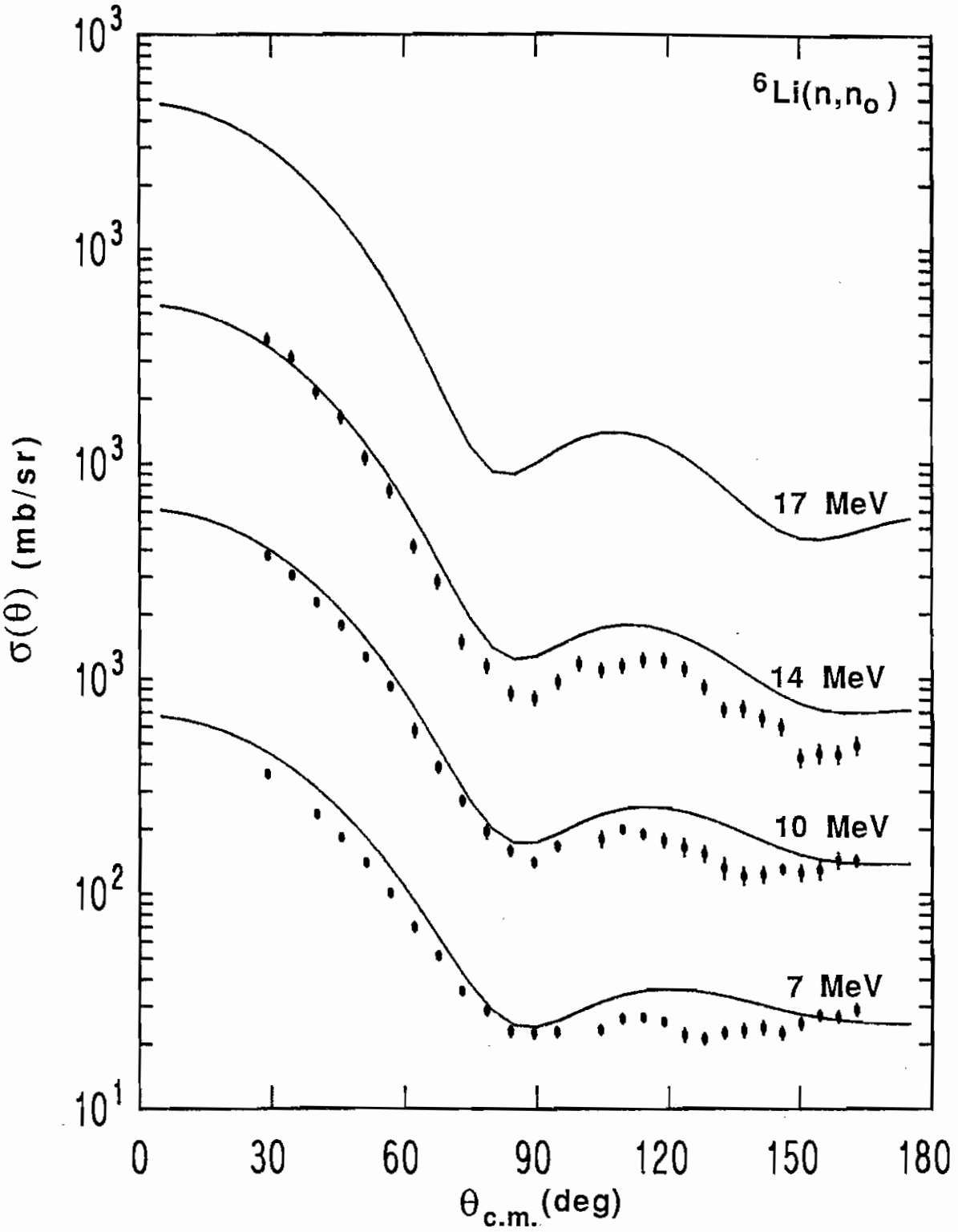

Fig. (4-14) Calculations of neutron elastic scattering cross sections for ^{6}Li based on the resonating group method shown along with the data. The data are from Hogue (Hogue 79).

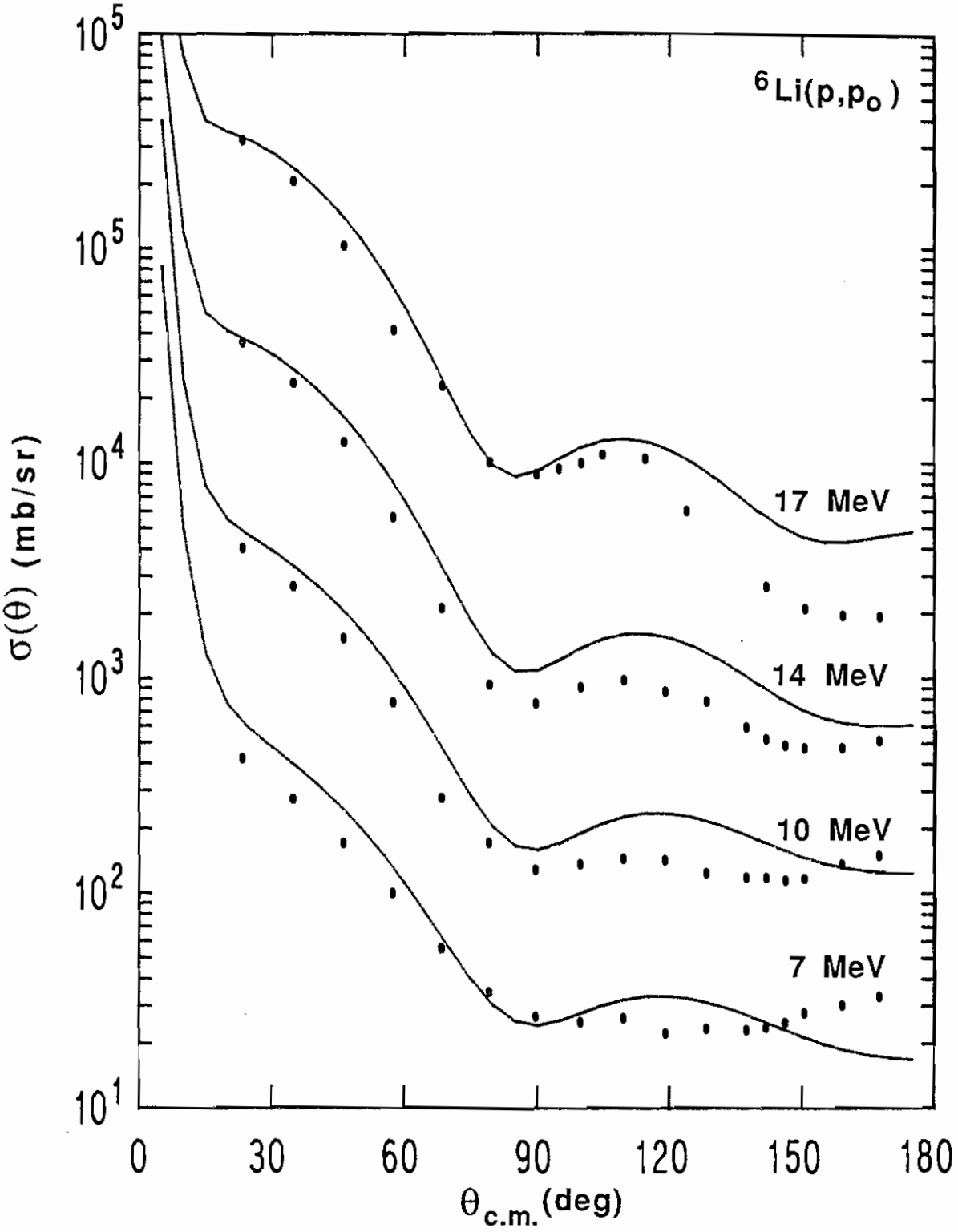

Fig. (4-15) Calculations of proton elastic scattering cross sections for ^{6}Li based on the resonating group method shown along with data.

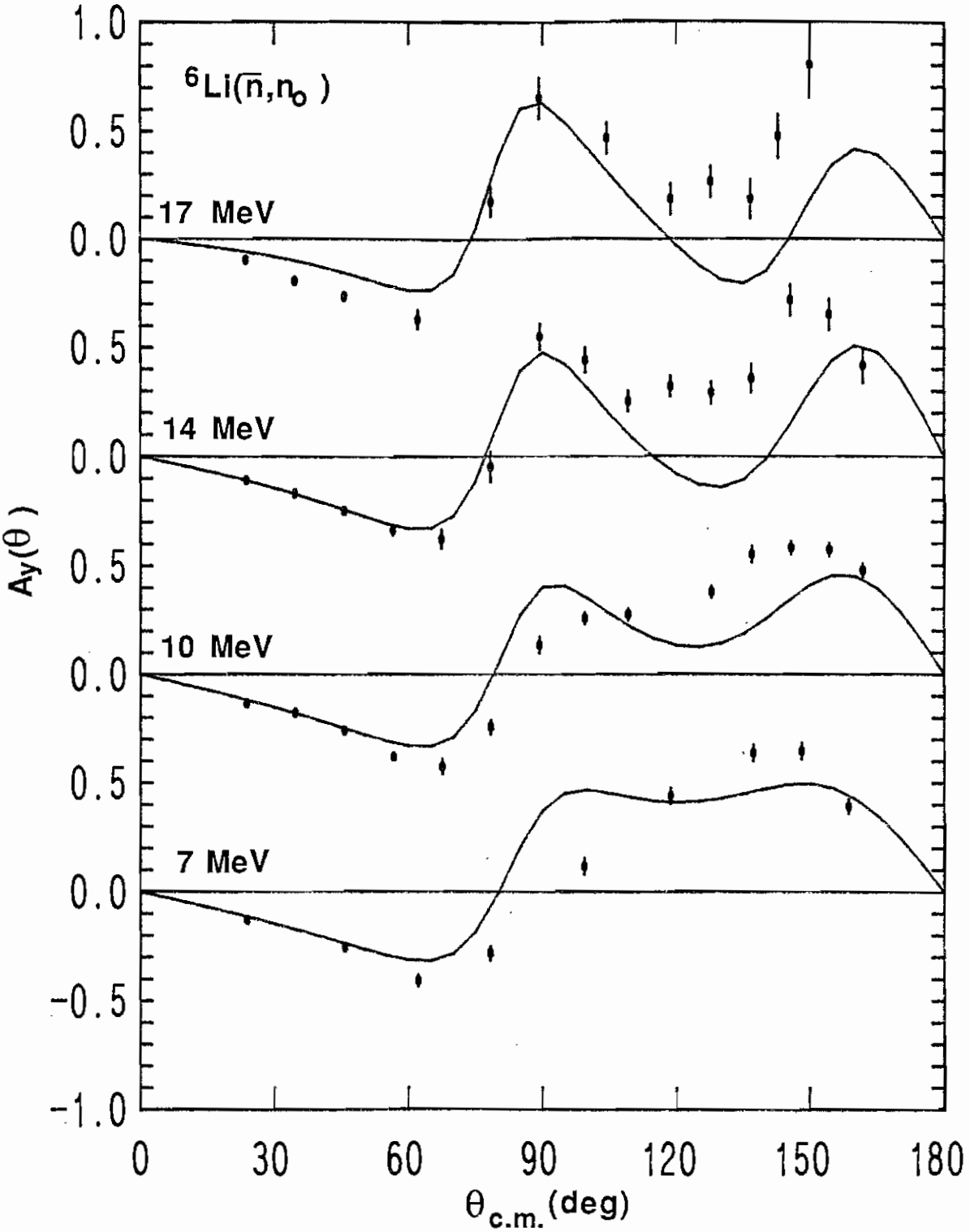

Fig. (4-16) Calculations of neutron elastic scattering analyzing powers for ^{6}Li based on the resonating group method shown along with the data.

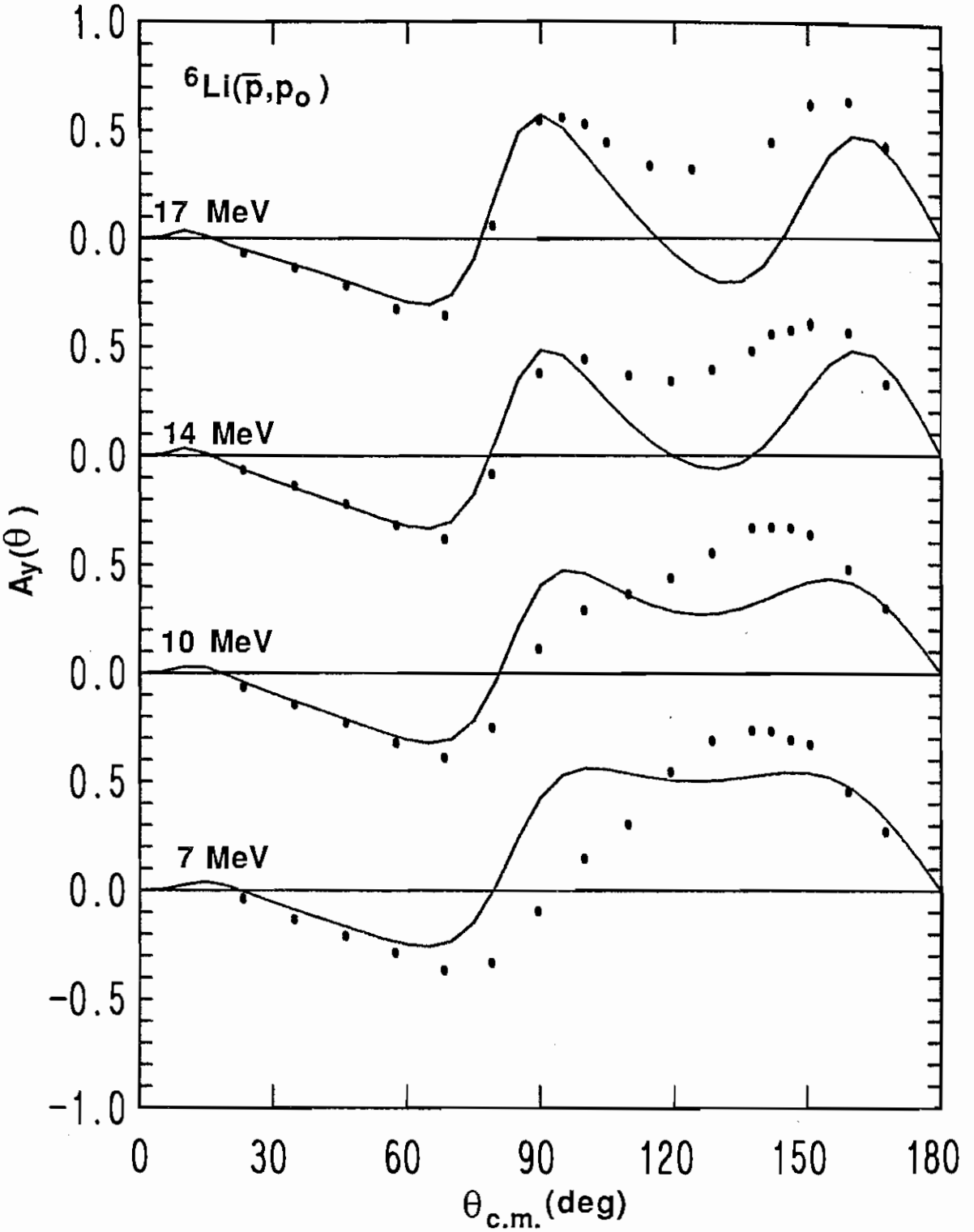

Fig. (4-17) Calculations of proton elastic scattering analyzing powers for ^{6}Li based on the resonating group method shown along with the data.

for proton and neutron elastic scattering along with the data. The cross-section data in Fig. (4-14) is that of Hogue (Hogue 79).

The calculations agree surprisingly well with the data considering that no variable parameters are allowed for, and that some of the excited states of the clusters might have wrong energies or quantum numbers assigned to them. The calculations of $A_y(\theta)$ reveal the emergence of the second hump around 100^o at an energy which is too low. This is the result of a root-mean-square radius for ^{6}Li used in the calculation which is too large. A later recalculation using the correct r.m.s. radius (discussed in Pfützner 86) eliminates this second hump at low energies.

Conclusions Drawn from ^{6}Li Resonating Group Calculations

A comparison of the fits from the optical model analysis to the resonating group predictions indicates that the resonating group method has considerable merit. The resonating group predictions at low energies better represent the data than do the poor optical model fits at low energies. Certainly, at the low energies the resonating group method is superior. At the higher energies, including 17 MeV, the predictions are respectable; perhaps further development of the calculations such as the inclusion of additional channels (for example additional excited states for some clusters) may produce predictions of comparable quality to the optical model fits.

Spherical Optical Model Analysis for Proton and Neutron Scattering from ^{27}Al

The intent of the optical model analysis for ^{27}Al was to extend the work of Martin *et al.* (Martin 86) to energies below 11 MeV. Fitting to the additional proton scattering data obtained here at higher energies would also ensure that the final parameter set arrived at gives the optimal description of the data in the range of 11 to 17 MeV.

One of the more recent analyses has been performed for ^{27}Al by Roy *et al.* (Roy 83). This analysis only included the proton scattering data obtained by that group, that is

for energies from 13 to 25 MeV. The optical model potential consisted of real central, volume imaginary, surface imaginary, and real spin-orbit terms. The single-energy fits of Roy are no better and in some cases worse than the global fits of Martin and Walter, which cover a larger energy range. These two earlier works, however, do indicate that satisfying results can be obtained for ^{27}Al with the spherical optical model, and therefore an attempt at improving the fits and the data base, and extending the energy range of the analysis is easily justified.

Several sets of data were included in the present optical model searches. The proton data included the $\sigma(\theta)$ and $A_y(\theta)$ elastic scattering data of the present work ranging from 5 to 17 MeV (excluding 15 MeV, where data were not obtained at TUNL). Full angular distributions of cross-section and analyzing power data available from Roy at 15, 19, and 23 MeV were also used. The neutron cross-section data at 11, 14, and 17 MeV of Whisnant *et al.* (Whisnant 84) was used along with the analyzing power data of Martin and Walter (Martin 86) at 14 and 17 MeV.

The starting values of the optical model parameters are given in Table (4-2) under the heading of "Martin-Walter parameters". These values are the global neutron and proton parameter set appearing in the publication of Martin and Walter (Martin 86); in this previous analysis, it was not necessary to include a volume absorption term, although it is expected that such a term will become more significant when the incident nucleon energy exceeds 20 MeV. In the present analysis as in the previous, real central, surface imaginary, and real spin-orbit potentials were included and the real central and surface imaginary potentials had asymmetry terms V_{1R} and W_{1D} which were kept fixed at the Martin-Walter values during the early part of the analysis. There was also a Coulonb correction term ΔV_c in the real central potential for proton scattering where b_c was kept fixed at 0.45 MeV during this analysis. Values for b_c in the 0.4 to 0.5 MeV range are common from analyses for nuclei heavier than ^{27}Al. Linear energy dependences in the

real central and surface imaginary potential depths were also allowed.

The approach taken in determining a suitable parameter set for neutron and proton elastic scattering data was similar to that used for the ^{6}Li data. The proton data were considered first, separate from the neutron data. A simultaneous search was performed on V_{oR}, α_R, r_R, W_{oD}, α_D, and a_D. The most significant result of this search was to reduce α_D to zero. In addition, the magnitude of W_{oD} dropped while V_{oR} increased somewhat. The other three parameters changed by only small amounts. This rather simple change resulted in significant improvements in all of the fits to both cross-section and analyzing power data. Improvements were particularly noticeable in the back-angle region.

Using this new parameter set as the next starting values, single-energy searches of the proton data were performed on W_{oD} and V_{oR}. These searches verified the need for aW_{oD} lower than that obtained by Martin and Walter. Unfortunately though, there was a surprisingly large amount of fluctuation in the values obtained at different energies for the two parameters. This can be attributed to an ambiguity which results from searching on W_{oD} and V_{oR} simultaneously. A similar problem in searching on the ^{6}Li data was encountered and mentioned in the section on the ^{6}Li proton analysis. The problem is most noticeable in cases where chi-squared is large. Subsequent searches on W_{oD} alone when V_{oR} was given a linear energy dependence revealed a more stable set of values.

A cursory test was done to check on the usefulness of a volume imaginary term W_V. A value of 5 MeV was assigned to W_V with $r_V = r_R$ and $a_V = a_R$ and with all other parameters left at the values obtained earlier. The fits to the cross-section data were not improved at all; the extra absorption term resulted in lower predictions for the cross-section. Improvements in the fits to the analyzing power data in the back-angle region at 5, 6, and 7 MeV were noted. Worsening of the fits to the analyzing power data at other energies suggested that pursuing the matter of a non-zero W_V term might not be fruitful. However, it is possible that a lower W_D term at higher energies to compensate for

the W_V may give better fits, but this was not attempted at the present time.

The second phase in the ^{27}Al analysis was to add the neutron data at 11, 14, and 17 MeV to form a global data set for nucleon scattering from ^{27}Al. The weighting of all the $\sigma(\theta)$ and $A_y(\theta)$ data at 9 MeV and below was reduced. This was done because the fits at low energies were generally poor. Reduced weight allowed the search routine to concentrate on improving fits at the higher energies where the model is more likely to be valid. Predictions for neutron scattering obtained with the parameter set derived for the proton data were unsatisfactory fits at all energies. The predicted cross sections were consistently higher than the data at angles greater than 40°. Clearly a larger W_D was needed for the neutron data but a larger W_D would destroy fits to the proton data. The asymmetry term εW_{1D} causes the total absorption potential to be greater for proton scattering than for neutron scattering. Setting W_{1D} equal to zero and increasing W_{oD} so that the total absorption strength is equal to its original value for the proton case has the desired effect of increasing W_D for neutrons only. A value for W_D of about 9 MeV was settled on, which is in contrast to values of W_D for heavier nuclei that are typically around 16 MeV. This step significantly improved the fits to the cross-section data without affecting the fits to the proton data at all. Fortunately the fits to the neutron analyzing power data were of comparable quality to the fits with W_{1D} not equal to zero.

After noting the improvement of the fits to the neutron data resulting from eliminating the asymmetry term in the imaginary surface potential, it was decided to do a global search on V_{oR} and V_{1R}. This search resulted in a much lower value for the asymmetry term in the real central potential, εV_{1R}. The search code simultaneously arrived at a larger value for V_{oR} . The new values of V_{oR} and V_{1R} had a compensating effect for the proton case so that the values of the total real central potential V_R for protons before and after this search were essentially the same. The new values of V_{oR} and V_{1R} resulted in a value of V_R for neutrons which was larger. These combined changes produced small

improvements to the fits to the neutron data and left the fits to the proton data unchanged. A value of V_{IR} in the range of 10 to 22 MeV is suitable for fitting the data. This is consistent with values of the asymmetry term for heavier nuclei which are typically between 20 and 24 MeV (Rapaport 82).

Final global searches were performed on the remaining parameters. Searches on several parameters at a time were performed in the order and in the groupings indicated: (V_{so}, r_{so}, a_{so}), (r_D, a_D), (r_R, a_R), (V_{oR}, α_R). These searches produced only small changes in the parameters and did not significantly affect the fits to the data.

Conclusions Drawn from ^{27}Al Optical Model Analysis

The parameters obtained in this analysis produce a reasonable representation of the proton scattering data above 10 MeV as can be seen from Figs. (4-22), (4-23), (4-26), and (4-27). They also produce acceptable fits to the neutron cross-section and analyzing power data as is evident from Figs. (4-24) and (4-28). The fits to the data at 10 MeV and below are of poorer quality [see Figs. (4-21) and (4-25)]. As in the case of ^{6}Li, it is apparent that compound nucleus and resonance effects are present in the low energy data which cannot be reproduced by the model. From Figs. (4-19) and (4-20) one can see that the present calculations compare favorably with the predictions of Martin and Walter. At back angles a noticeable improvement over the earlier model is evident. The magnitudes of the cross sections and analyzing powers in the back-angle region are better reproduced by the present model as is the shape of the analyzing power angular distribution in this same region. Both parameter sets give a prediction for the 11 MeV neutron analyzing powers at forward angles [see Fig. (4-28)] which one would not expect on the basis of comparison to the higher energy data. A sharp positive peak appears in the angular distribution at forward angles whereas the higher energy data and calculations show a distinct negative peak. It would certainly be interesting to measure the neutron analyzing powers at 11 MeV and at nearby energies to either verify or discount this prediction.

The parameter sets from the present model and from the Martin and Walter model are given in Table (4-2). The two parameter sets are similar in many respects. The geometry parameters for all three potentials are largely the same for the two models. The spin-orbit strengths are also the same. The major differences occur in the asymmetry terms in V_R and W_D. The fits to the additional proton data, which did not exist at the time of the earlier analysis, were greatly improved when W_{1D} was set to zero. The fits were improved slightly by a smaller V_{1R} as well. The energy dependence term in W_{oD}, α_D, searched to a value of zero and W_{oD} itself searched to a lower value. The present model in most cases fits equally well the data used in the earlier Martin and Walter analysis. In some cases, improvements were obtained. The present model however represents a large body of proton scattering data with reasonable quality fits which the previous model did not.

TABLE (4-2)

^{27}Al OPTICAL MODEL PARAMETERS

	Martin and Walter ^{27}Al model	^{27}Al Optimized n and p set
V_{oR}	53.5	55.337
α_R	0.32	0.412
r_R	1.19	1.187
a_R	0.64	0.669
V_{1R}	22.4	14.664
b_c	0.45	0.45
W_{oD}	11.5	9.204
α_D	0.23	--
r_D	1.29	1.337
a_D	0.54	0.388
W_{1D}	15.7	--
V_{so}	5.6	5.495
r_{so}	1.03	0.994
a_{so}	0.36	0.441

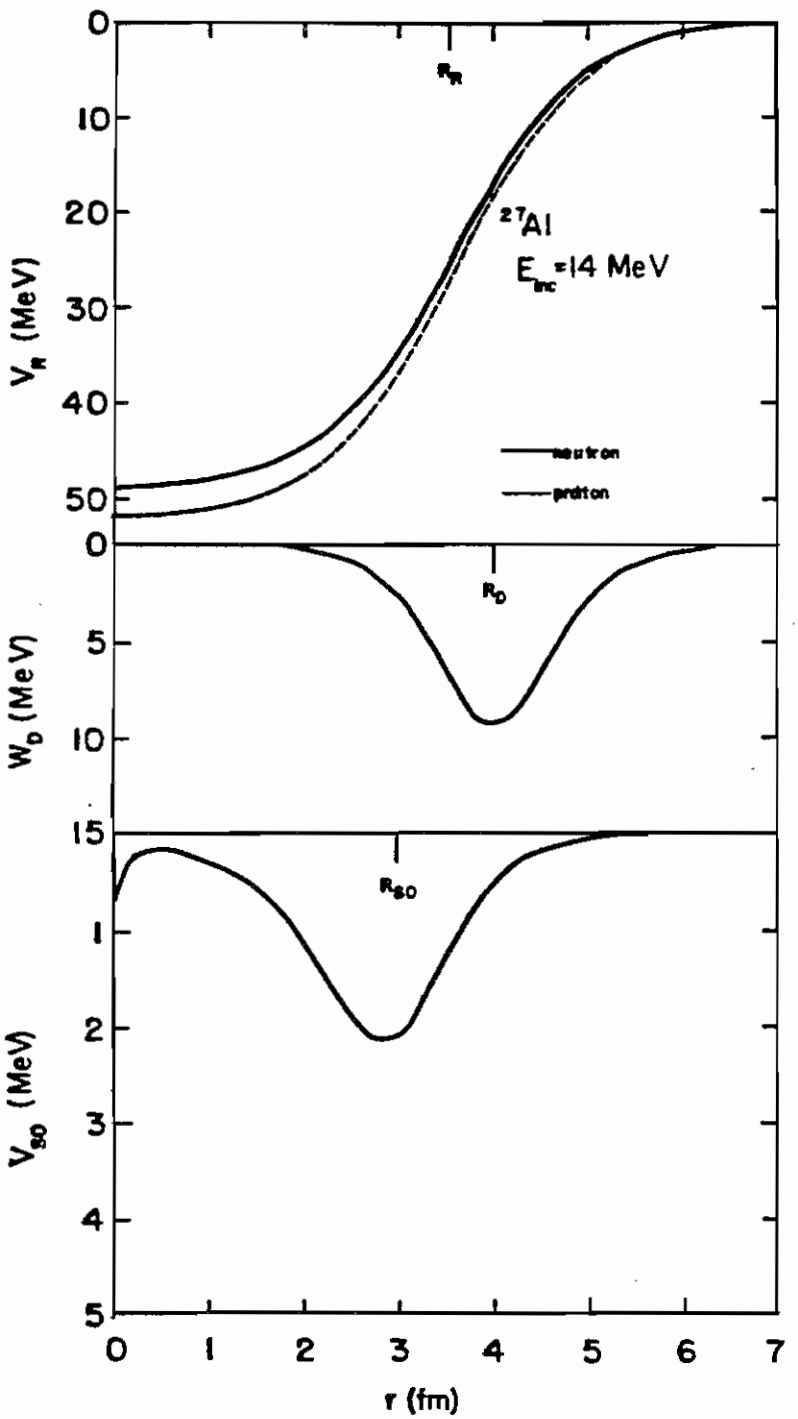

Fig. (4-18) The real central, surface imaginary, and spin-orbit potentials for ^{27}Al are shown as a function of nuclear radius at 14 MeV incident energy. V_{so} /($\sigma \cdot \ell$) is plotted for the spin-orbit potential.

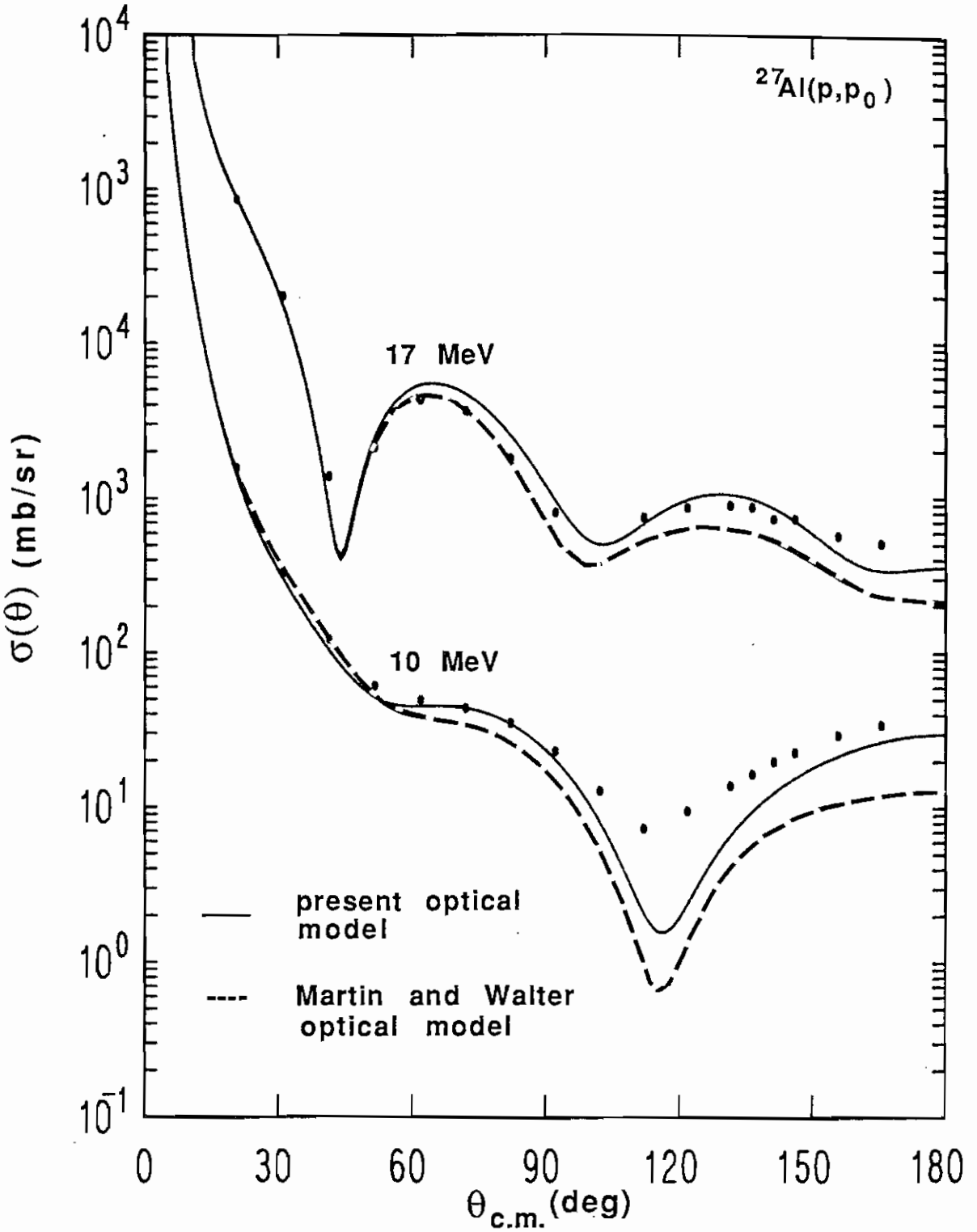

Fig. (4-19) Calculations of proton elastic scattering cross sections for ^{27}Al based on the present optical model and on the Martin and Walter model are shown with the data at 10 and 17 MeV.

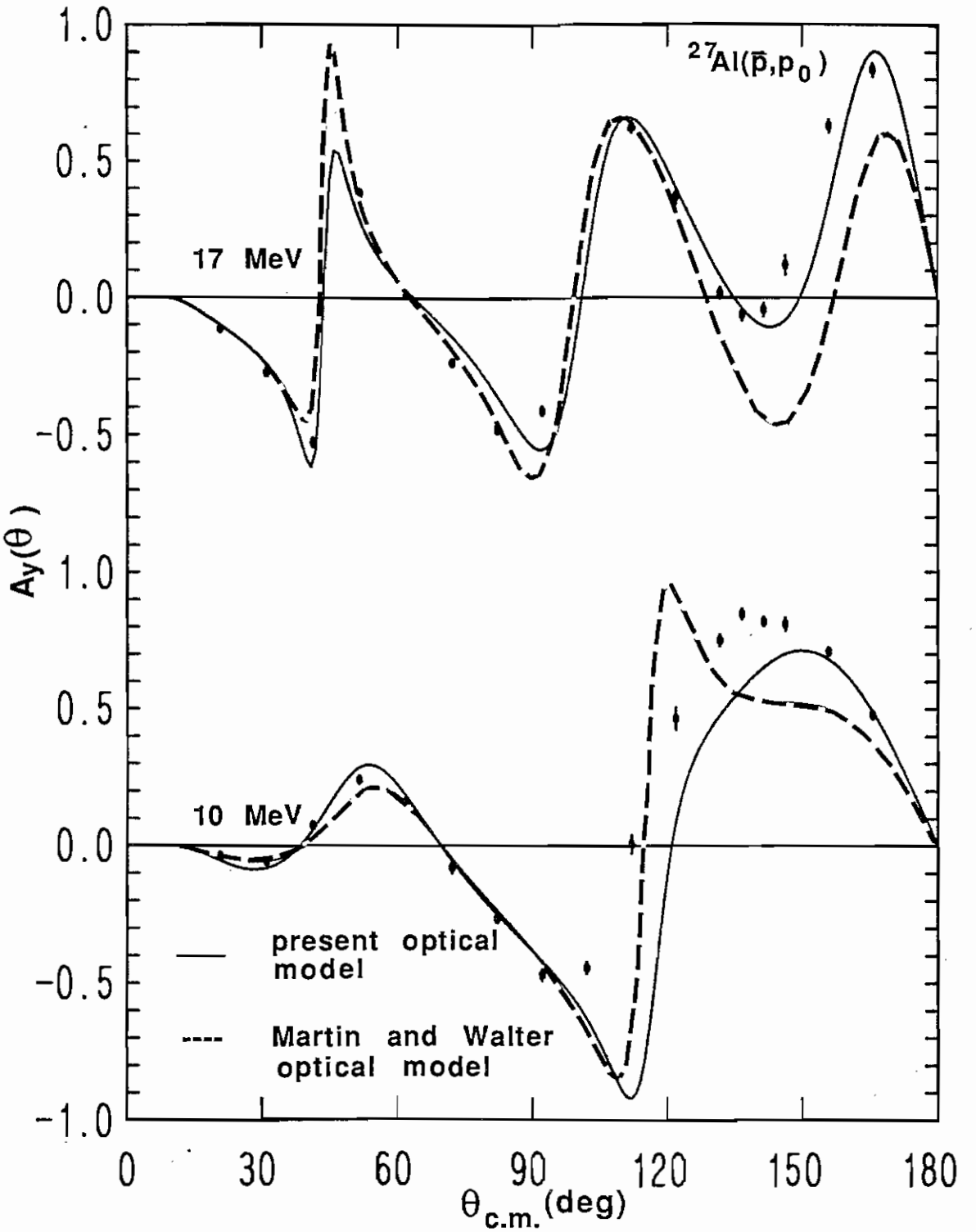

Fig. (4-20) Calculations of proton elastic scattering analyzing powers for ^{27}Al based on the present optical model and on the Martin and Walter model are shown with the data at 10 and 17 MeV.

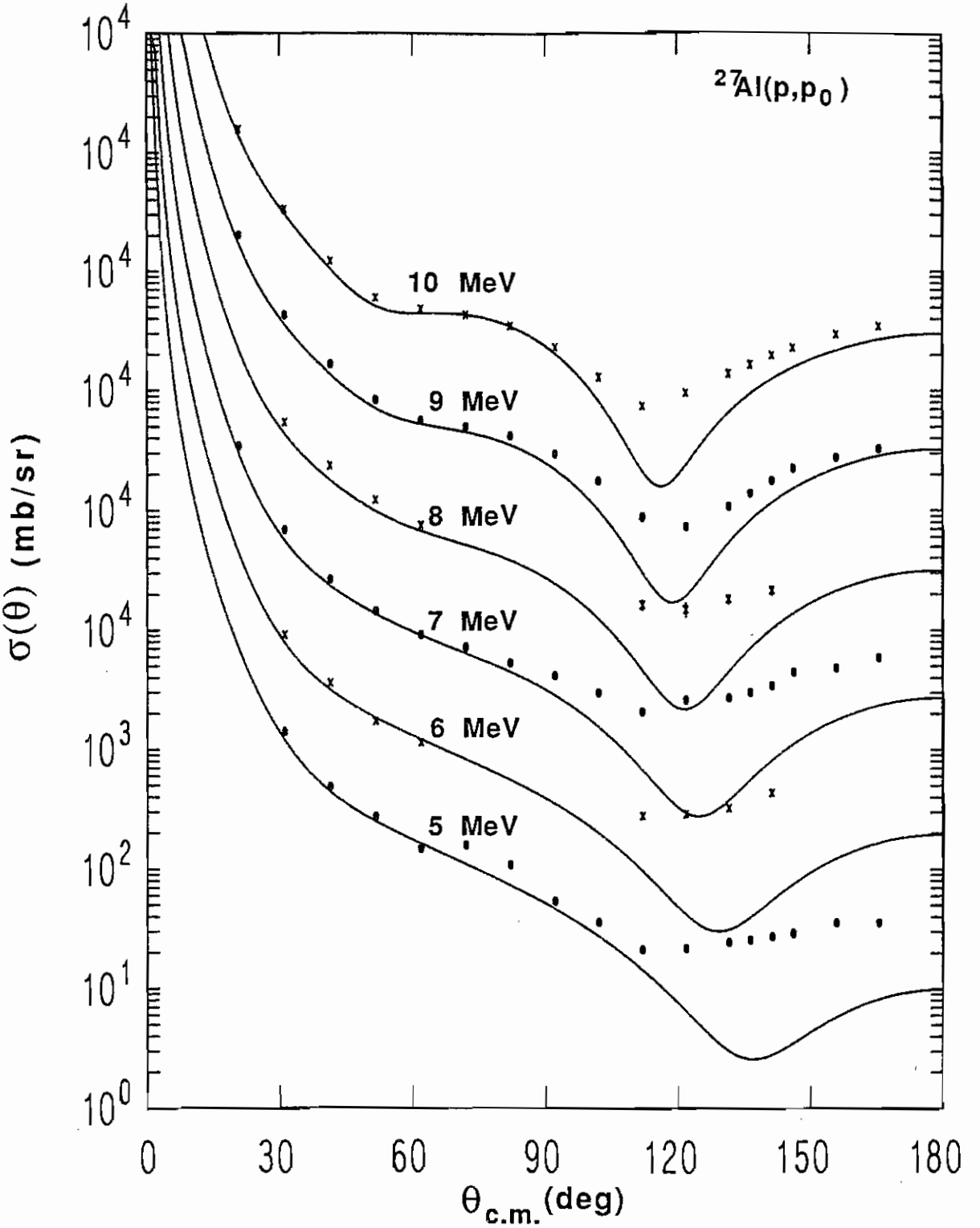

Fig. (4-21) Calculations of proton elastic scattering cross sections for ^{27}Al at 5 to 10 MeV based on the present optical model are shown with the data.

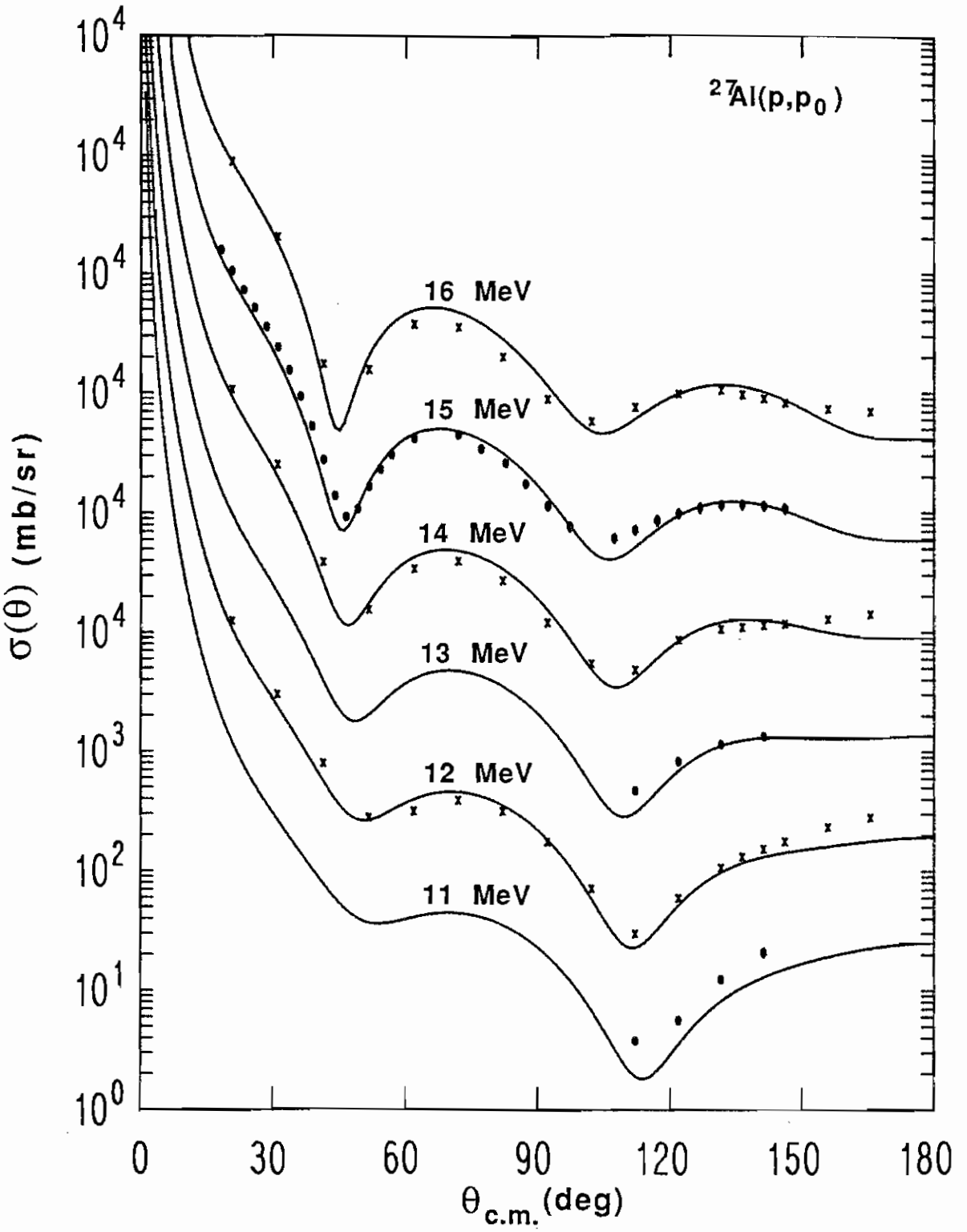

Fig. (4-22) Continuation of Fig. (4-21). Calculations of proton elastic scattering cross sections for ^{27}Al at 11 to 16 MeV based on the present optical model are shown with the data. The 15 MeV data are from Roy (Roy 83).

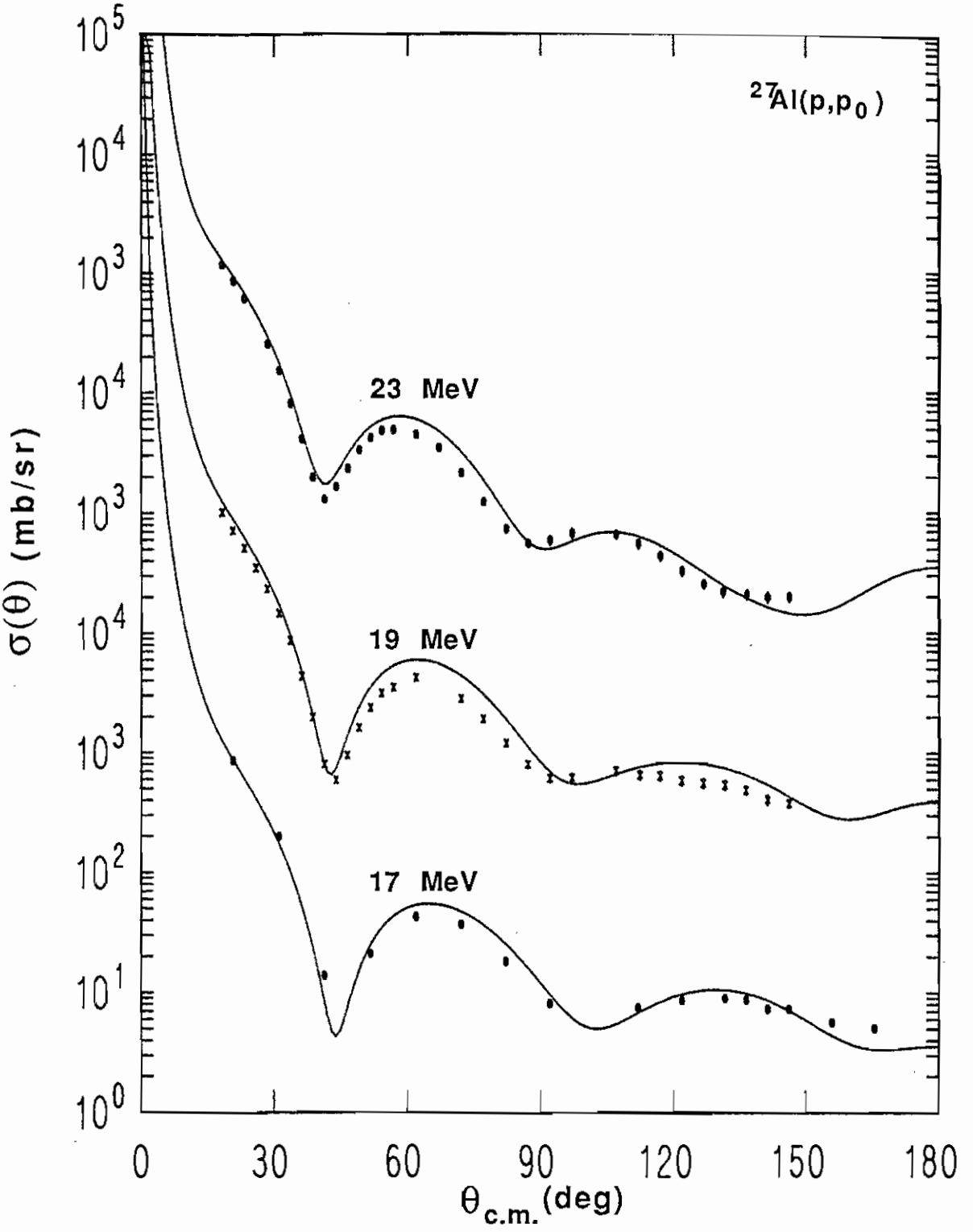

Fig. (4-23) Continuation of Fig. (4-21). Calculations of proton elastic scattering cross sections for ^{27}Al at 17, 19, and 23 MeV based on the present optical model are shown with the data. The 19 and 23 MeV data are from Roy (Roy 83).

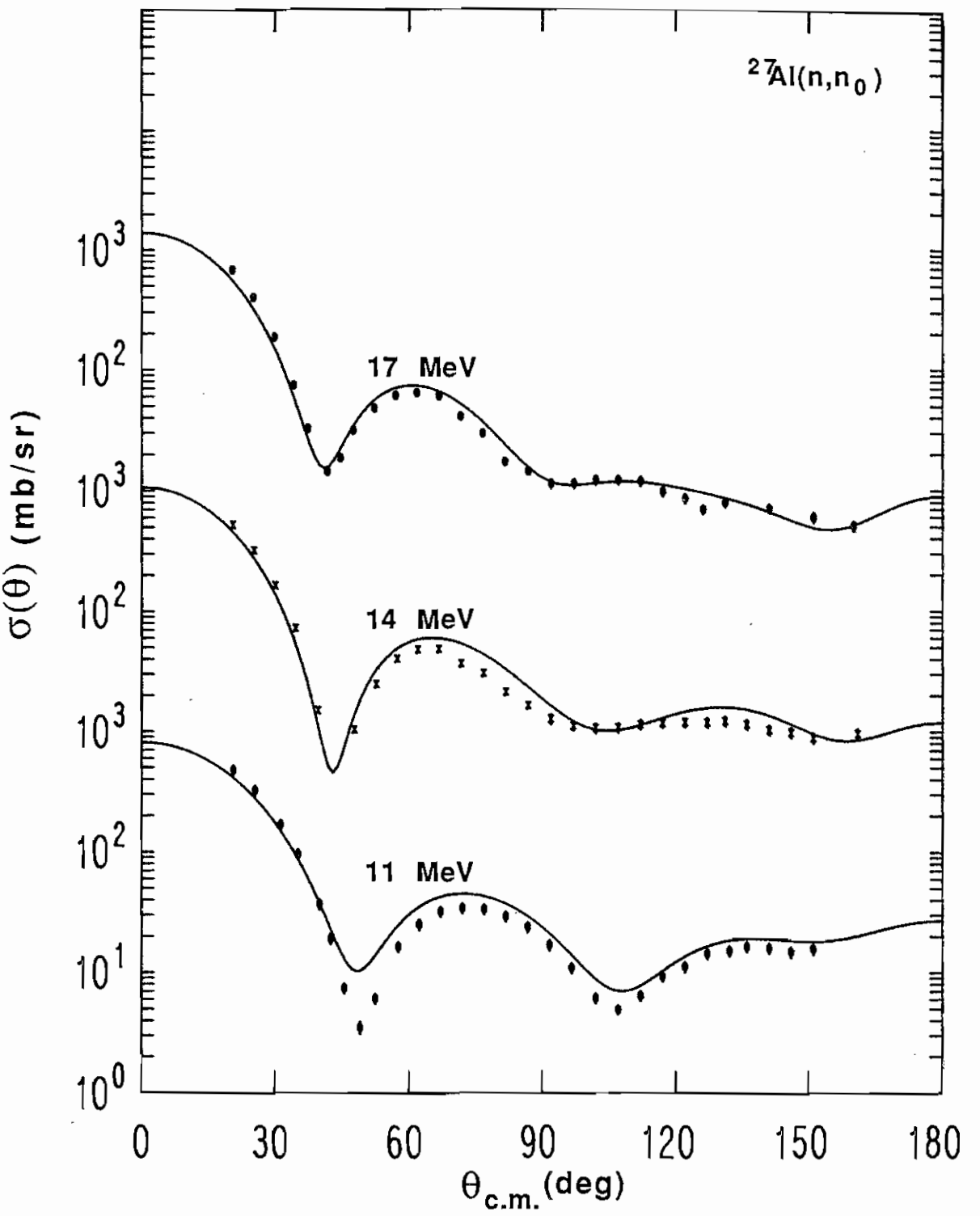

Fig. (4-24) Calculations of neutron elastic scattering cross sections for ^{27}Al at 11, 14, and 17 MeV based on the present optical model are shown with the data. The data are from Whisnant (Whisnant 84).

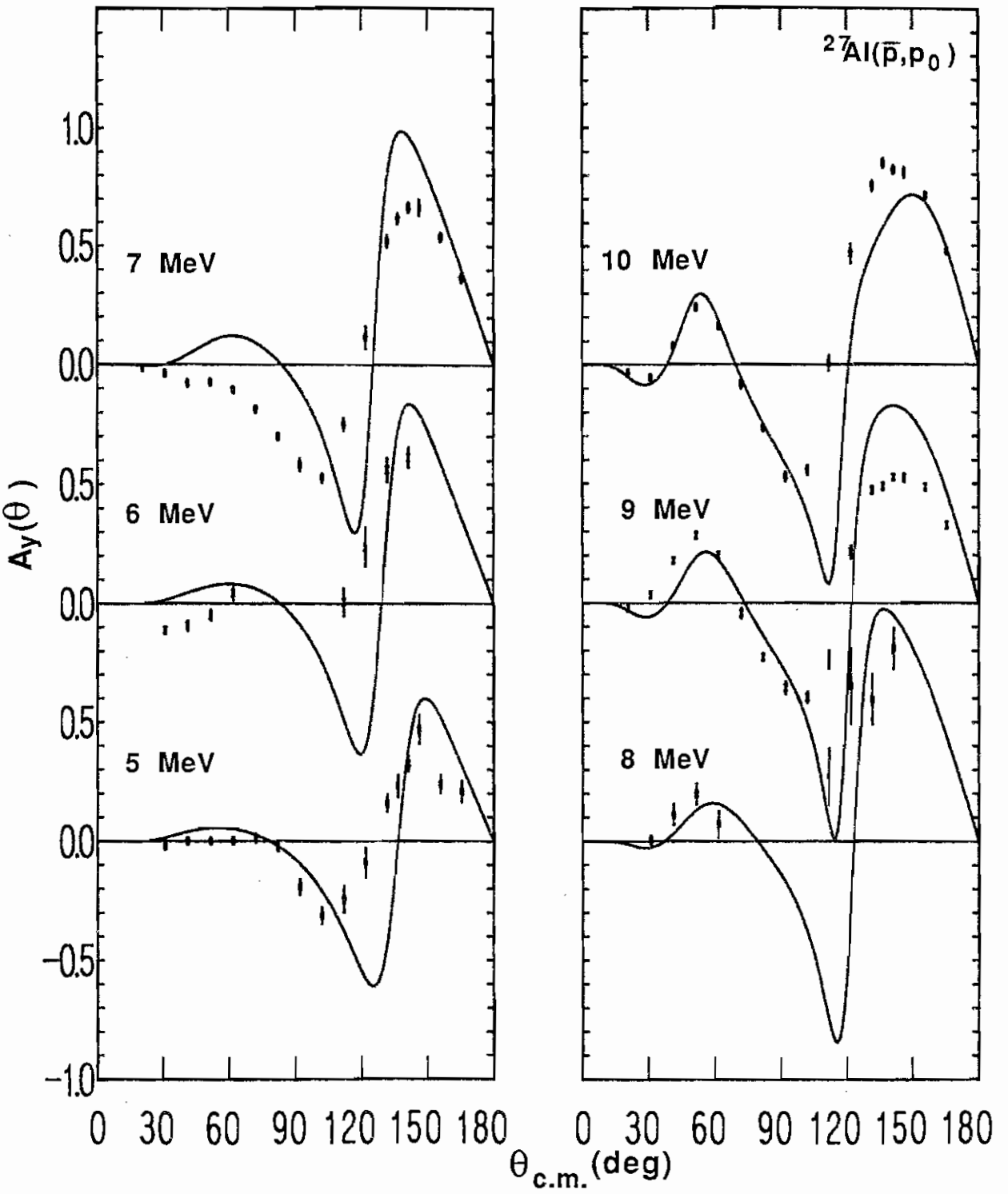

Fig. (4-25) Calculations of proton elastic scattering analyzing powers for ^{27}Al at 5 to 10 MeV based on the present optical model are shown with the data.

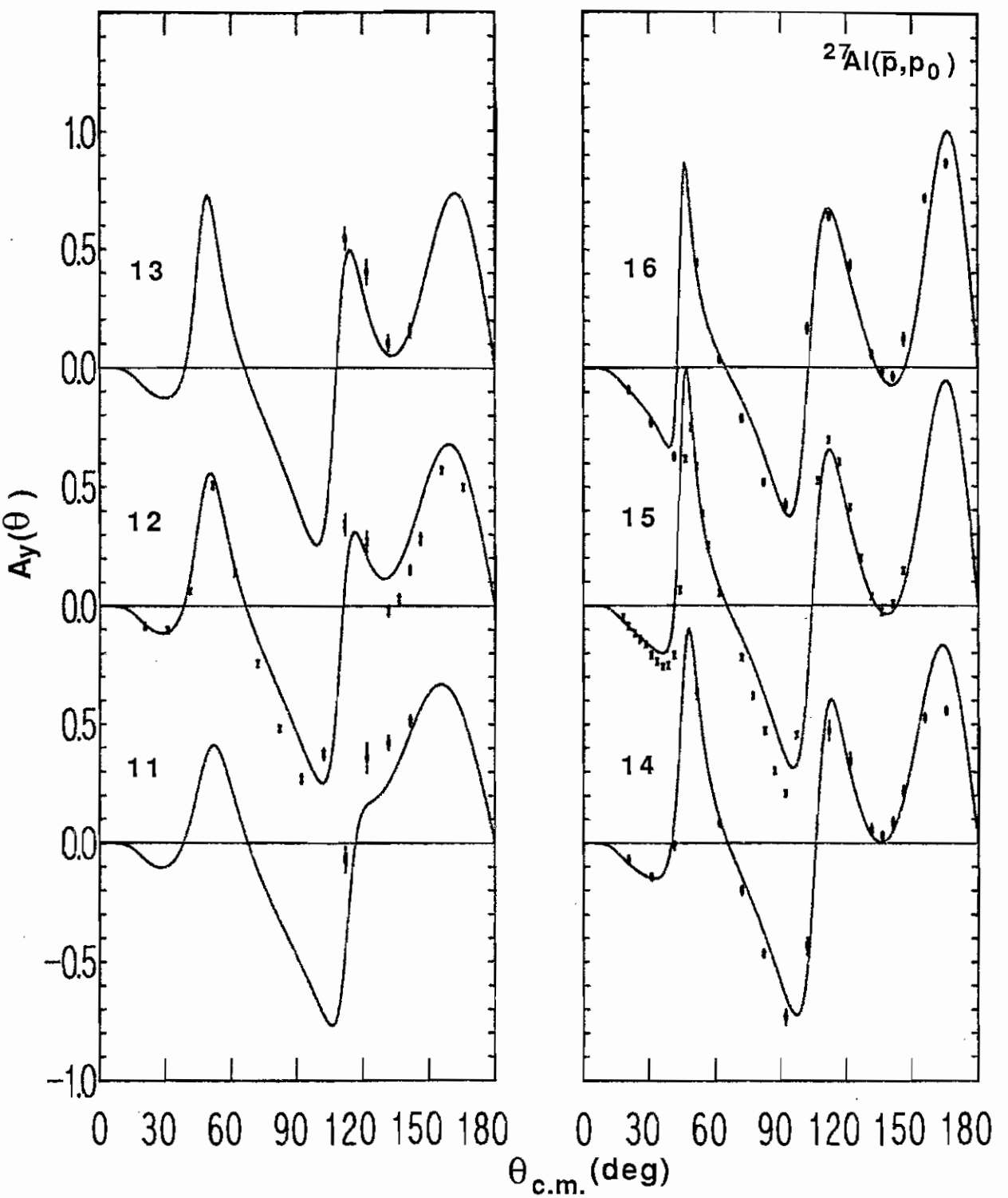

Fig. (4-26) Continuation of Fig. (4-25). Calculations of proton elastic scattering analyzing powers for ^{27}Al at 11 to 16 MeV based on the present optical model are shown with the data. The 15 MeV data are from Roy (Roy 83).

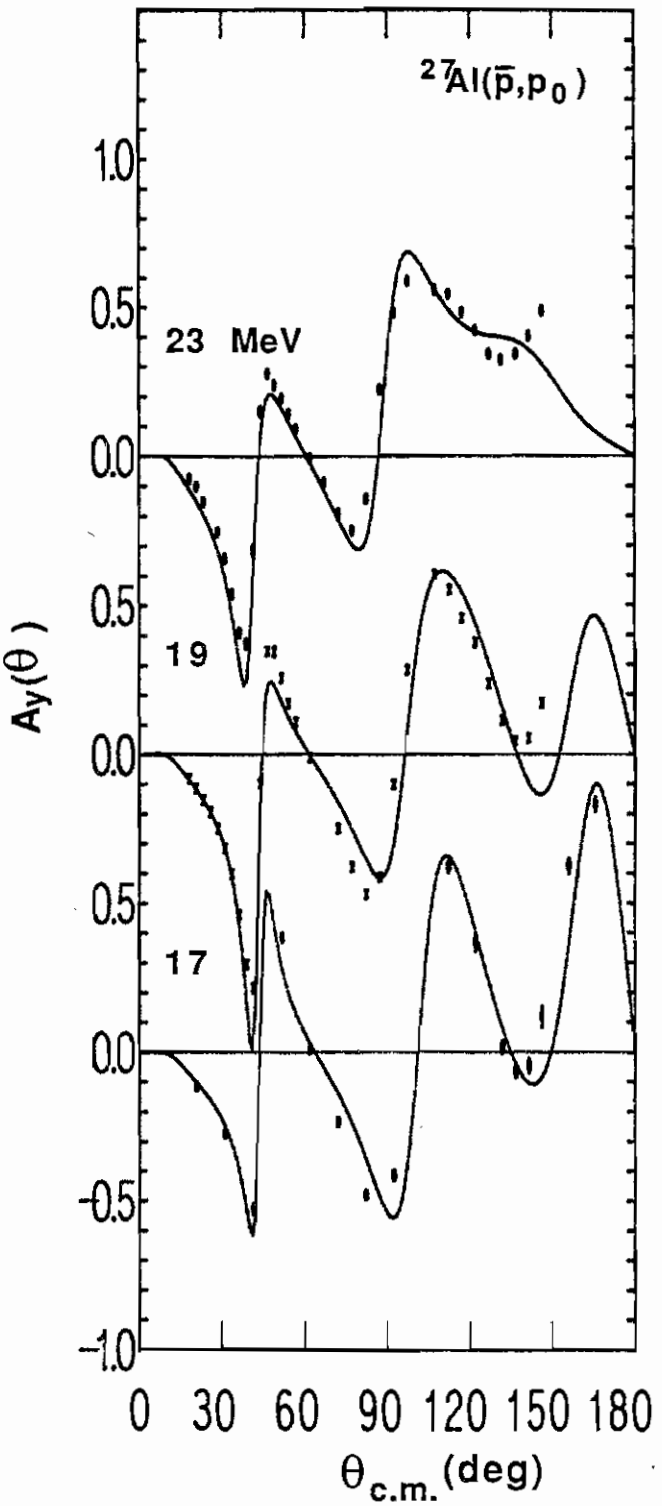

Fig. (4-27) Continuation of Fig. (4-25). Calculations of proton elastic scattering analyzing powers for ^{27}Al at 17, 19, and 23 MeV based on the present optical model are shown with the data. The 19 and 23 MeV data are from Roy (Roy 83).

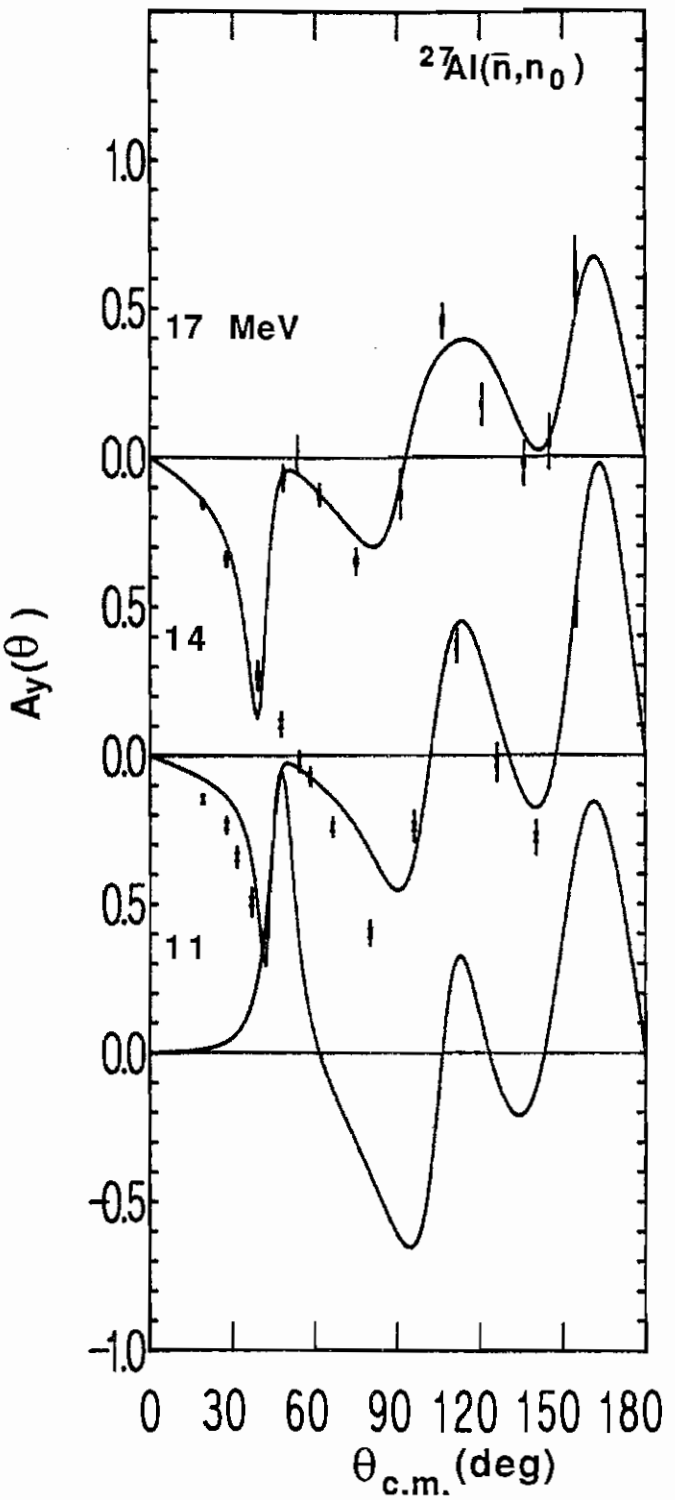

Fig. (4-28) Calculations of neutron elastic scattering analyzing powers for ^{27}Al at 11, 14, and 17 MeV based on the present optical model are shown with the data. The 14 and 17 MeV data are from Martin (Martin 86).

CHAPTER 5

SUMMARY AND CONCLUSIONS

Attempts have been made previously by others to extend the optical model into the region of light nuclei. For the case of ^{6}Li these attempts have been limited to fitting only cross-section data, since there was a notable lack of analyzing power data. There have also been efforts under way to provide other models which could perhaps be more suitable for nucleon scattering from light nuclei. A thorough data base of observables for nucleon scattering from ^{6}Li is necessary for proper testing and development of these optical models and other models. To provide this information we have measured neutron and proton elastic and inelastic scattering analyzing powers in the range from 5 to 17 MeV. Proton elastic and inelastic scattering cross sections have also been measured in the same energy range. The neutron scattering data were obtained with the time-of-flight spectrometer at TUNL using the two detector spin-flip method. Corrections were applied to account for multiple scattering and finite geometry effects. In addition corrections were made to the forward angle data for the effects of nitrogen and oxygen contaminants in the scattering sample. The proton data were obtained with silicon surface-barrier detectors also using the two detector spin-flip method. The proton cross-section data were derived from the analyzing power data by appropriately summing the yields for the left and right detectors, for the spin up and down conditions.

A new optical model was developed to provide a parametrization which best describes the neutron and proton scattering observables in the 5 to 17 MeV energy range. The earlier optical model parametrization for ^{6}Li by Davé, which was derived from only cross-section data in the range of 8 to 14 MeV, was used as the starting set for the present analysis. In fact, Davé's parametrization was a result of a larger optical model study of many of the 1-p shell nuclei.

Our optical model potential, following the pattern of Davé, included a real central potential, a surface imaginary potential, and a real spin-orbit potential. No isovector term is required since N = Z for ^{6}Li. The real central and surface imaginary potential strengths both had linear energy dependences in the early stages of our search process.

The present analysis was broken into three phases; the first a separate optical model analysis of the neutron scattering data, the second a separate analysis of the proton scattering data, and the third an analysis in which the neutron and proton scattering data made up a single global data set. The first phase of the analysis resulted in a model which fit the analyzing power data significantly better than Davé's model at energies above 9 MeV. The quality of the fits to the cross-section data are comparable for our first-phase model and Davé's model, although it should be remembered that the present model has been fit to data in a wider energy range and has been constrained by the analyzing power observable. The quality of the fits below 9 MeV is unsatisfactory for both models.

In the second phase of the analysis proton scattering data were fit with the optical model. Again Davé's model provided the starting parameter set. The same deficiencies in the fits at low energies appear and comparably good fits were obtained at the higher energies. A parameter set was obtained for proton scattering that is in many ways similar to the parameter set obtained above for neutron scattering. This similarity made it relatively simple to decide on a starting set of parameters for the third phase of the analysis in which fits to neutron and proton data were attempted simultaneously. It was evident through all phases of the analysis that the fits were particularly sensitive to the strengths of the surface imaginary well. Whereas Davé had a W_D which increased with energy, the data definitely preferred a lower W_D at the higher energies. In addition the differences in the neutron and proton data could be accounted for by having a larger W_D for the neutron model than the proton model. Including this ΔW_D made such a difference in the real potential unnecessary, *i.e.* $\Delta V_c = 0$. With the presence of analyzing power data in our data set, it

was possible to arrive at a value for V_{so} which was the same for neutrons and protons but which was not merely an estimate based on studies of other light nuclei. A value of 6.9 MeV for V_{so} gave improved fits to the analyzing power data when compared to the predictions of Davé's model which uses the standard value for V_{so} of 5.5 MeV. Finally, a parametrization was obtained for V_R which gave a constant energy dependence for nucleon energies below 9 MeV and gave a V_R which decreased linearly with energy above 9 MeV. The present model fits well the cross-section and analyzing power data above 9 MeV. Below this energy the fits deteriorate reflecting the onset of compound nucleus effects that cannot be handled in the optical model framework. The values of the geometry parameters and the strengths in the present model are fairly consistent with other optical models for light nuclei, for example the ^{11}B model of Murphy and the global model of Davé for 1-p shell nuclei.

The resonating group method has been pursued by H. Hofmann for several light nuclei. He has provided us with predictions for proton and neutron elastic scattering cross sections and analyzing powers based on his model for nucleons plus ^{6}Li. For the neutron plus ^{6}Li systems Hofmann's model includes the following channels: ^{6}Li + n, ^{6}Li* + n, ^{4}He + ^{3}H, ^{5}He + d, ^{5}He* + d, ^{6}He + p and ^{6}He* + p. For the proton plus ^{6}Li system he includes the following channels: ^{6}Li + p, ^{6}Li* + p, ^{5}Li + d, ^{5}Li* + d, and ^{4}He + ^{3}He. This model produces surprisingly good representations of the data considering that the model includes no free parameters in contrast to the optical model which has around 14 parameters. The model certainly shows great promise for predicting scattering observables as well as nuclear properties of light nuclei.

Because the ^{6}Li proton scattering target was fabricated with an aluminum foil backing it was convenient to obtain proton elastic scattering cross-section and analyzing power data for ^{27}Al in the range of 5 to 17 MeV. These data complement the data set used in the Martin and Walter analysis of ^{27}Al which included higher energy proton data and

neutron data between 11 and 17 MeV. Martin and Walter previously performed a spherical optical model analysis of neutron and proton scattering data from ^{27}Al. We extended this analysis using the expanded data set. Our analysis included real central, surface imaginary, and real spin-orbit potentials as did the Martin and Walter analysis. The addition of the large volume of proton scattering data at the lower energies provided the basis for certain improvements to the older model. The fits to the neutron and proton data were better without an asymmetry term in the surface imaginary well strength used by Martin and Walter. A smaller asymmetry term in the real central potential than that used by them produced fits of equal quality. Deficiencies in the present model exist at energies below 9 MeV where the fits are poor. Success was achieved in fitting both neutron and proton data above 9 MeV with our model in which the differences between proton and neutron are accounted for with only the standard Coulomb potential, a Coulomb correction to the real central potential ΔV_c, and a small asymmetry term in the real central potential.

The present work points up several possibilities for future efforts with ^{6}Li and ^{27}Al. The large quantity of neutron and proton inelastic data for ^{6}Li could be utilized in an analysis which incorporates a deformed optical model potential. This analysis is done in the coupled-channels framework. Such a study should be helpful in improving the optical model parametrization for the elastic scattering data, as well as providing a representation for the inelastic data. Certain extensions and improvements of the resonating group model for ^{6}Li may also be possible. One avenue would be the investigation of the channels used in the present calculation to determine which channels contribute most to the good quality predictions. Experimenting with additional channels not yet included should result in improved agreement with the data. It is also possible, in principle, in the resonating group model to predict scattering observables for the first excited state of ^{6}Li and compare these to the inelastic scattering data. This state is already included as one of the channels, so no new wave functions need be calculated for the system.

It would be desirable to extend the work on ^{27}Al as well. Providing a neutron data set as complete as the existing proton data set would be one possibility. The data at the lower energies could be obtained at TUNL. Certainly measuring analyzing powers at 11 MeV to complement the existing neutron cross-section data would be a minimal step. This has the added interest of being in an energy region where the predicted $A_y(\theta)$ is changing dramatically at forward angles. Extension of both the neutron and proton data sets above 25 MeV would be valuable for studying the onset of the need for W_V. A good constraint on the asymmetry term is provided by including ^{27}Al(p,n) isobaric analog data in an analysis which considers all the (N,N) data in an isospin consistent way. This approach is called the Lane model method and has had considerable success, even for light nuclear systems.

APPENDIX

DATA TABLES

In this Appendix the energy dependent Legendre polynomial coefficients for the cross sections and the energy dependent associated Legendre polynomial coefficients for the analyzing powers are tabulated. The quantities listed are the values of k_l^n of Eq. (2-11). In all cases the functional dependence on E is a simple polynomial (*i.e.* $f_l^n(E) = E^n$). The k_l^n's for neutron elastic and inelastic scattering from ^{6}Li are presented even though the data fitted by these coefficients are from the literature. They are necessary for extracting the complementary analyzing power values since the associated Legendre polynomials were fit to the product, $A_y(\theta) \times \sigma(\theta)$.

Following the tabulations of k_l^n are tables of the data. The quantities tabulated for the analyzing power data are defined here.

θ_{Lab} = the scattering angle in the laboratory reference frame without corrections applied,

$A_y(\theta_{Lab})$ = the analyzing power as measured without corrections applied,

$\Delta A_y(\theta_{Lab})$ = the statistical uncertainty in the analyzing power,

θ_{cm} = the scattering angle in the center-of-mass reference frame (with finite geometry corrections applied in the case of neutron scattering data),

$A_y(\theta_{cm})$ = for the neutron scattering data this is the analyzing power corrected for finite geometry, multiple scattering, and contaminant effects,

$\Delta A_y(\theta_{cm})$ = for the neutron scattering data this is the uncertainty in $A_y(\theta_{cm})$ reflecting the statistical uncertainty and uncertainties in the finite geometry, multiple scattering, and contaminant corrections.

Under the heading of "calculation" the following entries appear:

$A_y(\theta_{cm})$ = a calculation of $A_y(\theta_{cm})$ based on the energy dependent associated Legendre polynomial coefficients,

Dev = $A_y(\theta_{cm})_{calc} - A_y(\theta_{cm})_{corr}$

$$\chi^2 = \left(\frac{A_y(\theta_{cm})_{calc} - A_y(\theta_{cm})_{corr}}{\Delta A_y(\theta_{cm})}\right)^2.$$

For the cross-section data the following quantities are defined:

θ_{Lab} = the scattering angle in the laboratory reference frame,

$\sigma(\theta_{Lab})$ = the measured cross section in the laboratory reference frame normalized to the incorrect foil thickness,

$\Delta\sigma(\theta_{Lab})$ = the uncertainty in the measured cross section,

θ_{cm} = the scattering angle in the center-of-mass reference frame,

$\sigma(\theta_{cm})$ = the cross section in the center-of-mass frame renormalized to the correct foil thickness,

$\Delta\sigma(\theta_{cm})$ = the uncertainty in the renormalized cross section.

Under the heading of "calculation" are the following quantities:

$\sigma(\theta_{cm})$ = a calculation of the cross section based on the energy dependent Legendre polynomial coefficients,

$$Dev = \frac{\sigma(\theta_{cm})_{calc} - \sigma(\theta_{cm})_{corr}}{\sigma(\theta_{cm})_{corr}}$$

$$\chi^2 = \left(\frac{\sigma(\theta_{cm})_{calc} - \sigma(\theta_{cm})_{corr}}{\Delta\sigma(\theta_{cm})_{corr}}\right)^2.$$

^{6}Li NEUTRON ELASTIC SCATTERING CROSS SECTIONS

values of k_l^n

	$n=0$	$n=1$	$n=2$	$n=3$
$l=0$	121.842	-5.034	0.104	
$l=1$	39.063	28.834	-2.121	0.048
$l=2$	71.821	21.938	-1.412	0.028
$l=3$	-62.215	37.805	-2.287	0.046
$l=4$	-10.435	10.490	-0.287	
$l=5$	-25.421	5.702	-0.118	
$l=6$	-0.358	0.909		
$l=7$	2.569			

^{6}Li NEUTRON INELASTIC SCATTERING CROSS SECTIONS

values of k_l^n

	$n=0$	$n=1$	$n=2$
$l=0$	21.807	-1.508	0.025
$l=1$	7.903	-0.345	
$l=2$	-0.606		
$l=3$	-1.163		

^{6}Li NEUTRON ELASTIC SCATTERING ANALYZING POWERS

values of k_l^n

	$n=0$	$n=1$	$n=2$	$n=3$
$l=1$	0.851	3.293	-0.323	0.009
$l=2$	37.013	-2.666	0.067	
$l=3$	-11.640	4.653	-0.338	0.008
$l=4$	4.093			
$l=5$	-0.034	0.052		
$l=6$	0.076			

^{6}Li NEUTRON INELASTIC SCATTERING ANALYZING POWERS

values of k_l^n

	$n=0$	$n=1$	$n=2$
$l=1$	-3.475	0.829	-0.035
$l=2$	2.591	-0.132	
$l=3$	-0.944	0.047	

^{6}Li NEUTRON ELASTIC SCATTERING ANALYZING POWERS

Neutron Energy, Full Energy Spread 5.079, 0.448 MeV

Scale Uncertainty 2.0%

Excitation Energy (J^{π}) 0.00 MeV (1^{+})

uncorrected			corrected			calculation		
θ_{Lab}	$A_y(\theta_{Lab})$	$\Delta A_y(\theta_{Lab})$	θ_{cm}	$A_y(\theta_{cm})$	$\Delta A_y(\theta_{cm})$	$A_y(\theta_{cm})$	Dev	χ^2
40.0	-0.282	0.026	45.9	-0.288	0.028	-0.270	0.019	0.429
60.0	-0.277	0.040	67.8	-0.291	0.043	-0.370	-0.079	3.389
80.0	-0.114	0.077	89.1	-0.104	0.081	-0.141	-0.037	0.205
110.0	0.444	0.070	118.7	0.463	0.073	0.456	-0.008	0.011
130.0	0.610	0.062	137.1	0.634	0.064	0.692	0.057	0.816
155.0	0.454	0.062	158.6	0.474	0.054	0.410	-0.064	1.407

^{6}Li NEUTRON INELASTIC SCATTERING ANALYZING POWERS

Excitation Energy (J^{π}) 2.18 MeV (3^{+})

uncorrected			corrected			calculation		
θ_{Lab}	$A_y(\theta_{Lab})$	$\Delta A_y(\theta_{Lab})$	θ_{cm}	$A_y(\theta_{cm})$	$\Delta A_y(\theta_{cm})$	$A_y(\theta_{cm})$	Dev	χ^2
40.0	-0.095	0.091	48.6	-0.100	0.117	-0.103	-0.003	0.001
60.0	-0.080	0.129	71.3	-0.073	0.181	-0.132	-0.059	0.105
80.0	-0.036	0.125	92.8	0.022	0.172	-0.063	-0.085	0.246

^{6}Li NEUTRON ELASTIC SCATTERING ANALYZING POWERS

Neutron Energy, Full Energy Spread 5.904, 0.458 MeV

Scale Uncertainty 2.0%

Excitation Energy (J^{π}) 0.00 MeV (1^{+})

uncorrected			corrected			calculation		
θ_{Lab}	$A_y(\theta_{Lab})$	$\Delta A_y(\theta_{Lab})$	θ_{cm}	$A_y(\theta_{cm})$	$\Delta A_y(\theta_{cm})$	$A_y(\theta_{cm})$	Dev	χ^2
30.0	-0.183	0.019	34.8	-0.190	0.021	-0.199	-0.009	0.195
40.0	-0.220	0.038	45.9	-0.240	0.043	-0.273	-0.032	0.572
60.0	-0.425	0.031	67.6	-0.452	0.033	-0.383	0.069	4.415
80.0	-0.132	0.033	89.2	-0.127	0.035	-0.111	0.016	0.212
100.0	0.229	0.034	109.1	0.244	0.036	0.266	0.022	0.375
120.0	0.582	0.032	128.0	0.603	0.033	0.588	-0.015	0.210
130.0	0.622	0.031	137.1	0.644	0.032	0.672	0.028	0.746
145.0	0.539	0.034	150.2	0.559	0.035	0.568	0.009	0.073
155.0	0.340	0.031	158.6	0.356	0.032	0.419	0.063	3.834

^{6}Li NEUTRON INELASTIC SCATTERING ANALYZING POWERS

Excitation Energy (J^{π}) 2.18 MeV (3^{+})

uncorrected			corrected			calculation		
θ_{Lab}	$A_y(\theta_{Lab})$	$\Delta A_y(\theta_{Lab})$	θ_{cm}	$A_y(\theta_{cm})$	$\Delta A_y(\theta_{cm})$	$A_y(\theta_{cm})$	Dev	χ^2
30.0	-0.226	0.975	36.6	-0.260	0.113	-0.078	0.182	2.586
40.0	-0.070	0.071	48.1	-0.080	0.086	-0.109	-0.029	0.110
60.0	-0.363	0.083	70.6	-0.412	0.097	-0.141	0.271	7.776
80.0	-0.013	0.059	92.0	0.004	0.071	-0.073	-0.077	1.178
100.0	-0.045	0.092	111.9	-0.021	0.120	0.125	0.146	1.484
120.0	0.359	0.135	130.4	0.491	0.191	0.351	-0.140	0.540
130.0	0.201	0.176	139.1	0.276	0.247	0.416	0.140	0.319

^{6}Li NEUTRON ELASTIC SCATTERING ANALYZING POWERS

Neutron Energy, Full Energy Spread 6.916, 0.553 MeV

Scale Uncertainty 2.0%

Excitation Energy (J^{π}) 0.00 MeV (1^{+})

	uncorrected			corrected		calculation		
θ_{Lab}	$A_y(\theta_{Lab})$	$\Delta A_y(\theta_{Lab})$	θ_{cm}	$A_y(\theta_{cm})$	$\Delta A_y(\theta_{cm})$	$A_y(\theta_{cm})$	Dev	χ^2
20.0	-0.119	0.010	23.8	-0.129	0.013	-0.127	0.002	0.027
40.0	-0.245	0.015	45.8	-0.256	0.017	-0.275	-0.019	1.283
55.0	-0.392	0.023	62.0	-0.407	0.025	-0.383	0.024	0.967
70.0	-0.264	0.027	78.4	-0.282	0.032	-0.316	-0.034	1.184
90.0	0.101	0.036	99.4	0.120	0.038	0.138	0.018	0.228
110.0	0.427	0.034	118.6	0.441	0.036	0.397	-0.045	1.561
130.0	0.600	0.038	137.2	0.638	0.040	0.644	0.007	0.029
142.5	0.637	0.034	148.2	0.647	0.035	0.601	-0.046	1.715
155.0	0.389	0.031	158.7	0.395	0.031	0.430	0.036	1.299

^{6}Li NEUTRON INELASTIC SCATTERING ANALYZING POWERS

Excitation Energy (J^{π}) 2.18 MeV (3^{+})

	uncorrected			corrected		calculation		
θ_{Lab}	$A_y(\theta_{Lab})$	$\Delta A_y(\theta_{Lab})$	θ_{cm}	$A_y(\theta_{cm})$	$\Delta A_y(\theta_{cm})$	$A_y(\theta_{cm})$	Dev	χ^2
20.0	-0.065	0.046	24.9	-0.063	0.051	-0.058	0.005	0.011
40.0	0.020	0.046	47.8	0.035	0.049	-0.127	-0.162	10.705
55.0	-0.242	0.064	64.6	-0.251	0.069	-0.164	0.087	1.578
70.0	-0.118	0.050	80.9	-0.123	0.054	-0.155	-0.032	0.352
90.0	0.062	0.071	101.6	0.077	0.077	-0.028	-0.105	1.859
110.0	0.305	0.091	120.8	0.363	0.102	0.209	-0.154	2.262
130.0	0.432	0.123	138.7	0.502	0.142	0.395	-0.107	0.573
142.5	0.602	0.140	149.3	0.699	0.167	0.408	-0.291	3.052
155.0	0.238	0.148	159.4	0.270	0.180	0.332	0.063	0.120

^{6}Li NEUTRON ELASTIC SCATTERING ANALYZING POWERS

Neutron Energy, Full Energy Spread 7.918, 0.544 MeV

Scale Uncertainty 2.0%

Excitation Energy (J^{π}) 0.00 MeV (1^{+})

uncorrected			corrected			calculation		
θ_{Lab}	$A_y(\theta_{Lab})$	$\Delta A_y(\theta_{Lab})$	θ_{cm}	$A_y(\theta_{cm})$	$\Delta A_y(\theta_{cm})$	$A_y(\theta_{cm})$	Dev	χ^2
20.0	-0.105	0.013	23.8	-0.119	0.014	-0.123	-0.003	0.055
40.0	-0.274	0.014	45.8	-0.285	0.016	-0.276	0.009	0.338
55.0	-0.384	0.022	62.1	-0.393	0.024	-0.394	-0.001	0.002
70.0	-0.335	0.044	78.5	-0.353	0.047	-0.301	0.052	1.197
90.0	0.134	0.036	99.4	0.143	0.038	0.178	0.035	0.834
110.0	0.398	0.047	118.7	0.408	0.048	0.367	-0.041	0.720
130.0	0.617	0.049	137.0	0.630	0.051	0.611	-0.019	0.135
142.5	0.647	0.032	148.0	0.672	0.033	0.607	-0.065	3.758
155.0	0.483	0.032	158.5	0.515	0.034	0.449	-0.066	3.737

^{6}Li NEUTRON INELASTIC SCATTERING ANALYZING POWERS

Excitation Energy (J^{π}) 2.18 MeV (3^{+})

uncorrected			corrected			calculation		
θ_{Lab}	$A_y(\theta_{Lab})$	$\Delta A_y(\theta_{Lab})$	θ_{cm}	$A_y(\theta_{cm})$	$\Delta A_y(\theta_{cm})$	$A_y(\theta_{cm})$	Dev	χ^2
20.0	-0.195	0.070	24.8	-0.221	0.074	-0.068	0.153	4.313
40.0	-0.204	0.050	47.5	-0.220	0.054	-0.144	0.076	2.020
55.0	-0.213	0.065	64.3	-0.225	0.071	-0.187	0.037	0.282
70.0	-0.155	0.060	80.6	-0.158	0.065	-0.185	-0.027	0.175
90.0	-0.058	0.083	101.1	-0.059	0.089	-0.067	-0.008	0.008
110.0	0.160	0.150	120.4	0.171	0.161	0.172	0.001	0.000
130.0	0.409	0.173	138.3	0.445	0.186	0.373	-0.071	0.147
142.5	0.522	0.109	149.0	0.568	0.118	0.396	-0.173	2.142
155.0	0.473	0.144	159.2	0.535	0.159	0.327	-0.208	1.720

^{6}Li NEUTRON ELASTIC SCATTERING ANALYZING POWERS

Neutron Energy, Full Energy Spread 8.925, 0.601 MeV

Scale Uncertainty 2.0%

Excitation Energy (J^π) 0.00 MeV (1^+)

	uncorrected			corrected		calculation		
θ_{Lab}	$A_y(\theta_{Lab})$	$\Delta A_y(\theta_{Lab})$	θ_{cm}	$A_y(\theta_{cm})$	$\Delta A_y(\theta_{cm})$	$A_y(\theta_{cm})$	Dev	χ^2
20.0	-0.118	0.010	23.8	-0.129	0.012	-0.119	0.010	0.675
30.0	-0.183	0.009	34.7	-0.185	0.010	-0.190	-0.005	0.220
40.0	-0.277	0.013	45.8	-0.278	0.014	-0.275	0.002	0.032
55.0	-0.403	0.019	62.1	-0.416	0.021	-0.403	0.013	0.419
70.0	-0.252	0.029	78.5	-0.249	0.032	-0.278	-0.029	0.829
90.0	0.250	0.032	99.5	0.278	0.034	0.221	-0.057	2.861
110.0	0.352	0.034	118.7	0.359	0.036	0.339	-0.020	0.317
130.0	0.491	0.045	136.9	0.500	0.046	0.574	0.074	2.546
142.5	0.574	0.030	147.9	0.605	0.032	0.611	0.006	0.036
155.0	0.458	0.032	158.6	0.484	0.034	0.469	-0.015	0.190

^{6}Li NEUTRON INELASTIC SCATTERING ANALYZING POWERS

Excitation Energy (J^π) 2.18 MeV (3^+)

	uncorrected			corrected		calculation		
θ_{Lab}	$A_y(\theta_{Lab})$	$\Delta A_y(\theta_{Lab})$	θ_{cm}	$A_y(\theta_{cm})$	$\Delta A_y(\theta_{cm})$	$A_y(\theta_{cm})$	Dev	χ^2
20.0	-0.125	0.074	24.7	-0.123	0.079	-0.078	0.045	0.321
30.0	-0.072	0.037	36.0	-0.062	0.041	-0.119	-0.057	1.988
40.0	-0.058	0.056	47.3	-0.048	0.060	-0.161	-0.113	3.577
55.0	-0.276	0.067	64.1	-0.287	0.071	-0.209	0.077	1.174
70.0	-0.234	0.049	80.3	-0.250	0.052	-0.214	0.036	0.482
90.0	-0.152	0.069	100.9	-0.169	0.073	-0.105	0.064	0.767
110.0	0.002	0.083	120.1	-0.001	0.088	0.135	0.136	2.376
130.0	0.242	0.123	138.1	0.259	0.131	0.351	0.092	0.493
142.5	0.352	0.067	148.8	0.373	0.072	0.382	0.009	0.015
155.0	0.241	0.098	159.1	0.257	0.106	0.319	0.062	0.344

^{6}Li NEUTRON ELASTIC SCATTERING ANALYZING POWERS

Neutron Energy, Full Energy Spread 9.927, 0.524 MeV

Scale Uncertainty 2.0%

Excitation Energy (J^{π}) 0.00 MeV (1^{+})

uncorrected			corrected			calculation		
θ_{Lab}	$A_y(\theta_{Lab})$	$\Delta A_y(\theta_{Lab})$	θ_{cm}	$A_y(\theta_{cm})$	$\Delta A_y(\theta_{cm})$	$A_y(\theta_{cm})$	Dev	χ^2
20.0	-0.107	0.008	23.8	-0.133	0.010	-0.116	0.018	2.970
30.0	-0.164	0.010	34.7	-0.176	0.012	-0.186	-0.010	0.660
40.0	-0.251	0.012	45.7	-0.259	0.013	-0.274	-0.015	1.319
50.0	-0.383	0.014	56.7	-0.379	0.015	-0.370	0.009	0.343
60.0	-0.406	0.032	67.5	-0.424	0.034	-0.420	0.004	0.012
70.0	-0.234	0.029	78.4	-0.242	0.032	-0.245	-0.003	0.011
80.0	0.093	0.034	89.3	0.133	0.037	0.133	0.000	0.000
90.0	0.243	0.024	99.5	0.259	0.025	0.267	0.008	0.108
100.0	0.272	0.026	109.2	0.274	0.027	0.281	0.007	0.068
120.0	0.371	0.024	127.8	0.379	0.025	0.403	0.024	0.910
130.0	0.531	0.035	136.9	0.551	0.037	0.536	-0.016	0.178
140.0	0.558	0.028	145.8	0.583	0.030	0.616	0.033	1.234
150.0	0.545	0.029	154.4	0.573	0.031	0.562	-0.012	0.137
159.0	0.444	0.029	161.8	0.477	0.030	0.429	-0.048	2.522

^{6}Li NEUTRON INELASTIC SCATTERING ANALYZING POWERS

Excitation Energy (J^{π}) 2.18 MeV (3^{+})

uncorrected			corrected			calculation		
θ_{Lab}	$A_y(\theta_{Lab})$	$\Delta A_y(\theta_{Lab})$	θ_{cm}	$A_y(\theta_{cm})$	$\Delta A_y(\theta_{cm})$	$A_y(\theta_{cm})$	Dev	χ^2
20.0	-0.121	0.044	24.6	-0.129	0.048	-0.088	0.041	0.750
30.0	-0.065	0.063	35.9	-0.070	0.067	-0.132	-0.062	0.865
40.0	-0.300	0.116	47.2	-0.325	0.125	-0.177	0.148	1.402
50.0	-0.304	0.048	58.4	-0.325	0.051	-0.215	0.110	4.578
60.0	-0.181	0.056	69.4	-0.193	0.059	-0.240	-0.047	0.622
70.0	-0.287	0.044	80.1	-0.301	0.047	-0.241	0.060	1.642
80.0	-0.303	0.060	90.6	-0.316	0.063	-0.211	0.105	2.755
90.0	-0.097	0.044	100.7	-0.100	0.047	-0.142	-0.042	0.800
100.0	-0.079	0.052	110.5	-0.086	0.055	-0.034	0.052	0.887
120.0	0.154	0.045	129.1	0.161	0.048	0.231	0.070	2.106
130.0	0.127	0.075	138.0	0.135	0.079	0.328	0.194	6.018
140.0	0.282	0.072	146.6	0.299	0.076	0.368	0.069	0.836
150.0	0.301	0.064	155.0	0.324	0.068	0.344	0.020	0.085
159.0	0.379	0.069	162.3	0.414	0.074	0.276	-0.138	3.492

^{6}Li NEUTRON ELASTIC SCATTERING ANALYZING POWERS

Neutron Energy, Full Energy Spread 11.926, 0.418 MeV

Scale Uncertainty 2.0%

Excitation Energy (J^{π}) 0.00 MeV (1^{+})

uncorrected			corrected			calculation		
θ_{Lab}	$A_y(\theta_{Lab})$	$\Delta A_y(\theta_{Lab})$	θ_{cm}	$A_y(\theta_{cm})$	$\Delta A_y(\theta_{cm})$	$A_y(\theta_{cm})$	Dev	χ^2
20.0	-0.104	0.006	23.7	-0.104	0.009	-0.109	-0.005	0.316
30.0	-0.174	0.007	34.6	-0.182	0.009	-0.179	0.003	0.116
40.0	-0.273	0.009	45.6	-0.280	0.011	-0.269	0.011	1.006
55.0	-0.410	0.014	62.1	-0.425	0.016	-0.408	0.017	1.169
70.0	-0.136	0.026	78.4	-0.135	0.028	-0.136	-0.001	0.001
90.0	0.331	0.020	99.5	0.345	0.021	0.360	0.016	0.560
110.0	0.280	0.017	118.6	0.283	0.018	0.276	-0.006	0.125
130.0	0.447	0.024	136.8	0.458	0.025	0.459	0.002	0.004
155.0	0.471	0.027	158.6	0.503	0.029	0.546	0.043	2.198

^{6}Li NEUTRON INELASTIC SCATTERING ANALYZING POWERS

Excitation Energy (J^{π}) 2.18 MeV (3^{+})

uncorrected			corrected			calculation		
θ_{Lab}	$A_y(\theta_{Lab})$	$\Delta A_y(\theta_{Lab})$	θ_{cm}	$A_y(\theta_{cm})$	$\Delta A_y(\theta_{cm})$	$A_y(\theta_{cm})$	Dev	χ^2
20.0	-0.121	0.051	24.5	-0.134	0.056	-0.105	0.030	0.287
30.0	-0.211	0.054	35.7	-0.226	0.059	-0.154	0.071	1.469
40.0	-0.293	0.058	47.0	-0.309	0.062	-0.203	0.106	2.899
55.0	-0.222	0.036	63.7	-0.231	0.039	-0.263	-0.032	0.675
70.0	-0.291	0.038	79.8	-0.306	0.040	-0.286	0.020	0.248
90.0	-0.187	0.044	100.4	-0.202	0.046	-0.209	-0.007	0.021
110.0	0.103	0.045	119.7	0.104	0.047	0.027	-0.077	2.647
130.0	0.347	0.058	137.8	0.369	0.062	0.281	-0.087	1.990
155.0	0.257	0.057	159.0	0.275	0.061	0.291	0.016	0.067

^{6}Li NEUTRON ELASTIC SCATTERING ANALYZING POWERS

Neutron Energy, Full Energy Spread 13.919, 0.350 MeV

Scale Uncertainty 2.0%

Excitation Energy (J^{π}) 0.00 MeV (1^{+})

uncorrected			corrected			calculation		
θ_{Lab}	$A_y(\theta_{Lab})$	$\Delta A_y(\theta_{Lab})$	θ_{cm}	$A_y(\theta_{cm})$	$\Delta A_y(\theta_{cm})$	$A_y(\theta_{cm})$	Dev	χ^2
20.0	-0.105	0.010	23.7	-0.106	0.014	-0.105	0.002	0.016
30.0	-0.170	0.011	34.6	-0.168	0.013	-0.173	-0.005	0.153
40.0	-0.251	0.011	45.6	-0.246	0.013	-0.264	-0.018	1.880
50.0	-0.324	0.021	56.5	-0.335	0.022	-0.364	-0.029	1.653
60.0	-0.353	0.041	67.4	-0.377	0.044	-0.376	0.001	0.001
70.0	-0.058	0.062	78.4	-0.048	0.068	0.005	0.053	0.597
80.0	0.487	0.054	89.4	0.549	0.058	0.482	-0.067	1.321
90.0	0.424	0.055	99.6	0.442	0.058	0.444	0.001	0.001
100.0	0.251	0.045	109.2	0.253	0.047	0.318	0.066	1.946
110.0	0.319	0.046	118.6	0.323	0.047	0.257	-0.066	1.925
120.0	0.289	0.049	127.8	0.293	0.051	0.280	-0.013	0.066
130.0	0.349	0.062	136.8	0.359	0.065	0.406	0.047	0.513
140.0	0.677	0.064	145.6	0.719	0.068	0.591	-0.127	3.485
150.0	0.608	0.069	154.3	0.652	0.074	0.639	-0.013	0.032
159.0	0.387	0.074	161.9	0.418	0.079	0.498	0.079	1.010

^{6}Li NEUTRON INELASTIC SCATTERING ANALYZING POWERS

Excitation Energy (J^{π}) 2.18 MeV (3^{+})

uncorrected			corrected			calculation		
θ_{Lab}	$A_y(\theta_{Lab})$	$\Delta A_y(\theta_{Lab})$	θ_{cm}	$A_y(\theta_{cm})$	$\Delta A_y(\theta_{cm})$	$A_y(\theta_{cm})$	Dev	χ^2
20.0	-0.030	0.110	24.4	-0.008	0.125	-0.115	-0.107	0.729
30.0	-0.116	0.075	35.6	-0.104	0.084	-0.166	-0.062	0.549
40.0	-0.217	0.099	46.9	-0.213	0.107	-0.214	-0.001	0.000
50.0	-0.220	0.079	58.0	-0.217	0.084	-0.257	-0.041	0.232
60.0	-0.183	0.067	69.0	-0.194	0.070	-0.291	-0.096	1.865
70.0	-0.399	0.098	79.7	-0.424	0.104	-0.308	0.116	1.244
80.0	-0.344	0.098	90.1	-0.369	0.104	-0.300	0.069	0.442
90.0	-0.111	0.103	100.2	-0.121	0.109	-0.255	-0.134	1.504
100.0	0.020	0.103	110.0	0.017	0.109	-0.166	-0.183	2.828
110.0	-0.043	0.106	119.5	-0.050	0.112	-0.035	0.015	0.018
120.0	0.171	0.132	128.7	0.178	0.139	0.115	-0.063	0.207
130.0	0.308	0.193	137.7	0.325	0.204	0.239	-0.086	0.179
140.0	0.464	0.266	146.3	0.494	0.281	0.301	-0.193	0.470
150.0	0.231	0.153	154.8	0.247	0.161	0.294	0.047	0.085
159.0	0.277	0.215	162.1	0.299	0.230	0.238	-0.061	0.070

^{6}Li NEUTRON ELASTIC SCATTERING ANALYZING POWERS

Neutron Energy, Full Energy Spread 16.907, 0.283 MeV

Scale Uncertainty 2.0%

Excitation Energy (J^{π}) 0.00 MeV (1^{+})

	uncorrected			corrected		calculation		
θ_{Lab}	$A_y(\theta_{Lab})$	$\Delta A_y(\theta_{Lab})$	θ_{cm}	$A_y(\theta_{cm})$	$\Delta A_y(\theta_{cm})$	$A_y(\theta_{cm})$	Dev	χ^2
20.0	-0.107	0.014	23.6	-0.097	0.018	-0.101	-0.005	0.064
30.0	-0.208	0.014	34.5	-0.195	0.017	-0.170	0.025	2.037
40.0	-0.286	0.016	45.6	-0.264	0.019	-0.263	0.001	0.006
55.0	-0.333	0.035	62.0	-0.368	0.042	-0.372	-0.004	0.009
70.0	0.141	0.062	78.4	0.174	0.067	0.186	0.012	0.030
80.0	0.568	0.088	89.3	0.652	0.094	0.653	0.001	0.000
95.0	0.452	0.069	104.5	0.464	0.072	0.423	-0.041	0.332
110.0	0.186	0.068	118.7	0.185	0.071	0.224	0.039	0.309
120.0	0.258	0.069	127.7	0.263	0.072	0.214	-0.049	0.463
130.0	0.185	0.086	136.6	0.185	0.091	0.312	0.127	1.949
137.0	0.448	0.094	142.8	0.473	0.101	0.472	-0.001	0.000
145.0	0.729	0.137	149.9	0.802	0.150	0.695	-0.107	0.504

^{6}Li NEUTRON INELASTIC SCATTERING ANALYZING POWERS

Excitation Energy (J^{π}) 2.18 MeV (3^{+})

	uncorrected			corrected		calculation		
θ_{Lab}	$A_y(\theta_{Lab})$	$\Delta A_y(\theta_{Lab})$	θ_{cm}	$A_y(\theta_{cm})$	$\Delta A_y(\theta_{cm})$	$A_y(\theta_{cm})$	Dev	χ^2
20.0	0.040	0.136	24.5	0.060	0.145	-0.091	-0.151	1.085
30.0	-0.150	0.200	46.9	-0.245	0.285	-0.158	0.088	0.095
40.0	-0.307	0.266	63.5	-0.293	0.188	-0.199	0.094	0.249
55.0	-0.288	0.175	79.5	-0.370	0.177	-0.227	0.143	0.647
70.0	-0.292	0.166	89.9	-0.312	0.152	-0.229	0.083	0.295
80.0	-0.263	0.142	104.9	-0.080	0.173	-0.179	-0.099	0.326
95.0	-0.061	0.161	119.3	-0.165	0.229	-0.028	0.137	0.355
110.0	-0.147	0.214	128.6	0.031	0.156	0.115	0.084	0.289
120.0	0.036	0.145	137.5	0.207	0.185	0.236	0.029	0.025
130.0	0.197	0.172	143.7	0.193	0.180	0.280	0.087	0.231
137.0	0.181	0.168	150.5	0.625	0.438	0.283	-0.342	0.610
110.0	-0.043	0.106	119.5	-0.050	0.112	-0.035	0.015	0.018
120.0	0.171	0.132	128.7	0.178	0.139	0.115	-0.063	0.207
130.0	0.308	0.193	137.7	0.325	0.204	0.239	-0.086	0.179
140.0	0.464	0.266	146.3	0.494	0.281	0.301	-0.193	0.470
150.0	0.231	0.153	154.8	0.247	0.161	0.294	0.047	0.085
159.0	0.277	0.215	162.1	0.299	0.230	0.238	-0.061	0.070

^{6}Li PROTON ELASTIC SCATTERING CROSS SECTIONS

values of k_l^n

	$n=0$	$n=1$	$n=2$	$n=3$
$l=0$	127.152	-5.650	-0.031	0.006
$l=1$	47.406	29.831	-2.676	0.068
$l=2$	62.041	28.991	-2.605	0.066
$l=3$	34.696	23.698	-2.227	0.064
$l=4$	107.056	-2.925	-0.620	0.038
$l=5$	144.605	-22.603	0.933	
$l=6$	121.897	-20.318	0.828	
$l=7$	86.880	-14.537	0.582	
$l=8$	30.278	-4.871	0.187	

^{6}Li PROTON INELASTIC SCATTERING CROSS SECTIONS

values of k_l^n

	$n=0$	$n=1$	$n=2$	$n=3$
$l=0$	-4.299	4.739	-0.489	0.014
$l=1$	-21.438	6.610	-0.546	0.014
$l=2$	1.085	-1.001	0.141	-0.006
$l=3$	2.019	-0.410	0.008	
$l=4$	5.270	-0.979	0.037	

^{6}Li PROTON ELASTIC SCATTERING CROSS SECTIONS

Proton Energy	5.0 MeV	
Normalization, Normalization Uncertainty	0.41	5%
Excitation Energy (J^π)	0.00 MeV	(1^+)

not renormalized			renormalized			calculation		
θ_{Lab}	$\sigma(\theta_{Lab})$	$\Delta\sigma(\theta_{Lab})$	θ_{cm}	$\sigma(\theta_{cm})$	$\Delta\sigma(\theta_{cm})$	$\sigma(\theta_{cm})$	Dev	χ^2
20.0	1396.927	6.047	23.3	427.493	1.850	414.012	-0.032	53.075
30.0	739.707	6.327	34.8	231.645	1.981	244.021	0.053	39.016
40.0	486.134	2.697	46.2	157.120	0.872	155.946	-0.007	1.815
50.0	319.616	1.800	57.4	107.442	0.605	111.808	0.041	52.070
60.0	220.635	1.454	68.4	77.669	0.512	77.380	-0.004	0.318
70.0	173.099	1.822	79.1	64.186	0.676	53.626	-0.165	244.216
80.0	123.100	0.961	89.5	48.281	0.377	44.694	-0.074	90.574
90.0	107.194	1.138	99.7	44.591	0.473	42.062	-0.057	28.573
100.0	96.041	0.756	109.5	42.405	0.334	38.244	-0.098	155.335
110.0	84.686	0.677	119.1	39.652	0.317	34.844	-0.121	229.792
120.0	85.493	0.816	128.4	42.319	0.404	35.458	-0.162	288.890
130.0	82.824	0.487	137.4	43.133	0.254	39.478	-0.085	207.835
135.0	83.654	0.426	141.8	44.580	0.227	41.841	-0.061	145.704
140.0	81.304	0.465	146.2	44.255	0.253	44.070	-0.004	0.533
145.0	90.476	0.914	150.5	50.201	0.507	46.080	-0.082	65.962
155.0	94.748	0.590	159.1	54.253	0.338	49.607	-0.086	188.878
165.0	87.795	0.532	167.5	51.370	0.311	52.702	0.026	18.349

^{6}Li PROTON INELASTIC SCATTERING CROSS SECTIONS

Monitor Analyzing Power	0.964 ± 0.010	
Excitation Energy (J^π)	2.18 MeV	(3^+)

not renormalized			renormalized			calculation		
θ_{Lab}	$\sigma(\theta_{Lab})$	$\Delta\sigma(\theta_{Lab})$	θ_{cm}	$\sigma(\theta_{cm})$	$\Delta\sigma(\theta_{cm})$	$\sigma(\theta_{cm})$	Dev	χ^2
20.0	24.973	0.434	24.7	6.831	0.119	8.374	0.226	169.050
40.0	27.860	0.269	48.9	8.219	0.079	8.053	-0.020	4.388
50.0	21.541	0.231	60.6	6.713	0.072	8.578	0.278	671.915
60.0	27.871	0.274	72.0	9.270	0.091	9.299	0.003	0.102
70.0	25.872	0.395	83.0	9.263	0.141	9.856	0.064	17.600
80.0	26.703	0.261	93.7	10.361	0.101	10.016	-0.033	11.680
90.0	22.133	0.225	103.9	9.349	0.095	9.770	0.045	19.687
100.0	20.720	0.214	113.7	9.545	0.099	9.285	-0.027	6.909
110.0	17.042	0.235	123.0	8.552	0.118	8.786	0.027	3.905
130.0	14.777	0.147	140.6	8.670	0.086	8.344	-0.038	14.393
135.0	14.254	0.168	144.8	8.652	0.102	8.377	-0.032	7.271
140.0	14.109	0.181	148.9	8.835	0.113	8.456	-0.043	11.180
155.0	13.354	0.179	160.8	9.011	0.121	8.841	-0.019	1.977

^{6}Li PROTON ELASTIC SCATTERING CROSS SECTIONS

Proton Energy	6.0 MeV	
Normalization, Normalization Uncertainty	0.41	5%
Excitation Energy (J^{π})	0.00 MeV	(1^{+})

not renormalized			renormalized			calculation		
θ_{Lab}	$\sigma(\theta_{Lab})$	$\Delta\sigma(\theta_{Lab})$	θ_{cm}	$\sigma(\theta_{cm})$	$\Delta\sigma(\theta_{cm})$	$\sigma(\theta_{cm})$	Dev	χ^2
30.0	805.163	4.362	34.8	252.077	1.366	260.982	0.035	42.511
40.0	515.708	5.014	46.2	166.636	1.620	161.119	-0.033	11.598
50.0	312.006	1.991	57.4	104.871	0.669	103.884	-0.009	2.173
60.0	183.820	1.198	68.4	64.709	0.422	65.582	0.013	4.279
110.0	53.697	0.396	119.1	25.144	0.186	28.852	0.147	399.239
120.0	54.578	0.688	128.4	27.020	0.341	28.701	0.062	24.344
130.0	58.555	0.480	137.4	30.501	0.250	31.214	0.023	8.109
140.0	58.552	0.479	146.2	31.878	0.261	34.533	0.083	103.644

^{6}Li PROTON INELASTIC SCATTERING CROSS SECTIONS

Monitor Analyzing Power	0.970 ± 0.010	
Excitation Energy (J^{π})	2.18 MeV	(3^{+})

not renormalized			renormalized			calculation		
θ_{Lab}	$\sigma(\theta_{Lab})$	$\Delta\sigma(\theta_{Lab})$	θ_{cm}	$\sigma(\theta_{cm})$	$\Delta\sigma(\theta_{cm})$	$\sigma(\theta_{cm})$	Dev	χ^2
30.0	44.817	0.455	36.4	12.986	0.132	10.330	-0.205	406.652
40.0	46.963	0.674	48.2	14.171	0.203	10.321	-0.272	358.855
50.0	40.988	0.419	59.8	13.017	0.133	10.471	-0.196	366.394
60.0	33.275	0.368	71.1	11.224	0.124	10.633	-0.053	22.627
110.0	15.796	0.258	122.0	7.782	0.127	8.550	0.099	36.528
130.0	14.280	0.229	139.8	8.118	0.130	7.753	-0.045	7.887
140.0	10.901	0.196	148.2	6.578	0.118	7.632	0.160	79.301

^{6}Li PROTON ELASTIC SCATTERING CROSS SECTIONS

Proton Energy	7.0 MeV	
Normalization, Normalization Uncertainty	0.41	5%
Excitation Energy (J^π)	0.00 MeV	(1^+)

not renormalized			renormalized			calculation		
θ_{Lab}	$\sigma(\theta_{Lab})$	$\Delta\sigma(\theta_{Lab})$	θ_{cm}	$\sigma(\theta_{cm})$	$\Delta\sigma(\theta_{cm})$	$\sigma(\theta_{cm})$	Dev	χ^2
20.0	1388.918	5.661	23.3	424.871	1.732	427.057	0.005	1.593
30.0	880.007	7.531	34.8	275.473	2.358	272.110	-0.012	2.035
40.0	529.392	2.891	46.2	171.036	0.934	163.687	-0.043	61.928
50.0	299.173	1.666	57.4	100.545	0.560	96.400	-0.041	54.826
60.0	158.071	1.073	68.4	55.639	0.378	55.399	-0.004	0.402
70.0	93.660	1.085	79.1	34.726	0.402	35.058	0.010	0.683
80.0	68.030	0.550	89.6	26.682	0.216	29.321	0.099	149.858
90.0	60.517	0.694	99.7	25.177	0.289	28.391	0.128	123.888
100.0	59.586	0.486	109.5	26.314	0.215	26.376	0.002	0.084
110.0	47.765	0.396	119.1	22.370	0.185	23.905	0.069	68.478
120.0	47.502	0.559	128.4	23.521	0.277	23.220	-0.013	1.184
130.0	44.437	0.326	137.4	23.151	0.170	24.508	0.059	63.642
135.0	44.535	0.274	141.8	23.743	0.146	25.556	0.076	154.010
140.0	45.938	0.333	146.2	25.016	0.181	26.728	0.068	89.320
145.0	49.724	0.598	150.5	27.602	0.332	27.987	0.014	1.344
155.0	52.570	0.363	159.1	30.117	0.208	30.730	0.020	8.695
165.0	56.877	0.391	167.5	33.298	0.229	33.481	0.006	0.640

^{6}Li PROTON INELASTIC SCATTERING CROSS SECTIONS

Monitor Analyzing Power	0.972 ± 0.010	
Excitation Energy (J^π)	2.18 MeV	(3^+)

not renormalized			renormalized			calculation		
θ_{Lab}	$\sigma(\theta_{Lab})$	$\Delta\sigma(\theta_{Lab})$	θ_{cm}	$\sigma(\theta_{cm})$	$\Delta\sigma(\theta_{cm})$	$\sigma(\theta_{cm})$	Dev	χ^2
20.0	47.702	0.869	24.1	13.642	0.248	11.747	-0.139	58.157
30.0	44.879	0.542	36.1	13.204	0.159	11.764	-0.109	81.586
40.0	41.371	0.323	47.8	12.654	0.099	11.746	-0.072	84.362
50.0	39.777	0.313	59.3	12.775	0.100	11.634	-0.089	129.079
60.0	36.350	0.302	70.5	12.364	0.103	11.366	-0.081	94.566
70.0	30.941	0.438	81.4	11.229	0.159	10.909	-0.029	4.050
80.0	28.852	0.265	92.0	11.238	0.103	10.283	-0.085	85.978
90.0	24.470	0.333	102.2	10.265	0.140	9.551	-0.070	26.075
100.0	21.682	0.211	112.0	9.810	0.095	8.804	-0.102	111.233
110.0	18.263	0.193	121.4	8.902	0.094	8.127	-0.087	68.168
130.0	12.601	0.146	139.3	7.035	0.081	7.170	0.019	2.738
135.0	12.209	0.136	143.6	7.020	0.078	7.021	0.000	0.000
140.0	10.154	0.138	147.8	5.999	0.082	6.904	0.151	122.636
155.0	11.433	0.142	160.1	7.206	0.090	6.703	-0.070	31.588
165.0	9.533	0.145	168.1	6.177	0.094	6.651	0.077	25.444

^{6}Li PROTON ELASTIC SCATTERING CROSS SECTIONS

Proton Energy	8.0 MeV	
Normalization, Normalization Uncertainty	0.41	5%
Excitation Energy (J^{π})	0.00 MeV	(1^{+})

not renormalized			renormalized			calculation		
θ_{Lab}	$\sigma(\theta_{Lab})$	$\Delta\sigma(\theta_{Lab})$	θ_{cm}	$\sigma(\theta_{cm})$	$\Delta\sigma(\theta_{cm})$	$\sigma(\theta_{cm})$	Dev	χ^2
30.0	833.918	6.563	34.8	260.977	2.054	278.022	0.065	68.861
40.0	518.664	5.531	46.2	167.527	1.786	163.895	-0.022	4.134
50.0	263.026	2.152	57.4	88.375	0.723	89.345	0.011	1.800
60.0	128.935	1.188	68.4	45.378	0.418	46.726	0.030	10.396
110.0	39.668	0.503	119.1	18.580	0.235	19.893	0.071	31.088
120.0	37.228	0.751	128.4	18.437	0.372	18.859	0.023	1.287
130.0	34.897	0.498	137.4	18.184	0.260	19.175	0.055	14.600
140.0	36.338	0.506	146.2	19.793	0.275	20.466	0.034	5.976

^{6}Li PROTON INELASTIC SCATTERING CROSS SECTIONS

Monitor Analyzing Power	0.976 ± 0.010	
Excitation Energy (J^{π})	2.18 MeV	(3^{+})

not renormalized			renormalized			calculation		
θ_{Lab}	$\sigma(\theta_{Lab})$	$\Delta\sigma(\theta_{Lab})$	θ_{cm}	$\sigma(\theta_{cm})$	$\Delta\sigma(\theta_{cm})$	$\sigma(\theta_{cm})$	Dev	χ^2
30.0	39.375	0.618	35.9	11.701	0.184	12.439	0.063	16.131
40.0	37.959	0.809	47.5	11.714	0.250	12.452	0.063	8.732
50.0	35.724	0.546	59.0	11.558	0.177	12.162	0.052	11.697
60.0	32.926	0.526	70.2	11.261	0.180	11.571	0.027	2.955
110.0	12.782	0.312	121.0	6.188	0.151	7.554	0.221	81.580
120.0	12.883	0.449	130.2	6.679	0.233	7.013	0.050	2.070
130.0	12.089	0.301	139.0	6.671	0.166	6.582	-0.013	0.286
140.0	10.042	0.290	147.5	5.851	0.169	6.245	0.067	5.448

^{6}Li PROTON ELASTIC SCATTERING CROSS SECTIONS

Proton Energy 9.0 MeV

Normalization, Normalization Uncertainty 0.41 5%

Excitation Energy (J^{π}) 0.00 MeV (1^{+})

not renormalized			renormalized			calculation		
θ_{Lab}	$\sigma(\theta_{Lab})$	$\Delta\sigma(\theta_{Lab})$	θ_{cm}	$\sigma(\theta_{cm})$	$\Delta\sigma(\theta_{cm})$	$\sigma(\theta_{cm})$	Dev	χ^2
20.0	1337.742	6.563	23.3	408.997	2.007	418.657	0.024	23.177
30.0	912.017	8.033	34.8	285.381	2.514	279.298	-0.021	5.857
40.0	520.299	3.150	46.2	168.034	1.017	161.970	-0.036	35.542
50.0	256.250	1.574	57.4	86.088	0.529	82.723	-0.039	40.515
60.0	115.099	0.861	68.4	40.504	0.303	39.455	-0.026	11.965
70.0	59.866	0.724	79.1	22.194	0.268	22.134	-0.003	0.049
80.0	51.427	0.469	89.6	20.170	0.184	18.498	-0.083	82.510
90.0	42.375	0.542	99.7	17.629	0.225	18.673	0.059	21.433
100.0	41.697	0.392	109.6	18.417	0.173	18.136	-0.015	2.643
110.0	36.537	0.358	119.1	17.115	0.168	16.703	-0.024	6.013
120.0	31.126	0.457	128.4	15.417	0.226	15.465	0.003	0.045
130.0	28.178	0.288	137.4	14.686	0.150	15.034	0.024	5.370
135.0	28.122	0.264	141.8	14.999	0.141	15.173	0.012	1.522
140.0	27.414	0.285	146.2	14.935	0.155	15.555	0.041	15.971
145.0	29.498	0.443	150.5	16.381	0.246	16.176	-0.013	0.697
155.0	31.790	0.310	159.1	18.222	0.177	18.008	-0.012	1.446
165.0	34.349	0.325	167.5	20.119	0.190	20.100	-0.001	0.010

^{6}Li PROTON INELASTIC SCATTERING CROSS SECTIONS

Monitor Analyzing Power 0.980 ± 0.010

Excitation Energy (J^{π}) 2.18 MeV (3^{+})

not renormalized			renormalized			calculation		
θ_{Lab}	$\sigma(\theta_{Lab})$	$\Delta\sigma(\theta_{Lab})$	θ_{cm}	$\sigma(\theta_{cm})$	$\Delta\sigma(\theta_{cm})$	$\sigma(\theta_{cm})$	Dev	χ^2
30.0	40.308	0.582	35.7	12.064	0.174	12.497	0.036	6.167
40.0	39.037	0.384	47.4	12.122	0.119	12.572	0.037	14.231
50.0	37.298	0.366	58.8	12.130	0.119	12.175	0.004	0.141
60.0	31.849	0.313	69.9	10.936	0.108	11.354	0.038	15.073
70.0	28.929	0.426	80.8	10.562	0.155	10.295	-0.025	2.962
90.0	19.953	0.314	101.5	8.349	0.131	8.251	-0.012	0.559
100.0	16.527	0.199	111.3	7.425	0.090	7.478	0.007	0.340
110.0	12.908	0.203	120.8	6.220	0.098	6.875	0.105	44.855
120.0	11.399	0.257	129.9	5.870	0.132	6.395	0.089	15.730
130.0	10.431	0.168	138.8	5.709	0.092	5.992	0.050	9.457
135.0	10.038	0.162	143.1	5.647	0.091	5.811	0.029	3.236
140.0	9.568	0.164	147.3	5.521	0.095	5.642	0.022	1.603
145.0	9.520	0.231	151.5	5.621	0.137	5.485	-0.024	1.000
155.0	9.038	0.158	159.8	5.542	0.097	5.215	-0.059	11.347
165.0	8.286	0.173	167.9	5.215	0.109	5.019	-0.038	3.221

^{6}Li PROTON ELASTIC SCATTERING CROSS SECTIONS

Proton Energy 10.0 MeV

Normalization, Normalization Uncertainty 0.41 5%

Excitation Energy (J^{π}) 0.00 MeV (1^{+})

not renormalized			renormalized			calculation		
θ_{Lab}	$\sigma(\theta_{Lab})$	$\Delta\sigma(\theta_{Lab})$	θ_{cm}	$\sigma(\theta_{cm})$	$\Delta\sigma(\theta_{cm})$	$\sigma(\theta_{cm})$	Dev	χ^2
20.0	1329.033	5.719	23.3	406.226	1.748	408.907	0.007	2.353
30.0	865.111	7.504	34.8	270.633	2.347	276.529	0.022	6.310
40.0	475.618	2.735	46.2	153.585	0.883	158.133	0.030	26.512
50.0	230.832	1.411	57.4	77.540	0.474	76.522	-0.013	4.613
60.0	79.187	0.600	68.4	27.863	0.211	33.480	0.202	706.937
70.0	46.232	0.578	79.1	17.139	0.214	17.514	0.022	3.056
80.0	32.741	0.323	89.6	12.841	0.127	14.597	0.137	192.164
90.0	32.819	0.443	99.7	13.655	0.184	15.145	0.109	65.249
100.0	32.770	0.324	109.6	14.475	0.143	15.192	0.050	25.059
110.0	30.391	0.321	119.1	14.238	0.150	14.225	-0.001	0.008
120.0	25.055	0.392	128.4	12.412	0.194	12.885	0.038	5.929
130.0	22.629	0.251	137.4	11.796	0.131	11.901	0.009	0.642
135.0	22.192	0.229	141.9	11.838	0.122	11.721	-0.010	0.922
140.0	21.059	0.239	146.2	11.475	0.130	11.805	0.029	6.409
145.0	21.151	0.353	150.6	11.749	0.196	12.161	0.035	4.412
155.0	23.799	0.256	159.1	13.644	0.147	13.537	-0.008	0.537
165.0	25.557	0.269	167.5	14.974	0.158	15.237	0.018	2.793

^{6}Li PROTON INELASTIC SCATTERING CROSS SECTIONS

Monitor Analyzing Power 0.984 ± 0.010

Excitation Energy (J^{π}) 2.18 MeV (3^{+})

not renormalized			renormalized			calculation		
θ_{Lab}	$\sigma(\theta_{Lab})$	$\Delta\sigma(\theta_{Lab})$	θ_{cm}	$\sigma(\theta_{cm})$	$\Delta\sigma(\theta_{cm})$	$\sigma(\theta_{cm})$	Dev	χ^2
20.0	36.945	0.373	23.8	10.827	0.109	11.494	0.062	37.246
30.0	41.534	0.565	35.6	12.497	0.170	12.079	-0.033	6.054
40.0	35.290	0.353	47.2	11.011	0.110	12.243	0.112	125.309
50.0	34.327	0.343	58.6	11.207	0.112	11.800	0.053	27.948
60.0	24.577	0.255	69.7	8.464	0.088	10.832	0.280	724.446
70.0	26.734	0.385	80.6	9.778	0.141	9.600	-0.018	1.592
80.0	19.627	0.228	91.1	7.663	0.089	8.391	0.095	66.857
90.0	16.476	0.277	101.3	6.890	0.116	7.391	0.073	18.829
100.0	13.694	0.177	111.1	6.140	0.079	6.656	0.084	42.578
120.0	9.427	0.227	129.7	4.832	0.116	5.746	0.189	61.975
130.0	9.566	0.163	138.6	5.204	0.089	5.408	0.039	5.311
135.0	9.207	0.160	142.9	5.146	0.089	5.245	0.019	1.235
140.0	8.874	0.161	147.2	5.085	0.092	5.086	0.000	0.000
145.0	8.489	0.228	151.4	4.974	0.133	4.930	-0.009	0.108
155.0	8.650	0.155	159.7	5.260	0.094	4.646	-0.117	42.137
165.0	7.874	0.169	167.9	4.911	0.106	4.428	-0.098	20.889

^{6}Li PROTON ELASTIC SCATTERING CROSS SECTIONS

Proton Energy	11.0 MeV	
Normalization, Normalization Uncertainty	0.41	5%
Excitation Energy (J^{π})	0.00 MeV	(1^{+})

not renormalized			renormalized			calculation		
θ_{Lab}	$\sigma(\theta_{Lab})$	$\Delta\sigma(\theta_{Lab})$	θ_{cm}	$\sigma(\theta_{cm})$	$\Delta\sigma(\theta_{cm})$	$\sigma(\theta_{cm})$	Dev	χ^2
110.0	27.961	0.199	119.1	13.101	0.093	12.346	-0.058	65.854
120.0	22.800	0.295	128.4	11.297	0.146	10.963	-0.030	5.245
130.0	19.140	0.176	137.4	9.980	0.092	9.592	-0.039	17.734
140.0	17.163	0.164	146.2	9.354	0.089	9.026	-0.035	13.471

^{6}Li PROTON INELASTIC SCATTERING CROSS SECTIONS

Monitor Analyzing Power	0.986 ± 0.010	
Excitation Energy (J^{π})	2.18 MeV	(3^{+})

not renormalized			renormalized			calculation		
θ_{Lab}	$\sigma(\theta_{Lab})$	$\Delta\sigma(\theta_{Lab})$	θ_{cm}	$\sigma(\theta_{cm})$	$\Delta\sigma(\theta_{cm})$	$\sigma(\theta_{cm})$	Dev	χ^2
110.0	10.641	0.127	120.4	5.096	0.061	5.390	0.058	23.216
120.0	10.235	0.182	129.6	5.226	0.093	5.096	-0.025	1.959
130.0	10.031	0.120	138.5	5.432	0.065	4.840	-0.109	82.944
140.0	9.735	0.182	147.1	5.548	0.104	4.572	-0.176	88.195

^{6}Li PROTON ELASTIC SCATTERING CROSS SECTIONS

Proton Energy 12.0 MeV

Normalization, Normalization Uncertainty 0.41 5%

Excitation Energy (J^{π}) 0.00 MeV (1^{+})

not renormalized			renormalized			calculation		
θ_{Lab}	$\sigma(\theta_{Lab})$	$\Delta\sigma(\theta_{Lab})$	θ_{cm}	$\sigma(\theta_{cm})$	$\Delta\sigma(\theta_{cm})$	$\sigma(\theta_{cm})$	Dev	χ^2
20.0	1281.140	5.838	23.3	391.429	1.784	383.289	-0.021	20.827
30.0	824.443	7.047	34.9	257.809	2.204	261.214	0.013	2.387
40.0	441.132	2.466	46.2	142.394	0.796	145.679	0.023	17.029
50.0	198.841	1.154	57.5	66.777	0.388	65.349	-0.021	13.575
60.0	79.656	0.565	68.4	28.025	0.199	24.988	-0.108	233.104
70.0	35.018	0.410	79.1	12.980	0.152	11.405	-0.121	107.576
80.0	26.535	0.241	89.6	10.407	0.094	9.428	-0.094	107.650
90.0	28.164	0.346	99.7	11.719	0.144	10.456	-0.108	77.036
100.0	29.216	0.261	109.6	12.908	0.115	11.290	-0.125	197.234
110.0	23.302	0.218	119.1	10.920	0.102	10.955	0.003	0.119
120.0	19.975	0.269	128.4	9.899	0.133	9.546	-0.036	7.054
130.0	15.402	0.152	137.4	8.032	0.079	7.924	-0.013	1.829
135.0	14.108	0.132	141.9	7.529	0.070	7.346	-0.024	6.804
140.0	13.015	0.138	146.2	7.095	0.075	7.026	-0.010	0.837
145.0	13.080	0.205	150.6	7.269	0.114	6.979	-0.040	6.499
155.0	13.458	0.139	159.1	7.719	0.080	7.536	-0.024	5.299
165.0	13.589	0.145	167.5	7.965	0.085	8.442	0.060	31.588

^{6}Li PROTON INELASTIC SCATTERING CROSS SECTIONS

Monitor Analyzing Power 0.988 ± 0.010

Excitation Energy (J^{π}) 2.18 MeV (3^{+})

not renormalized			renormalized			calculation		
θ_{Lab}	$\sigma(\theta_{Lab})$	$\Delta\sigma(\theta_{Lab})$	θ_{cm}	$\sigma(\theta_{cm})$	$\Delta\sigma(\theta_{cm})$	$\sigma(\theta_{cm})$	Dev	χ^2
20.0	30.361	0.260	23.7	8.968	0.077	9.457	0.055	40.733
30.0	31.745	0.396	35.5	9.622	0.120	10.385	0.079	40.343
40.0	33.515	0.270	47.0	10.524	0.085	10.789	0.025	9.796
50.0	32.869	0.266	58.4	10.789	0.087	10.414	-0.035	18.427
60.0	27.085	0.228	69.5	9.366	0.079	9.366	0.000	0.000
70.0	22.784	0.295	80.3	8.355	0.108	7.994	0.043	11.163
80.0	18.129	0.178	90.8	7.084	0.069	6.681	-0.057	33.740
90.0	14.414	0.206	101.0	6.021	0.086	5.674	-0.058	16.314
100.0	11.899	0.131	110.8	5.319	0.058	5.035	-0.054	23.809
110.0	9.386	0.117	120.3	4.485	0.056	4.680	0.043	11.998
120.0	9.107	0.164	129.5	4.637	0.083	4.474	-0.035	3.842
130.0	8.246	0.109	138.4	4.449	0.059	4.299	-0.034	6.503
135.0	7.295	0.097	142.7	4.041	0.054	4.202	0.040	8.952
140.0	6.941	0.099	147.0	3.938	0.056	4.096	0.040	7.851
145.0	6.692	0.140	151.3	3.881	0.081	3.982	0.026	1.536
155.0	6.033	0.094	159.6	3.627	0.056	3.749	0.034	4.719
165.0	5.316	0.102	167.8	3.276	0.063	3.552	0.084	19.328

^{6}Li PROTON ELASTIC SCATTERING CROSS SECTIONS

Proton Energy	13.0 MeV	
Normalization, Normalization Uncertainty	0.41	5%
Excitation Energy (J^{π})	0.00 MeV	(1^{+})

not renormalized			renormalized			calculation		
θ_{Lab}	$\sigma(\theta_{Lab})$	$\Delta\sigma(\theta_{Lab})$	θ_{cm}	$\sigma(\theta_{cm})$	$\Delta\sigma(\theta_{cm})$	$\sigma(\theta_{cm})$	Dev	χ^2
110.0	22.135	0.170	119.1	10.374	0.080	9.940	-0.042	29.652
120.0	17.859	0.246	128.4	8.852	0.122	8.479	-0.042	9.367
130.0	13.458	0.139	137.4	7.020	0.073	6.714	-0.044	17.745
140.0	10.685	0.120	146.2	5.826	0.066	5.616	-0.036	10.238

^{6}Li PROTON INELASTIC SCATTERING CROSS SECTIONS

Monitor Analyzing Power	0.987 ± 0.010	
Excitation Energy (J^{π})	2.18 MeV	(3^{+})

not renormalized			renormalized			calculation		
θ_{Lab}	$\sigma(\theta_{Lab})$	$\Delta\sigma(\theta_{Lab})$	θ_{cm}	$\sigma(\theta_{cm})$	$\Delta\sigma(\theta_{cm})$	$\sigma(\theta_{cm})$	Dev	χ^2
110.0	8.786	0.104	120.2	4.192	0.050	4.057	-0.032	7.259
120.0	7.798	0.149	129.4	3.961	0.076	3.908	-0.013	0.484
130.0	7.255	0.101	138.3	3.902	0.055	3.796	-0.027	3.779
140.0	6.235	0.092	146.9	3.526	0.052	3.653	0.036	5.989

^{6}Li PROTON ELASTIC SCATTERING CROSS SECTIONS

Proton Energy 14.0 MeV

Normalization, Normalization Uncertainty 0.41 5%

Excitation Energy (J^{π}) 0.00 MeV (1^{+})

not renormalized			renormalized			calculation		
θ_{Lab}	$\sigma(\theta_{Lab})$	$\Delta\sigma(\theta_{Lab})$	θ_{cm}	$\sigma(\theta_{cm})$	$\Delta\sigma(\theta_{cm})$	$\sigma(\theta_{cm})$	Dev	χ^2
20.0	1193.807	4.799	23.3	364.550	1.466	356.148	-0.023	32.870
30.0	757.331	6.442	34.9	236.698	2.013	236.819	0.001	0.004
40.0	390.047	2.172	46.3	125.856	0.701	128.381	0.020	12.980
50.0	168.335	0.988	57.5	56.511	0.332	55.773	-0.013	4.947
60.0	60.174	0.450	68.4	21.166	0.158	20.39	-0.037	23.884
70.0	25.094	0.309	79.2	9.301	0.115	8.740	-0.060	24.027
80.0	19.534	0.187	89.6	7.661	0.073	7.248	-0.054	31.673
90.0	21.784	0.277	99.7	9.065	0.115	8.521	-0.060	22.342
100.0	22.264	0.208	109.6	9.839	0.092	9.540	-0.030	10.505
110.0	18.538	0.180	119.2	8.690	0.084	9.190	0.058	35.054
120.0	15.783	0.225	128.4	7.824	0.112	7.608	-0.028	3.735
130.0	11.367	0.124	137.4	5.930	0.065	5.778	-0.026	5.477
135.0	9.769	0.106	141.9	5.215	0.056	5.079	-0.026	5.864
140.0	8.898	0.108	146.2	4.853	0.059	4.60	-0.051	17.804
145.0	8.525	0.153	150.6	4.740	0.085	4.354	-0.081	20.574
155.0	8.285	0.103	159.1	4.754	0.059	4.341	-0.087	49.026
165.0	8.774	0.107	167.5	5.146	0.063	4.591	-0.108	77.794

^{6}Li PROTON INELASTIC SCATTERING CROSS SECTIONS

Monitor Analyzing Power 0.985 ± 0.010

Excitation Energy (J^{π}) 2.18 MeV (3^{+})

not renormalized			renormalized			calculation		
θ_{Lab}	$\sigma(\theta_{Lab})$	$\Delta\sigma(\theta_{Lab})$	θ_{cm}	$\sigma(\theta_{cm})$	$\Delta\sigma(\theta_{cm})$	$\sigma(\theta_{cm})$	Dev	χ^2
20.0	25.808	0.223	23.7	7.662	0.066	7.247	-0.054	39.403
30.0	27.879	0.357	35.4	8.491	0.109	8.485	-0.001	0.002
40.0	30.318	0.254	46.9	9.561	0.080	9.201	-0.038	20.239
50.0	29.070	0.238	58.2	9.575	0.079	9.072	-0.053	41.077
60.0	24.853	0.217	69.3	8.618	0.075	8.174	-0.051	34.779
70.0	19.386	0.257	80.1	7.121	0.094	6.864	-0.036	7.425
80.0	14.759	0.153	90.6	5.771	0.060	5.553	-0.038	13.296
90.0	11.907	0.177	100.8	4.971	0.074	4.532	-0.088	35.216
100.0	8.815	0.104	110.6	3.934	0.046	3.893	-0.010	0.783
110.0	7.849	0.111	120.1	3.739	0.053	3.571	-0.045	10.222
120.0	7.433	0.147	129.3	3.769	0.074	3.430	-0.090	20.684
130.0	6.512	0.095	138.2	3.495	0.051	3.345	-0.043	8.580
135.0	6.307	0.087	142.6	3.473	0.048	3.298	-0.050	13.350
140.0	6.106	0.090	146.9	3.443	0.051	3.241	-0.059	15.791
145.0	5.829	0.125	151.1	3.358	0.072	3.175	-0.054	6.380
155.0	5.493	0.084	159.5	3.278	0.050	3.028	-0.076	24.875
165.0	4.952	0.084	167.8	3.027	0.051	2.893	-0.044	6.849

^{6}Li PROTON ELASTIC SCATTERING CROSS SECTIONS

Proton Energy 16.0 MeV

Normalization, Normalization Uncertainty 0.41 5%

Excitation Energy (J^π) 0.00 MeV (1^+)

not renormalized			renormalized			calculation		
θ_{Lab}	$\sigma(\theta_{Lab})$	$\Delta\sigma(\theta_{Lab})$	θ_{cm}	$\sigma(\theta_{cm})$	$\Delta\sigma(\theta_{cm})$	$\sigma(\theta_{cm})$	Dev	χ^2
20.0	1095.185	4.487	23.3	334.300	1.370	335.443	0.003	0.696
30.0	682.772	5.799	34.9	213.312	1.812	208.038	-0.025	8.473
40.0	338.797	1.873	46.3	109.278	0.604	108.050	-0.011	4.129
50.0	135.322	0.783	57.5	45.417	0.263	47.734	0.051	77.751
60.0	48.873	0.363	68.5	17.187	0.128	18.833	0.096	166.475
70.0	20.109	0.257	79.2	7.452	0.095	8.641	0.159	155.874
80.0	16.190	0.162	89.6	6.350	0.064	7.437	0.171	292.411
90.0	17.940	0.241	99.8	7.466	0.100	8.862	0.187	193.400
100.0	18.399	0.177	109.6	8.132	0.078	9.353	0.150	242.956
110.0	14.401	0.147	119.2	6.752	0.069	8.033	0.190	346.197
120.0	10.780	0.133	128.4	5.346	0.066	5.837	0.092	55.809
130.0	7.439	0.068	137.5	3.882	0.036	3.995	0.029	10.010
135.0	6.146	0.046	141.9	3.282	0.025	3.400	0.036	22.973
140.0	4.991	0.054	146.2	2.723	0.029	3.016	0.107	99.700
145.0	4.698	0.066	150.6	2.613	0.037	2.795	0.070	24.355
155.0	4.299	0.042	159.1	2.468	0.024	2.615	0.059	37.672
165.0	4.100	0.046	167.5	2.406	0.027	2.525	0.050	19.429

^{6}Li PROTON INELASTIC SCATTERING CROSS SECTIONS

Monitor Analyzing Power 0.974 ± 0.010

Excitation Energy (J^π) 2.18 MeV (3^+)

not renormalized			renormalized			calculation		
θ_{Lab}	$\sigma(\theta_{Lab})$	$\Delta\sigma(\theta_{Lab})$	θ_{cm}	$\sigma(\theta_{cm})$	$\Delta\sigma(\theta_{cm})$	$\sigma(\theta_{cm})$	Dev	χ^2
20.0	21.363	0.173	23.6	6.365	0.052	5.993	-0.058	52.043
30.0	25.352	0.301	35.3	7.746	0.092	7.508	-0.031	6.704
50.0	26.812	0.205	58.1	8.854	0.068	8.849	-0.001	0.004
60.0	23.133	0.200	69.2	8.035	0.069	8.273	0.030	11.740
70.0	17.867	0.245	80.0	6.570	0.090	7.139	0.087	39.716
90.0	9.851	0.158	100.6	4.111	0.066	4.656	0.133	68.406
100.0	7.637	0.095	110.5	3.403	0.042	3.776	0.110	77.666
110.0	5.886	0.079	120.0	2.798	0.038	3.201	0.144	115.188
120.0	5.190	0.082	129.2	2.624	0.042	2.856	0.088	30.950
135.0	4.752	0.042	142.5	2.606	0.023	2.565	-0.016	3.248
140.0	4.417	0.053	146.8	2.479	0.030	2.494	0.006	0.260
145.0	4.105	0.061	151.1	2.354	0.035	2.430	0.032	4.659
155.0	3.938	0.042	159.5	2.338	0.025	2.313	-0.010	0.938
165.0	2.936	0.048	167.7	1.785	0.029	2.222	0.245	227.084

^{6}Li PROTON ELASTIC SCATTERING CROSS SECTIONS

Proton Energy 17.0 MeV

Normalization, Normalization Uncertainty 0.41 5%

Excitation Energy (J^π) 0.00 MeV (1^+)

not renormalized			renormalized			calculation		
θ_{Lab}	$\sigma(\theta_{Lab})$	$\Delta\sigma(\theta_{Lab})$	θ_{cm}	$\sigma(\theta_{cm})$	$\Delta\sigma(\theta_{cm})$	$\sigma(\theta_{cm})$	Dev	χ^2
20.0	1054.161	4.085	23.3	321.691	1.247	330.001	0.026	44.438
30.0	662.141	5.649	34.9	206.839	1.765	193.482	-0.065	57.291
40.0	319.811	1.786	46.3	103.141	0.576	97.317	-0.056	102.182
50.0	124.227	0.748	57.5	41.689	0.251	44.266	0.062	105.505
60.0	65.557	0.492	68.5	23.054	0.173	18.924	-0.179	569.151
70.0	27.350	0.359	79.2	10.135	0.133	9.279	-0.084	41.341
80.0	22.634	0.230	89.6	8.877	0.090	8.226	-0.073	52.288
85.0	23.375	0.196	94.7	9.442	0.079	8.996	-0.047	31.699
90.0	24.135	0.207	99.8	10.045	0.086	9.736	-0.031	12.846
95.0	25.561	0.292	104.7	10.963	0.125	10.016	-0.086	57.289
105.0	23.105	0.176	114.4	10.522	0.080	8.720	-0.171	505.425
115.0	12.438	0.109	123.8	6.001	0.053	5.961	-0.007	0.598
135.0	4.992	0.054	141.9	2.667	0.029	2.307	-0.135	154.618
145.0	3.776	0.073	150.6	2.101	0.040	1.949	-0.072	14.062
155.0	3.400	0.047	159.1	1.952	0.027	1.884	-0.035	6.330
165.0	3.292	0.057	167.5	1.932	0.033	1.800	-0.069	15.825

^{6}Li PROTON INELASTIC SCATTERING CROSS SECTIONS

Monitor Analyzing Power 0.968 ± 0.010

Excitation Energy (J^π) 2.18 MeV (3^+)

not renormalized			renormalized			calculation		
θ_{Lab}	$\sigma(\theta_{Lab})$	$\Delta\sigma(\theta_{Lab})$	θ_{cm}	$\sigma(\theta_{cm})$	$\Delta\sigma(\theta_{cm})$	$\sigma(\theta_{cm})$	Dev	χ^2
20.0	19.462	0.185	23.6	5.807	0.055	6.077	0.047	23.896
30.0	25.021	0.331	35.3	7.655	0.101	7.718	0.008	0.383
40.0	27.380	0.232	46.8	8.670	0.074	8.998	0.038	19.886
50.0	25.621	0.219	58.1	8.468	0.072	9.495	0.121	201.070
60.0	32.510	0.286	69.2	11.302	0.100	9.126	-0.193	477.811
80.0	17.773	0.193	90.4	6.953	0.076	6.752	-0.029	7.075
85.0	15.497	0.146	95.6	6.260	0.059	6.064	-0.031	10.941
90.0	13.133	0.142	100.6	5.480	0.059	5.409	-0.013	1.425
95.0	11.389	0.166	105.5	4.910	0.072	4.808	-0.021	2.026
105.0	9.492	0.100	115.2	4.368	0.046	3.809	-0.128	147.632
115.0	5.748	0.071	124.6	2.817	0.035	3.088	0.097	60.390
135.0	4.331	0.054	142.5	2.372	0.030	2.273	-0.041	11.114
145.0	4.028	0.081	151.0	2.305	0.047	2.055	-0.109	28.906
155.0	3.719	0.056	159.4	2.203	0.033	1.907	-0.135	81.192
165.0	2.930	0.064	167.7	1.777	0.039	1.812	0.019	0.781

^{6}Li PROTON ELASTIC SCATTERING ANALYZING POWERS

values of k_l^n

	$n=0$	$n=1$	$n=2$	$n=3$
$l=1$	0.107	1.698	-0.130	0.002
$l=2$	12.480	1.791	-0.245	0.007
$l=3$	-19.045	4.877	-0.312	0.006
$l=4$	-5.119	1.103	-0.043	
$l=5$	-1.709	0.006	0.020	-0.001
$l=6$	-0.625	-0.028	0.003	
$l=7$	-0.105	-0.061	0.004	
$l=8$	-0.083			

^{6}Li PROTON INELASTIC SCATTERING ANALYZING POWERS

values of k_l^n

	$n=0$	$n=1$	$n=2$	$n=3$
$l=1$	-4.753	1.361	-0.111	0.003
$l=2$	-1.782	0.821	-0.076	0.002
$l=3$	0.467	-0.266	0.027	-0.001
$=l=4$	-0.173	0.050	-0.003	
$l=5$	0.061	-0.023	0.001	

^{6}Li PROTON ELASTIC SCATTERING ANALYZING POWERS

Proton Energy 5.0 MeV

Monitor Analyzing Power 0.964 ± 0.010

Excitation Energy (J^π) 0.00 MeV (1^+)

experimental data			calculation			
θ_{Lab}	$A_y(\theta_{Lab})$	$\Delta A_y(\theta_{Lab})$	θ_{cm}	$A_y(\theta_{cm})$	Dev	χ^2
20.0	-0.015	0.001	23.3	-0.020	-0.005	10.378
30.0	-0.090	0.003	34.8	-0.085	0.005	3.610
40.0	-0.196	0.002	46.2	-0.189	0.007	8.362
50.0	-0.273	0.003	57.4	-0.263	0.010	10.390
60.0	-0.301	0.003	68.4	-0.302	0.000	0.026
70.0	-0.260	0.005	79.1	-0.283	-0.023	26.099
80.0	-0.154	0.003	89.5	-0.152	0.002	0.378
90.0	0.033	0.005	99.7	0.033	-0.001	0.021
100.0	0.233	0.004	109.5	0.233	0.000	0.000
110.0	0.403	0.005	119.1	0.438	0.035	58.157
120.0	0.506	0.006	128.4	0.563	0.057	104.331
130.0	0.535	0.004	137.4	0.573	0.038	75.059
135.0	0.513	0.005	141.8	0.551	0.038	49.260
140.0	0.479	0.004	146.2	0.518	0.039	82.810
145.0	0.447	0.007	150.5	0.475	0.028	15.497
155.0	0.333	0.005	159.1	0.364	0.031	41.953
165.0	0.207	0.005	167.5	0.225	0.018	12.631

^{6}Li PROTON INELASTIC SCATTERING ANALYZING POWERS

Excitation Energy (J^π) 2.18 MeV (3^+)

experimental data			calculation			
θ_{Lab}	$A_y(\theta_{Lab})$	$\Delta A_y(\theta_{Lab})$	θ_{cm}	$A_y(\theta_{cm})$	Dev	χ^2
20.0	-0.009	0.024	24.7	-0.004	0.005	0.044
40.0	-0.040	0.012	48.9	-0.051	-0.011	0.861
50.0	-0.049	0.016	60.6	-0.060	-0.011	0.474
60.0	-0.036	0.011	72.0	-0.050	-0.014	1.775
70.0	-0.028	0.016	83.0	-0.025	0.003	0.039
80.0	0.018	0.009	93.7	0.010	-0.008	0.694
90.0	0.028	0.010	103.9	0.054	0.025	6.010
100.0	0.100	0.010	113.7	0.104	0.004	0.134
110.0	0.151	0.015	123.0	0.155	0.004	0.067
130.0	0.229	0.012	140.6	0.216	-0.013	1.146
135.0	0.172	0.016	144.8	0.216	0.044	7.709
140.0	0.189	0.017	148.9	0.209	0.020	1.378
155.0	0.143	0.017	160.8	0.153	0.010	0.305

^{6}Li PROTON ELASTIC SCATTERING ANALYZING POWERS

Proton Energy 6.0 MeV

Monitor Analyzing Power 0.970 ± 0.010

Excitation Energy (J^π) 0.00 MeV (1^+)

experimental data			calculation			
θ_{Lab}	$A_y(\theta_{Lab})$	$\Delta A_y(\theta_{Lab})$	θ_{cm}	$A_y(\theta_{cm})$	Dev	χ^2
30.0	-0.102	0.002	34.8	-0.101	0.001	0.088
40.0	-0.181	0.004	46.2	-0.202	-0.021	23.942
50.0	-0.257	0.004	57.4	-0.285	-0.028	48.407
60.0	-0.308	0.005	68.4	-0.326	-0.018	12.195
110.0	0.523	0.009	119.1	0.465	-0.058	40.023
120.0	0.645	0.012	128.4	0.592	-0.053	19.193
130.0	0.685	0.009	137.4	0.609	-0.076	75.059
140.0	0.642	0.009	146.2	0.555	-0.088	99.319

^{6}Li PROTON INELASTIC SCATTERING ANALYZING POWERS

Excitation Energy (J^π) 2.18 MeV (3^+)

experimental data			calculation			
θ_{Lab}	$A_y(\theta_{Lab})$	$\Delta A_y(\theta_{Lab})$	θ_{cm}	$A_y(\theta_{cm})$	Dev	χ^2
30.0	-0.077	0.012	36.4	-0.062	0.014	1.393
40.0	-0.083	0.016	48.2	-0.090	-0.006	0.164
50.0	-0.119	0.012	59.8	-0.103	0.017	1.921
60.0	-0.110	0.014	71.1	-0.096	0.014	0.972
110.0	0.126	0.023	122.0	0.139	0.014	0.350
130.0	0.216	0.022	139.8	0.245	0.029	1.876
140.0	0.201	0.028	148.2	0.256	0.054	3.831

^{6}Li PROTON ELASTIC SCATTERING ANALYZING POWERS

Proton Energy 7.0 MeV

Monitor Analyzing Power 0.972 ± 0.010

Excitation Energy (J^π) 0.00 MeV (1^+)

experimental data			calculation			
θ_{Lab}	$A_y(\theta_{Lab})$	$\Delta A_y(\theta_{Lab})$	θ_{cm}	$A_y(\theta_{cm})$	Dev	χ^2
20.0	-0.038	0.001	23.3	-0.044	-0.005	16.559
30.0	-0.133	0.002	34.8	-0.112	0.021	80.922
40.0	-0.209	0.002	46.2	-0.212	-0.002	0.826
50.0	-0.285	0.003	57.4	-0.303	-0.018	35.482
60.0	-0.365	0.003	68.4	-0.349	0.016	23.408
70.0	-0.331	0.006	79.1	-0.285	0.046	63.148
80.0	-0.094	0.005	89.6	-0.091	0.003	0.373
90.0	0.147	0.008	99.7	0.111	-0.036	22.587
100.0	0.304	0.005	109.5	0.301	-0.004	0.453
110.0	0.545	0.006	119.1	0.487	-0.058	89.814
120.0	0.691	0.010	128.4	0.615	-0.075	57.714
130.0	0.737	0.007	137.4	0.644	-0.092	164.552
135.0	0.735	0.007	141.8	0.628	-0.107	228.521
140.0	0.691	0.007	146.2	0.595	-0.096	183.889
145.0	0.672	0.010	150.5	0.547	-0.125	165.852
155.0	0.456	0.006	159.1	0.415	-0.041	41.482
165.0	0.272	0.006	167.5	0.253	-0.019	9.153

^{6}Li PROTON INELASTIC SCATTERING ANALYZING POWERS

Excitation Energy (J^π) 2.18 MeV (3^+)

experimental data			calculation			
θ_{Lab}	$A_y(\theta_{Lab})$	$\Delta A_y(\theta_{Lab})$	θ_{cm}	$A_y(\theta_{cm})$	Dev	χ^2
20.0	-0.032	0.025	24.1	-0.048	-0.016	0.394
30.0	-0.071	0.012	36.1	-0.080	-0.010	0.660
40.0	-0.117	0.008	47.8	-0.109	0.008	1.010
50.0	-0.128	0.008	59.3	-0.124	0.004	0.278
60.0	-0.128	0.007	70.5	-0.122	0.006	0.745
70.0	-0.123	0.013	81.4	-0.103	0.020	2.434
80.0	-0.051	0.008	92.0	-0.069	-0.018	4.894
90.0	-0.002	0.014	102.2	-0.018	-0.016	1.405
100.0	0.064	0.009	112.0	0.047	-0.016	3.014
110.0	0.105	0.013	121.4	0.125	0.021	2.631
130.0	0.294	0.014	139.3	0.265	-0.029	4.075
135.0	0.337	0.015	143.6	0.284	-0.053	12.960
140.0	0.390	0.019	147.8	0.292	-0.097	27.461
155.0	0.249	0.016	160.1	0.248	-0.001	0.003
165.0	0.170	0.021	168.1	0.167	-0.003	0.022

^{6}Li PROTON ELASTIC SCATTERING ANALYZING POWERS

Proton Energy 8.0 MeV

Monitor Analyzing Power 0.976 ± 0.010

Excitation Energy (J^{π}) 0.00 MeV (1^{+})

experimental data			calculation			
θ_{Lab}	$A_y(\theta_{Lab})$	$\Delta A_y(\theta_{Lab})$	θ_{cm}	$A_y(\theta_{cm})$	Dev	χ^2
30.0	-0.139	0.004	34.8	-0.120	0.019	23.734
40.0	-0.217	0.007	46.2	-0.217	0.000	0.001
50.0	-0.342	0.007	57.4	-0.317	0.025	12.481
60.0	-0.400	0.010	68.4	-0.370	0.030	9.733
110.0	0.513	0.016	119.1	0.501	-0.013	0.629
120.0	0.664	0.023	128.4	0.628	-0.036	2.490
130.0	0.719	0.016	137.4	0.675	-0.045	7.369
140.0	0.703	0.016	146.2	0.636	-0.067	17.394

^{6}Li PROTON INELASTIC SCATTERING ANALYZING POWERS

Excitation Energy (J^{π}) 2.18 MeV (3^{+})

experimental data			calculation			
θ_{Lab}	$A_y(\theta_{Lab})$	$\Delta A_y(\theta_{Lab})$	θ_{cm}	$A_y(\theta_{cm})$	Dev	χ^2
30.0	-0.080	0.020	35.9	-0.091	-0.011	0.297
40.0	-0.086	0.027	47.5	-0.120	-0.034	1.586
50.0	-0.153	0.019	59.0	-0.137	0.016	0.675
60.0	-0.170	0.021	70.2	-0.138	0.032	2.273
110.0	0.221	0.034	121.0	0.113	-0.108	10.123
120.0	0.269	0.046	130.2	0.202	-0.067	2.095
130.0	0.248	0.033	139.0	0.278	0.029	0.786
140.0	0.289	0.040	147.5	0.319	0.030	0.564

^{6}Li PROTON ELASTIC SCATTERING ANALYZING POWERS

Proton Energy 9.0 MeV

Monitor Analyzing Power 0.980 ± 0.010

Excitation Energy (J^π) 0.00 MeV (1^+)

experimental data			calculation			
θ_{Lab}	$A_y(\theta_{Lab})$	$\Delta A_y(\theta_{Lab})$	θ_{cm}	$A_y(\theta_{cm})$	Dev	χ^2
20.0	-0.056	0.002	23.3	-0.059	-0.003	2.412
30.0	-0.129	0.003	34.8	-0.126	0.003	1.415
40.0	-0.228	0.003	46.2	-0.221	0.007	5.977
50.0	-0.326	0.004	57.4	-0.327	-0.001	0.024
60.0	-0.390	0.005	68.4	-0.388	0.002	0.250
70.0	-0.276	0.009	79.1	-0.270	0.007	0.599
80.0	-0.071	0.007	89.6	0.000	0.071	107.702
90.0	0.266	0.010	99.7	0.205	-0.061	33.552
100.0	0.365	0.008	109.6	0.359	-0.006	0.627
110.0	0.479	0.010	119.1	0.502	0.023	5.681
120.0	0.596	0.014	128.4	0.625	0.028	4.083
130.0	0.700	0.010	137.4	0.694	-0.006	0.355
135.0	0.694	0.010	141.8	0.697	0.003	0.087
140.0	0.707	0.010	146.2	0.675	-0.032	9.462
145.0	0.653	0.014	150.5	0.628	-0.025	3.055
155.0	0.487	0.010	159.1	0.476	-0.011	1.182
165.0	0.294	0.010	167.5	0.286	-0.007	0.515

^{6}Li PROTON INELASTIC SCATTERING ANALYZING POWERS

Excitation Energy (J^π) 2.18 MeV (3^+)

experimental data			calculation			
θ_{Lab}	$A_y(\theta_{Lab})$	$\Delta A_y(\theta_{Lab})$	θ_{cm}	$A_y(\theta_{cm})$	Dev	χ^2
30.0	-0.086	0.016	35.7	-0.098	-0.012	0.630
40.0	-0.139	0.011	47.4	-0.126	0.013	1.422
50.0	-0.129	0.011	58.8	-0.144	-0.015	1.794
60.0	-0.160	0.010	69.9	-0.149	0.012	1.470
70.0	-0.151	0.014	80.8	-0.138	0.013	0.785
90.0	-0.077	0.016	101.5	-0.061	0.015	0.858
100.0	0.019	0.013	111.3	0.011	-0.008	0.430
110.0	0.111	0.018	120.8	0.102	-0.009	0.247
120.0	0.234	0.027	129.9	0.199	-0.035	1.623
130.0	0.299	0.020	138.8	0.284	-0.015	0.614
135.0	0.307	0.020	143.1	0.315	0.008	0.155
140.0	0.353	0.021	147.3	0.335	-0.018	0.732
145.0	0.302	0.029	151.5	0.342	0.041	1.916
155.0	0.264	0.022	159.8	0.311	0.048	4.806
165.0	0.215	0.027	167.9	0.219	0.004	0.023

^{6}Li PROTON ELASTIC SCATTERING ANALYZING POWERS

Proton Energy 10.0 MeV

Monitor Analyzing Power 0.984 ± 0.010

Excitation Energy (J^π) 0.00 MeV (1^+)

experimental data			calculation			
θ_{Lab}	$A_y(\theta_{Lab})$	$\Delta A_y(\theta_{Lab})$	θ_{cm}	$A_y(\theta_{cm})$	Dev	χ^2
20.0	-0.064	0.002	23.3	-0.064	0.000	0.053
30.0	-0.144	0.003	34.8	-0.130	0.015	24.635
40.0	-0.228	0.003	46.2	-0.223	0.005	3.098
50.0	-0.322	0.004	57.4	-0.332	-0.011	6.227
60.0	-0.390	0.006	68.4	-0.400	-0.009	2.576
70.0	-0.249	0.010	79.1	-0.249	0.000	0.000
80.0	0.113	0.009	89.6	0.062	-0.052	36.490
90.0	0.288	0.012	99.7	0.257	-0.031	6.911
100.0	0.363	0.009	109.6	0.379	0.016	3.412
110.0	0.438	0.011	119.1	0.488	0.050	21.451
120.0	0.552	0.016	128.4	0.600	0.048	8.523
130.0	0.667	0.012	137.4	0.694	0.027	4.971
135.0	0.668	0.012	141.9	0.715	0.047	16.208
140.0	0.664	0.013	146.2	0.706	0.042	11.252
145.0	0.634	0.017	150.6	0.666	0.032	3.791
155.0	0.475	0.012	159.1	0.509	0.034	8.161
165.0	0.298	0.012	167.5	0.305	0.007	0.387

^{6}Li PROTON INELASTIC SCATTERING ANALYZING POWERS

Excitation Energy (J^π) 2.18 MeV (3^+)

experimental data			calculation			
θ_{Lab}	$A_y(\theta_{Lab})$	$\Delta A_y(\theta_{Lab})$	θ_{cm}	$A_y(\theta_{cm})$	Dev	χ^2
20.0	-0.065	0.012	23.8	-0.071	-0.006	0.232
30.0	-0.079	0.014	35.6	-0.103	-0.024	2.919
40.0	-0.156	0.011	47.2	-0.130	0.026	5.278
50.0	-0.140	0.011	58.6	-0.148	-0.008	0.514
60.0	-0.157	0.011	69.7	-0.155	0.001	0.012
70.0	-0.087	0.014	80.6	-0.149	-0.062	18.853
80.0	-0.140	0.012	91.1	-0.125	0.015	1.516
90.0	-0.075	0.018	101.3	-0.078	-0.003	0.034
100.0	-0.040	0.014	111.1	-0.004	0.036	6.790
120.0	0.216	0.031	129.7	0.194	-0.022	0.507
130.0	0.275	0.022	138.6	0.284	0.009	0.181
135.0	0.347	0.022	142.9	0.318	-0.029	1.788
140.0	0.357	0.023	147.2	0.341	-0.016	0.494
145.0	0.317	0.033	151.4	0.351	0.034	1.096
155.0	0.320	0.022	159.7	0.325	0.005	0.053
165.0	0.244	0.029	167.9	0.232	-0.012	0.158

^{6}Li PROTON ELASTIC SCATTERING ANALYZING POWERS

Proton Energy 11.0 MeV

Monitor Analyzing Power 0.986 ± 0.010

Excitation Energy (J^{π}) 0.00 MeV (1^{+})

experimental data			calculation			
θ_{Lab}	$A_y(\theta_{Lab})$	$\Delta A_y(\theta_{Lab})$	θ_{cm}	$A_y(\theta_{cm})$	Dev	χ^2
110.0	0.435	0.010	119.1	0.458	0.023	5.611
120.0	0.496	0.015	128.4	0.553	0.057	15.189
130.0	0.642	0.011	137.4	0.668	0.025	5.060
140.0	0.683	0.012	146.2	0.721	0.038	10.387

^{6}Li PROTON INELASTIC SCATTERING ANALYZING POWERS

Excitation Energy (J^{π}) 2.18 MeV (3^{+})

experimental data			calculation			
θ_{Lab}	$A_y(\theta_{Lab})$	$\Delta A_y(\theta_{Lab})$	θ_{cm}	$A_y(\theta_{cm})$	Dev	χ^2
110.0	0.115	0.018	120.4	0.082	-0.033	3.362
120.0	0.146	0.025	129.6	0.187	0.041	2.649
130.0	0.254	0.017	138.5	0.278	0.024	2.070
140.0	0.257	0.025	147.1	0.337	0.080	10.039

^{6}Li PROTON ELASTIC SCATTERING ANALYZING POWERS

Proton Energy 12.0 MeV

Monitor Analyzing Power 0.988 ± 0.010

Excitation Energy (J^π) 0.00 MeV (1^+)

experimental data			calculation			
θ_{Lab}	$A_y(\theta_{Lab})$	$\Delta A_y(\theta_{Lab})$	θ_{cm}	$A_y(\theta_{cm})$	Dev	χ^2
20.0	-0.062	0.002	23.3	-0.071	-0.009	35.522
30.0	-0.158	0.003	34.9	-0.134	0.024	79.342
40.0	-0.227	0.003	46.2	-0.223	0.004	1.881
50.0	-0.325	0.004	57.5	-0.334	-0.009	4.575
60.0	-0.374	0.005	68.4	-0.401	-0.027	35.067
70.0	-0.171	0.009	79.1	-0.169	0.002	0.027
80.0	0.251	0.007	89.6	0.225	-0.026	12.222
90.0	0.367	0.007	99.7	0.364	-0.003	0.122
100.0	0.380	0.007	109.6	0.390	0.009	1.723
110.0	0.373	0.010	119.1	0.415	0.042	17.087
120.0	0.481	0.015	128.4	0.487	0.006	0.161
130.0	0.563	0.012	137.4	0.613	0.050	16.912
135.0	0.603	0.012	141.9	0.674	0.071	34.165
140.0	0.650	0.013	146.2	0.709	0.059	20.988
145.0	0.702	0.017	150.6	0.701	-0.001	0.002
155.0	0.521	0.013	159.1	0.561	0.041	10.377
165.0	0.316	0.013	167.5	0.341	0.025	3.689

^{6}Li PROTON INELASTIC SCATTERING ANALYZING POWERS

Excitation Energy (J^π) 2.18 MeV (3^+)

experimental data			calculation			
θ_{Lab}	$A_y(\theta_{Lab})$	$\Delta A_y(\theta_{Lab})$	θ_{cm}	$A_y(\theta_{cm})$	Dev	χ^2
20.0	-0.070	0.012	23.7	-0.081	-0.011	0.872
30.0	-0.125	0.015	35.5	-0.110	0.015	0.992
40.0	-0.129	0.010	47.0	-0.134	-0.004	0.216
50.0	-0.150	0.010	58.4	-0.152	-0.001	0.021
60.0	-0.119	0.008	69.5	-0.163	-0.045	32.842
70.0	-0.182	0.012	80.3	-0.166	0.017	1.854
80.0	-0.164	0.009	90.8	-0.151	0.013	1.966
90.0	-0.103	0.011	101.0	-0.107	-0.004	0.128
100.0	-0.045	0.012	110.8	-0.029	0.016	1.784
110.0	0.022	0.017	120.3	0.073	0.051	9.035
120.0	0.120	0.024	129.5	0.179	0.059	6.069
130.0	0.280	0.018	138.4	0.268	-0.011	0.370
135.0	0.296	0.019	142.7	0.302	0.005	0.076
140.0	0.319	0.020	147.0	0.325	0.006	0.088
145.0	0.260	0.028	151.3	0.335	0.075	7.083
155.0	0.289	0.022	159.6	0.312	0.024	1.203
165.0	0.248	0.027	167.8	0.225	-0.023	0.682

^{6}Li PROTON ELASTIC SCATTERING ANALYZING POWERS

Proton Energy 13.0 MeV

Monitor Analyzing Power 0.987 ± 0.010

Excitation Energy (J^{π}) 0.00 MeV (1^{+})

experimental data			calculation			
θ_{Lab}	$A_y(\theta_{Lab})$	$\Delta A_y(\theta_{Lab})$	θ_{cm}	$A_y(\theta_{cm})$	Dev	χ^2
110.0	0.366	0.010	119.1	0.365	-0.001	0.009
120.0	0.420	0.016	128.4	0.411	-0.009	0.297
130.0	0.521	0.013	137.4	0.537	0.015	1.344
140.0	0.634	0.014	146.2	0.668	0.034	5.489

^{6}Li PROTON INELASTIC SCATTERING ANALYZING POWERS

Excitation Energy (J^{π}) 2.18 MeV (3^{+})

experimental data			calculation			
θ_{Lab}	$A_y(\theta_{Lab})$	$\Delta A_y(\theta_{Lab})$	θ_{cm}	$A_y(\theta_{cm})$	Dev	χ^2
110.0	0.077	0.018	120.2	0.066	-0.011	0.400
120.0	0.145	0.027	129.4	0.171	0.026	0.937
130.0	0.300	0.020	138.3	0.256	-0.045	5.012
140.0	0.292	0.021	146.9	0.305	0.013	0.401

^{6}Li PROTON ELASTIC SCATTERING ANALYZING POWERS

Proton Energy 14.0 MeV

Monitor Analyzing Power 0.985 ± 0.010

Excitation Energy (J^{π}) 0.00 MeV (1^{+})

experimental data			calculation			
θ_{Lab}	$A_y(\theta_{Lab})$	$\Delta A_y(\theta_{Lab})$	θ_{cm}	$A_y(\theta_{cm})$	Dev	χ^2
20.0	-0.065	0.002	23.3	-0.072	-0.007	17.988
30.0	-0.136	0.003	34.9	-0.134	0.002	0.329
40.0	-0.220	0.003	46.3	-0.222	-0.001	0.213
50.0	-0.318	0.005	57.5	-0.328	-0.010	4.455
60.0	-0.383	0.006	68.4	-0.371	0.012	3.952
70.0	-0.086	0.012	79.2	-0.049	0.037	9.615
80.0	0.381	0.009	89.6	0.402	0.021	5.010
90.0	0.445	0.013	99.7	0.450	0.004	0.123
100.0	0.368	0.009	109.6	0.373	0.005	0.317
110.0	0.342	0.011	119.2	0.320	-0.022	3.637
120.0	0.394	0.017	128.4	0.339	-0.055	10.115
130.0	0.481	0.014	137.4	0.454	-0.028	3.706
135.0	0.557	0.015	141.9	0.535	-0.022	2.225
140.0	0.576	0.016	146.2	0.606	0.030	3.463
145.0	0.604	0.022	150.6	0.641	0.037	2.948
155.0	0.562	0.016	159.1	0.566	0.004	0.051
165.0	0.326	0.016	167.5	0.364	0.039	5.763

^{6}Li PROTON INELASTIC SCATTERING ANALYZING POWERS

Excitation Energy (J^{π}) 2.18 MeV (3^{+})

experimental data			calculation			
θ_{Lab}	$A_y(\theta_{Lab})$	$\Delta A_y(\theta_{Lab})$	θ_{cm}	$A_y(\theta_{cm})$	Dev	χ^2
20.0	-0.066	0.013	23.7	-0.090	-0.024	3.313
30.0	-0.149	0.017	35.4	-0.115	0.034	4.120
40.0	-0.161	0.011	46.9	-0.135	0.026	5.565
50.0	-0.157	0.011	58.2	-0.154	0.003	0.087
60.0	-0.188	0.009	69.3	-0.171	0.017	3.552
70.0	-0.194	0.014	80.1	-0.182	0.012	0.765
80.0	-0.176	0.011	90.6	-0.175	0.001	0.006
90.0	-0.146	0.018	100.8	-0.134	0.011	0.405
100.0	-0.034	0.014	110.6	-0.050	-0.016	1.287
110.0	0.085	0.019	120.1	0.060	-0.025	1.783
120.0	0.200	0.027	129.3	0.165	-0.035	1.598
130.0	0.264	0.021	138.2	0.243	-0.021	1.001
135.0	0.265	0.020	142.6	0.268	0.003	0.031
140.0	0.294	0.021	146.9	0.283	-0.011	0.262
145.0	0.281	0.029	151.1	0.288	0.007	0.050
155.0	0.253	0.021	159.5	0.260	0.007	0.106
165.0	0.182	0.024	167.8	0.184	0.002	0.004

^{6}Li PROTON ELASTIC SCATTERING ANALYZING POWERS

Proton Energy 16.0 MeV

Monitor Analyzing Power 0.974 ± 0.010

Excitation Energy (J^π) 0.00 MeV (1^+)

experimental data			calculation			
θ_{Lab}	$A_y(\theta_{Lab})$	$\Delta A_y(\theta_{Lab})$	θ_{cm}	$A_y(\theta_{cm})$	Dev	χ^2
20.0	-0.067	0.001	23.3	-0.067	-0.001	0.328
30.0	-0.136	0.002	34.9	-0.132	0.004	3.683
40.0	-0.228	0.002	46.3	-0.226	0.002	0.771
50.0	-0.329	0.004	57.5	-0.329	-0.001	0.026
60.0	-0.366	0.005	68.5	-0.340	0.026	25.231
70.0	0.032	0.011	79.2	0.030	-0.002	0.026
80.0	0.511	0.008	89.6	0.495	-0.016	3.715
90.0	0.501	0.011	99.8	0.504	0.003	0.065
100.0	0.390	0.008	109.6	0.386	-0.004	0.231
110.0	0.315	0.009	119.2	0.288	-0.027	9.379
120.0	0.331	0.011	128.4	0.260	-0.071	39.271
130.0	0.392	0.010	137.5	0.357	-0.035	13.376
135.0	0.481	0.009	141.9	0.448	-0.032	14.556
140.0	0.577	0.011	146.2	0.537	-0.040	12.808
145.0	0.647	0.013	150.6	0.593	-0.054	17.306
155.0	0.601	0.010	159.1	0.559	-0.043	18.233
165.0	0.394	0.013	167.5	0.380	-0.014	1.257

^{6}Li PROTON INELASTIC SCATTERING ANALYZING POWERS

Excitation Energy (J^π) 2.18 MeV (3^+)

experimental data			calculation			
θ_{Lab}	$A_y(\theta_{Lab})$	$\Delta A_y(\theta_{Lab})$	θ_{cm}	$A_y(\theta_{cm})$	Dev	χ^2
20.0	-0.099	0.009	23.6	-0.096	0.003	0.084
30.0	-0.125	0.011	35.3	-0.118	0.007	0.417
50.0	-0.160	0.007	58.1	-0.162	-0.002	0.055
60.0	-0.185	0.008	69.2	-0.186	-0.002	0.042
70.0	-0.207	0.013	80.0	-0.204	0.003	0.045
90.0	-0.145	0.016	100.6	-0.155	-0.010	0.406
100.0	-0.039	0.013	110.5	-0.063	-0.024	3.248
110.0	0.056	0.015	120.0	0.059	0.003	0.043
120.0	0.182	0.018	129.2	0.171	-0.010	0.335
135.0	0.240	0.011	142.5	0.256	0.016	2.290
140.0	0.293	0.014	146.8	0.259	-0.034	5.960
145.0	0.249	0.016	151.1	0.251	0.002	0.020
155.0	0.230	0.012	159.5	0.208	-0.022	3.255
165.0	0.160	0.021	167.7	0.136	-0.024	1.326

^{6}Li PROTON ELASTIC SCATTERING ANALYZING POWERS

Proton Energy 17.0 MeV

Monitor Analyzing Power 0.968 ± 0.010

Excitation Energy (J^π) 0.00 MeV (1^+)

experimental data			calculation			
θ_{Lab}	$A_y(\theta_{Lab})$	$\Delta A_y(\theta_{Lab})$	θ_{cm}	$A_y(\theta_{cm})$	Dev	χ^2
20.0	-0.068	0.001	23.3	-0.063	0.005	11.127
30.0	-0.136	0.002	34.9	-0.130	0.005	4.666
40.0	-0.219	0.003	46.3	-0.233	-0.013	24.741
50.0	-0.327	0.004	57.5	-0.340	-0.013	9.640
60.0	-0.354	0.006	68.5	-0.339	0.015	6.807
70.0	0.061	0.012	79.2	0.036	-0.025	4.371
80.0	0.543	0.009	89.6	0.509	-0.034	14.298
85.0	0.558	0.007	94.7	0.556	-0.002	0.053
90.0	0.527	0.009	99.8	0.530	0.003	0.112
95.0	0.441	0.010	104.7	0.479	0.038	15.162
105.0	0.333	0.007	114.4	0.371	0.039	27.619
115.0	0.317	0.011	123.8	0.298	-0.019	3.058
135.0	0.439	0.014	141.9	0.552	0.113	70.175
145.0	0.617	0.021	150.6	0.722	0.105	24.482
155.0	0.634	0.016	159.1	0.649	0.015	0.873
165.0	0.422	0.022	167.5	0.429	0.007	0.089

^{6}Li PROTON INELASTIC SCATTERING ANALYZING POWERS

Excitation Energy (J^π) 2.18 MeV (3^+)

experimental data			calculation			
θ_{Lab}	$A_y(\theta_{Lab})$	$\Delta A_y(\theta_{Lab})$	θ_{cm}	$A_y(\theta_{cm})$	Dev	χ^2
20.0	-0.080	0.012	23.6	-0.096	-0.015	1.781
30.0	-0.137	0.014	35.3	-0.119	0.018	1.789
40.0	-0.150	0.009	46.8	-0.142	0.008	0.915
50.0	-0.148	0.009	58.1	-0.170	-0.021	5.578
60.0	-0.189	0.008	69.2	-0.197	-0.008	1.046
80.0	-0.241	0.011	90.4	-0.208	0.033	9.397
85.0	-0.191	0.009	95.6	-0.190	0.002	0.026
90.0	-0.159	0.013	100.6	-0.160	-0.001	0.011
95.0	-0.126	0.016	105.5	-0.118	0.008	0.222
105.0	0.007	0.012	115.2	-0.002	-0.009	0.545
115.0	0.140	0.018	124.6	0.131	-0.009	0.279
135.0	0.242	0.016	142.5	0.283	0.041	6.495
145.0	0.216	0.025	151.0	0.266	0.050	4.122
155.0	0.218	0.019	159.4	0.206	-0.012	0.388
165.0	0.144	0.029	167.7	0.127	-0.017	0.355

^{27}Al PROTON ELASTIC SCATTERING CROSS SECTIONS

values of k_l^n

	$n=0$	$n=1$	$n=2$	$n=3$
$l=0$	680.090	-91.822	4.772	-0.085
$l=1$	1517.100	-195.417	9.742	-0.166
$l=2$	1769.624	-200.168	8.799	-0.131
$l=3$	1729.504	-184.624	7.930	-0.118
$l=4$	1402.805	-110.605	2.735	
$l=5$	1129.089	-84.526	2.096	
$l=6$	868.940	-68.169	1.820	
$l=7$	557.230	-32.453	-0.160	0.038
$l=8$	348.494	-23.307	0.418	
$l=9$	152.579	-7.346		
$l=10$	47.729	-2.412		

^{27}Al PROTON ELASTIC SCATTERING ANALYZING POWERS

values of k_l^n

	$n=0$	$n=1$	$n=2$	$n=3$
$l=1$	55.242	-14.091	1.213	-0.033
$l=2$	35.538	-8.074	0.635	-0.015
$l=3$	25.383	-8.312	0.744	-0.019
$l=4$	3.283	0.186		
$l=5$	-6.362	1.655	-0.050	
$l=6$	-7.760	1.866	-0.061	
$l=7$	0.051	0.153		
$l=8$	0.010	0.078		
$l=9$	0.384			

^{27}Al PROTON ELASTIC SCATTERING CROSS SECTIONS

Proton Energy	5.0 MeV	
Normalization, Normalization Uncertainty	0.65	5%
Excitation Energy (J^{π})	0.00 MeV	($5/2^{+}$)

not renormalized			renormalized			calculation		
θ_{Lab}	$\sigma(\theta_{Lab})$	$\Delta\sigma(\theta_{Lab})$	θ_{cm}	$\sigma(\theta_{cm})$	$\Delta\sigma(\theta_{cm})$	$\sigma(\theta_{cm})$	Dev	χ^2
30.0	2327.887	23.330	31.1	1419.615	14.227	1160.939	-0.182	330.568
40.0	800.803	6.834	41.4	491.945	4.198	448.530	-0.088	106.929
50.0	448.809	4.665	51.6	278.248	2.892	258.788	-0.070	45.277
60.0	237.698	2.811	61.9	148.942	1.762	161.067	0.081	47.382
70.0	250.308	4.342	72.0	158.698	2.753	99.563	-0.373	461.458
80.0	170.356	2.490	82.1	109.380	1.598	79.562	-0.273	347.979
90.0	82.857	2.397	92.2	53.895	1.559	61.371	0.139	22.993
100.0	54.375	1.420	102.1	35.835	0.936	41.659	0.163	38.744
110.0	31.833	1.176	112.0	21.246	0.785	33.059	0.556	226.378
120.0	32.207	1.433	121.9	21.755	0.968	29.044	0.335	56.740
130.0	35.720	0.919	131.6	24.390	0.627	27.502	0.128	24.589
135.0	37.411	1.263	136.5	25.671	0.867	28.894	0.126	13.816
140.0	39.459	0.964	141.4	27.197	0.664	31.051	0.142	33.655
145.0	42.069	1.969	146.2	29.114	1.362	32.855	0.128	7.539
155.0	50.923	1.410	155.9	35.477	0.983	34.418	-0.030	1.161
165.0	50.834	1.605	165.6	35.576	1.123	39.075	0.098	9.705

^{27}Al PROTON ELASTIC SCATTERING ANALYZING POWERS

Monitor Analyzing Power	0.964 ± 0.010	
Excitation Energy (J^{π})	0.00 MeV	($5/2^{+}$)

experimental data			calculation			
θ_{Lab}	$A_y(\theta_{Lab})$	$\Delta A_y(\theta_{Lab})$	θ_{cm}	$A_y(\theta_{cm})$	Dev	χ^2
30.0	-0.020	0.008	31.1	-0.023	-0.003	0.132
40.0	0.000	0.010	41.4	-0.050	-0.050	26.751
50.0	0.001	0.013	51.6	-0.078	-0.080	37.024
60.0	0.002	0.014	61.9	-0.100	-0.101	50.033
70.0	0.013	0.020	72.0	-0.111	-0.124	38.802
80.0	-0.023	0.019	82.1	-0.124	-0.101	28.839
90.0	-0.191	0.032	92.2	-0.191	0.000	0.000
100.0	-0.312	0.035	102.1	-0.284	0.028	0.632
110.0	-0.245	0.056	112.0	-0.246	-0.001	0.000
120.0	-0.090	0.062	121.9	-0.043	0.047	0.576
130.0	0.159	0.035	131.6	0.267	0.107	9.343
135.0	0.232	0.046	136.5	0.392	0.160	11.988
140.0	0.326	0.033	141.4	0.463	0.137	17.331
145.0	0.470	0.061	146.2	0.483	0.013	0.045
155.0	0.241	0.037	155.9	0.398	0.158	17.843
165.0	0.208	0.043	165.6	0.192	-0.017	0.154

^{27}Al PROTON ELASTIC SCATTERING CROSS SECTIONS

Proton Energy	6.0 MeV	
Normalization, Normalization Uncertainty	0.65	5%
Excitation Energy (J^{π})	0.00 MeV	($5/2^{+}$)

not renormalized			renormalized			calculation		
θ_{Lab}	$\sigma(\theta_{Lab})$	$\Delta\sigma(\theta_{Lab})$	θ_{cm}	$\sigma(\theta_{cm})$	$\Delta\sigma(\theta_{cm})$	$\sigma(\theta_{cm})$	Dev	χ^2
30.0	1514.248	13.484	31.1	923.336	8.222	980.580	0.062	48.475
40.0	597.427	10.737	41.4	367.008	6.596	353.437	-0.037	4.234
50.0	283.184	4.802	51.7	175.566	2.977	201.099	0.145	73.557
60.0	184.781	3.822	61.9	115.784	2.395	126.943	0.096	21.706
110.0	41.290	1.659	112.0	27.561	1.107	24.284	-0.119	8.757
120.0	42.592	2.422	121.9	28.770	1.636	20.946	-0.272	22.875
130.0	47.282	1.800	131.6	32.289	1.229	21.468	-0.335	77.533
140.0	62.713	2.080	141.4	43.229	1.434	28.307	-0.345	108.289

^{27}Al PROTON ELASTIC SCATTERING ANALYZING POWERS

Monitor Analyzing Power	0.970 ± 0.010	
Excitation Energy (J^{π})	0.00 MeV	($5/2^{+}$)

experimental data			calculation			
θ_{Lab}	$A_y(\theta_{Lab})$	$\Delta A_y(\theta_{Lab})$	θ_{cm}	$A_y(\theta_{cm})$	Dev	χ^2
30.0	-0.112	0.010	31.1	-0.021	0.091	86.642
40.0	-0.093	0.022	41.4	-0.028	0.065	8.529
50.0	-0.048	0.023	51.7	-0.035	0.013	0.326
60.0	0.043	0.029	61.9	-0.060	-0.103	12.905
110.0	0.005	0.058	112.0	-0.247	-0.252	18.877
120.0	0.238	0.080	121.9	0.021	-0.216	7.284
130.0	0.563	0.050	131.6	0.379	-0.184	13.476
140.0	0.615	0.043	141.4	0.537	-0.078	3.302

^{27}Al PROTON ELASTIC SCATTERING CROSS SECTIONS

Proton Energy 7.0 MeV

Normalization, Normalization Uncertainty 0.72 5%

Excitation Energy (J^{π}) 0.00 MeV ($5/2^{+}$)

not renormalized			renormalized			calculation		
θ_{Lab}	$\sigma(\theta_{Lab})$	$\Delta\sigma(\theta_{Lab})$	θ_{cm}	$\sigma(\theta_{cm})$	$\Delta\sigma(\theta_{cm})$	$\sigma(\theta_{cm})$	Dev	χ^2
20.0	5188.798	41.941	20.7	3485.627	28.174	2227.805	-0.361	1993.120
30.0	1033.266	13.437	31.1	697.901	9.076	825.997	0.184	199.218
40.0	398.584	3.105	41.4	271.197	2.112	274.002	0.010	1.763
50.0	213.277	2.008	51.7	146.450	1.379	153.238	0.046	24.236
60.0	133.021	1.120	61.9	92.318	0.777	98.920	0.072	72.119
70.0	103.075	1.606	72.0	72.388	1.128	66.453	-0.082	27.681
80.0	74.415	0.914	82.1	52.920	0.650	59.281	0.120	95.841
90.0	57.405	1.426	92.2	41.360	1.028	44.791	0.083	11.140
100.0	40.663	0.659	102.1	29.684	0.481	25.761	-0.132	66.521
110.0	27.769	0.661	112.0	20.531	0.489	17.382	-0.153	41.521
120.0	34.567	1.276	121.9	25.866	0.955	14.966	-0.421	130.275
130.0	35.485	0.706	131.7	26.842	0.534	16.978	-0.367	340.812
135.0	39.293	0.725	136.5	29.869	0.551	20.810	-0.303	270.219
140.0	44.626	0.801	141.4	34.074	0.612	25.730	-0.245	186.011
145.0	57.644	1.744	146.2	44.193	1.337	30.359	-0.313	107.063
155.0	62.336	0.964	155.9	48.114	0.744	35.844	-0.255	272.099
165.0	75.146	1.068	165.6	58.266	0.828	39.665	-0.319	504.642

^{27}Al PROTON ELASTIC SCATTERING ANALYZING POWERS

Monitor Analyzing Power 0.972 ± 0.010

Excitation Energy (J^{π}) 0.00 MeV ($5/2^{+}$)

experimental data			calculation			
θ_{Lab}	$A_y(\theta_{Lab})$	$\Delta A_y(\theta_{Lab})$	θ_{cm}	$A_y(\theta_{cm})$	Dev	χ^2
20.0	-0.013	0.002	20.7	-0.016	-0.004	1.982
30.0	-0.036	0.008	31.1	-0.022	0.014	3.200
40.0	-0.078	0.008	41.4	-0.004	0.073	84.135
50.0	-0.074	0.011	51.7	0.018	0.092	71.379
60.0	-0.107	0.008	61.9	-0.014	0.093	148.487
70.0	-0.187	0.014	72.0	-0.104	0.082	33.099
80.0	-0.300	0.014	82.1	-0.192	0.108	57.346
90.0	-0.417	0.026	92.2	-0.282	0.135	26.948
100.0	-0.474	0.019	102.1	-0.372	0.101	28.885
110.0	-0.248	0.027	112.0	-0.241	0.007	0.067
120.0	0.115	0.047	121.9	0.106	-0.009	0.039
130.0	0.519	0.025	131.7	0.480	-0.039	2.554
135.0	0.614	0.023	136.5	0.563	-0.052	5.047
140.0	0.661	0.021	141.4	0.582	-0.079	13.826
145.0	0.661	0.033	146.2	0.572	-0.089	7.256
155.0	0.538	0.019	155.9	0.496	-0.042	5.042
165.0	0.366	0.018	165.6	0.312	-0.054	9.159

^{27}Al PROTON ELASTIC SCATTERING CROSS SECTIONS

Proton Energy 8.0 MeV

Normalization, Normalization Uncertainty 0.65 5%

Excitation Energy (J^{π}) 0.00 MeV ($5/2^{+}$)

not renormalized			renormalized			calculation		
θ_{Lab}	$\sigma(\theta_{Lab})$	$\Delta\sigma(\theta_{Lab})$	θ_{cm}	$\sigma(\theta_{cm})$	$\Delta\sigma(\theta_{cm})$	$\sigma(\theta_{cm})$	Dev	χ^2
30.0	903.226	15.302	31.1	550.697	9.330	695.053	0.262	239.395
40.0	395.776	13.034	41.4	243.106	8.006	208.784	-0.141	18.378
50.0	202.563	6.493	51.7	125.570	4.025	114.306	-0.090	7.831
60.0	122.506	4.875	61.9	76.754	3.055	76.499	-0.003	0.007
110.0	23.991	2.115	112.0	16.013	1.412	12.158	-0.241	7.456
120.0	21.754	2.888	121.9	14.696	1.951	10.819	-0.264	3.950
130.0	26.400	2.237	131.7	18.030	1.528	13.811	-0.234	7.629
140.0	30.854	2.419	141.4	21.270	1.667	23.315	0.096	1.504

^{27}Al PROTON ELASTIC SCATTERING ANALYZING POWERS

Monitor Analyzing Power 0.976 ± 0.010

Excitation Energy (J^{π}) 0.00 MeV ($5/2^{+}$)

experimental data			calculation			
θ_{Lab}	$A_y(\theta_{Lab})$	$\Delta A_y(\theta_{Lab})$	θ_{cm}	$A_y(\theta_{cm})$	Dev	χ^2
30.0	0.005	0.021	31.1	-0.026	-0.030	2.168
40.0	0.113	0.044	41.4	0.021	-0.092	4.409
50.0	0.199	0.043	51.7	0.085	-0.114	6.987
60.0	0.071	0.056	61.9	0.037	-0.034	0.374
110.0	0.269	0.119	112.0	-0.219	-0.488	16.742
120.0	0.653	0.161	121.9	0.208	-0.446	7.662
130.0	0.596	0.106	131.7	0.545	-0.052	0.238
140.0	0.810	0.088	141.4	0.596	-0.214	5.978

^{27}Al PROTON ELASTIC SCATTERING CROSS SECTIONS

Proton Energy	9.0 MeV	
Normalization, Normalization Uncertainty	0.72	5%
Excitation Energy (J^{π})	0.00 MeV	($5/2^{+}$)

not renormalized			renormalized			calculation		
θ_{Lab}	$\sigma(\theta_{Lab})$	$\Delta\sigma(\theta_{Lab})$	θ_{cm}	$\sigma(\theta_{cm})$	$\Delta\sigma(\theta_{cm})$	$\sigma(\theta_{cm})$	Dev	χ^2
20.0	3020.155	15.257	20.7	2028.384	10.247	1729.450	-0.147	851.025
30.0	637.992	6.700	31.1	430.828	4.524	585.609	0.359	1170.435
40.0	248.896	2.228	41.4	169.331	1.516	156.263	-0.077	74.351
50.0	124.777	1.437	51.7	85.671	0.987	83.426	-0.026	5.177
60.0	83.195	0.984	61.9	57.738	0.683	59.181	0.025	4.469
70.0	72.212	1.310	72.0	50.709	0.920	45.647	-0.100	30.258
80.0	59.449	0.840	82.1	42.277	0.597	45.082	0.066	22.050
90.0	41.212	0.930	92.2	29.693	0.670	32.380	0.090	16.076
100.0	23.864	0.481	102.1	17.421	0.351	14.903	-0.145	51.308
110.0	11.751	0.304	112.0	8.689	0.225	8.414	-0.032	1.494
120.0	9.712	0.223	121.9	7.268	0.167	8.224	0.132	32.919
130.0	14.225	0.192	131.7	10.761	0.145	11.749	0.092	46.170
135.0	18.179	0.251	136.5	13.821	0.190	15.907	0.151	119.988
140.0	23.087	0.258	141.4	17.632	0.197	21.057	0.194	302.217
145.0	28.997	0.506	146.2	22.235	0.388	25.977	0.168	93.030
155.0	35.665	0.393	155.9	27.530	0.303	32.019	0.163	219.470
165.0	41.980	0.433	165.6	32.553	0.336	35.004	0.075	53.300

^{27}Al PROTON ELASTIC SCATTERING ANALYZING POWERS

Monitor Analyzing Power	0.980 ± 0.010	
Excitation Energy (J^{π})	0.00 MeV	($5/2^{+}$)

experimental data			calculation			
θ_{Lab}	$A_y(\theta_{Lab})$	$\Delta A_y(\theta_{Lab})$	θ_{cm}	$A_y(\theta_{cm})$	Dev	χ^2
20.0	-0.021	0.003	20.7	-0.028	-0.006	4.439
30.0	0.033	0.009	31.1	-0.034	-0.067	58.937
40.0	0.177	0.010	41.4	0.047	-0.129	173.836
50.0	0.283	0.014	51.7	0.169	-0.115	71.142
60.0	0.199	0.013	61.9	0.089	-0.110	68.840
70.0	-0.044	0.020	72.0	-0.135	-0.091	19.967
80.0	-0.228	0.016	82.1	-0.287	-0.059	13.963
90.0	-0.357	0.026	92.2	-0.396	-0.039	2.256
100.0	-0.396	0.024	102.1	-0.496	-0.100	17.219
110.0	-0.237	0.039	112.0	-0.163	0.075	3.735
120.0	0.213	0.028	121.9	0.310	0.097	11.832
130.0	0.472	0.016	131.7	0.548	0.075	23.071
135.0	0.489	0.017	136.5	0.574	0.086	25.793
140.0	0.527	0.012	141.4	0.578	0.050	16.965
145.0	0.525	0.019	146.2	0.576	0.051	7.359
155.0	0.486	0.012	155.9	0.544	0.058	21.960
165.0	0.325	0.012	165.6	0.389	0.064	30.259

^{27}Al PROTON ELASTIC SCATTERING CROSS SECTIONS

Proton Energy 10.0 MeV

Normalization, Normalization Uncertainty 0.72 5%

Excitation Energy (J^{π}) 0.00 MeV ($5/2^{+}$)

not renormalized			renormalized			calculation		
θ_{Lab}	$\sigma(\theta_{Lab})$	$\Delta\sigma(\theta_{Lab})$	θ_{cm}	$\sigma(\theta_{cm})$	$\Delta\sigma(\theta_{cm})$	$\sigma(\theta_{cm})$	Dev	χ^2
20.0	2343.049	10.031	20.7	1573.629	6.737	1530.258	-0.028	41.448
30.0	493.432	5.035	31.1	333.209	3.400	495.529	0.487	2279.537
40.0	181.036	1.573	41.4	123.164	1.070	114.933	-0.067	59.178
50.0	89.063	0.996	51.7	61.150	0.684	59.714	-0.023	4.406
60.0	71.148	0.890	61.9	49.372	0.617	46.470	-0.059	22.101
70.0	62.833	1.200	72.0	44.122	0.843	39.080	-0.114	35.790
80.0	49.959	0.750	82.1	35.528	0.534	39.781	0.120	63.495
90.0	32.203	0.619	92.2	23.202	0.446	27.484	0.185	92.109
100.0	17.674	0.303	102.1	12.904	0.221	11.118	-0.138	65.026
110.0	9.963	0.280	112.0	7.367	0.207	5.955	-0.192	46.473
120.0	12.773	0.424	121.9	9.559	0.317	6.898	-0.278	70.468
130.0	18.268	0.361	131.7	13.821	0.273	10.574	-0.235	141.379
135.0	21.582	0.382	136.5	16.408	0.290	14.339	-0.126	50.720
140.0	25.876	0.438	141.4	19.762	0.334	18.946	-0.041	5.946
145.0	29.683	0.686	146.2	22.761	0.526	23.354	0.026	1.272
155.0	38.059	0.543	155.9	29.381	0.419	28.787	-0.020	2.008
165.0	44.239	0.589	165.6	34.308	0.457	31.342	-0.086	42.137

^{27}Al PROTON ELASTIC SCATTERING ANALYZING POWERS

Monitor Analyzing Power 0.984 ± 0.010

Excitation Energy (J^{π}) 0.00 MeV ($5/2^{+}$)

experimental data			calculation			
θ_{Lab}	$A_y(\theta_{Lab})$	$\Delta A_y(\theta_{Lab})$	θ_{cm}	$A_y(\theta_{cm})$	Dev	χ^2
20.0	-0.035	0.003	20.7	-0.036	-0.001	0.058
30.0	-0.056	0.009	31.1	-0.047	0.009	1.113
40.0	0.076	0.010	41.4	0.072	-0.004	0.162
50.0	0.241	0.015	51.7	0.273	0.032	4.751
60.0	0.161	0.015	61.9	0.137	-0.024	2.543
70.0	-0.078	0.023	72.0	-0.168	-0.090	15.979
80.0	-0.264	0.018	82.1	-0.342	-0.079	20.163
90.0	-0.470	0.021	92.2	-0.459	0.012	0.316
100.0	-0.443	0.020	102.1	-0.565	-0.123	38.365
110.0	0.007	0.033	112.0	-0.046	-0.052	2.485
120.0	0.465	0.041	121.9	0.375	-0.090	4.734
130.0	0.750	0.022	131.7	0.477	-0.273	155.418
135.0	0.846	0.019	136.5	0.504	-0.343	325.518
140.0	0.818	0.018	141.4	0.527	-0.290	262.929
145.0	0.807	0.023	146.2	0.550	-0.257	119.609
155.0	0.708	0.016	155.9	0.558	-0.150	91.720
165.0	0.479	0.016	165.6	0.422	-0.057	13.320

^{27}Al PROTON ELASTIC SCATTERING CROSS SECTIONS

Proton Energy	11.0 MeV	
Normalization, Normalization Uncertainty	0.72	5%
Excitation Energy (J^{π})	0.00 MeV	$(5/2^{+})$

not renormalized			renormalized			calculation		
θ_{Lab}	$\sigma(\theta_{Lab})$	$\Delta\sigma(\theta_{Lab})$	θ_{cm}	$\sigma(\theta_{cm})$	$\Delta\sigma(\theta_{cm})$	$\sigma(\theta_{cm})$	Dev	χ^2
110.0	5.110	0.182	112.0	3.778	0.135	4.583	0.213	35.615
120.0	7.510	0.320	121.9	5.620	0.239	6.558	0.167	15.355
130.0	16.308	0.337	131.7	12.338	0.255	10.067	-0.184	79.444
140.0	27.229	0.446	141.4	20.797	0.341	16.979	-0.184	125.648

^{27}Al PROTON ELASTIC SCATTERING ANALYZING POWERS

Monitor Analyzing Power	0.986 ± 0.010	
Excitation Energy (J^{π})	0.00 MeV	$(5/2^{+})$

experimental data			calculation			
θ_{Lab}	$A_y(\theta_{Lab})$	$\Delta A_y(\theta_{Lab})$	θ_{cm}	$A_y(\theta_{cm})$	Dev	χ^2
110.0	-0.068	0.055	112.0	0.147	0.214	15.353
120.0	0.360	0.063	121.9	0.377	0.017	0.077
130.0	0.424	0.030	131.7	0.350	-0.074	6.194
140.0	0.516	0.023	141.4	0.447	-0.070	9.462

^{27}Al PROTON ELASTIC SCATTERING CROSS SECTIONS

Proton Energy 12.0 MeV

Normalization, Normalization Uncertainty 0.72 5%

Excitation Energy (J^{π}) 0.00 MeV ($5/2^{+}$)

not renormalized			renormalized			calculation		
θ_{Lab}	$\sigma(\theta_{Lab})$	$\Delta\sigma(\theta_{Lab})$	θ_{cm}	$\sigma(\theta_{cm})$	$\Delta\sigma(\theta_{cm})$	$\sigma(\theta_{cm})$	Dev	χ^2
20.0	1860.315	7.926	20.7	1249.150	5.322	1218.411	-0.025	33.361
30.0	448.501	4.445	31.1	302.835	3.002	364.910	0.205	427.692
40.0	117.922	1.073	41.4	80.217	0.730	59.945	-0.253	771.569
50.0	40.748	0.561	51.7	27.975	0.385	30.253	0.081	34.948
60.0	45.843	0.424	61.9	31.812	0.294	32.863	0.033	12.748
70.0	55.647	0.733	72.0	39.072	0.514	32.064	-0.179	185.557
80.0	44.218	0.451	82.1	31.445	0.321	31.813	0.012	1.310
90.0	24.211	0.405	92.2	17.444	0.292	19.799	0.135	65.264
100.0	9.757	0.161	102.1	7.123	0.118	6.343	-0.110	43.854
110.0	4.035	0.129	112.0	2.984	0.095	4.101	0.375	137.637
120.0	7.882	0.240	121.9	5.899	0.180	6.922	0.173	32.392
130.0	14.012	0.226	131.7	10.602	0.171	10.010	-0.056	11.951
135.0	17.243	0.243	136.5	13.111	0.185	12.355	-0.058	16.746
140.0	19.943	0.276	141.4	15.232	0.211	15.149	-0.005	0.155
145.0	22.997	0.434	146.2	17.637	0.333	17.798	0.009	0.234
155.0	30.065	0.354	155.9	23.212	0.273	20.979	-0.096	66.685
165.0	36.178	0.401	165.6	28.059	0.311	22.634	-0.193	304.835

^{27}Al PROTON ELASTIC SCATTERING ANALYZING POWERS

Monitor Analyzing Power 0.988 ± 0.010

Excitation Energy (J^{π}) 0.00 MeV ($5/2^{+}$)

experimental data			calculation			
θ_{Lab}	$A_y(\theta_{Lab})$	$\Delta A_y(\theta_{Lab})$	θ_{cm}	$A_y(\theta_{cm})$	Dev	χ^2
20.0	-0.086	0.003	20.7	-0.057	0.029	118.729
30.0	-0.104	0.008	31.1	-0.091	0.013	2.742
40.0	0.062	0.011	41.4	0.086	0.024	5.109
50.0	0.507	0.017	51.7	0.534	0.027	2.476
60.0	0.138	0.010	61.9	0.171	0.033	10.160
70.0	-0.244	0.013	72.0	-0.251	-0.007	0.262
80.0	-0.518	0.011	82.1	-0.447	0.071	41.943
90.0	-0.730	0.020	92.2	-0.579	0.151	57.290
100.0	-0.624	0.023	102.1	-0.637	-0.013	0.322
110.0	0.345	0.043	112.0	0.367	0.022	0.254
120.0	0.271	0.044	121.9	0.332	0.062	1.994
130.0	-0.022	0.023	131.7	0.203	0.225	95.117
135.0	0.029	0.021	136.5	0.251	0.222	117.432
140.0	0.152	0.019	141.4	0.341	0.189	95.969
145.0	0.283	0.025	146.2	0.440	0.157	39.413
155.0	0.571	0.015	155.9	0.575	0.004	0.072
165.0	0.499	0.014	165.6	0.490	-0.009	0.425

^{27}Al PROTON ELASTIC SCATTERING CROSS SECTIONS

Proton Energy	13.0 MeV	
Normalization, Normalization Uncertainty	0.72	5%
Excitation Energy (J^{π})	0.00 MeV	($5/2^{+}$)

not renormalized			renormalized			calculation		
θ_{Lab}	$\sigma(\theta_{Lab})$	$\Delta\sigma(\theta_{Lab})$	θ_{cm}	$\sigma(\theta_{cm})$	$\Delta\sigma(\theta_{cm})$	$\sigma(\theta_{cm})$	Dev	χ^2
110.0	6.344	0.203	112.0	4.691	0.150	4.313	-0.081	6.346
120.0	11.002	0.391	121.9	8.235	0.292	7.706	-0.064	3.264
130.0	15.186	0.324	131.7	11.491	0.245	10.184	-0.114	28.466
140.0	17.476	0.349	141.4	13.349	0.266	13.450	0.008	0.145

^{27}Al PROTON ELASTIC SCATTERING ANALYZING POWERS

Monitor Analyzing Power	0.987 ± 0.010	
Excitation Energy (J^{π})	0.00 MeV	($5/2^{+}$)

experimental data			calculation			
θ_{Lab}	$A_y(\theta_{Lab})$	$\Delta A_y(\theta_{Lab})$	θ_{cm}	$A_y(\theta_{cm})$	Dev	χ^2
110.0	0.547	0.046	112.0	0.525	-0.022	0.218
120.0	0.404	0.052	121.9	0.282	-0.122	5.548
130.0	0.105	0.032	131.7	0.073	-0.031	0.955
140.0	0.155	0.030	141.4	0.218	0.063	4.484

^{27}Al PROTON ELASTIC SCATTERING CROSS SECTIONS

Proton Energy 14.0 MeV

Normalization, Normalization Uncertainty 0.72 5%

Excitation Energy (J^{π}) 0.00 MeV ($5/2^{+}$)

not renormalized			renormalized			calculation		
θ_{Lab}	$\sigma(\theta_{Lab})$	$\Delta\sigma(\theta_{Lab})$	θ_{cm}	$\sigma(\theta_{cm})$	$\Delta\sigma(\theta_{cm})$	$\sigma(\theta_{cm})$	Dev	χ^2
20.0	1593.684	6.623	20.7	1070.000	4.447	1005.225	-0.061	212.167
30.0	378.592	3.854	31.1	255.577	2.602	286.102	0.119	137.627
40.0	58.229	0.685	41.4	39.606	0.466	31.895	-0.195	273.689
50.0	22.776	0.404	51.7	15.634	0.278	18.852	0.206	134.404
60.0	49.862	0.553	61.9	34.598	0.384	31.695	-0.084	57.252
70.0	56.146	0.884	72.0	39.423	0.621	31.136	-0.210	178.240
80.0	37.832	0.489	82.1	26.904	0.348	26.071	-0.031	5.748
90.0	16.518	0.415	92.2	11.901	0.299	14.245	0.197	61.380
100.0	7.429	0.185	102.1	5.424	0.135	4.639	-0.145	33.916
110.0	6.475	0.164	112.0	4.788	0.121	5.022	0.049	3.750
120.0	11.384	0.290	121.9	8.521	0.217	8.629	0.013	0.248
130.0	13.886	0.224	131.7	10.508	0.170	10.371	-0.013	0.650
135.0	14.289	0.182	136.5	10.866	0.138	11.082	-0.020	2.436
140.0	14.839	0.233	141.4	11.336	0.178	11.877	0.048	9.286
145.0	15.176	0.287	146.2	11.640	0.220	12.564	0.079	17.701
155.0	16.474	0.209	155.9	12.721	0.161	13.109	0.030	5.763
165.0	18.049	0.221	165.6	14.001	0.172	13.780	-0.016	1.660

^{27}Al PROTON ELASTIC SCATTERING ANALYZING POWERS

Monitor Analyzing Power 0.985 ± 0.010

Excitation Energy (J^{π}) 0.00 MeV ($5/2^{+}$)

experimental data			calculation			
θ_{Lab}	$A_y(\theta_{Lab})$	$\Delta A_y(\theta_{Lab})$	θ_{cm}	$A_y(\theta_{cm})$	Dev	χ^2
20.0	-0.069	0.004	20.7	-0.083	-0.014	12.376
30.0	-0.142	0.011	31.1	-0.153	-0.011	0.941
40.0	-0.009	0.020	41.4	-0.034	-0.024	1.436
50.0	0.636	0.031	51.7	0.659	0.024	0.585
60.0	0.084	0.014	61.9	0.094	0.010	0.505
70.0	-0.198	0.019	72.0	-0.296	-0.098	25.710
80.0	-0.464	0.016	82.1	-0.513	-0.048	8.893
90.0	-0.732	0.032	92.2	-0.650	0.082	6.493
100.0	-0.432	0.036	102.1	-0.368	0.064	3.159
110.0	0.473	0.041	112.0	0.596	0.123	8.917
120.0	0.344	0.037	121.9	0.255	-0.089	5.734
130.0	0.057	0.024	131.7	-0.017	-0.074	9.169
135.0	0.029	0.019	136.5	-0.012	-0.041	4.591
140.0	0.086	0.023	141.4	0.092	0.006	0.067
145.0	0.214	0.026	146.2	0.258	0.044	2.704
155.0	0.528	0.017	155.9	0.583	0.055	10.110
165.0	0.557	0.016	165.6	0.588	0.031	3.536

^{27}Al PROTON ELASTIC SCATTERING CROSS SECTIONS

Proton Energy 16.0 MeV

Normalization, Normalization Uncertainty 0.72 5%

Excitation Energy (J^{π}) 0.00 MeV ($5/2^{+}$)

not renormalized			renormalized			calculation		
θ_{Lab}	$\sigma(\theta_{Lab})$	$\Delta\sigma(\theta_{Lab})$	θ_{cm}	$\sigma(\theta_{cm})$	$\Delta\sigma(\theta_{cm})$	$\sigma(\theta_{cm})$	Dev	χ^2
20.0	1317.009	5.329	20.7	884.145	3.578	869.884	-0.016	15.891
30.0	303.070	3.032	31.1	204.572	2.047	241.972	0.183	333.941
40.0	26.050	0.364	41.4	17.717	0.248	18.839	0.063	20.533
50.0	23.165	0.341	51.7	15.900	0.234	18.450	0.160	118.642
60.0	55.368	0.488	61.9	38.414	0.338	38.983	0.015	2.834
70.0	51.706	0.693	72.0	36.305	0.487	33.813	-0.069	26.205
80.0	28.611	0.328	82.1	20.347	0.234	21.014	0.033	8.174
90.0	12.376	0.265	92.2	8.917	0.191	10.006	0.122	32.604
100.0	7.891	0.143	102.1	5.761	0.104	5.218	-0.094	27.232
110.0	10.223	0.163	112.0	7.561	0.121	7.141	-0.056	12.111
120.0	13.069	0.265	121.9	9.782	0.198	9.757	-0.003	0.016
130.0	13.898	0.188	131.7	10.518	0.142	9.910	-0.058	18.240
135.0	12.669	0.171	136.5	9.635	0.130	9.536	-0.010	0.584
140.0	11.709	0.171	141.4	8.945	0.130	9.085	0.016	1.152
145.0	10.720	0.234	146.2	8.223	0.180	8.541	0.039	3.117
155.0	9.446	0.154	155.9	7.295	0.119	7.252	-0.006	0.126
165.0	8.963	0.153	165.6	6.954	0.119	6.824	-0.019	1.200

^{27}Al PROTON ELASTIC SCATTERING ANALYZING POWERS

Monitor Analyzing Power 0.974 ± 0.010

Excitation Energy (J^{π}) 0.00 MeV ($5/2^{+}$)

experimental data			calculation			
θ_{Lab}	$A_y(\theta_{Lab})$	$\Delta A_y(\theta_{Lab})$	θ_{cm}	$A_y(\theta_{cm})$	Dev	χ^2
20.0	-0.092	0.002	20.7	-0.106	-0.015	37.771
30.0	-0.230	0.007	31.1	-0.213	0.017	5.919
40.0	-0.374	0.016	41.4	-0.351	0.023	2.051
50.0	0.440	0.017	51.7	0.459	0.019	1.319
60.0	0.034	0.008	61.9	0.022	-0.012	2.078
70.0	-0.214	0.012	72.0	-0.254	-0.040	11.035
80.0	-0.484	0.011	82.1	-0.496	-0.012	1.243
90.0	-0.578	0.022	92.2	-0.587	-0.008	0.139
100.0	0.165	0.022	102.1	0.147	-0.018	0.665
110.0	0.637	0.017	112.0	0.634	-0.003	0.032
120.0	0.429	0.023	121.9	0.319	-0.110	22.853
130.0	0.055	0.016	131.7	-0.024	-0.079	22.912
135.0	-0.017	0.017	136.5	-0.099	-0.083	23.435
145.0	0.119	0.027	146.2	0.098	-0.022	0.658
155.0	0.714	0.017	155.9	0.606	-0.108	38.290
165.0	0.863	0.017	165.6	0.791	-0.072	18.760

^{27}Al PROTON ELASTIC SCATTERING CROSS SECTIONS

Proton Energy 17.0 MeV

Normalization, Normalization Uncertainty 0.72 5%

Excitation Energy (J^{π}) 0.00 MeV ($5/2^{+}$)

not renormalized			renormalized			calculation		
θ_{Lab}	$\sigma(\theta_{Lab})$	$\Delta\sigma(\theta_{Lab})$	θ_{cm}	$\sigma(\theta_{cm})$	$\Delta\sigma(\theta_{cm})$	$\sigma(\theta_{cm})$	Dev	χ^2
20.0	1274.889	5.122	20.7	855.777	3.438	824.999	-0.036	80.134
30.0	298.983	3.022	31.1	201.814	2.040	227.608	0.128	159.893
40.0	20.547	0.319	41.4	13.973	0.217	14.208	0.017	1.177
50.0	31.147	0.404	51.7	21.379	0.278	20.169	-0.057	19.018
60.0	62.392	0.534	61.9	43.287	0.371	44.554	0.029	11.676
70.0	52.672	0.704	72.0	36.979	0.495	35.728	-0.034	6.404
80.0	25.658	0.303	82.1	18.244	0.215	18.263	0.001	0.007
90.0	11.264	0.176	92.2	8.116	0.127	8.124	0.001	0.004
110.0	10.159	0.185	112.0	7.513	0.137	8.156	0.086	21.951
120.0	11.573	0.293	121.9	8.663	0.220	9.396	0.085	11.144
130.0	11.896	0.206	131.7	9.003	0.156	8.828	-0.019	1.265
135.0	11.469	0.196	136.5	8.722	0.149	8.354	-0.042	6.122
140.0	9.552	0.184	141.4	7.298	0.140	7.856	0.077	15.867
145.0	9.530	0.267	146.2	7.311	0.205	7.260	-0.007	0.061
155.0	7.318	0.161	155.9	5.652	0.125	5.728	0.013	0.374
165.0	6.498	0.162	165.6	5.042	0.126	4.695	-0.069	7.644

^{27}Al PROTON ELASTIC SCATTERING ANALYZING POWERS

Monitor Analyzing Power 0.968 ± 0.010

Excitation Energy (J^{π}) 0.00 MeV ($5/2^{+}$)

experimental data			calculation			
θ_{Lab}	$A_y(\theta_{Lab})$	$\Delta A_y(\theta_{Lab})$	θ_{cm}	$A_y(\theta_{cm})$	Dev	χ^2
20.0	-0.114	0.002	20.7	-0.115	-0.001	0.124
30.0	-0.273	0.007	31.1	-0.235	0.038	29.297
40.0	-0.526	0.018	41.4	-0.560	-0.033	3.621
50.0	0.384	0.015	51.7	0.368	-0.016	1.150
60.0	0.010	0.008	61.9	0.017	0.007	0.888
70.0	-0.235	0.012	72.0	-0.199	0.036	9.368
80.0	-0.481	0.011	82.1	-0.437	0.043	14.334
90.0	-0.414	0.017	92.2	-0.454	-0.040	5.346
110.0	0.624	0.021	112.0	0.664	0.039	3.388
120.0	0.370	0.030	121.9	0.447	0.077	6.563
130.0	0.016	0.022	131.7	0.107	0.090	17.282
135.0	-0.062	0.022	136.5	0.004	0.066	9.126
140.0	-0.044	0.024	141.4	0.010	0.054	4.904
145.0	0.119	0.035	146.2	0.136	0.017	0.239
155.0	0.627	0.025	155.9	0.649	0.022	0.791
165.0	0.832	0.025	165.6	0.960	0.128	26.830

BIBLIOGRAPHY

Adair 54 — R.K. Adair, S.E. Darden, and R.E. Fields, "Scattering of Polarized Neutrons from Heavy Nuclei," Physical Review 96 (1954) 503-507.

Ajzenberg 74 — F. Ajzenberg-Selove and T. Lauritsen, "Energy Levels of Light Nuclei A = 5 - 10," Nuclear Physics A227 (1974) 1-244.

Barschall 52 — H.H. Barschall, "Regularities in the Total Cross Sections for Fast Neutrons," Physical Review 86 (1952) 431.

Batchelor 63 — R. Batchelor and J.H. Towle, "The Interactions of Neutrons with ^{6}Li and ^{7}Li between 1.5 and 7.5 MeV," Nuclear Physics 47 (1963) 385-407.

Becchetti 69 — F.D. Becchetti, Jr. and G.W. Greenlees, "Nucleon-Nucleus Optical-Model Parameters, A > 40, E < 50 MeV," Physical Review 182 (1969) 1190-1209.

Beyerle 81 — A.G. Beyerle, "Double Differential Continuum Neutron Scattering Cross Sections in Iron and Nickel for Incident Energies of 7.5, 10 and 12 MeV," Ph.D. Dissertation, N.C. State University, 1981.

BNL 64 — J.R. Stehn, M.D. Goldberg, B.A. Magurno, and R. Wiener-Chasman, "Neutron Cross Sections Volume 1, Z = 1 to 20," Brookhaven National Laboratory Report 325, Second Edition, Supplement No. 2, 1964.

Brieva 77A — F.A. Brieva and J.R. Rook, "Nucleon-Nucleus Optical Model Potential (I). Nuclear Matter Approach," Nuclear Physics A291 (1977) 299-316.

Brieva 77B — F.A. Brieva and J.R. Rook, "Nucleon-Nucleus Optical Model Potential (II). Finite Nuclei," Nuclear Physics A291 (1977) 317-341.

Clegg 74 — T. Clegg, G. Bissinger, and T. Trainor, " A Lamb-Shift Polarized Ion

Source for the TUNL Tandem Accelerator," Nuclear Instruments and Methods 120 (1974) 445-464.

Cook 49 L.J. Cook, E.M. McMillan, J.M. Peterson, and D.C. Sewell, "Total Cross Sections of Nuclei for 90-MeV Neutrons," Physical Review 75 (1949) 7-14.

Davé 83 J.H. Davé and C.R. Gould, "Optical Model Analysis of Scattering of 7-to 15-MeV Neutrons from 1-p Shell Nuclei," Physical Review C28 (1983) 2212-2221.

Fernbach 49 S. Fernbach, R. Serber, and T.B. Taylor, "The Scattering of High Energy Neutrons by Nuclei," Physical Review 75 (1949) 1352-1355.

Feshbach 53 H. Feshbach, C.E. Porter and V.F. Weisskopf, "The Formation of a Compound Nucleus in Neutron Reactions," Physical Review 90 (1953) 166-167.

Feshbach 54 H. Feshbach, C.E. Porter, and V.F. Weisskopf, "Model for Nuclear Reactions with Neutrons," Physical Review 96 (1954) 448-464.

Glasgow 76 D.W. Glasgow, F.O. Purser, H. Hogue, J.C. Clement, K. Stelzer, G. Mack, J.R. Boyce, D.H. Epperson, S.G. Buccino, P.W. Lisowski, S.G. Glendinning, E.G. Bilpuch, H.W. Newson, and C.R. Gould, "Differential Elastic and Inelastic Scattering of 9- to 15-MeV Neutrons from Carbon," Nuclear Science and Engineering 61 (1976) 521-533.

Greenlees 69 G.W. Greenlees, G.J. Pyle, and Y.C.Tang, "Nuclear-Matter Radii from a Reformulated Optical Model," Physical Review 171 (1968) 1115-1136.

Haeberli 74 W. Haeberli, "Direct Interaction," Lecture Notes in Physics 30 (1974) 229-267.

Hansen 85 L.F. Hansen, F.S. Dietrich, B.A. Pohl, C.H. Poppe, and C. Wong, "Test of Microscopic Optical Model Potentials for Neutron Elastic Scattering at

14.6 MeV Over a Wide Mass Range," Physical Review C31 (1985) 111-119.

Harrison 63 W.D. Harrison and A.B. Whitehead, "Elastic Scattering of Protons by ^{6}Li," Physical Review 132 (1963) 2607-2613.

Hodgson 63 P.E. Hodgson, The Optical Model of Elastic Scattering, (Clarendon Press, Oxford, 1963).

Hodgson 71 P.E. Hodgson, Nuclear Reactions and Nuclear Structure, (Clarendon Press, Oxford, 1971).

Hofmann 83 H.M. Hofmann and T. Mertelmeier, "The Nuclear Systems ^{7}Li and ^{7}Be in a Resonating Group Model," Nuclear Physics A410 (1983) 208-236.

Hofmann 84 H. M. Hofmann, "Resonating Group Calculations in Nuclear Few Cluster Systems," Nuclear Physics A416 (1984) 363-378.

Hogue 79 H.H. Hogue, P.L. von Behren, D.W. Glasgow, S.G. Glendinning, P.W. Lisowski, C.E. Nelson, F.O. Purser, and W. Tornow, "Elastic and Inelastic Scattering of 7- to 14-MeV Neutrons from ^{6}Li and ^{7}Li," Nuclear Science and Engineering 69 (1979) 22-29.

Honoré 83 G.M. Honoré, "JANE User's Manual," 1983 (unpublished).

Howell 84 C.R. Howell, "Neutron Scattering from ^{28}Si and ^{32}S: Cross Sections and Analyzing Powers from 8 to 40 MeV," Ph.D. Dissertation, Duke University, 1984.

Jeukenne 77A J.-P. Jeukenne, A. Lejeune, and C. Mahaux, "Microscopic Calculation of the Symmetry and Coulomb Components of the Complex Optical-Model Potential," Physical Review C15 (1977) 10-28.

Jeukenne 77B J.-P. Jeukenne, A. Lejeune, and C. Mahaux, "Optical-Model Potential in Finite Nuclei from Reid's Hard Core Interaction," Physical Review C16

(1977) 80-96.

Knox 79 H.D. Knox, R.M. White, and R.O. Lane, "Differential Neutron Scattering Cross Sections of ^{6}Li and ^{7}Li for Neutrons of 4 to 7.5 MeV Energy," Nuclear Science and Engineering 69 (1979) 223-230.

Lane 64 R.O. Lane, A.J. Elwyn, and A. Langsdorf, Jr., "Polarization and Differential Cross Section for Neutrons Scattered from ^{6}Li and ^{7}Li," Physical Review 136 (1964) 1710-1719.

Li 85 A. Li, C.R. Howell, R.K. Murphy, H.G. Pfützner, M.L. Roberts, and R.L. Walter, "Analyzing Powers for Elastic Neutron Scattering from ^{14}N and ^{16}O," Bulletin of the American Physical Society, 30 (1985) 797.

Li 86 A. Li, H.G. Pfützner, M.L. Roberts, C.R. Howell, K. Murphy, and R.L. Walter, "Analyzing Power Measurements for Neutron Elastic Scattering from ^{14}N," Journal of the Physical Society of Japan 55 (1986) 564-565.

Lisowski 75 P.W. Lisowski, R.L. Walter, C.E. Busch, and T.B. Clegg, "Polarization Transfer in the ^{2}H($\bar{d}$,$\bar{n}$)^{3}He Reaction at $\theta = 0^{o}$," Nuclear Physics A242 (1975) 298-308.

Marmier 69 P. Marmier and E. Sheldon, Physics of Nuclei and Particles Vol. I, (Academic Press, New York, 1969).

Martin 86 P. Martin and R.L. Walter, "Analyzing Power of ^{27}Al($\bar{n}$,n_{o}) at 14 and 17 MeV and the Isospin Dependence of the Optical Model," Physical Review C34 (1986) 384-388.

Mellema 83 S. Mellema, R.W. Finlay, F.S. Dietrich, and F. Petrovich, "Microscopic and Conventional Optical Model Analysis of Fast Neutron Scattering from ^{54,56}Fe," Physical Review C28 (1983) 2267-2277.

Murphy 84 R.K. Murphy, "The Nucleon-Nucleus Systems for ^{9}Be, ^{11}B, and ^{10}B - the Lane Model and the Role of Isospin," Ph.D. Dissertation, Duke

University, 1984.

Murphy 87 K. Murphy, R.C. Byrd, C.E. Floyd, P.P. Guss, G. Tungate, C.R. Howell, H.G. Pfützner, A. Li, P.D. Felsher, and R.L. Walter, "Measurements of $\sigma(\theta)$ and $A_y(\theta)$ for $^{10}B(n,n)^{10}B$ and $^{10}B(p,p)^{10}B$ and Determination of Coulomb Corrections for ^{10}B," Nuclear Physics, in press.

Pedroni 86 R.S. Pedroni, "Cross Sections and Analyzing Powers in the 8- to 17-MeV Range for Neutron Scattering from $^{54,56}Fe$, $^{58,60}Ni$, ^{93}Nb, and ^{120}Sn," Ph.D. Dissertation, Duke University 1986.

Perey 63 F.G. Perey, "Optical-Model Analysis of Proton Elastic Scattering in the Range of 9 to 22 MeV," Physical Review 131 (1963) 745-763.

Petler 85 J.S. Petler, M.S. Islam, R.W. Finlay, and F.S. Dietrich, "Microscopic Optical Model Analysis of Nucleon Scattering from Light Nuclei," Physical Review C32 (1985) 673-684.

Pfützner 86 H.G. Pfützner, A. Li, K. Murphy, C.R. Howell, M.L. Roberts, I. Slaus, R.L. Walter, M. Herman, and H.M. Hofmann, "Measurements of $A_y(\theta)$ for Neutron and Proton Scattering from ^6Li between 5 and 17 MeV Compared to Resonating Group Calculations," Journal of the Physical Society of Japan 55 (1986) 556-557.

Rapaport 82 J. Rapaport, "An Optical Model Analysis of Neutron Scattering," Physics Reports 87 (1982) 25-75.

Roy 83 R. Roy, C.R. Lamontagne, R.J. Slobodrian, J. Arvieux, J. Birchall, and H.E. Conzett, "Diffusion des Protons Polarisés sur ^{24}Mg, ^{27}Al et ^{32}S et Anomalies dans la Région des Résonances Géantes de l'^{25}Al, du ^{28}Si et du ^{33}Cl," Nuclear Physics A411 (1983) 1-16.

Satchler 83 G.R. Satchler, Direct Nuclear Reactions, (Clarendon Press, Oxford, 1983).

Schwandt 71 P. Schwandt, T.B. Clegg, and W. Haeberli, "Polarization Measurements and Phase Shifts for p-^{4}He Scattering between 3 and 8 MeV," Nuclear Physics A163 (1974) 432-448.

Smith 82 A.B. Smith, P.T. Guenther, and J.F. Whalen, "Neutron Total and Scattering Cross Sections of ^{6}Li in the Low-MeV Range," Nuclear Physics A373 (1982) 305-325.

Tamura 65 T. Tamura, "Analyses of the Scattering of Nuclear Particles by Collective Nuclei in Terms of the Coupled-Channel Calculation," Reviews of Modern Physics 37 (1965) 679-708.

Trainor 73 T.A. Trainor, "Polarized Ion Source Development and the Lowest T = 3/2 Level in ^{41}Sc," Ph.D. Dissertation, University of North Carolina at Chapel Hill, 1973.

Varner 85 R.L. Varner, "UNC XSYStem Programming Guide," 1985 (unpublished).

Varner 86 R.L. Varner, "A Parameterization of the Nucleon-Nucleus Optical Model Potential," Ph. D. Dissertation, University of North Carolina at Chapel Hill, 1986.

Walt 54 M. Walt and H.H. Barschall, "Scattering of 1-MeV Neutrons by Intermediate and Heavy Elements," Physical Review 93 (1954) 1062-1068.

Wheeler 37A J.A. Wheeler, "Molecular Viewpoints in Nuclear Structure," Physical Review 52 (1937) 1083-1106.

Wheeler 37B J.A. Wheeler, "On the Mathematical Description of Light Nuclei by the Method of Resonating Group Structure," Physical Review 52 (1937) 1107-1122.

Whisnant 84 C.S. Whisnant, J.H. Dave, and C.R. Gould, "Elastic and Inelastic Neutron Scattering from ^{27}Al at 11, 14, and 17 MeV," Physical Review C30 (1984) 1435-1441.

Wildermuth 77 K. Wildermuth and Y.C. Tang, A Unified Theory of the Nucleus, (Academic Press, New York, 1977).

Wong 75 C.W. Wong, "Generator-Coordinate Methods in Nuclear Physics," Physics Reports 15 (1975) 283-357.

BIOGRAPHY

Harold Gerdes Pfützner

Born: April 23, 1959
New York, New York

Education: Randolph-Macon College B.S. with honors 1980
Duke University A.M. 1982

Positions: Research Assistant, Duke University 1982-1987
Teaching Assistant, Duke University 1980-1982

Honorary Societies:

Phi Beta Kappa
Chi Beta Phi (honorary science fraternity)
Sigma Pi Sigma
Omicron Delta Kappa (national honorary service fraternity)

Professional Societies: American Physical Society

Publications:

1. "Measurements of $A_y(\theta)$ for Neutron and Proton Elastic Scattering from ^{6}Li between 5 and 17 MeV Compared to Resonating Group Calculations," H.G. Pfützner, A. Li, K. Murphy, C.R. Howell, M.L. Roberts, I. Slaus, R.L. Walter, M. Herman, and H.M. Hofmann, Proceedings of the Sixth International Symposium on Polarization Phenomena in Nuclear Physics Osaka, edited by M. Kondo, S. Kobayashi, M. Tanifuji, T. Yamazaki, K.I. Kubo, and N. Onishi. (Supplement to Journal of the Physical Society of Japan, Vol. 55, 1986.) 556-557.

2. "Analyzing Power Measurements for Neutron Elastic Scattering from ^{14}N," A. Li, H.G. Pfützner, M.L. Roberts, C.R. Howell, K. Murphy, and R.L. Walter, *ibid.* 564-565.

3. "^{7}Li + p Elastic Scattering as a Proposed Test of Time Reversal Invariance," K.E. Sale, T.R. Donoghue, A. Abduljalil, J. Cummings, C. Rolfs, P. Schmalbrock,

R.G. Seyler, T. Clegg, E.J. Ludwig, R. Fauber, H. Pfützner, T. Spencer, R. Varner, S.E. Darden, and S. Sen, *ibid.* 992-993.

4. "Differential Cross Sections and Analyzing Powers for Neutron Elastic Scattering from ^{89}Y between 8 and 17 MeV," G.M. Honoré, R.S. Pedroni, C.R. Howell, H.G. Pfützner, R.C. Byrd, G. Tungate, and R.L. Walter, Physical Review C, 34 (1986) 825-834.

5. "Vector Analyzing Powers for N-d Elastic Scattering from 10 to 14 MeV," C.R. Howell, W. Tornow, I. Slaus, P.A. Treado, K. Murphy, H.G. Pfützner, M.L. Roberts, P.D. Felsher, and R.L. Walter, Bulletin of the American Physical Society, 31 (1986) 854.

6. "A Study of the n-d Breakup Reaction with Polarized Neutrons," C.R. Howell, I. Slaus, W. Tornow, P.A. Treado, H.G. Pfützner, Anli Li, M.L. Roberts, K. Murphy, P.D. Felsher, A. Naqvi, and R.L. Walter, Bulletin of the American Physical Society, 30 (1985) 1267.

7. "Nucleon Scattering from ^{11}B," K. Murphy, C.R. Howell, H.G. Pfützner, M.L. Roberts, Anli Li, and R.L. Walter, *ibid*, p. 796.

8. "Analyzing Powers for Elastic Neutron Scattering from ^{27}Al," P. Martin, H.G. Pfützner, Anli Li, M.L. Roberts, B. Smith, C.R. Howell and R.L. Walter, *ibid*, p. 1268.

9. "Analyzing Powers for Elastic Neutron Scattering from ^{14}N and ^{16}O," Anli Li, C.R. Howell, R.K. Murphy, H.G. Pfützner, M.L. Roberts, and R.L. Walter, *ibid*, p. 797.

10. "Analyzing Powers for Elastic and Inelastic Neutron Scattering from ^{6}Li," H.G. Pfützner, Anli Li, C.R. Howell, M.L. Roberts, I. Slaus, and R.L. Walter, Bulletin of the American Physical Society, 29 (1984) 1036.

11. "Scattering of 17-MeV Polarized Neutrons," C.R. Howell, R.S. Pedroni, G.M. Honoré, H.G. Pfützner, R.C. Byrd, and R.L. Walter, Bulletin of the American Physical Society, 28 (1983) 736.

12. "Elastic and Inelastic Scattering of Neutrons at Small Angles," R.E. Anderson, C.R. Gould, B.C. Karp, K.E. Nash, R.S. Pedroni, H.G. Pfützner, and R.L. Walter, *ibid*, p. 648.